EXAMINATION OF SMALL AND LARGE AMPLITUDE AEROELASTIC OSCILLATIONS IN PITCH OF A NACA0012 AIRFOIL

ÉTUDE D'OSCILLATIONS AÉROÉLASTIQUES EN TANGAGE DE PETITE ET GRANDE AMPLITUDES D'UNE AILE NACA0012

A Thesis Submitted to the Division of Graduate Studies
of the Royal Military College of Canada
by

Luke H. Peristy, BSc

In Partial Fulfillment of the Requirements for the Degree of
Masters of Applied Science in Mechanical and Aerospace Engineering

October, 2014

Dedicated to Susan Howard-Peristy (1958-2013)

Acknowledgements

First of all, I'd like to thank Dr. Poirel for all his guidance throughout my research. He has been an invaluable resource, and always knew what direction to point me in before I took the next step in the process. I would also like to thank Dr. Yuan at the NRC for his assistance and expertise in performing the CFD calculations. Dr. Yuan was always available via phone or email to help me get past any technical bugs or flaws in my understanding. I also thank him for personally hacking together the code that allowed post-processing of the C_f data after the Neptune server was taken offline for reasons of National Security. I would also like to thank Andre Charbonneau at the NRC for his technical assistance.

I'd like to thank past and current members of The Junior Choir including Omar, Dan, Des, Sean, Brenda, Ruben (or Dr. Perez as he insists on being called at work), Jon, Steve, Pete, Dave, Austin, and New Steve. You were always up for a beer and a discussion about anything except our research. I'd especially like to acknowledge Jon's contributions to the social calendar, as he was always willing to open up his home so we could enjoy some brews and some BBQ.

I'd like to thank Dave and Tom for always being ready and willing to compare notes on the various day-to-day frustrations, and I thank them for being valuable outlets. Similarly, a special thanks goes to my Ph.D student friends Ross, Kyle, Atif, Jordan, and Amelia for their encouragement and commiseration.

I'd like to thank my housemates, Garrett, Colin, and Charlie. We survived two moves and innumerable nights out, and it is in spite, not because, of them that my Masters was not the best 3 years of my life.

I'd like to acknowledge the contributions of various friends. I thank the West Coast Offices of Nathan and Jake, The North West Company headed by Kieran, the Western Ontario Dynamic Duo of Derrick and Isabelle, the Toronto Bureau consisting of Peter, Andy, Liz, Angie, Mackenzie, Amanda, Carolyn, and Janson, the Cobourg Crew including Matt, Brad, Shawn, Cas-

sandra, and Adam, and of course the Ottawa Division AKA Adam. These people were all annoyingly interested in my progress and I knew that if I didn't finish, they'd never let me live it down.

I'd also like thank Jeff and Madelaine for many lunches and dinners they graciously provided me at their home.

Finally,I'd also like to acknowledge the support of my family over the past two years. They've been hugely supportive throughout my time at RMC.

Abstract

One degree of freedom aeroelastic oscillations in pitch of a NACA0012 airfoil at transitional Reynolds numbers were examined experimentally in a wind tunnel using a pitching wing whose elastic axis is at 35% of the chord length from the leading edge. It was found that over the range of airspeeds between 5.2 and 10.3 m/s ($5.3\times10^4 < \mathrm{Re} < 1.1\times10^5$) two distinct limit cycle oscillation regimes existed. The large amplitude oscillation (LAO) regime was characterized by oscillation amplitudes of >25 degrees. The small amplitude oscillation regime (SAO) was characterized by oscillation amplitudes of <3 degrees. The regime that is exhibited by the system is dependant on the initial conditions. Two-dimensional unsteady Reynolds averaged Navier Stokes computations using the $\gamma - Re_\theta$ model were performed in order to gain physical insight into the flow field and aerodynamic forces at play.

Examination of the flow field throughout a small amplitude oscillation cycle shows trailing edge separation which moves towards the leading edge of the wing as the AOA increases. Turbulent transition also occurs near the trailing edge. This leads to a lag between the aerodynamic moment and pitch as the wing pitches through a small amplitude oscillation cycle. It is this lag that feeds the small amplitude limit cycle oscillations by applying the pitching moment about zero degrees AOA. The power spectral density of the small amplitude oscillation computational C_m and C_l data shows frequency peaks at the fundamental frequency of the limit cycle oscillations, the third harmonic, and also a peak that corresponds to von Karman vortex shedding.

Examination of the flow field throughout an LAO cycle shows that trailing edge separation starts at low AOAs (5 degrees) and quickly moves up towards the leading edge as the angle of attack increases. Counter-rotating vortices meet at the leading edge of the wing close to the maximum angle of attack leading to massive stall which causes the wing to pitch down and maintains the oscillation cycle. The power spectral density of the large amplitude oscillation computational Cm and Cl data shows only the fundamental oscillation frequency and several harmonics, indicating that flow transition is not related

to the large amplitude oscillations.

Résumé

Des oscillations aéroélastiques à un degré de liberté en tangage d'une aile NACA0012 à des nombres de Reynolds transitionnels sont étudiées expérimentalement dans une soufflerie à l'aide d'une aile libre dont l'axe de rotation est situé à 0.35c. On a observé que sur la gamme de vitesses de l'air entre 5.2 et 10.3 m/s ($5.3 \times 10^4 < \mathrm{Re} < 1.1 \times 10^5$) deux régimes distincts de cycle limite existaient. Le régime d'oscillations à grandes amplitudes était caractérisé par des amplitudes d'oscillation >25 degrés. Le régime d'oscillations à petites amplitudes était caractérisé par des amplitudes d'oscillation <3 degrés. Le régime exhibé par le système dépend des conditions initiales. Des simulations numériques en deux dimensions de type URANS (Unsteady Reynolds Averaged Navier-Stokes) qui utilisent le modèle $\gamma - Re_\theta$ furent entreprises afin de solidifier une compréhension physique de l'écoulement et des forces aérodynamiques en présence. L'examen de l'écoulement durant un cycle d'oscillations à petites amplitudes indique un décollement de la couche limite au bord de fuite qui remonte vers le bord d'attaque à mesure que l'angle d'attaque augmente. La transition vers la turbulence se produit aussi près du bord de fuite. Ceci amène à un retard du moment aérodynamique alors que l'aile tangue autour de son axe de rotation. C'est ce retard qui produit et maintient les oscillations à petites amplitudes. La densité spectrale de puissance des C_m et C_l provenant des simulations numériques montre des pics à la fréquence fondamentale du cycle limite, à sa troisième harmonique et aussi à des fréquences qui correspondent à des lâchers de tourbillons de type von Karman. L'examen de l'écoulement durant un cycle d'oscillations à grandes amplitudes indique un décollement de la couche limite au bord de fuite qui commence à de faibles angles d'attaque (5 degrés) et qui remonte rapidement vers le bord d'attaque à mesure que l'angle d'attaque augmente. Des tourbillons contrarotatifs se rencontrent au bord d'attaque lorsque l'aile est près de son angle maximum amenant à un décollement massif qui cause un tangage vers le bas et le maintien du cycle d'oscillations. La densité spectrale de puissance des Cm et Cl provenant des simulations numériques montre seulement des pics à la fréquence fondamen-

tale du cycle limite et à plusieurs de ses harmoniques, cela indiquant que la transition n'est pas reliée aux oscillations de grandes amplitudes.

Contents

List of Tables

List of Figures

Nomenclature

α	Angle of attack	^{o}
μ_t	Eddy viscosity	Pa· s
ω_d	Natural frequency	rad/s
ω_n	Natural frequency	$\frac{rads}{s}$
ρ	Air density	kg/m^3
τ_{ij}	Subgrid stresses used in the Smagorinsky-SGS CFD model	m^2/s
θ	Angle of attack or wing pitch	^{o}
ζ	Simple harmonic oscillator damping ratio	
c	Wing chord length	m
C_l	Lift coefficient	
C_m	Pitching moment coefficient	
D_θ	Pitch damping coefficient	N·m·s/rad
e	Distance from the aerodynamic centre to the elastic axis	m
I_{EA}	Airfoil moment of inertia about the elastic axis	kg·m^2
k	Turbulent kinetic energy	m/s
K_θ	Pitch stiffness	N·m/rad
L_e	Turbulent length scale	m
M_{EA}	Pitching moment about the elastic axis	N·m
n	Direction normal to the surface	
s	Wing span	m
T_u	Turbulent intensity	
U	Airspeed	m/s
u'	Turbulent fluctuation from the mean airspeed in the U direction	m/s

U_{div}	Divergence airspeed	m/s
v'	Turbulent fluctuation from the mean airspeed in the V direction	m/s
Re_θ	Reynolds number based on momentum thickness	
Re_c	Reynolds number based on chord length	
St	Strouhal number	

1 Introduction

1.1 Motivation and Objectives

This work focuses on free oscillations in pitch of a NACA0012 airfoil at transitional Reynolds numbers (4.8×10^4 — 1.1×10^5) where the airfoil has an elastic axis that is located 35% of the chord length ($0.35c$) from the leading edge. Smooth airfoils are noted to undergo a drastic change in performance at this range of Reynolds numbers such that the lift-to-drag ratio improves by an order of magnitude [1]. This is related to the phenomena of laminar separation, turbulent transition, and reattachment. These types of flow conditions are common for aircraft of small sizes, such as UAVs or micro air vehicles, or for high altitude flight where the density of the air is drastically decreased. Wind turbine rotors also operate within the transitional Reynolds number regime.

In this operational regime and given that the airfoil in question has an elastic axis (EA) aft of the aerodynamic centre (AC), the aerodynamic moment would be expected to statically destabilize the wing in a phenomenon known as divergence. However, divergence is a linear aeroelastic phenomenon and due to the transitional Reynolds number effects, non-linear dynamics are observed resulting in limit cycle oscillations (LCOs).

Existing research on this particular problem is limited. Therefore, this work seeks to characterize the limit cycle oscillations, make use of numerical models to gain insights into the flow field, and examine stability phenomena that may exist in the airfoil's pitch dynamics at these Reynolds numbers.

The experimental work has been carried out using a pitch-heave aeroelastic test rig at the Royal Military College of Canada (RMCC), and builds on the work of previous students, researchers, and collaborators such as Harris [2], Metivier [3], Rudmin [4], Mendes [5], Khalil [6], Sandhu [7], Benaissa [4], Yuan [8], and Dumas [9]. In addition, two-dimensional (2D) computations have been performed in order to attain greater insight into both the aerodynamics and the interaction between the structure and the airflow. The computational

fluid dynamics (CFD) work has been done in collaboration with Dr. Weixing Yuan at the National Research Council of Canada (NRC).

1.2 Conceptual Background

1.2.1 Linear Aeroelasticity

Aeroelastic phenomena involve the interaction between structural dynamics and aerodynamics. These two dynamics can act in a feedback loop wherein a change in the structural dynamics will cause a change in the aerodynamics, and vice versa. This can be modelled generally in one degree of freedom (1DOF) as seen in equation (1.1) below, where the aerodynamic forces are shown on the right hand side.

$$I_{EA}\ddot{\theta} + D_\theta\dot{\theta} + K_\theta\theta = M_{aero}(\theta, \dot{\theta}, \ddot{\theta}, t) \tag{1.1}$$

In linear aerodynamics, the coefficient of lift is assumed to be linear with angle of attack (AOA), and the lift force can be treated as acting from the point known as the aerodynamic centre (AC). The AC is defined as the point on the airfoil at which the pitching moment coefficient (C_m) does not vary with the AOA, or more generally $dC_m/d\alpha = 0$. The AC is assumed to be at the quarter chord point ($0.25c$ from the leading edge) for thin airfoils in subsonic flow. The coefficient of lift of a 2D airfoil is defined as

$$C_l \equiv \frac{F_L}{\frac{1}{2}\rho U_\infty^2 c} \tag{1.2}$$

where F_L is the lift force per unit length of span of the wing. Since $C_l = 2\pi\alpha$ for a symmetrical airfoil in steady, unstalled conditions transitional Reynolds numbers, the lift force can be obtained as follows:

$$L = \rho U^2 c\pi\theta \tag{1.3}$$

where θ is the AOA. For 1DOF in pitch, the elastic axis (EA) is the term given to the point about which the airfoil pitches. Assuming a distance of e from the AC to the EA, the moment from the lift force about the EA is given as follows:

$$M_{EA} = e(\rho U^2 c\pi\theta) + M_{AC} \tag{1.4}$$

A schematic of a symmetrical wing which visualizes these terms can be seen in Figure 1.1 below.

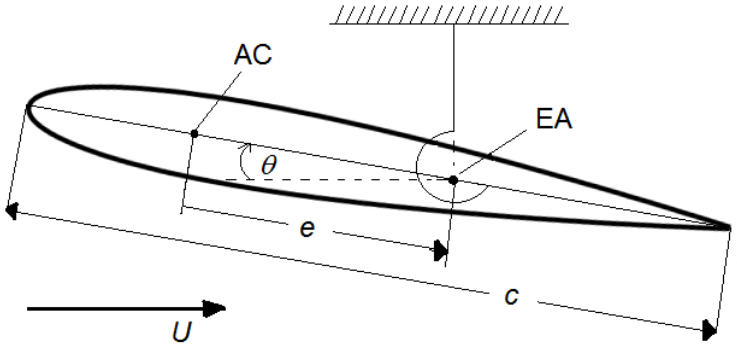

Figure 1.1: Schematic of a spring-supported, symmetric airfoil.

If the EA is aft of the AC, and $M_{AC} = 0$ for a symmetrical airfoil, which is the case here, then given a high enough airspeed there will be a statically destabilizing effect on the airfoil which will manifest as divergence i.e. the airfoil will pitch up and flip to its maximum physical limit. However, in this work, divergence does not occur because of non-linear aerodynamic effects such as boundary layer separation, laminar separation bubble formation, and stall.

1.2.2 Boundary Layer Separation and Laminar Separation Bubbles

The separation of the boundary layer leads to a non-linear relationship between the aerodynamic loads and the airfoil AOA. Boundary layer separation requires an adverse pressure gradient, such that the static pressure in the boundary layer increases in the streamwise direction along the surface i.e. $\partial P/\partial s > 0$. The adverse pressure gradient decelerates the fluid in the boundary layer, and reversed flow can occur. Analytically, the point of separation is defined as the location on the surface where the shear stress becomes zero i.e. $\mu(\partial u/\partial n) = 0$. Following the separation of the boundary layer, a laminar separation bubble or a free shear layer may occur. A laminar separation bubble is typified by a recirculation region within the bubble, transition of the flow from laminar to turbulent, and the reattachment of the flow as a turbulent boundary layer, whereas if the flow does not reattach, a free shear layer results. A schematic of the development of a laminar separation bubble can be seen in Figure 1.2.

Turbulent flows inherently contain more momentum than laminar flows of

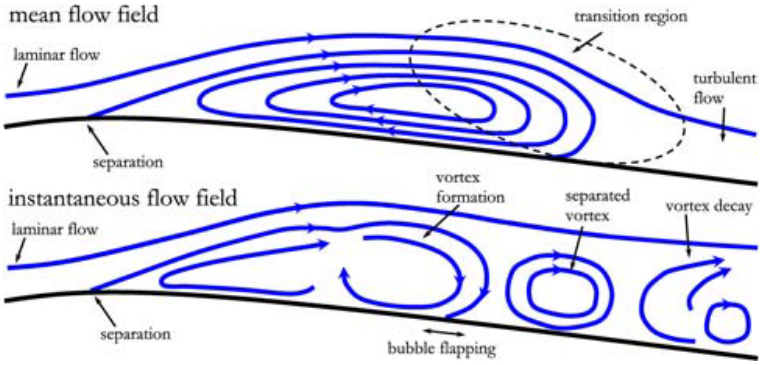

Figure 1.2: Mean and instantaneous flow field of a separation bubble. Taken from Burgmann and Schroeder [10]

the same mean speed, and therefore may stay attached to the surface when laminar flows do not. At the Reynolds numbers in question, these boundary layer separations generally do not reattach to the airfoil. Separation, transition, and reattachment are closely related to stall. In particular, leading edge stall is common on symmetrical airfoils with thickness-to-chord ratios of between 0.09 and 0.15, as is used in this work.

Static stall refers to a drop in the lift force on the airfoil at a certain critical angle of attack. There may be unsteady aerodynamic effects in static stall, but typically the structure is considered to be steady or quasi-steady such that the time scale of the structural changes (i.e. change in angle of attack) is much longer than the time scale of the unsteady aerodynamics. This is in contrast to dynamic stall in which airfoils move through their static stall angles fast enough that the boundary layer stays attached as a layer of reversed flow starts from the trailing edge and works its way up towards the leading edge. This results in a large vortex near the leading edge of the wing. Stall flutter is more closely related to dynamic stall. In stall flutter, at a high angle of attack, the C_l curve slope, C_{l_α}, will be locally negative. This causes negative aerodynamic damping that may result in self-sustained oscillations in a neighbourhood where there is both negative and positive damping. The negative damping causes the initial loss of equilibrium whereas the positive damping causes the re-stabilization resulting in an LCO.

1.2.3 Limit Cycle Oscillations

Limit cycle oscillations (LCOs) are a dynamic behaviour typical of nonlinear systems. A classic example of a non-linear system that results in LCOs is the

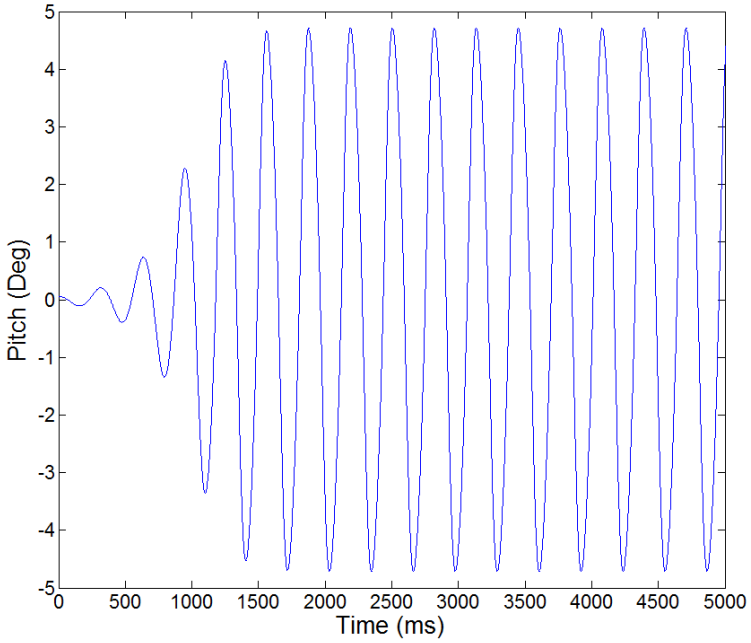

Figure 1.3: Typical dynamic response of a van der Pol oscillator given a small initial perturbation.

van der Pol Equation.

$$\ddot{\theta} + \nu(\theta^2 - 1)\dot{\theta} + \kappa\theta = 0, \nu > 0 \tag{1.5}$$

In equation (1.5), there is a negative linear damping term such that the amplitude of the oscillations grow until the θ^2 term becomes large enough to limit the amplitude. An LCO is therefore characterized by a stable oscillation of constant amplitude following a period of transient destabilization. This can be seen in Figure 1.3. The nature of the transient oscillations is dependant on the initial conditions or perturbation given to the system. These characteristics make the van der Pol model a good phenomenological representation of the system dynamics, as LCOs are seen throughout this work.

2 Literature Review

2.1 Limit Cycle Oscillations

Most research on aeroelastic LCOs has focussed on oscillations caused either by non-linear structural elements, shockwave-boundary layer interaction, or stall flutter at high angles of attack. This work focusses on flutter caused by Reynolds number dependant non-linear aerodynamics and builds on the work of Poirel, Harris, and Benaissa. Poirel *et al.* examined self-sustained aeroelastic oscillations of a NACA0012 airfoil. These were characterized using the same rig detailed in this work but focused on cases where the elastic axis (EA) was positioned at 0.10c, 0.18c, and 0.27c [11]. It was found that the behaviour of the airfoil was defined by constant amplitude oscillations about zero degrees angle of attack (AOA) for Reynolds numbers between ($4.5 \times 10^4 \leq Re_c \leq 1.3 \times 10^5$) and that these oscillations were not sustained outside of this range, although it has also been shown that for a high enough structural stiffness, no LCO results. Poirel *et al.* also examined the effect of varying the structural stiffness of the airfoil over a range of Reynolds numbers. It was found that regardless of the EA position or structural stiffness, the LCO pitch frequency is characterized by a monotonic increase with airspeed. In addition, the LCO amplitude increases initially with airspeed before reaching a critical level (5 deg) and then declining as the airspeed is increased. It should also be noted that when the EA is aft of the quarter chord point (EA= $0.25c$), which is generally thought to be the aerodynamic centre (AC) of a airfoil in subsonic flow, there is no oscillation for the $K_\theta = 0$ case in accordance with linear aerodynamic theory, which predicts that an elastic axis aft of the AC should have a statically destabilizing effect. The case where $K_\theta = 0.30$ N·m/rad is of particular interest as it is equal to the structural parameters in this work. For this case, the range of LCO frequencies as airspeed increases becomes more narrow as the EA is moved aft.

Poirel *et al.* also examined the flowfield one chord length aft of the airfoil using a hot wire probe. One dimensional turbulent kinetic energy spectra

displayed peaks at f, where f is the frequency of the LCO, as well as odd and even harmonics. The even harmonics are attributed an imperfect alignment between the airfoil and flow; the odd harmonics are attributed to non-linear aerodynamic effects. The hotwire measurements also revealed a broadband peak at 236 Hz in the wake which is not found in the pitch spectra due to the inability of the potentiometer to detect the super high frequencies. In order to further examine this high frequency peak in the wake, the wake was examined for the case of a non-pitching airfoil. In this case, the wake displayed a peak at 253 Hz in both velocity components in addition to a secondary peak at 506 Hz. There is no peak at any frequencies less than 100 Hz. This indicates that the low frequency spectral peaks in the wake are related to the frequency of the structural oscillation rather than aerodynamic behaviour.

Poirel *et al.* conclude that this high frequency spectral peak, which corresponds to a Strouhal number of $St_T = 0.62$, is representative of von Karman vortex shedding, as per Huang and Lee [12] [13] [14]. This vortex shedding frequency was shown to be highly sensitive to the airfoil AOA, as an increase in AOA would transform the shedding into the subcritical mode and then the transitional or supercritical mode. The subcritical mode is characterized by purely laminar boundary layer separation whereas the supercritical mode is characterized by either a dramatic rise in Strouhal number. The lowering of the spectral peak when the airfoil is oscillating is therefore an average of the vortex shedding frequencies at each angle of the pitching motion.

Poirel *et al.* then speculate that a laminar separation bubble (LSB) and trailing edge separation are the physical processes at work. This is consistent with the fact that the oscillations disappeared for free-stream turbulence intensities larger than 0.4% [8]. Ultimately, they conclude by speculating that the oscillations are somehow initiated by laminar trailing edge separation, with the limit cycle being associated with the presence of an LSB.

Dimitriadis and Li [15] examined a NACA0012 airfoil undergoing stall flutter at similar Reynolds numbers, but with a wing that had a higher structural stiffness than what was used in this work. Dimitriadus and Li also allowed for two degree of freedom (2DOF) oscillations in pitch and heave. They found was that the system was prone to both symmetric and asymmetric LCOs where stall flutter was a significant factor. The symmetric LCOs were characterized by being centred about 0 degrees AOA, whereas the asymmetric LCOs were centred about ± 15 degrees AOA. The symmetric LCOs occurred at an airspeed from 13 to >27 m/s (Re$\approx 4.5 \times 10^4 - > 1.3 \times 10^5$), whereas the asymmetric LCOs were present from 18 to 27 m/s (Re$\approx 6.5 \times 10^4 - 1.3 \times 10^5$). They describe the stall flutter induced LCOs using different types of bifurcation. The symmetric LCOs are described using a subcritical Hopf bifurcation

coupled with a fold. This is caused by dynamic stall. The asymmetric LCOs are described using a homoclinic figure-eight bifurcation. The homoclinic bifurcation allows for symmetric or asymmetric LCOs to be present at the same airspeed. They speculate that the asymmetric LCOs are driven by static divergence. The presence of the symmetric LCOs in a airspeed regime where the asymmetric LCOs are present is caused by the interaction of the static divergence and dynamic stall.

Razak *et al.* [16] examined a pitch/plunge system similar to that of Dimitriadis and Li using a NACA0018 wing to allow for instrumentation with pressure sensors. Particle image velocimetry (PIV) measurements were also used. They examined only the asymmetric LCOs where the wing had a static equilibrium angle of attack of $11^o - 16^o$ and Reynolds numbers between 2.6×10^5 and 6.3×10^5. The presence of the supercritical Hopf bifurcation was seen in addition to the presence of both low amplitude and high amplitude LCOs. The PIV measurements showed that the low-amplitude LCOs were characterized by periodically stalled flow covering the rear part of the wing, whereas the high-amplitude LCOs were characterized by both unsteady trailing edge separation and steady leading edge separation.

2.2 Flow Separation on Airfoils

Laminar flow separation and vortex shedding of airfoils have been examined by different groups using a variety of techniques.

Rudmin *et al.* [4] used uncalibrated surface hot films and phase analysis to determine the location of the flow separation and reattachment of a NACA0012 airfoil. Reynolds numbers of 6.2×10^4, 8.2×10^4, and 1.13×10^5 were examined. The work consisted of static cases where the airfoil AOA was fixed between 0 and 5 degrees, and a quasi-static case where the AOA was varied between 0 and 6 degrees at a low frequency of $f = 0.0025$ Hz. The static and quasi-static results show that as Reynolds number is increased for a given AOA, the separation starts farther aft along the airfoil, but the length of the separation bubble also becomes shorter. At the two lower Reynolds numbers, the data showed late onset flow separation with no reattachment below 2 degrees AOA. A lack of re-attachment was thought to be indicative of continuous recirculation, whereas the unsteady reattachment was thought to be associated with vortex roll-up at a high frequency. The results were quantitatively different than Huang *et al.* [12], but this was thought to be due to the prevalence of 3D effects in Huang's work, whereas Rudmin *et al.* used endplates in the apparatus to achieve 2D flow.

Burgmann and Schroeder used scanning particle-image velocimetry (PIV) measurements on the suction side of an SD7003 airfoil to examine the separation bubble [10] between Reynolds numbers of 2.0×10^4 and 6.0×10^4 and AOAs from 4 to 8 degrees. Their results show a strong dependence between the flow separation/reattachment point(s) and AOA, and a weaker, but still significant dependence between separation/reattachment point(s) and Reynolds number. At constant Reynolds numbers, increasing AOA leads to the separation and reattachment point moving forward. At constant AOA, increasing Reynolds number keeps the separation point roughly the same, but the bubble length decreases as the reattachment point moves forward. The Strouhal number of the associated Kelvin-Helmholtz (KH) instabilities was also noted, given that this phenomenon had been analysed numerically and experimentally by Watmuff [17], Yang and Voke [18], and Lang *et al.* [19] among others. Kelvin-Helmholtz instabilities typically occur where there is a velocity shear, such as in the boundary layer of the flow over an airfoil. At constant Reynolds number, the KH Strouhal number decreases with increasing AOA, and at constant AOA, the KH Strouhal number increases with Reynolds number. By varying the turbulent intensity, it was found that the separation bubble would either disappear or was unable to be resolved due to the lack of sufficient spatial resolution. Bergmann and Schroeder also examined the 3D geometry of the associated vortices, showing the development of c-shaped vortices into arc-like structures into a pair of counter-rotating vortex arms (i.e. a screwdriver vortex pair) across a variety of Reynolds numbers. Again, these vortices are thought to occur from a mechanism similar to a Kelvin-Helmholtz instability.

Yarusevych *et al.* [20] examined the development of coherent structures in the separated shear layer and wake of a NACA0025 airfoil using hot wire probes and a smoke wire for flow visualization. This was done over the range of Reynolds numbers $5.5 \times 10^4 \leq Re_c \leq 2.1 \times 10^5$ and at AOAs of 0, 5 and 10 degrees. They found a vortex breakdown process and Strouhal number trends similar to those observed by Bergmann and Schroeder, but conclude that the behaviour is highly dependant on Reynolds number and the nature of the flow regime.

McAuliffe and Yaras [21] investigated the instability mechanism leading to transition and separation bubbles using direct numerical simulation (DNS). Although the simulations took place at a higher Reynolds number than the previous work ($3 \times 10^5 \leq \mathrm{Re} \leq 5 \times 10^5$), they found similar trends and concluded that transition is induced by shear layer instability consistent with Kelvin-Helmholtz type, and that higher Reynolds numbers result in both an earlier transition and a reduction in separation bubble length.

2.3 Computational Fluid Dynamics and LCOs

Yuan *et al.* [22] built on the work of Poirel *et al.* [11] by coupling a one degree of freedom (1DOF) structural model with an in-house CFD code known as INSFLOW. These calculations were performed using identical physical parameters as used experimentally. Initial calculations were performed using both three dimensional (3D) and two dimensional (2D) large eddy simulation (LES). The calculations exhibited behaviour that was quantitatively and qualitatively similar to the experiments in both the presence of LCOs and the frequency and amplitude thereof. The preliminary conclusion was that the over the course of an oscillation cycle, laminar separation moved forwards and backwards along the chord length of the wing causing a fluctuation. It is the delay between the movement of the separation point and the pitching of the wing that feeds the LCO.

Subsequent work by Wang *et al.* [23] and Yuan *et al.* [8] then examined the effect of turbulent intensity (T_u) on the simulation of LCOs. To this effect, a modified version of Menter's SST two-equation model known as the $\gamma - Re_\theta$ model was used in 2D URANS simulations. Increasing the T_u resulted in smaller LCO amplitudes, with LCOs disappearing altogether when the freestream turbulence reached 1.25 %. Effect of the turbulent length scale (L_e) was also examined. An increase in L_e led to an increase in pitch amplitude at constant T_u, although it was found that ${}_Le$ was of secondary importance.

Following the success of the 1DOF simulations, Yuan *et al.* then examined the 2DOF pitch-heave problem [24]. What was thought to be classical flutter had been observed experimentally in the 2DOF at Re= $77,000$ with a frequency of 2.9 Hz, pitch amplitude of 5.7 degrees, and heave amplitude of 1.36 mm. The simulations showed a frequency of 3.1 Hz, and pitch and heave amplitudes of 5.6 degrees and 1.1 mm respectively. The heave oscillations showed slight phase lag behind the pitch oscillations. It was also determined that the heave DOF did not appreciably affect the dynamics of the pitch LCOs as the pitch amplitude and frequency was only slightly increased. In addition, as the heave is of small amplitude, these LCOs can be thought of as a pitch-driven phenomenon.

Yabili *et al.* [25] performed 2D URANS simulations of stall flutter based on the experimental work of Dimitriadis discussed in Section 2.1 [15]. Yabili *et al.* developed their own solver using *OpenFOAM* known as $fsiFoam$ that would capture both the structural dynamics and aerodynamics in pitch and heave. They also noted that the damping of the experimental system was linear at high pitch angles but non-linear at low pitch angles. They developed an 11^{th} order polynomial to be used as the structural damping function. This

damping function was highly non-linear between ±10 degrees AOA, and linear outside of that range. Like in Wang *et al.* above, Menter's SST turbulence model was used. The solver had a 13% difference in the prediction of the stall angle when compared to experiment. The $fsiFoam$ simulations were able to demonstrate an LCO that was reasonably accurate when compared to the experimental frequency and amplitude, although they did this only at a single airspeed. However, they conclude by saying that detached eddy simulation or a hybrid RANS/LES scheme should be considered to better capture the detached flow.

Lapointe and Dumas [9] performed 2D URANS simulations of self-sustained pitch oscillations of a NACA0012 airfoil using the $\gamma - Re_\theta$ model. In contrast to the simulations in this work, Lapointe and Dumas fixed the airfoil at $0.186c$ from the leading edge. They used a non-conformal sliding interface in $OpenFOAM$ where the inner mesh containing the airfoil rotated inside a stationary outer mesh. The mesh was unstructured and contained roughly 80,000 points. Their results showed good agreement with Poirel *et al.* [11] in terms of the trend of the oscillation amplitudes and frequencies with increasing Reynolds number. They also investigated the effect of free stream turbulence intensity on the oscillations finding that the oscillations would not always be sustained at a turbulence level of 1%, and that no oscillations would appear when the free stream turbulence was increased to 2%. They conclude that laminar boundary layer separation is one of the necessary triggers of the oscillations, and that turbulent boundary layers are not conducive to LCOs.

3 Experimental Work

3.1 Experimental Setup

3.1.1 Physical Parameters

The test rig for the experiments has been used by Poirel, Benaissa, and others in the Department of Mechanical and Aerospace Engineering at the Royal Military College of Canada in a variety of other studies. The rig is in a test section which is 108.5 cm in width by 76 cm in height. This test section is, in turn, part of a closed-circuit wind tunnel. The free stream turbulence intensity has been measured at 0.16% in previous experiments [26]. A three-dimensional (3D) view of the test rig can be seen in Figure 3.1.

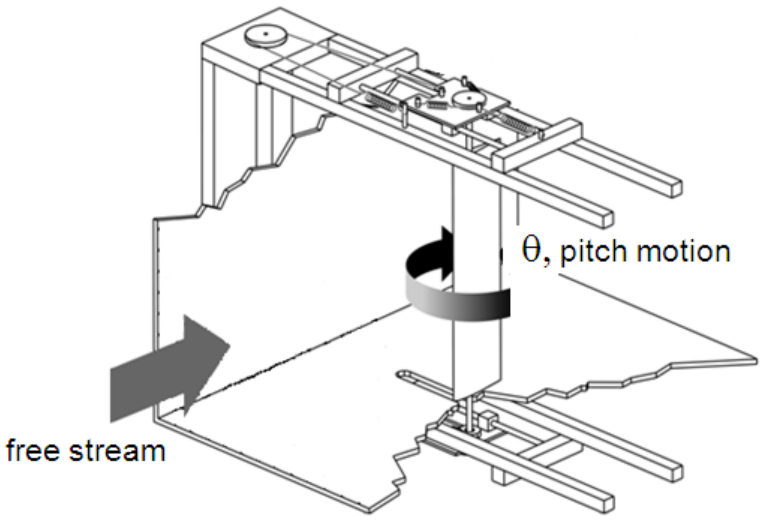

Figure 3.1: 3D view of test rig for aeroelastic oscillations in pitch.

The rig consists of two rods which are used to attach the airfoil to pulleys which are, in turn, attached to two coplanar springs using fishing line wrapped around the pulley. This is done to provide the wing with structural stiffness in the pitch degree of freedom. The rod and pulley assembly is also attached to translating heave plates on ball bearing assemblies which provided heave motion. However, these heave plates were fixed during the entirety of the experimental testing as only the pitch degree of freedom was of interest to this work. Both the pulleys and heave plates are outside the area of the test section through which there is flow. The structural properties of the NACA0012 wing can be seen in Table 3.1. Note that even though the aspect ratio (AR) is not large, end plates are installed in order to minimize 3D aerodynamic effects. While the test rig is capable of accommodating a variety of elastic axis (EA) positions on the airfoil, the EA remained fixed at 35% of the chord length from the leading edge of the wing for this current experimental study. This is a value that is a realistic comparison to the elastic axis of a real wing.

Table 3.1: Physical parameters of the experimental wing

Parameter	Constant
c (m)	0.156
l (m)	0.61
AR	3.91
EA	0.35c

3.1.2 Dynamic Parameters

For the case of no airflow, the airfoil and spring/pulley system can be modelled dynamically using the common viscous damped linear simple harmonic oscillator framework.

$$I_{EA}\ddot{\theta} + D_\theta\dot{\theta} + K_\theta\theta = 0 \tag{3.1}$$

By dividing equation (3.1) by the I_{EA}, defining the natural frequency, ω_n, as $\omega_n = \sqrt{K_\theta/I_{EA}}$, and defining the damping ratio, ζ, as $D_\theta/I_{EA} = 2\zeta\omega_n$, we arrive at the following canonical form of the simple harmonic oscillator.

$$\ddot{\theta} + 2\zeta\omega_n\dot{\theta} + {\omega_n}^2\theta = 0 \tag{3.2}$$

For the underdamped case where $0 < \zeta < 1$, it can be shown that the system will exhibit oscillatory behaviour with a damped natural frequency,

in addition to amplitudes displaying exponential decay. Given mathematical initial conditions $\theta(t_0) = theta_0$ and $\dot{\theta}(t_0) = 0$, the general mathematical form of this behaviour is

$$\theta(t) = e^{-\zeta\omega_n t}[\theta_0 \cos(\omega_d t)] \tag{3.3}$$

where $\omega_d = \omega_n\sqrt{1-\zeta^2}$. The moment of inertia (I_{EA}) of the setup was determined via previous experiments [2]. The damping and stiffness coefficients were determined by the results of a free-decay test, an example of which can be seen in Figure 3.2 below. Each peak of the free decay test has an amplitude and time associated with it. The amplitude will be related to the envelope function $e^{-\zeta\omega_n t}$. If the natural logarithm of the peak values are taken, this should result in points placed along a line with the slope $m = -\zeta\omega_n$. ω_d can be found by dividing the time elapsed between peaks by the number of oscillations and further dividing by 2π. Having determined the slope (m), and noting the damped frequency, the damping ratio can be found as follows:

$$\zeta = \sqrt{\frac{m^2}{m^2 + {\omega_d}^2}} \tag{3.4}$$

By definition, $\omega_n = \omega_d/\sqrt{1-\zeta^2}$. It is then trivial to find D_θ and K_θ as $D_\theta = 2I_{EA}\zeta\omega_n$ and $K_\theta = I_{EA}{\omega_n}^2$.

The individual stiffness and damping values calculated from the free decay test seen in Figure 3.2 can be seen in Figures 3.3 and 3.4 respectively. Figure 3.3 shows that the stiffness does not vary by more than 0.06 N·m/rad as the amplitude of the peaks decreases, and what variance does exist is caused by dry friction at low amplitudes. However, Figure 3.4 shows highly non-linear damping behaviour for peak amplitudes lower than 5 degrees. This is due to dry friction inherent in the system. When the oscillation amplitude is low, the corresponding derivative is small enough to allow the dry friction to dominate the linear viscous damping. This is what causes the non-linear damping at low amplitudes. In order to better capture this behaviour, when doing analysis the rig can be treated as having two different sets of dynamic properties for small and large amplitude oscillations. These parameters are summarized in Table 3.2 and Table 3.3.

In order to calculate the airspeed in the test section, the dynamic pressure was measured using a pitot-static tube connected to a manometer. This was measured at the beginning and end of each test in order to confirm a consistent airspeed throughout the test. An additional airflow concern was that of wind tunnel blockage or solid blockage. Solid blockage occurs when there is

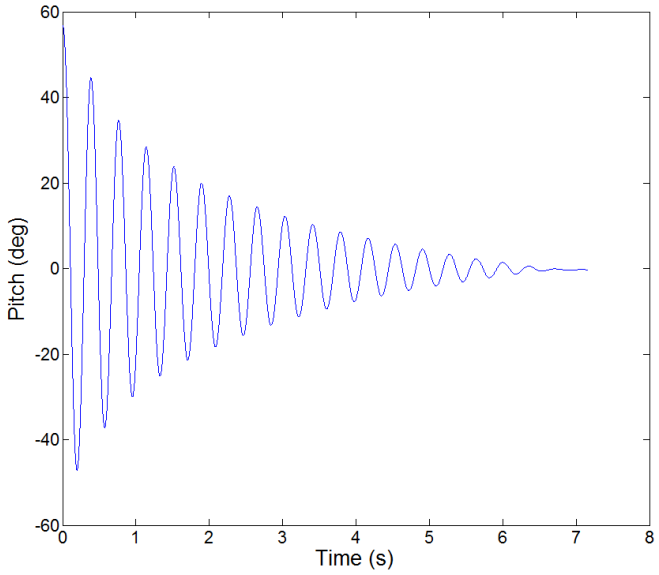

Figure 3.2: Pitch response of a typical free decay test.

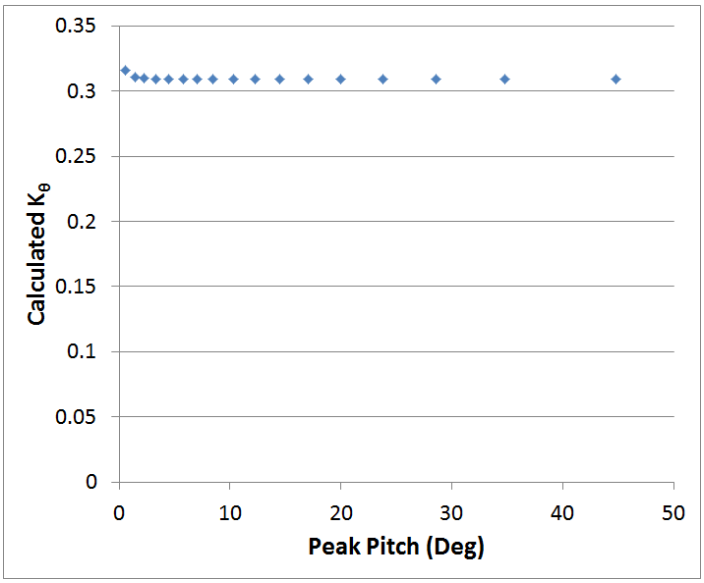

Figure 3.3: Plot of measured stiffness as a function of free decay test peak.

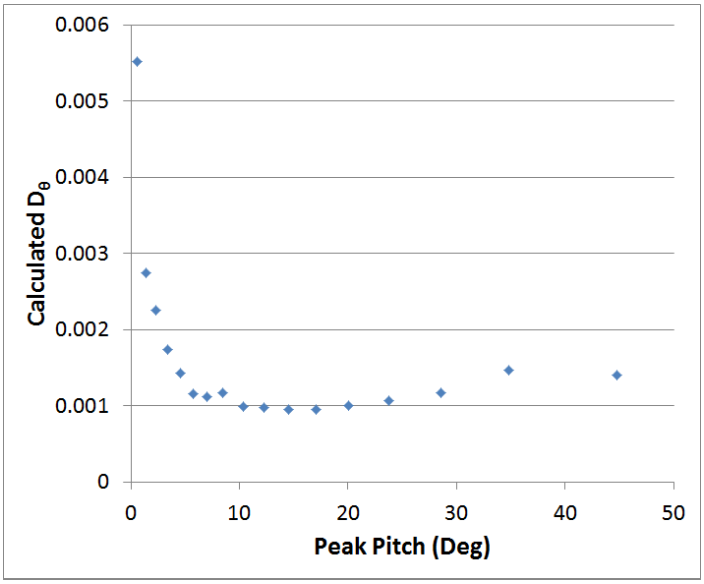

Figure 3.4: Plot of measured damping as a function of free decay test peak.

Table 3.2: Dynamic properties of the experimental rig for oscillations <5 deg.

Parameter	Constant
I_{EA} (kg m^2)	0.00110 ± 0.00002
D_θ (N m s)	0.0020 ± 0.0005
K_θ (N m/rad)	0.309 ± 0.006

Table 3.3: Dynamic properties of the experimental rig for oscillations >5 deg.

Parameter	Constant
I_{EA} (kg m^2)	0.00110 ± 0.00002
D_θ (N m s)	0.0010 ± 0.0001
K_θ (N m/rad)	0.309 ± 0.006

a reduction in flow (compared to the unrestricted free stream) caused by a reduction in test-section area. This can lead to locally increased velocities in the area of the test model or airfoil. Given the dimensions of the wind tunnel test section (108.5 cm $\times$ 76 cm) and the dimensions of the wing (61 cm $\times$ 15.6 cm), if we assume a maximum AOA of 40 degrees, the blockage ratio at this maximum AOA would be 7.4%. Barlow, Rae, and Pope suggest a maximum frontal-area to test section cross sectional area 7.5% [27] for low speed wind

tunnels. Given that the maximum blockage ratio is beneath this ratio and also transient, it can be assumed that wind tunnel blockage is a negligible effect.

3.1.3 Signal Acquisition and Processing

The pitch displacement of the airfoil was measured using a potentiometer mounted to the lower pitch pulley. The analog voltage across the potentiometer was measured using a LabVIEW-based data logging program. The sampling rate for each test was 1000 Hz, and each test was measured for 20 seconds. The potentiometer was calibrated and found to have a calibration constant of -0.0508 V/deg, which was linear in the range of interest. This can be seen in Figure 3.5. The analog data collected from each experiment was filtered using a digital low-pass finite impulse response filter whose cutoff frequency was selected to be high enough to preserve the higher harmonics, but also avoided artificial attenuation of the signal. A cutoff frequency of 12 Hz was used.

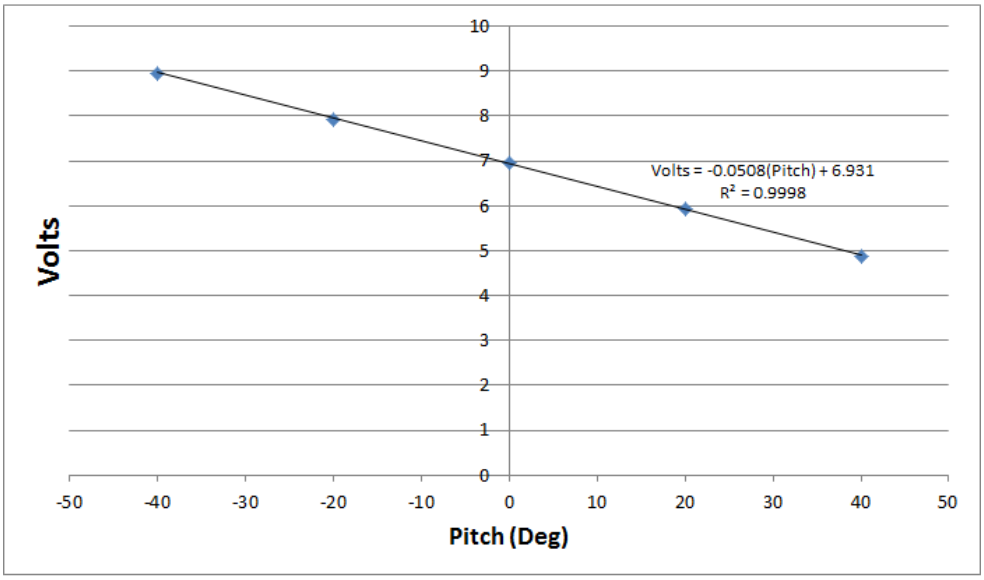

Figure 3.5: Calibration curve of the test potentiometer.

3.2 Experimental Results

3.2.1 Test Procedure

The experiments were carried out using a procedure in which the airspeed in the test section, as measured by pitot tube, was increased slowly until steady state oscillatory behaviour was observed. After this point, the wind tunnel airspeed was increased by increasing the wind tunnel fan speed by 10 to 15 RPM following each test. During each test, the wing was initially positioned with a zero degree angle of attack. Due to a small amount of dry friction neglected in equation (4.20), it was often necessary to provide a perturbation to the wing in order to destabilize the system. As will be seen, the size of the perturbation would affect the system response, so using variable perturbation size (3 to 15 degrees) was part of the test procedure. At certain airspeeds, two 20 second periods of pitch motion would be recorded, one to observe the transient behaviour following perturbation, and one to observe steady state behaviour. The wind tunnel fan speed was kept constant throughout each test to maintain airspeed. The pitot pressure gauge was capable of discerning between 0.5 Pa of pressure, giving each measured airspeed an error of less than 0.1 m/s.

3.2.2 LCO Behaviour

According to linear aerodynamics, it would be expected that any non-decaying response of the system would occur at or above the divergence airspeed. If one focusses only on the stiffness in pitch of the airfoil, the moment induced on a symmetrical airfoil about the EA by the lift is given as follows:

$$M_{EA} = e\left(\tfrac{1}{2}\rho U^2 cs2\pi\right)\theta \tag{3.5}$$

where e is the distance from the EA to the aerodynamic centre (AC) and is positive in the aft direction. If the EA is aft of the AC, this will have a statically destabilizing effect and is represented as a negative aerodynamic stiffness. The divergence airspeed is then given as the airspeed at which the aerodynamic stiffness is equal to the structural stiffness leading to

$$U_{div} = \sqrt{\frac{K_\theta}{e\rho cs\pi}} \tag{3.6}$$

For this airfoil structure, a divergence airspeed of U_{div}=7.45 m/s was calculated.

Of particular interest was the amplitude of the eventual limit cycle oscillations at different airspeeds. It was found that over the range of airspeeds between 5.25 and 10.3 m/s, two distinct LCO regimes existed. One regime was characterized by oscillation amplitudes of >25 degrees. This was called the large amplitude oscillation (LAO) regime. The second is characterized by oscillation amplitudes of <3 degrees. This was called the small amplitude oscillation (SAO) regime. These results are summarized in Figure 3.6. The airspeed was not increased past 10.3 m/s so as to maintain the structural integrity of the rig and airfoil. Some of the LCOs in the SAO regime were noted to decay and become damped out with time. However, this was not universal across all experiments and is thought to be a function of the effect of dry friction at small amplitudes. It should also be noted that while SAO amplitude was steady to within 0.5 degrees, LAO amplitudes could vary by as much as 2 degrees, although the amplitudes had a well defined average.

Where the LAO and SAO regimes overlap in terms of airspeed, the type of oscillation being observed was a function of the size of the perturbation given to the system. Examples of this can be seen in Figures 3.7 and 3.8. Figure 3.7 shows an LCO in the SAO regime caused by an initial perturbation of 8 degrees. Figure 3.8 shows an LCO in the LAO regime resulting from a much larger perturbation of roughly 30 degrees.

Also of interest is the frequency of the LCOs. The LAO regime exhibits a gradual increase in frequency with airspeed, whereas the SAO regime's frequencies start out higher at airspeeds below 7 m/s, make a sudden dip, and then increase with airspeed after 7.75 m/s. These results are summarized in Figure 3.9. The decrease in LCO frequency that starts at 7 m/s can likely be partially explained using linear aerodynamics. The M_{EA} as defined in (3.5) can be thought of as an aerodynamic stiffness term that acts on the same degree of freedom, θ, as the structural stiffness. If we substitute equation (3.5) into equation (4.20), we arrive at the following:

$$I_{EA}\ddot{\theta} + D_\theta\dot{\theta} + \left[K_\theta - e\left(\frac{1}{2}\rho U^2 cs2\pi\right)\right]\theta = 0 \tag{3.7}$$

This is obviously a very simplistic view of the situation, but from it we can see that as the airspeed, U, increases, it will decrease the effective stiffness of the system. This, in turn, will lower the frequency of oscillation as ω is proportional to $\sqrt{k}$. This is further supported by the fact that the frequency decreases around the divergence airspeed, when the effective stiffness of the system should be zero.

In order to determine the dominant frequency of the LAOs, the time between multiple peaks was divided by the number of peaks counted. This was

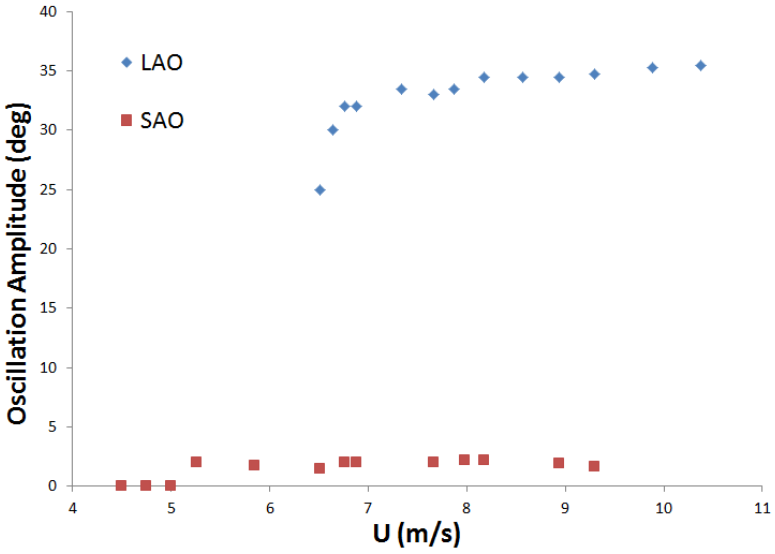

Figure 3.6: Experimental results showing LCO amplitude as a function of airspeed.

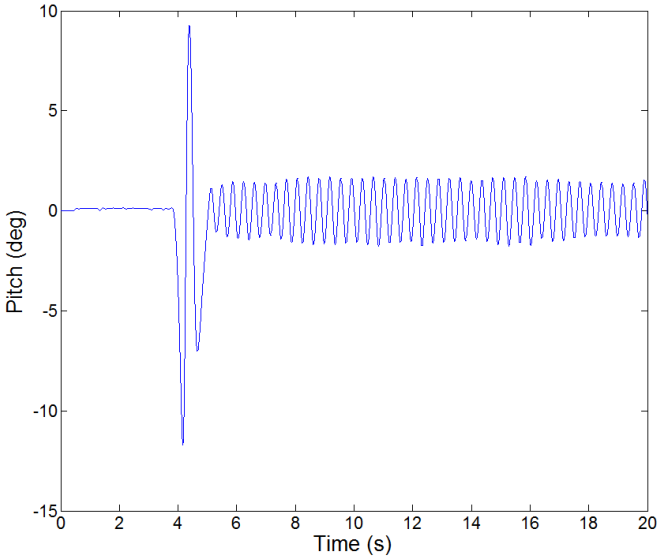

Figure 3.7: Pitch-time trace of an experiment run at 6.51 m/s where the system is given a perturbation of 9 degrees.

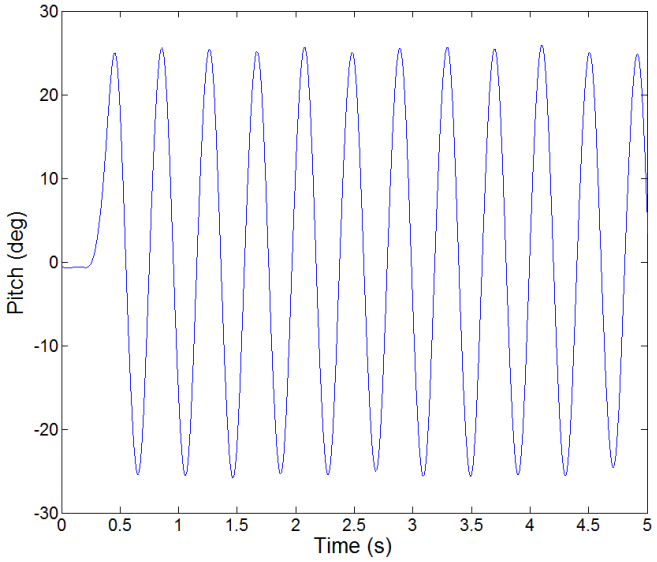

Figure 3.8: Pitch-time trace of an experiment run at 6.51 m/s where the system is given a perturbation of 25 degrees.

typically done over 10 cycles, or the greatest number of steady cycles available from the test results. This can also be compared to the dominant frequency according to the power spectral density (PSD) analysis. The PSDs for Figures 3.7 and 3.8 can be seen in Figures 3.10 and 3.11. Electrical noise that has a power of around 10^{-4} can be seen in these figures. This means that any SAO frequency data above 20 Hz cannot be relied upon, whereas the frequency data for the LAOs are accurate up to about Hz.

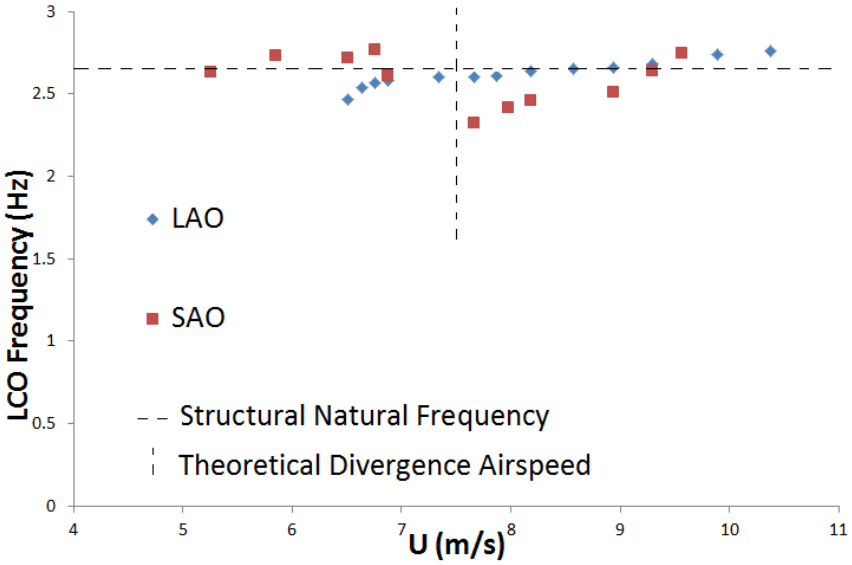

Figure 3.9: Experimental results showing LCO frequency as a function of airspeed.

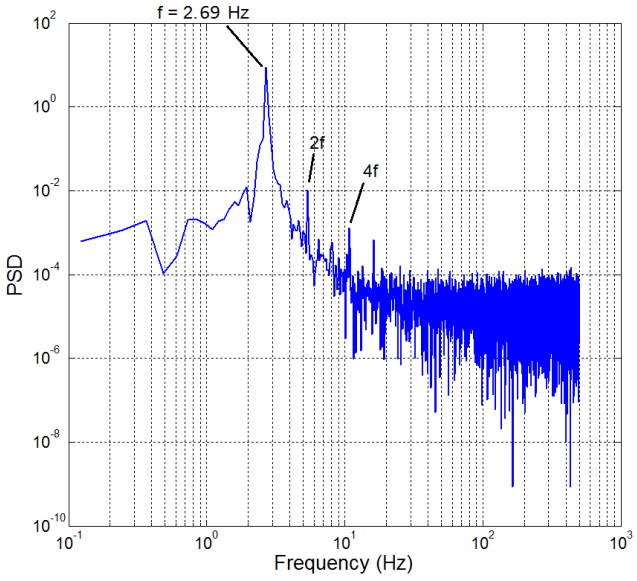

Figure 3.10: Pitch PSD of a SAO experiment run at 6.51 m/s. $\Delta f_{DFT} = 0.07$ Hz

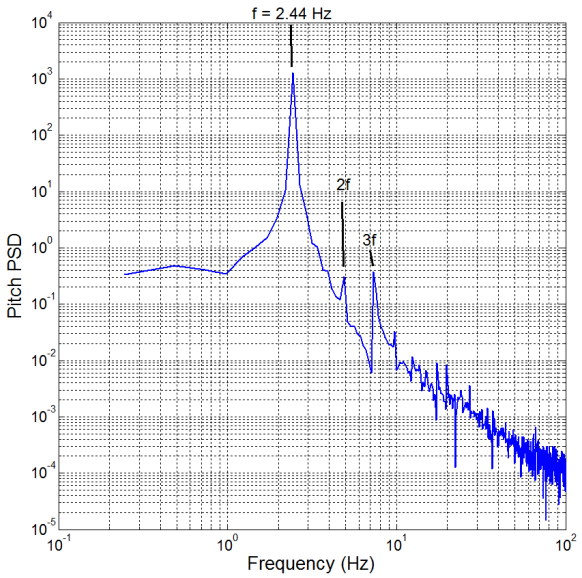

Figure 3.11: Pitch PSD of a LAO experiment run at 6.51 m/s. $\Delta f_{DFT} = 0.05$ Hz

3.3 Error Discussion

Given tests done days apart the LAO regime shows good stability in terms of frequency with some variation in terms of amplitude. The SAO regime shows good stability in terms of amplitude with some minor variation in terms of frequency. The uncertainty in the LAO amplitude is derived from different results for different tests, whereas the uncertainty in the SAO amplitude is a derived the nature of the SAOs where they are prone to transient amplitude modulation. The uncertainties are summarized in Table 3.4 below.

Table 3.4: Uncertainties for experimental data.

Parameter	Uncertainty
LAO Amplitude	3 deg
LAO Frequency	0.03 Hz
SAO Amplitude	0.3 deg
SAO Frequency	0.05 Hz

These values are consistent with the work of Harris who displayed results of various tests and showed good consistency throughout in the SAO regime[2].

4 Numerical Work

4.1 CFD Background

This section will give a basic overview of computational fluid dynamics and turbulence modelling so as to provide context for the methods used in this work.

4.1.1 Turbulence and Turbulence Modelling

While laminar flow is typified by orderly and smooth fluid motion, the kinematic properties and pressure of turbulent flow varies chaotically. In order to describe this behaviour, the instantaneous fluid motion is expressed as an addition of a mean value, U, with a time dependant fluctuation $u'(t)$. This expression, $u(t) = U + u'(t)$ is known as Reynolds decomposition. U is also a function of time, but over larger time and spatial scales than u'. More rigorously, the mean of a value is defined as follows:

$$\Phi = \frac{1}{\Delta t} \int_0^{\Delta t} \phi(t) dt \tag{4.1}$$

While Δt should in principle be close to infinity, in practise it is adequate if Δt is much larger than the time scales associated with the largest turbulent eddies. By definition, the fluctuations ϕ' have a time average of zero. However, the fluctuations will have second moments that are non-zero. Given arbitrary signals $\phi = \Phi + \phi'$ and $\psi = \Psi + \psi'$, their second moment is defined as follows:

$$\overline{\phi'\psi'} = \frac{1}{\Delta t} \int_0^{\Delta t} \phi'\psi' dt \tag{4.2}$$

The second moments are non-zero due to the inherently vortical structures of turbulence. These second moments become important when the Reynolds decomposed velocities are substituted into the Navier-Stokes Equations. For

an incompressible Newtonian fluid, which are the physical parameters of interest in this work, the Reynolds-averaged Navier-Stokes equations (RANS equations) are expressed in tensor notation as follows:

$$\rho\frac{\partial U_i}{\partial t} + \rho U_j\frac{\partial U_i}{\partial x_j} = \rho\bar{f}_i + \frac{\partial}{\partial x_j}\left[-\bar{p}\delta_{ij} + \mu(\frac{\partial U_i}{\partial x_j} + \frac{\partial U_j}{\partial x_i}) - \rho\overline{u_i'u_j'}\right] \tag{4.3}$$

Defining the mean rate of strain tensor, $\bar{S}_{ij} = \frac{1}{2}\left(\partial U_i/\partial x_j + \partial U_j/\partial x_i\right)$, the RANS equations are as follows:

$$\rho\frac{\partial U_i}{\partial t} + \rho U_j\frac{\partial U_i}{\partial x_j} = \rho\bar{f}_i + \frac{\partial}{\partial x_j}\left[-\bar{p}\delta_{ij} + 2\mu\bar{S}_{ij} - \rho\overline{u_i'u_j'}\right] \tag{4.4}$$

Note that though we have defined U as a time averaged value, the $\partial U/\partial t$ term is refers to the change in momentum in the mean flow field. The introduction of the second moment stress terms, $\rho\overline{u_i'u_j'}$ (known as the Reynolds stresses), means that the RANS equations require the addition of extra equations in order for closure to be possible. This can be done using empirical relations/models to provide extra equations that will close the RANS equations.

4.1.2 k-ϵ Model

The two-equation RANS models, $k-\epsilon$ and $k-\omega$ models, use the turbulent kinetic energy (TKE) to define a velocity scale and length scale. TKE is defined as $k = \sqrt{\overline{u'^2} + \overline{v'^2} + \overline{w'^2}}$, and ϵ is the rate of viscous dissipation. The velocity scale, u^*, is then defined as $u^* = \sqrt{k}$ and the length scale L_e is defined as $L_e = k^{\frac{3}{2}}/\epsilon$. The eddy viscosity can then be defined as follows using dimensional analysis:

$$\mu_t = C\rho u^* L_e = \rho C_\mu\frac{k^2}{\epsilon} \tag{4.5}$$

where C_μ is a dimensionless constant that must be defined in the model. The standard $k-\epsilon$ then uses the following transport equations for k and ϵ:

$$\rho\frac{\partial k}{\partial t} + \rho\frac{\partial}{\partial x_j}(kU_j) = \nabla\cdot\left[\frac{\mu_t}{\sigma_k}\nabla k\right] + \wp - \rho\epsilon \tag{4.6}$$

$$\rho\frac{\partial \epsilon}{\partial t} + \rho\frac{\partial}{\partial x_j}(\epsilon U_j) = \nabla\cdot\left[\frac{\mu_t}{\sigma_\epsilon}\nabla\epsilon\right] + C_{\epsilon 1}\frac{\wp\epsilon}{k} - \rho C_{\epsilon 2}\frac{\epsilon^2}{k} \tag{4.7}$$

where $\wp = 2\overline{u_i' u_j'}\bar{S}_{ij}$ and the Reynolds stresses are computed using the Boussinesq relationship: $-\rho\overline{u_i' u_j'} = 2\mu_t \bar{S}_{ij} - \frac{2}{3}\rho k \delta_{ij}$. These equations contain five constants whose values are given as follows: $C_\mu = 0.09, \sigma_k = 1.00, \sigma_\epsilon = 1.30, C_{\epsilon 1} = 1.44, C_{\epsilon 1} = 1.92$ [28]. The standard $k-\epsilon$ model values may be modified depending on the type of flow present (eg: high Reynolds number), but these values are canonical for the model and used in a variety of different calculations.

4.1.3 $k-\omega$ Model

The k-ω model modifies the k-ϵ model by replacing the ϵ equation with an equation for the turbulent frequency $\omega = \frac{k}{\epsilon}$. This leads to the following transport equations:

$$\rho\frac{\partial k}{\partial t} + \rho\frac{\partial}{\partial x_j}(kU_j) = \nabla \cdot \left[\frac{\mu_t}{\sigma_k}\nabla k\right] + \wp - \rho\epsilon \tag{4.8}$$

$$\rho\frac{\partial \omega}{\partial t} + \rho\frac{\partial}{\partial x_j}(\omega U_j) = \nabla \cdot \left[\frac{\mu_t}{\sigma_\omega}\nabla \omega\right] + C_{\omega 1}\frac{\wp\omega}{k} - \rho C_{\omega 2}\omega^2 \tag{4.9}$$

The model constants are as follows: $\sigma_k = 2.0, \sigma_\omega = 2.0, C_{\omega 1} = 0.553, C_{\omega 2} = 0.075$ [28]

The k-ω would be identical to the k-ϵ model if a $\rho 2\mu_t/\sigma_\omega k \nabla\omega \cdot \nabla k$ term was added to the ω equation. Menter noted that while the k-ϵ equation performed poorly in situations involving adverse pressure gradients, the k-ω model has difficulties at free stream interfaces and intermittency i.e. locations where flow is sometimes turbulent and sometimes laminar. In order to overcome this issue, Menter proposed a blend of the two models where the k-ω model is active near the wall and the k-ϵ model is active away from the wall. This model then took the following form known as the shear stress transport (SST) k-ω model:

$$\rho\frac{\partial \omega}{\partial t} + \rho\frac{\partial}{\partial x_j}(\omega U_j) = \nabla \cdot \left[\mu + \frac{\mu_t}{\sigma_\omega}\nabla\omega\right] + C_{\omega 1}\frac{\wp\omega}{k} - \rho C_{\epsilon 2}\omega^2 + (1-F_1)\rho\frac{2\mu_t}{\sigma_\omega k}\nabla\omega\cdot\nabla k \tag{4.10}$$

F_1 is a blending function that goes to zero away from the wall, and is equal to 1 inside the boundary layer. Typically the blending function is related to the ratio of turbulence $L_{e_t} = \sqrt{k}/\omega$ and the distance to the wall.

4.1.4 γ-Re_θ Model

The $\gamma - Re_\theta$ model was recently developed in an effort to solve some of the remaining problems with the $k - \omega$ model. The $\gamma - Re_\theta$ model performs laminar-turbulent transition modelling based on local correlations. The model utilizes a transport equation for intermittency and a transport equation for a transition onset criterion in terms of momentum-thickness Reynolds number in addition to k and ω equations. The model does not directly compute the transition physics, but is more able to accurately predict flow transition and separation due to the empirical models used [29].

The transport equation for intermittency γ is as follows:

$$\frac{\partial(\rho\gamma)}{\partial t} + \frac{\partial(\rho U_j\gamma)}{\partial x_j} = P_\gamma + E_\gamma + \frac{\partial}{\partial x_j}\left[\left(\mu + \frac{\mu_t}{\sigma_f}\right)\frac{\partial\gamma}{\partial x_j}\right] \tag{4.11}$$

where P_γ is a transition source related to strain-rate magnitude, and E_γ is a destruction/relaminarization source related to vorticity magnitude and Reynolds function correlations.

The transport equation for transition momentum thickness Reynolds number $\tilde{Re}_{\theta t}$ is as follows:

$$\frac{\partial(\rho\tilde{Re}_{\theta t})}{\partial t} + \frac{\partial(\rho U_j\tilde{Re}_{\theta t})}{\partial x_j} = P_{\theta t} + \frac{\partial}{\partial x_j}\left[\sigma_{\theta t}(\mu + \mu_t)\frac{\partial\tilde{Re}_{\theta t}}{\partial x_j}\right] \tag{4.12}$$

where $P_{\theta t}$ is a source term. For a more complete treatment of this model, please see the original paper [29] as the full model is very mathematically involved and contains more than 40 relations and correlations that predict transition.

4.1.5 Large Eddy Simulation

Rather than dealing with the RANS equations, large eddy simulation (LES) applies a spatial filter to the Navier-Stokes equations in order to divide the flow into small modelled scales and large computed scales. Large turbulent scales are most dependant on geometry and boundary conditions, whereas small turbulence scales are more or less universal regardless of boundary conditions. The filtering function is applied as follows:

$$\bar{u}(\boldsymbol{x}) = \int_D u(\boldsymbol{x'})G(\boldsymbol{x'}, \boldsymbol{x}; \bar{\Delta})d\boldsymbol{x'} \tag{4.13}$$

Applying a filter of spatial width $\bar{\Delta}$, $G(\boldsymbol{x'}, \boldsymbol{x}; \bar{\Delta})$, to the Navier-Stokes equations gives the filtered Navier-Stokes equations as follows:

$$\rho\frac{\partial\bar{u}_i}{\partial t}+\rho\frac{\partial}{\partial x_j}(\bar{u}_i\bar{u}_j)=\frac{\partial\bar{p}}{\partial x_i}+\frac{\partial\tau_{ij}}{\partial x_j}+\mu\frac{\partial^2\bar{u}_i}{\partial x_j^2} \tag{4.14}$$

In equation (4.14), the term $\tau_{ij}=\overline{u_iu_j}-\bar{u}_i\bar{u}_j$ is known as the sub-grid-scale (SGS) stresses. The SGS stresses must be modelled in terms of filtered variables. In the Smagorinsky-SGS model used, τ_{ij} takes the following form:

$$\tau_{ij}=-2\mu_{SGS}\bar{S}_{ij}+\tfrac{1}{3}\tau_{ii}\delta_{ij} \tag{4.15}$$

where $\mu_{SGS}=\rho(C_s\Delta)^2|\bar{S}|$ and y^+ is the non-dimensional distance to the wall. In this particular work, however, the Smagorinsky SGS model is slightly modified by the addition of a wall damping function as the unmodified Smagorinsky SGS model tends to over-predict eddy viscosity in the boundary layer. Therefore, $\mu_{SGS}=\rho(C_sf_s\Delta)^2|\bar{S}|$ where f_s is defined as follows:

$$f_s=\left[1-exp\left(-\frac{y^+}{25}\right)^3\right] \tag{4.16}$$

The value of C_s is variable depending on flow conditions and geometry. A value of $C_s=0.1$ was used here, and is often used in other CFD work [28].

4.1.6 INSFLOW

The 2D computational fluid dynamics (CFD) calculations were performed using a National Research Council of Canada (NRC) in-house CFD code known as the Incompressible Navier-Stokes Flow Solver or INSflow[30]. This code has been used in the past for calculations of unsteady aerodynamics, low-Reynolds number aerodynamics, and flapping wing aerodynamics. The code uses the integral form of the conservation laws.

Implicit temporal differencing with second-order accuracy was used in the temporal discretization, which made the algorithm stable for large timesteps. This was applied to the descretized convective and diffusive fluxes using the finite volume approach. The momentum equation in the can be written in the following second order form:

$$\frac{3(\Delta V\rho u_i)^{n+1}-4(\Delta V\rho u_i)n+(\Delta V\rho u_i)^{n-1}}{2\Delta t}+(\Sigma F_c)^{n+1}=[\Sigma F_d-\Sigma(p\vec{i}_i\cdot\vec{n}dA)]^{n+1} \tag{4.17}$$

where ΔV is the volume of the control cell, and F_c and F_d are the convective and diffusive fluxes accross the surfaces of the control volumes. The convective

flux $F_c = \rho(\overrightarrow{u} - \overrightarrow{w}) \cdot \overrightarrow{n}\, dA$ includes the grid velocity. i_i is the axis unit vectors, n is the direction normal to the surface, and A is the area of the cell face. A "deferred correction" scheme was used in the discretisation:

$$F_c^{n+1,s+1} = F_{c,L}^{n+1,s+1} + \beta(F_{c,H} - F_{c,L})^{n+1,s} \tag{4.18}$$

$$F_d^{n+1,s+1} = F_{c,L}^{n+1,s+1} + (F_{d,H} - F_{d,L})^{n+1,s} \tag{4.19}$$

In the above equations, the superscript n is the timestep index and s is the internal iteration index in a timestep. The subscript L indicates a low-order approximation, and H a higher-order approximation. The use of the deferred correction scheme provided the ability to dampen numerical oscillations while solving the equations and to improve the diagonal dominance of the coefficient matrix. By adjusting the value of the blending factor, $0 \leq \beta \leq 1$, an upwind scheme (low order), a central differencing scheme (higher order) or a hybrid upwind/centred scheme can be used.

The INSflow code was used to solve the dynamic equations of motion, for which the parameters can be seen in Table 4.1, simultaneously with the Navier-Stokes equations using 3D large-eddy simulations (LES)[24]. The numerical procedure is based on a finite volume method for the flow variables, and a finite difference method for body motion. The solutions are couple at each outer iteration by first updating the mesh movement according to the boundary movement or flow field results from the previous outer iteration, then computing the flow. The system of equations is solved by using a modified version of lower-upper (LU) composition known as strongly implicit procedure (SIP). SIP was developed specifically to solve systems of equations that arise from the discretisation of partial differential equations and is an incomplete version of LU composition where a preconditioner matrix is used.

Table 4.1: Dynamic properties used in the CFD simulations.

Parameter	Constant
I_{EA} (kg m^2)	0.00135
D_θ (N m s)	0.002
K_θ (N m/rad)	0.30

The dynamic behaviour of the airfoil is determined by starting from

$$I_{EA}\ddot{\theta} + D_\theta\dot{\theta} + K_\theta\theta = M_{EA} \tag{4.20}$$

and given that the terms are calculated implicitly such that

$$I_{EA}\ddot{\theta}^{n+1} + D_\theta\dot{\theta}^{n+1} + K_\theta\theta^{n+1} = M_{EA}^{n+1} \tag{4.21}$$

the terms for each time step are calculated implicitly using the following 2^{nd} order, 5-point equations:

$$\theta^{n+1} = \frac{M_{EA}^{n+1} - \left(\frac{-24\theta^n+22\theta^{n-1}-8\theta^{n-2}+\theta^{n-3}}{4\Delta t^2}I_s + \frac{-4\theta^n+\theta^{n-1}}{2\Delta t}D_s\right)}{\frac{9I_s}{4\Delta t^2} + \frac{3D_s}{2\Delta t} + K_s} \tag{4.22}$$

$$\dot{\theta}^{n+1} = \frac{3\theta^{n+1} - 4\theta^n + \theta^{n-1}}{2\Delta t} + O(\Delta t^2) \tag{4.23}$$

$$\ddot{\theta}^{n+1} = \frac{9\theta^{n+1} - 24\theta^n + 22\theta^{n-1} - 8\theta^{n-2} + \theta^{n-3}}{4\Delta t^2} + O(\Delta t^2) \tag{4.24}$$

4.2 2D LES Setup and Results

4.2.1 Setup

The O-ring NACA0012 airfoil mesh used in this work had been used in previous simulations. On the 2D sectional O-type meshes, the airfoil had a blunt trailing edge. In Ref. [24], the LES was first performed on a mesh with a coarse 481 × 65 × 17 grid for an assumed span of 0.064c, as successfully used in previous work, in which a simple harmonic-motion schedule was prescribed in accordance with the experimental observations [31]. The span was then extended to 0.2c for the other two refined grids (baseline 481 × 97 × 33 and refined 961 × 129 × 33) for assessment of the grid accuracy for the coupled fluid–structure interaction simulations. Corresponding to the baseline mesh used in the grid convergence studies in Ref. [24], a 2D mesh with 481 × 97 was applied in this study. These mesh dimensions refer to the number of grid points around the wing and the number of rings going out from the wing. In this case, the wing surface has 481 points, and there is 97 rings from the surface of the wing to the outermost extents of the computational domain. The mesh can be seen in Figure 4.1.

Two types of boundary conditions were used in the calculations. The first involved an inflow-outflow boundary interface that moved according to the geometric angle of attack of the wing based on the angular displacement of the wing. In this case, the inflow and outflow at the boundary was automatically adjusted according to the boundary normal vectors for each time step of the

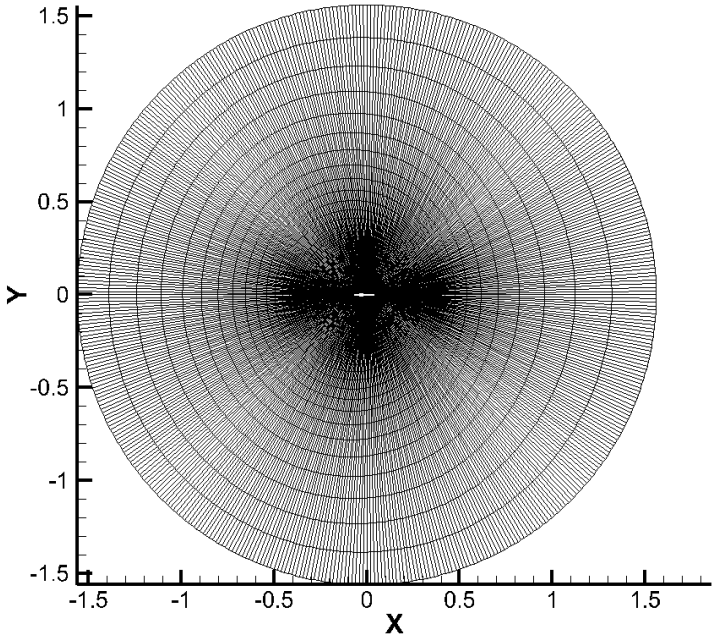

Figure 4.1: 2D mesh for simulation of NACA 0012 airfoil.

calculations, which allowed a blockwise movement. These were called the variable inflow-outflow or VIO calculations. A constant pressure was applied to the outflow boundaries in this study. The second type of boundary conditions involved fixing a constant freestream velocity at the far-field boundaries and defining a reference pressure at some point in the flow at each time step. This reference pressure was used to ensure that the pressure field was solvable in the computational domain. These were called the reference pressure or REFP calculations.

For each set of calculations, the simulations were second order in both time and space, and were started using a 2D LES. 2D LES was chosen as it had been shown capable to provide a quick solution for the test cases with an elastic axis located at $0.186c$ [22], without solving the additional turbulence transport equations or a fully 3D flowfield. 3D turbulence differs from 2D turbulence in the way the energy cascade occurs. In 3D turbulence, energy is transferred from the large eddy scales to the smaller eddy scales, which are then damped out. In 2D turbulence, energy is transferred from the small eddy scales to the large eddy scales.

The time step used for all calculations was $\Delta t = 1.0016 \times 10^{-4}$ s. Initial

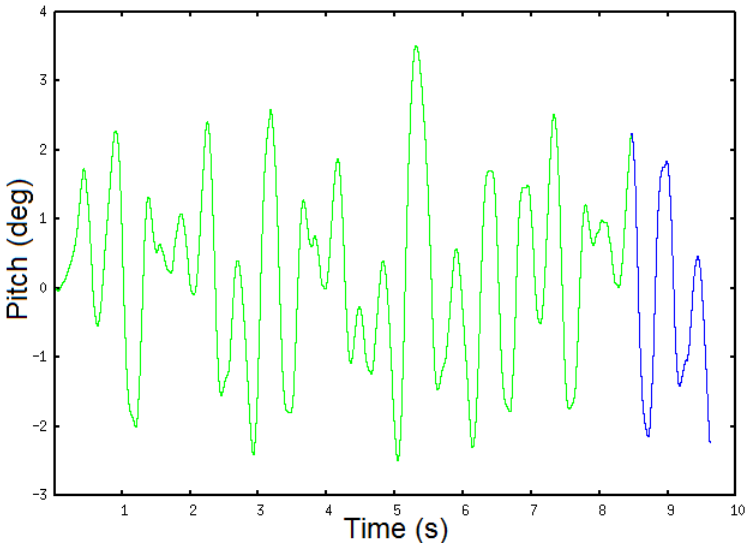

Figure 4.2: 2D LES simulation; pitch behaviour at 7.5 m/s.

URANS simulations were performed with a maximum number of inner iterations of 60 per time step. Later calculations were performed at 200 iterations per time step to confirm convergence. The 200 iteration results are presented in this work.

4.2.2 Results

At airspeeds less than 10 m/s, the 2D LES simulations display pseudo-chaotic behaviour in pitch, a typical example of which can be seen in Figure 4.2.

While the amplitude of these oscillations is relatively small and of the scale of the experiments performed at this airspeed, the behaviour is not periodic as is seen in the experiments. This is the case for the simulations at 6.13, 7.0, 7.5, 7.75, 8.0, and 8.5 m/s. It is mainly attributed to the inaccuracy of the laminar separation prediction and laminar-turbulent transition modelling. It is well known that 2D simulations over-predict the laminar separation and the related vortex shedding [32].

The 2D LES simulations whose airspeed was 10 m/s or greater exhibited oscillatory behaviour more consistent with the LAO regime, however. This can be seen in Figure 4.3.

This behaviour cannot yet be classified as an LCO because the amplitude of the oscillation differs from cycle to cycle, although it seems to be trending towards an LCO. Since the flow may be severely separated or stalled, as evi-

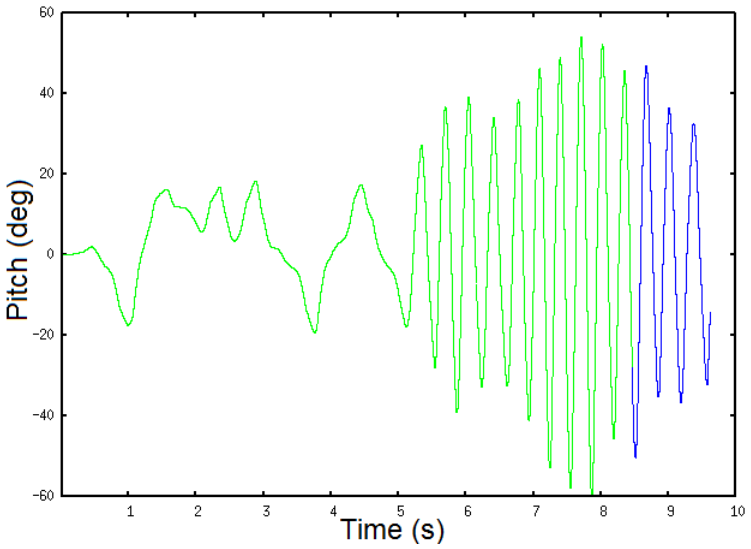

Figure 4.3: 2D LES simulation; pitch behaviour at 10.0 m/s.

denced in Figure 4.4, it is fully 3D, which is to say instantaneously anisotropic and turbulent at high angles. Improved turbulence modelling, or fully 3D LES would improve the prediction accuracy.

4.3 2D URANS Setup and Results

4.3.1 Setup

For the 2D URANS simulations, the $\gamma - Re_\theta$ and the Launder-Sharma low-Re $k - \epsilon$ models were used. The low-Re $k - \epsilon$ simulations did not produce stable LCO behaviour, whereas the $\gamma - Re_\theta$ simulations did. The results that used the $\gamma - Re_\theta$ model will be presented here. The free stream turbulence intensity (T_u) was set at 0.2% based on previous calculations and proximity to the measured value of the wind tunnel [23]. The turbulence length scale (L_e) was set at 0.087 m, although previous work has shown that this value is of secondary importance in terms of its impact on the accuracy of the calculations [23]. The integral turbulence length scale was estimated based on the measured velocity fluctuations by using one-point autocorrelations when a turbulence screen was placed at 6.9c ahead of the airfoil, while 0.17 m was used in Ref. [23] by assuming isotropic turbulence in the freestream. The most recent time step of the 2D LES calculations was used as the initial solution for

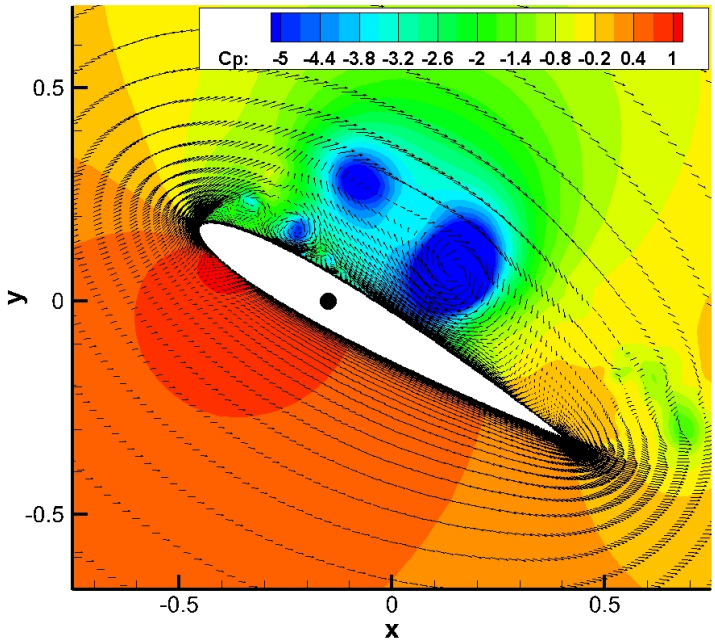

Figure 4.4: Instantaneous flowfield of a 2D LES simulation at 10.38 m/s.

the URANS calculations. The same grid was used for both the 2D URANS and 2D LES calculations.

Calculations were performed at airspeeds of 5.0, 6.13, 7.0, 7.5, 7.75, 8.0, 8.5, 10.0, and 10.38 m/s with a constant time step of $\Delta t = 1.0016 \times 10^{-4}$ s. These airspeeds were chosen in order to study an appropriate range of transitional Reynolds numbers. In addition, these airspeeds were close to the exact airspeeds at which experimental tests had been run.

4.3.2 Results

Previous flowfield conditions from the 2D LES simulations were used as the starting point for the set of URANS calculations. The URANS simulations show much more stable behaviour. Figures 4.5 and 4.6 show the LAO at 10 m/s and SAO at 7.5 m/s, respectively; they indicate a steady frequency and amplitude and as such can be classified as LCOs.

In order to confirm the LAOs for other conditions, a set of the previous 2D LES results from 10 m/s was used as a starting point for simulations at other freestream velocities, by rescaling the solution via a reference velocity.

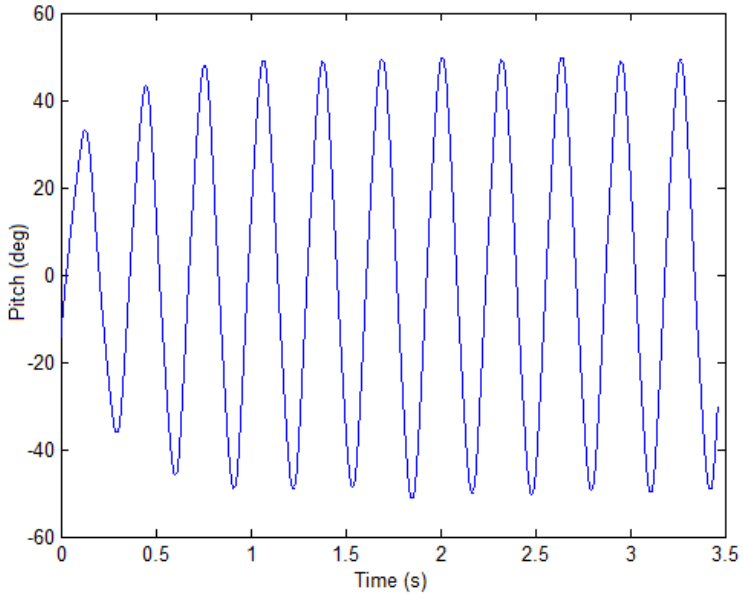

Figure 4.5: URANS simulation; LCO behaviour at 10 m/s.

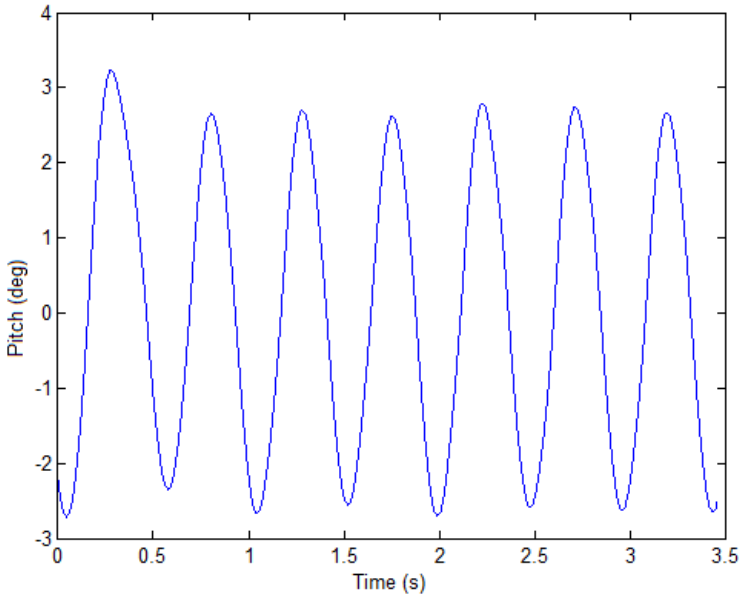

Figure 4.6: URANS simulation; LCO behaviour at 7.5 m/s.

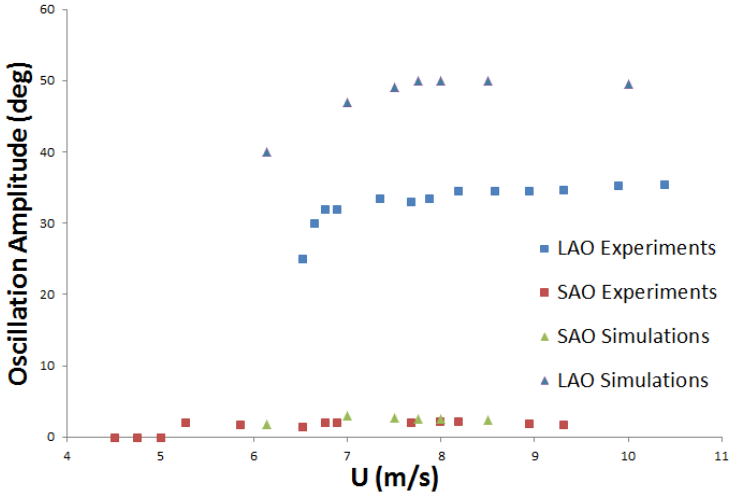

Figure 4.7: LCO amplitude as a function of airspeed for simulation and experiments in the LAO and SAO regimes.

These simulations maintain their state in the LAO regime, thus confirming the existence of the system bifurcation in the simulation. A comparison between the URANS simulation and experimental LCO amplitudes and frequencies can be seen in Figures 4.7 and 4.8. While the general trends are similar, the simulation LAO amplitudes differ significantly from the experiments, and there is little consistency between the frequencies of the simulations and the experiments. This is mainly attributed to the inaccuracy of the turbulence model when it attempts to model large flow separations, which is a well-known result.

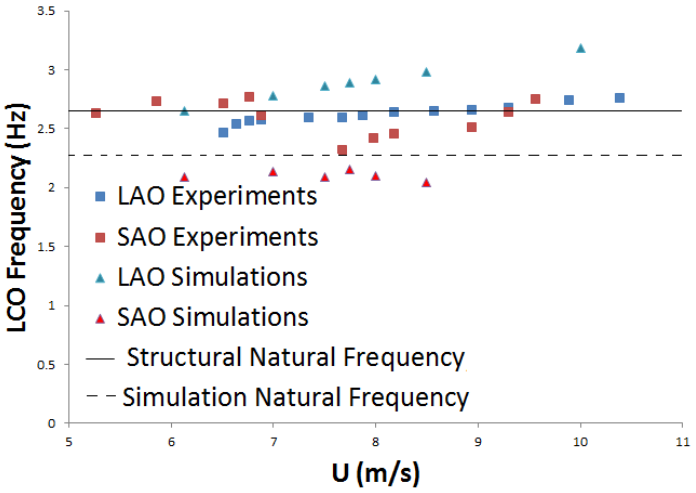

Figure 4.8: LCO frequency as a function of airspeed for simulation and experiments in the LAO and SAO regimes.

5 Analysis and Discussion

As discussed in Chapter 3, the experimental results show large non-linear behaviour in terms of amplitude and steady state response that is dependant on the initial conditions. Essentially, limit cycle oscillations are reached over a variety of airspeeds, but the amplitude of the LCOs is dependent on the system's initial perturbation. A good example of this can be seen in Figure 5.1, where the LCO amplitude is dramatically different despite only a small change in the size of the perturbation given to the system. In Figure 5.1, the first two perturbations of roughly 10.5 degrees lead to an SAO that is eventually damped out by the dry friction present in the system. However, when the system is given a perturbation of 13.8 degrees, the system develops into the LAO regime following a brief transient increase in oscillation amplitude. What we see, then, is that the system has three different stable states across a range of different airspeeds: an equilibrium point at zero, the SAO regime, and the LAO regime, and which state the system happens to be in is dependent on the input or perturbation provided to the system.

This led to the identification of two oscillatory regimes that are known as the large amplitude oscillation or LAO regime and small amplitude oscillation or SAO regime. The LAOs are characterized by LCO amplitudes of greater than 25 degrees, whereas the SAOs are characterized by LCO amplitudes of less than 5 degrees. Therefore, the system is characterized by two bifurcations, where there exists an unstable attractor between the steady state amplitudes of the two regimes, and the steady state behaviour of the system between 6.5 and 9 m/s airspeed depends on initial conditions. Qualitatively, this system behaviour can be mapped as seen in Figure 5.2.

In order to examine the characteristics of the SAO and LAO regimes, experiments and simulations performed at Re $\approx 8.0 \times 10^4$ will be used as an example of typical results. Figures for individual tests may be found in the appendices.

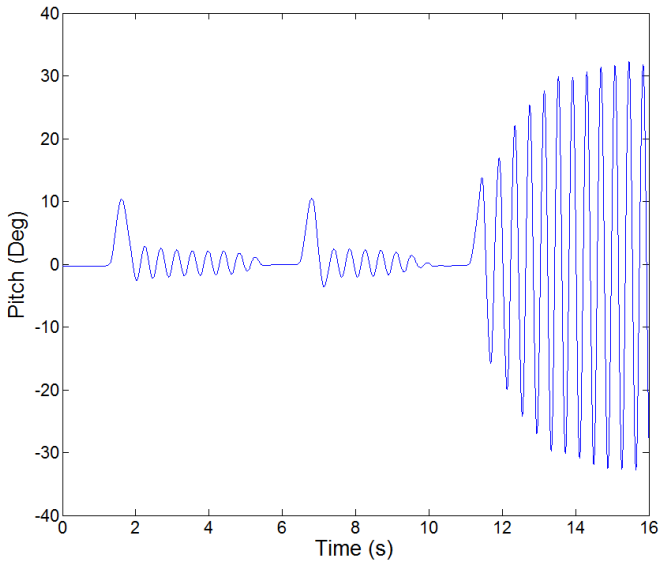

Figure 5.1: Pitch-time trace of an experiment run at 7.67 m/s.

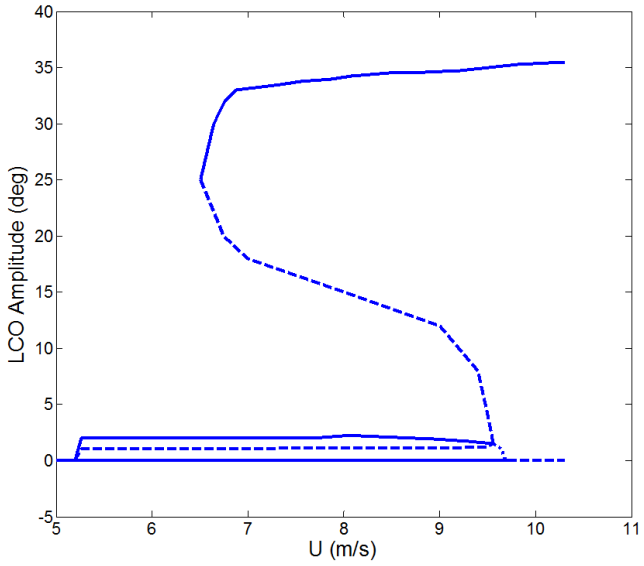

Figure 5.2: Schematic bifurcation map. Solid lines are accurate stable attractors, dotted lines are estimates of unstable attractors.

5.1 Small Amplitude Oscillations

5.1.1 Time Trace and Frequency Analysis

Figures 5.3 through 5.6 show the time trace and resulting power spectral density (PSD) of small amplitude oscillations at a Reynolds number of 80000. The amplitudes of the experiment and simulation are consistent with each other. However the simulated LCOs display a dominant frequency that is $\sim$ 0.35 Hz lower than the experimental LCOs. In addition, examining the PSDs shows that the experiment has a number of higher harmonics that are not present in the simulation. Both these results are consistent with previous calculations done by Yuan *et al* [24].

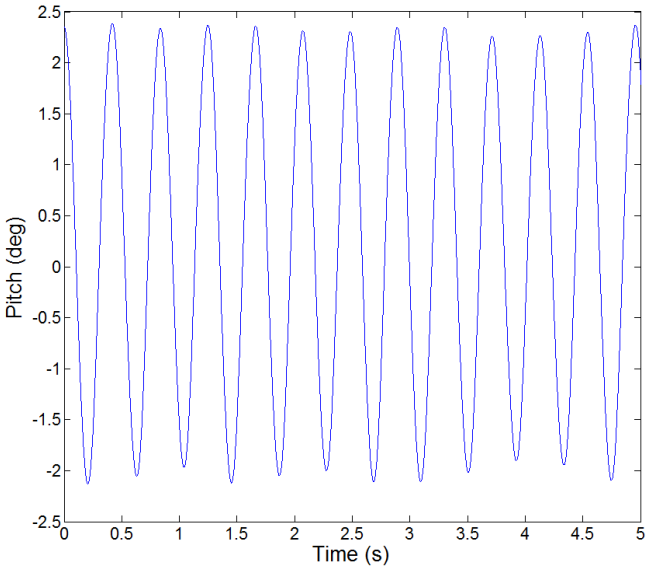

Figure 5.3: Filtered pitch time trace of experiment at $U = 7.98$ m/s, Re = 80000

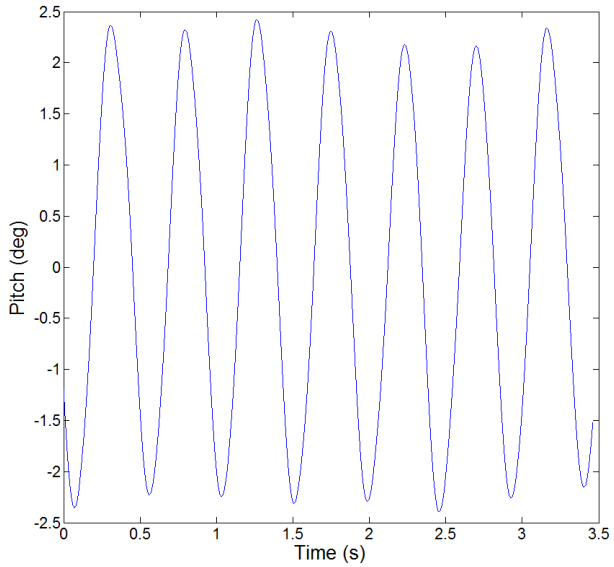

Figure 5.4: Time trace of simulation at $U = 8.00$ m/s, Re $= 80500$

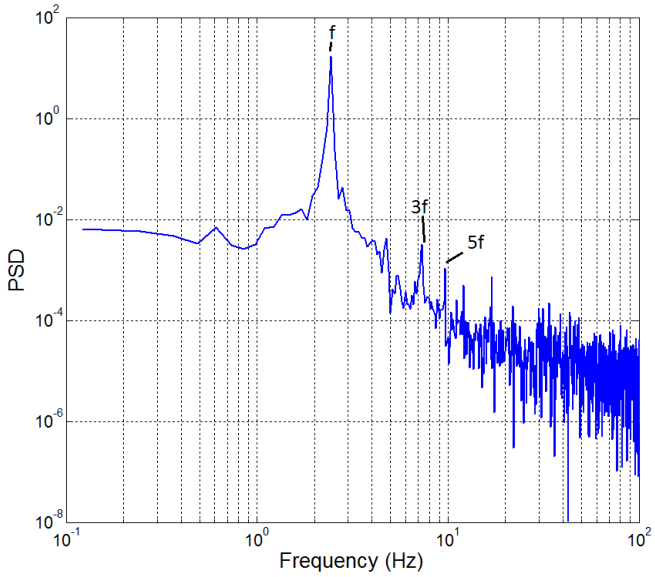

Figure 5.5: Pitch PSD of experiment at $U = 7.98$ m/s, Re $= 80000$, $f = 2.44$ Hz, $\Delta f_{DFT} = 0.15$ Hz

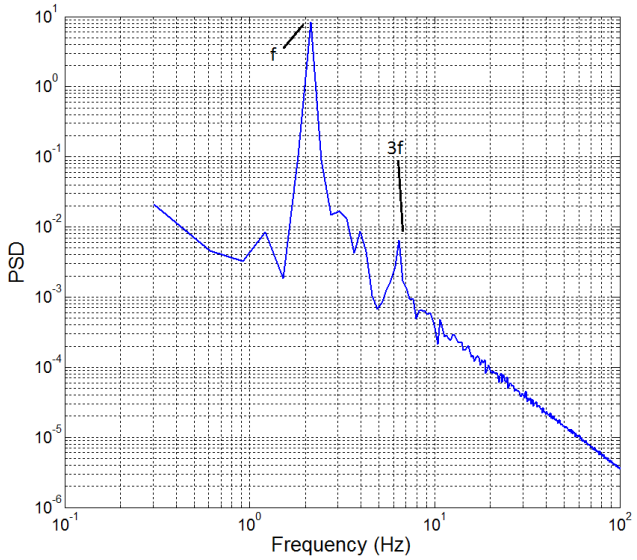

Figure 5.6: Pitch PSD of simulation at $U = 8.00$ m/s, Re $= 80500$, $f = 2.13$ Hz, $\Delta f_{DFT} = 0.28$ Hz

It should be noted that the difference in the dominant frequency of the PSDs is less than the difference noted above. This is due to the nature of the fast Fourier transform. A fast Fourier transform (FFT) is a type of discrete Fourier transform (DFT) which is defined as follows:

$$X_k = \sum_{n=0}^{N-1} x_n e^{-i2\pi kn/N}, k \in \mathbb{Z} \tag{5.1}$$

Equation (5.1) can be understood as a set of complex numbers that encodes both the amplitude and phase of the Fourier representation of a signal. Each member of the set has an amplitude, phase, and frequency. When added together in a linear superposition, the DFT recreates the original discrete signal. Each member of the DFT set corresponds to a sinusoid with frequency k/N cycles per sample. n is a subscript in the time domain, N is the number of samples, and k must be an integer. Therefore, the frequencies that a DFT is able to represent are discretized. The frequency resolution of a DFT is $\Delta f = f_s/N$ where f_s is the sampling frequency. For tests where the LCO was recorded for the full 20 seconds, $\Delta f_{DFT} = 0.05$ Hz, but for tests where a LCO was not present for the whole test, which was more likely for in the SAO regime, $\Delta f_{DFT} = 0.15$ Hz. Thus, the difference in frequency between

the simulation and experiment is 0.31 Hz based on the PSDs, but is larger when the frequency is calculated by dividing the time elapsed by the number of oscillatory peaks. This can be attributed to the difference in their Δf_{DFT}.

5.1.2 Symmetry Analysis

Figures 5.7 through 5.10 show the histograms and phase plane plots of small amplitude oscillations at a Reynolds number of 80000.

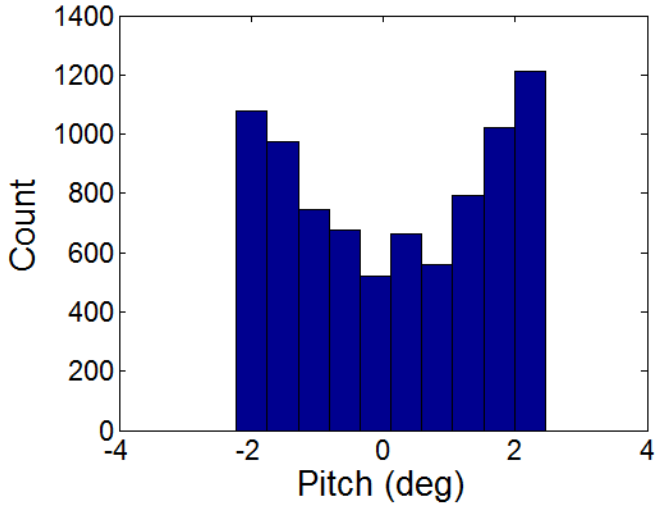

Figure 5.7: Histogram of experiment at $U = 7.98$ m/s, Re = 80000

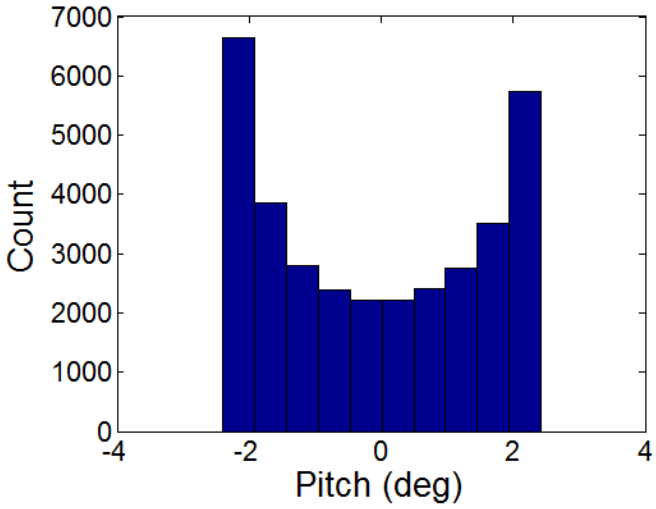

Figure 5.8: Histogram of simulation at $U = 8.00$ m/s, Re = 80500

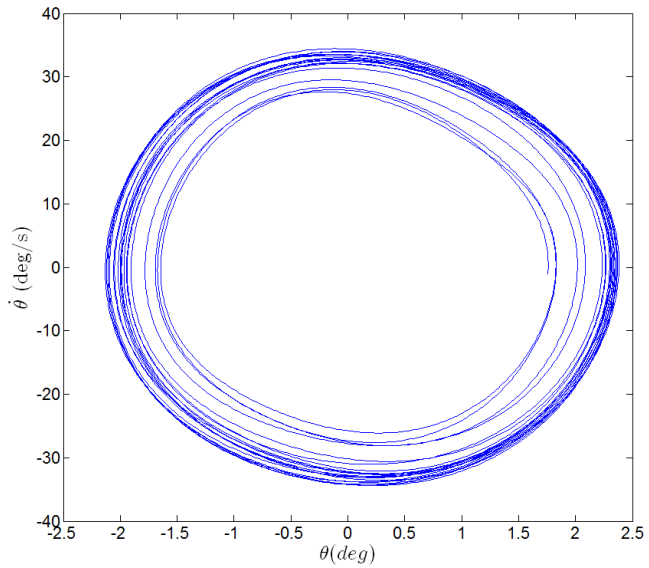

Figure 5.9: Phase plane plot of experiment at $U = 7.98$ m/s, Re = 80000 (Filtered data with cutoff frequency of 12 Hz)

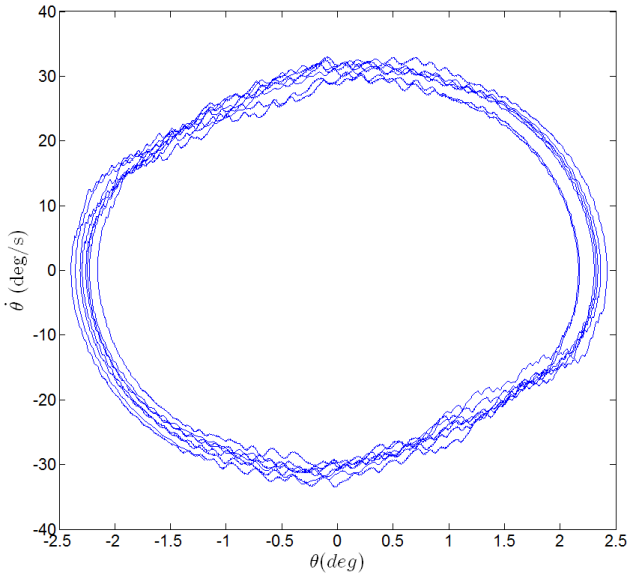

Figure 5.10: Phase plane plot of simulation at $U = 8.00$ m/s, Re = 80500

The histograms of both the experiment and calculation display a comparable symmetry. It is expected to see a bowl shape, as the wing spends the most time at high AOA because that is the point at which the angular velocity is the lowest.

The phase plane plots have very similar shapes and extents. It should be noted that the time step for the computational phase plane is small enough to pick up the small fluctuations in the first derivative in the pitch that have been filtered out in the experimental data. It makes sense that the simulations are very symmetrical given the perfect alignment of the wing, and the lack of even harmonics as can be seen in Figure 5.6. There is some asymmetry in the experimental results due to asymmetry in the rig itself (for example, the wing being aligned slightly off 0 degrees AOA) which leads to the even harmonics present in the PSD.

5.1.3 Dynamic Coefficient Curves

Figures 5.11 through 5.13 show the histograms and phase plane plots of small amplitude oscillations at a Reynolds number of 80000.

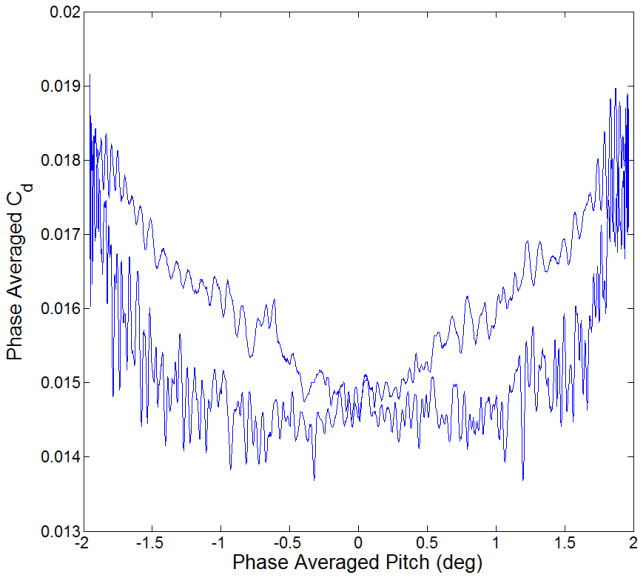

Figure 5.11: Phase averaged C_d curve of simulation at $U = 8.00$ m/s, Re = 80500

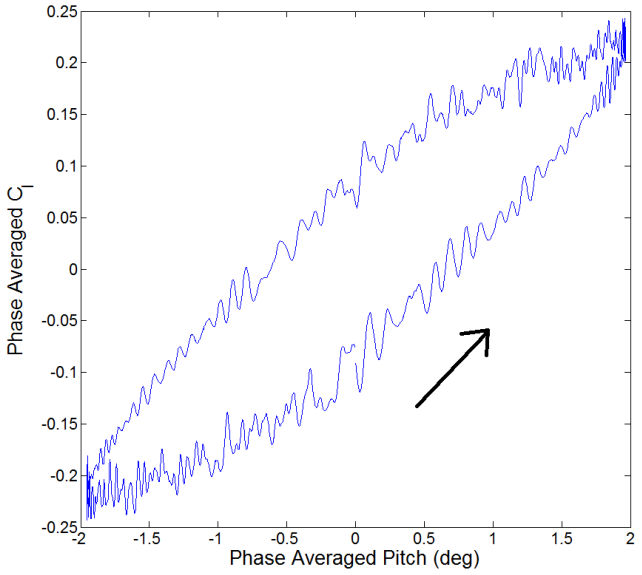

Figure 5.12: Phase averaged C_l curve of simulation at $U = 8.00$ m/s, Re = 80500

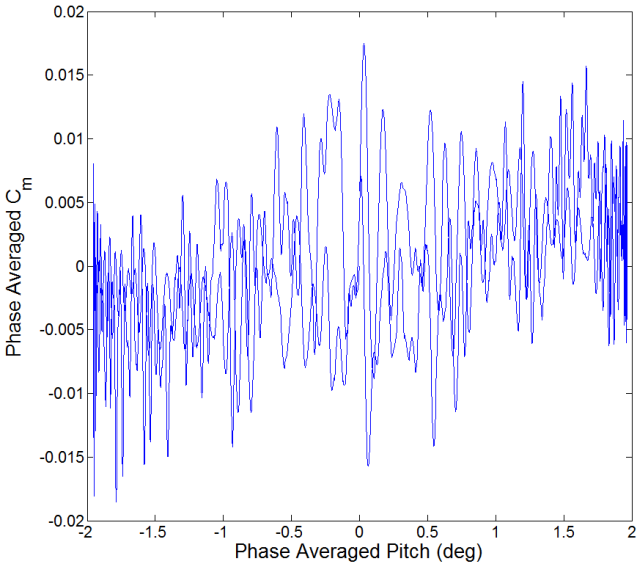

Figure 5.13: Phased averaged $C_{m_{EA}}$ curve of simulation at $U = 8.00$ m/s, Re = 80500

Even after being phase-averaged over six cycles, the SAO numerical dynamic C_d, C_l, and C_m curves remain noisy due to the high frequency fluctuations caused by von Karman vortex shedding and boundary layer separation. In order to get a clearer picture, this data was re-sampled and filtered. First, every 10 data points were selected in order to have a effective sampling frequency of 998 Hz. This data was then filtered using a digital filter with a cutoff frequency of 12 Hz. This effectively removed any frequencies that were not contributing directly to the LCO dynamics.

The phase averaging process was as follows: first, the pitch data was divided up into individual cycles. This would be triggered by the crossing of the 0 axis in pitch. Next, the longest cycle would be selected. This cycle would be used for normalization. Then, nearest neighbour identification in the time domain would begin. Essentially, every pitch point is associated with a time point. A loop would go through the time points of the normalization cycle, and find the time points in the other cycles that were closest. In this way, there would be a set of cycles that all had the same length in time. Finally, the data values would be averaged across equivalent times in order to have a fully phase averaged data set.

Figures 5.14 and 5.15 show the filtered and phase averaged C_l and $C_{m_{EA}}$ respectively of small amplitude oscillations at a Reynolds number of 80000.

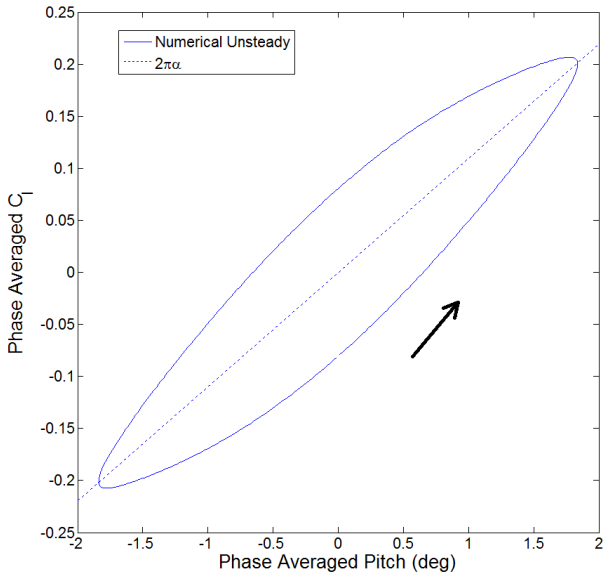

Figure 5.14: Filtered and phase averaged C_l curve of simulation at $U = 8.00$ m/s, Re = 80500 (Filtered data with cutoff frequency of 12 Hz)

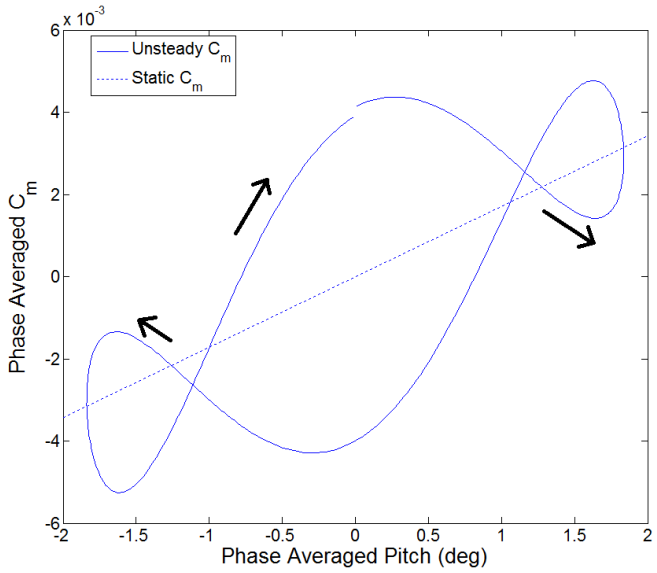

Figure 5.15: Filtered and phase averaged $C_{m_{EA}}$ curve of simulation at $U = 8.00$ m/s, Re = 80500 (Filtered data with cutoff frequency of 12 Hz)

The C_l curve is consistent with what one would expect to see from an inviscid analysis which is to say it is an ellipse whose major axis is aligned with the static C_l of $2\pi\alpha$. It is also well behaved with a well defined elliptical shape which indicates that the lift is acting linearly. The direction of the loop indicates that the lift slightly lags the pitch angle. The C_m curve in Figure 5.15 shows that the pitch lags the C_m, and it is this lag that ultimately feeds the small amplitude LCOs as it pitches through 0 degrees AOA. The work is done on the wing by the airflow between -1 and 1 degree AOA. The double figure 8 shape of the $C_{m_{EA}}$ curve is also typical of what one would expect to see from a van der Pol oscillator. This is qualitatively similar to what is seen in Poirel and Yuan [31]. Poirel and Yuan performed 3D LES simulations of a NACA0012 airfoil the EA at $0.186c$ undergoing prescribed oscillations of 5 degrees. This simulations shows that the work done on the airfoil occurred between -3 and 3 degrees AOA.

Although the moment on the wing is not measured experimentally, it can be found using equation (5.2) and the values found in Table 3.2.

$$I_{EA}\ddot{\theta} + D_\theta\dot{\theta} + K_\theta\theta = M_{EA} \tag{5.2}$$

The first and second derivatives were calculated numerically using central differencing. The central differencing formulae for first and second derivatives are as follows:

$$\nabla\theta(t_n) = \frac{\theta(t_{n+1}) - \theta(t_{n-1})}{2t} + \mathbb{O}(t^2) \tag{5.3}$$

$$\nabla^2\theta(t_n) = \frac{\nabla\theta(t_{n+1}) - \nabla\theta(t_{n-1})}{2t} + \mathbb{O}(t^2) \tag{5.4}$$

The central differencing formulae have round off error on the order of t^2, where t is the time step.

When looking at the experimental C_m curve, Figure 5.16 shows a C_m response that is similar to Figure 5.15 although it lacks the small loops at the highest oscillation amplitudes. The experimental C_m cycle is also slightly asymmetrical due to the presence of the even harmonics in the system. This, in turn, is caused by the imperfect alignment between the wing and the flow. The lag between the C_m and pitch angle is obvious in Figure 5.16 with the C_m crossing the 0 axis near the maximum amplitude of the LCO.

Figures 5.17 and 5.18 show the PSDs of the numerical C_l and C_m curves from small amplitude oscillations at a Reynolds number of 80000.

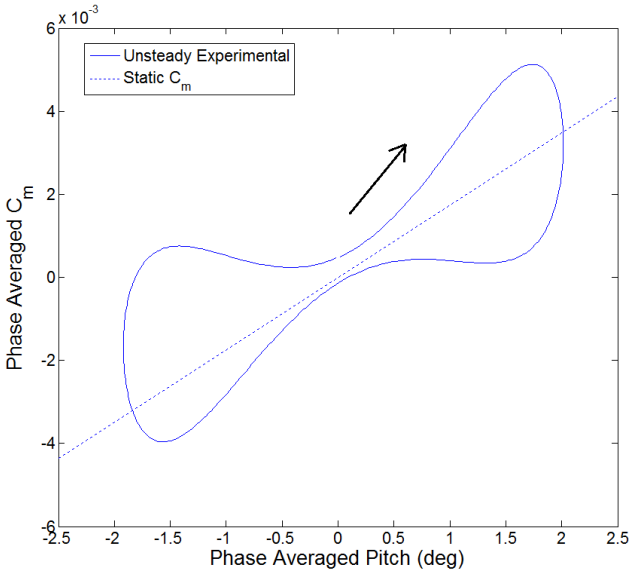

Figure 5.16: Filtered eight cycle phase averaged $C_{m_{EA}}$ curve of experiment at $U = 7.98$ m/s, Re = 80000

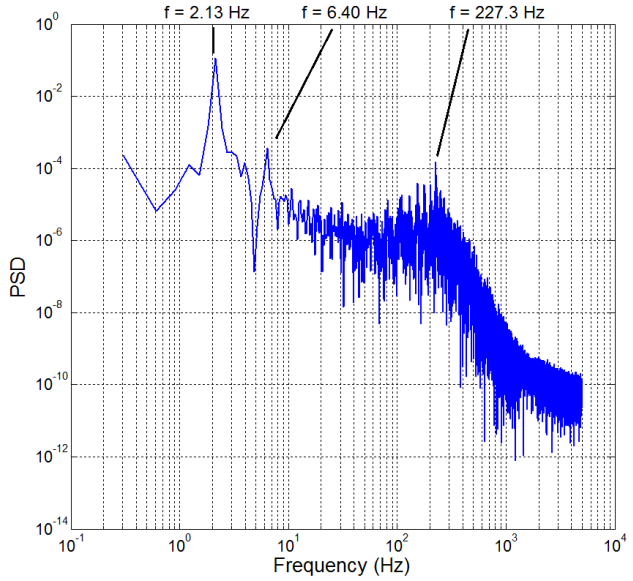

Figure 5.17: PSD of C_l curve of simulation at $U = 8.00$ m/s, Re = 80500, $\Delta f_{DFT} = 0.28$ Hz

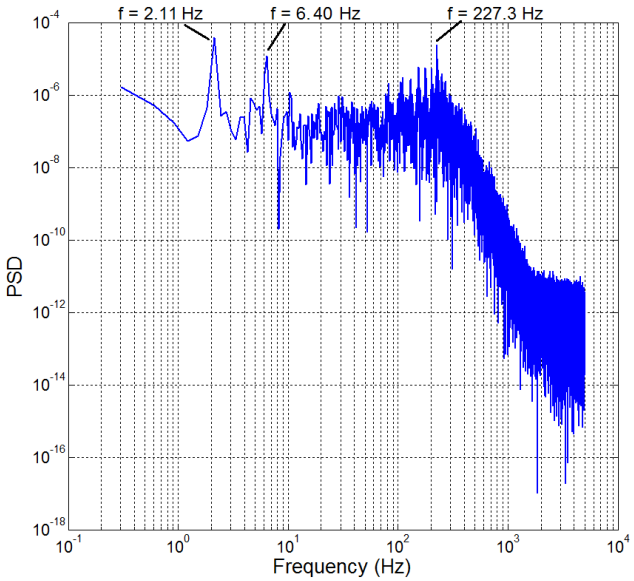

Figure 5.18: PSD of C_m curve of simulation at $U = 8.00$ m/s, Re = 80500, $\Delta f_{DFT} = 0.28$ Hz

Examining the PSDs of the unfiltered C_m and C_l curves indicates that in addition to the dominant frequency of the oscillation and its third harmonic, there is a large peak at 227 Hz corresponding to von Karmen vortex shedding and a Strouhal number of St= 0.53. The Strouhal number remains constant over the range of Reynolds numbers at which the numerical SAOs are present. This indicates that the vortex shedding frequency is roughly linear with airspeed over this range. This is a result that is comparable to the work done by Yuan *et al* [22].

5.1.4 CFD Flow Field Analysis

At a low angle of attack, as seen in Figures 5.19 and 5.20, the trailing edge separation can be seen developing. As the pitch increases, the separation point moves forward on the upper surface of the wing as seen in Figures 5.21 and 5.22. The separation point is defined as the point where the skin friction coefficient, C_f, is equal to 0. C_f is the wall shear stress non-dimensionalized as follows: $C_f = \tau_w / \frac{1}{2}\rho U_\infty^2$ where $\tau_w = \mu(\partial u/\partial y)$ evaluated at the wall. Thus, where the wall shear stress is zero, that is the point at which separation occurs, by definition. The exact point can be determined from either the C_f profile or by visually inspecting the z-vorticity. The magnitude of the z-vorticity is

defined as $\partial u_y/\partial x - \partial u_x/\partial y$, or more generally twice the magnitude of the angular velocity vector. A change in the sign of the flow's angular velocity indicates reversed or separated flow.

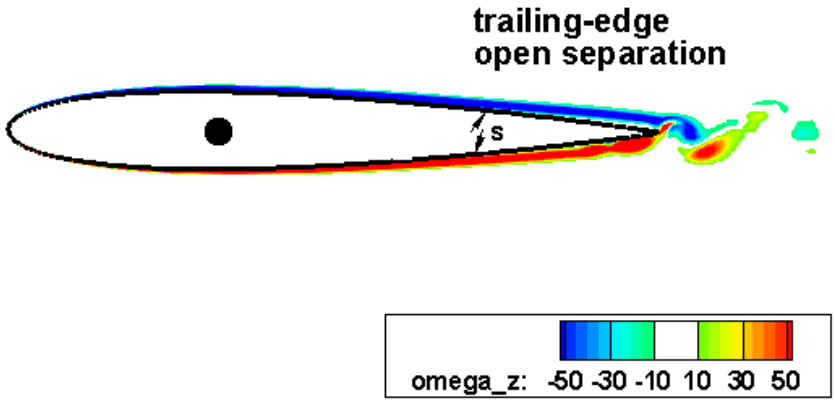

Figure 5.19: Vorticity contours, AOA = 0.3 degrees, pitching up

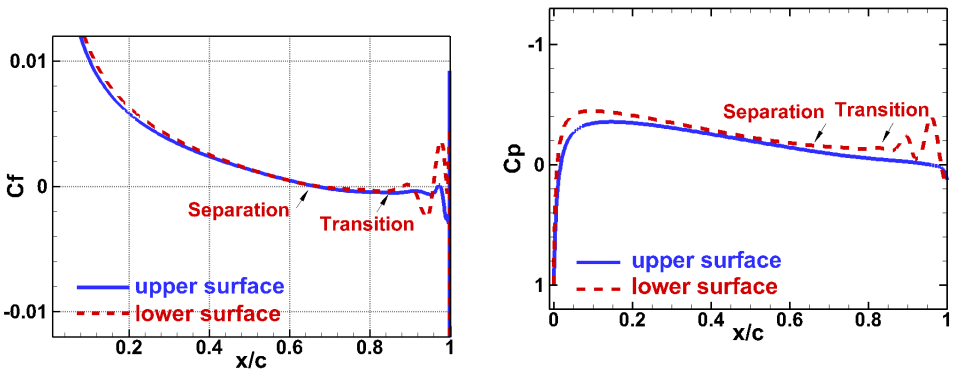

(a) C_f profile

(b) C_p profile

Figure 5.20: Profiles of the C_f and C_p at AOA = 0.3 degrees, pitching up

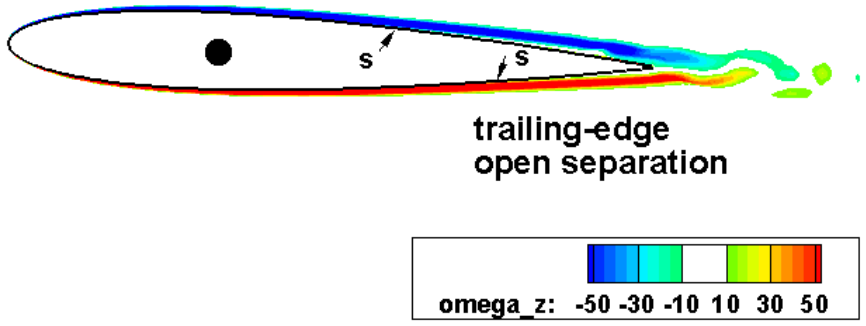

Figure 5.21: Vorticity contours, AOA = 2.2 degrees, pitching up

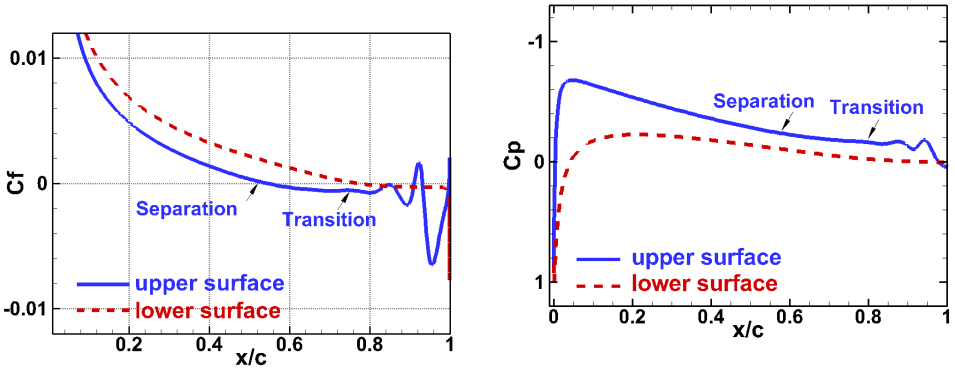

(a) C_f profile

(b) C_p profile

Figure 5.22: Profiles of the C_f and C_p at AOA = 2.2 degrees, pitching up

Transition to turbulence can also be seen occurring close to the trailing edge of the airfoil. Where transition occurs can be observed from where fluctuations begin in the C_p and C_f profiles. As the wing pitches down through 0 degrees AOA as seen in Figures 5.23 and 5.24, there is a lag between the pitching angle and which side of the airfoil is the suction side, based purely

on the C_p profile. Even as the wing pitches down, the trailing edge separation on the top side is further forward than the separation on the bottom side.

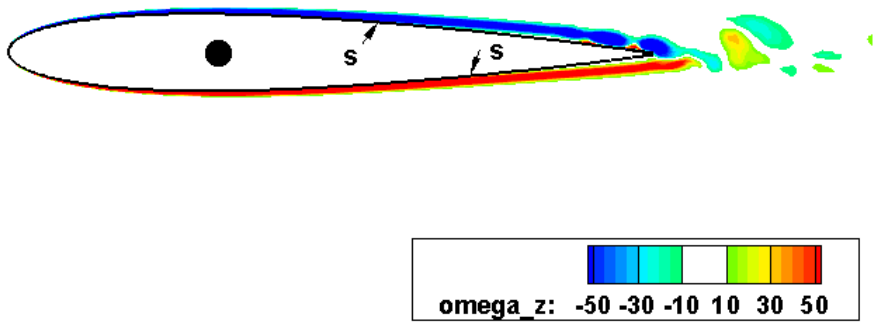

Figure 5.23: Vorticity contours, AOA = 0.2 degrees, pitching down

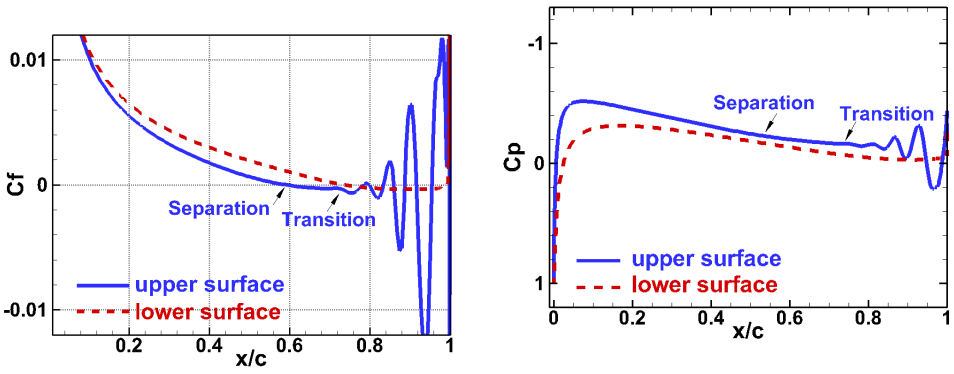

(a) C_f profile

(b) C_p profile

Figure 5.24: Profiles of the C_f and C_p at AOA = 0.2 degrees, pitching down

The bottom side separation point is further forward by the time the maximum negative pitch angle is reached in Figures 5.25 and 5.26, but again there is a lag as the airfoil pitches up and restarts the cycle.

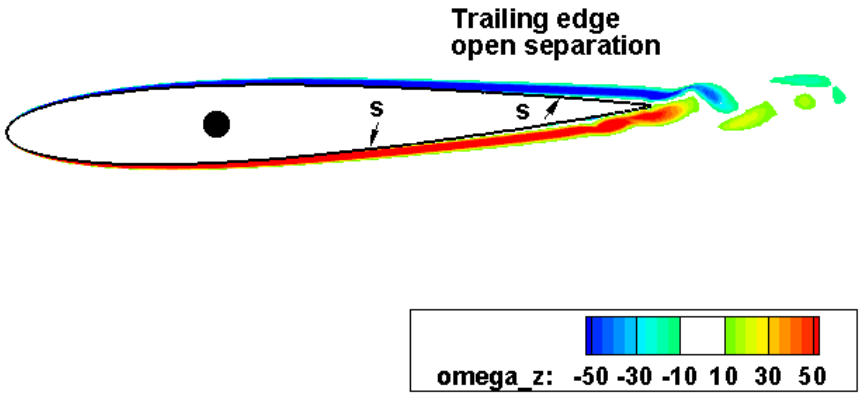

Figure 5.25: Vorticity contours, AOA = -2.4 degrees, pitching down, roughly max pitch

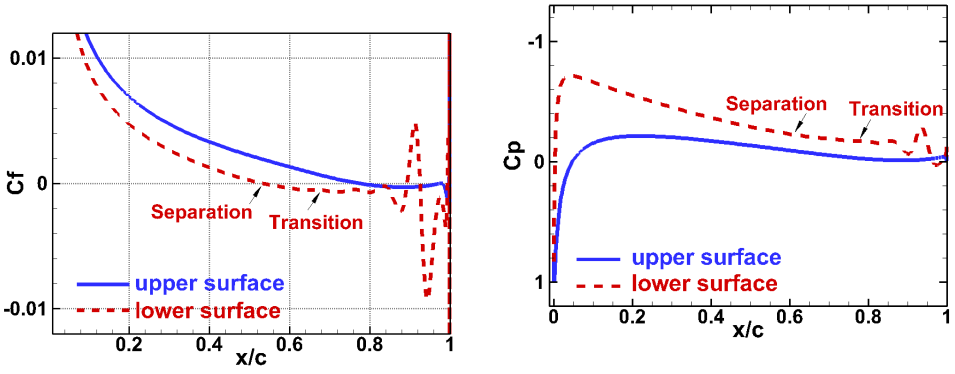

(a) C_f profile

(b) C_p profile

Figure 5.26: AOA = Profiles of the C_f and C_p at -2.4 degrees, pitching down, roughly max pitch

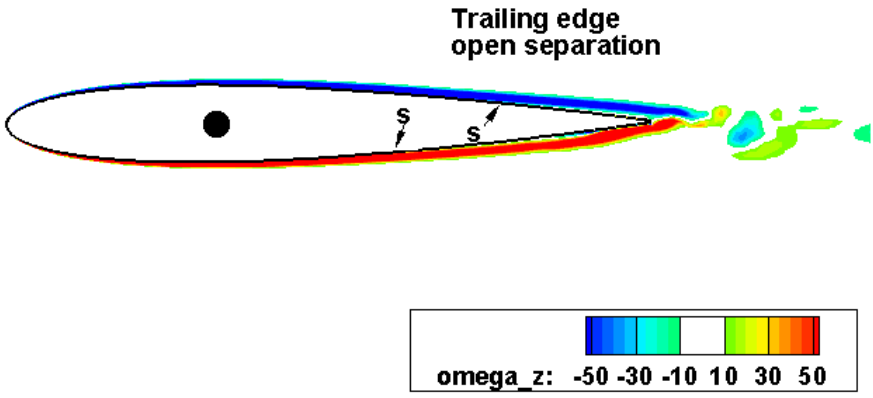

Figure 5.27: Vorticity contours, AOA = −0.3 degrees, pitching up

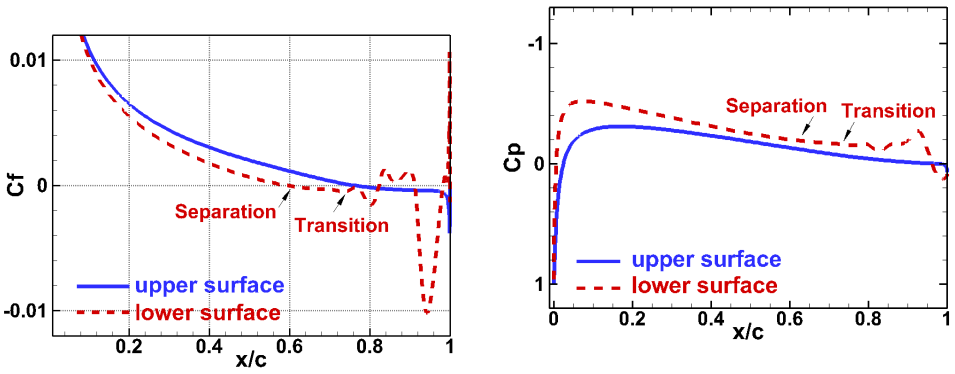

(a) C_f profile

(b) C_p profile

Figure 5.28: Profiles of the C_f and C_p at AOA = −0.3 degrees, pitching up

In general, it can be seen that the SAOs are typified by a loss of lift caused by flow separation and von Karman vortex shedding. The moment of the wing is lagged behind by the pitch as the wing moves through zero degrees AOA as can be seen in Figures 5.15 and 5.16. This can be seen in both the experimental and simulation $C_{M_{EA}}$ curves, although exactly what form the curves take differs slightly.

5.2 Large Amplitude Oscillations

5.2.1 Time Trace and Frequency Analysis

In contrast to the SAOs, the simulation LAOs display both amplitudes and frequencies that are larger than their experimental counterparts as can be seen in Figures 5.29 through 5.32. The discrepancy between the experiment and simulations is likely caused by URANS simulations' weakness in modelling massively separated flow. The $\gamma - Re_\theta$ model predicts transition accurately, but like other URANS models, it under-predicts the turbulent shear stress in separated regions. The experimental flow likely separates sooner than in the calculations leading to a smaller oscillation amplitude.

Also of interest is the difference in the PSD spectra as the experimental PSD displays both even and odd harmonics, whereas the calculations display only odd harmonics. A comparison of which harmonics are present at certain Reynolds numbers can be seen in Table 5.1. Harmonic peaks of $2f$ can be seen across most experimental Reynolds numbers, but not in any of the simulation results. Again, the presence of $2f$ or other even harmonics is due to the imperfect physical alignment between the wing and the flow.

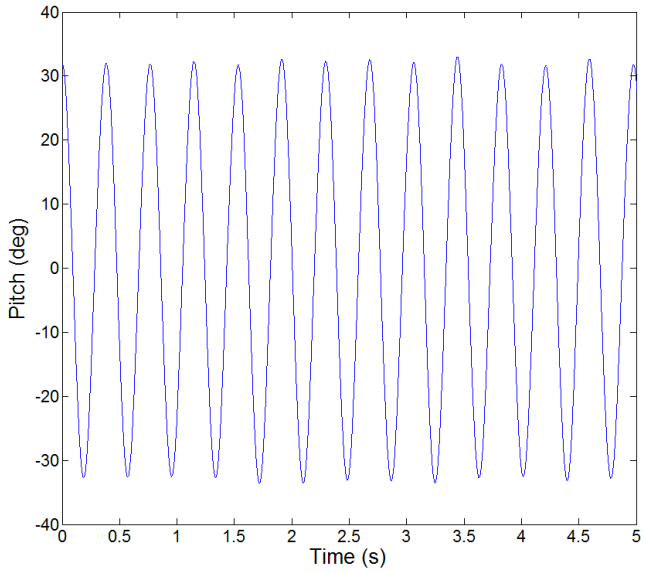

Figure 5.29: Time trace of experiment at $U = 7.87$ m/s, Re = 79000

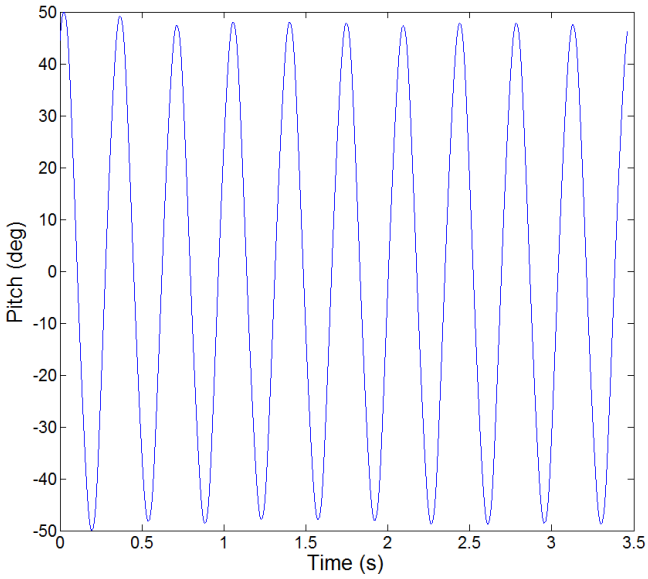

Figure 5.30: Time trace of simulation at $U = 8.00$ m/s, Re = 80500

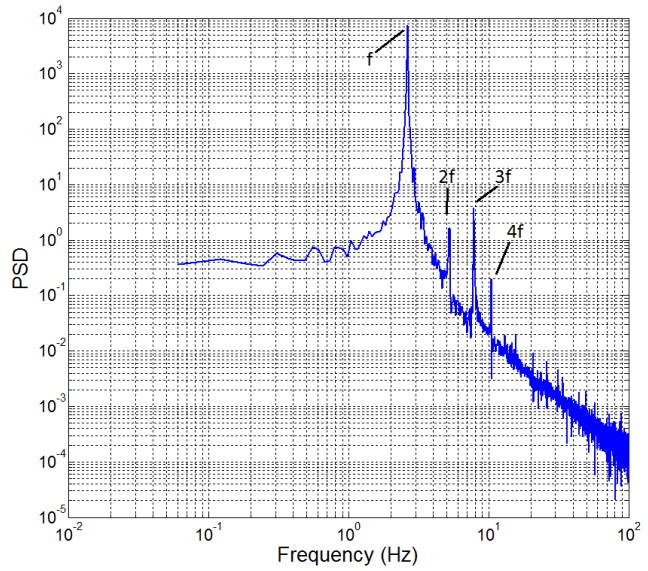

Figure 5.31: PSD of experiment at $U = 7.87$ m/s, Re = 79000, $f = 2.63$ Hz, $\Delta f_{DFT} = 0.05$

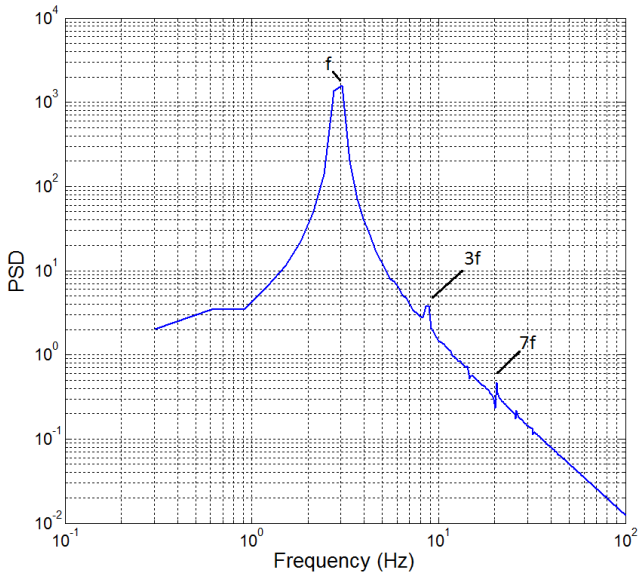

Figure 5.32: PSD of simulation at $U = 8.00$ m/s, Re = 80500, $f = 3.05$ Hz, $\Delta f_{DFT} = 0.28$ Hz

5.2.2 Symmetry Analysis

Figures 5.33 through 5.36 show the histograms and phase plane plots of large amplitude oscillations at a Reynolds number of 80000.

Table 5.1: Summary of frequency harmonics present at a variety of simulation and experimental Reynolds numbers.

LCO Regime	Re	2f		3f		4f		5f		6f		7f	
		Exp	Sim	Exp	Sim	Exp	Sim	Exp	Sim	Exp	Sim	Exp	Sim
SAO	~70000												
	~78000			X	X								
	~80000	X		X	X	X		X					
LAO	~70000	X		X	X				X				X
	~78000	X		X	X				X				
	~80000	X		X	X	X							X
	~85000	X		X	X				X				X
	~100000	X		X	X				X				X

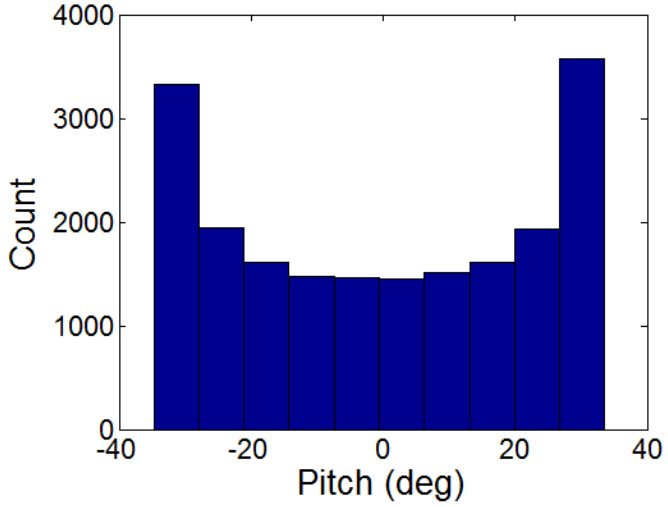

Figure 5.33: Histogram of experiment at $U = 7.87$ m/s, Re = 79000

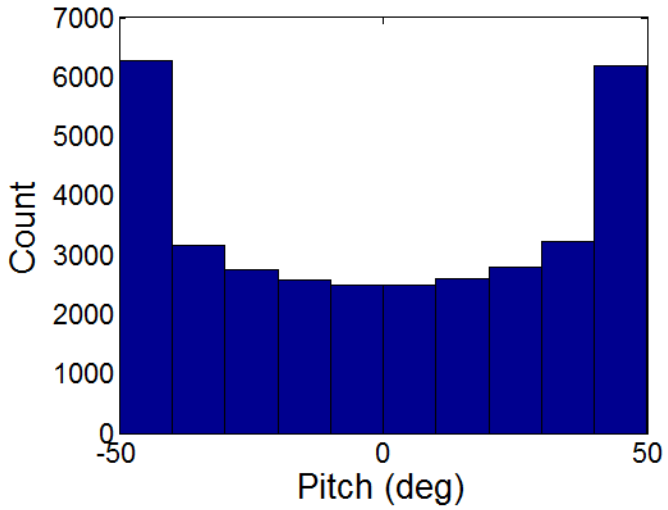

Figure 5.34: Histogram of simulation at $U = 8.00$ m/s, Re = 80500

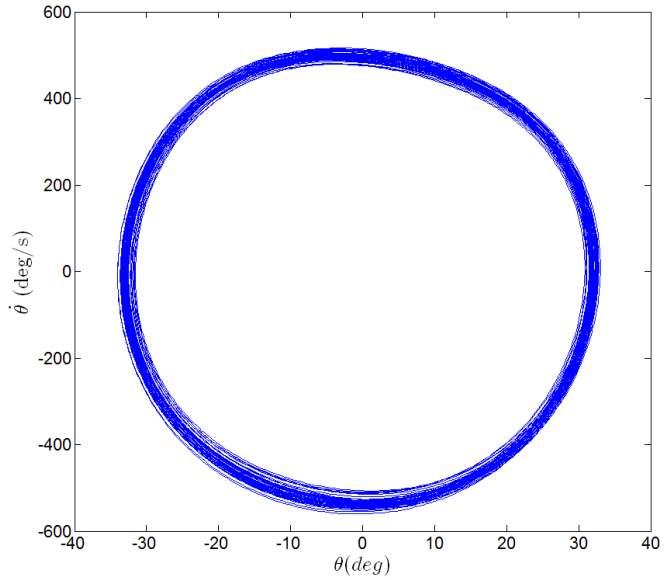

Figure 5.35: Filtered phase plane plot of experiment at $U = 7.87$ m/s, Re = 79000

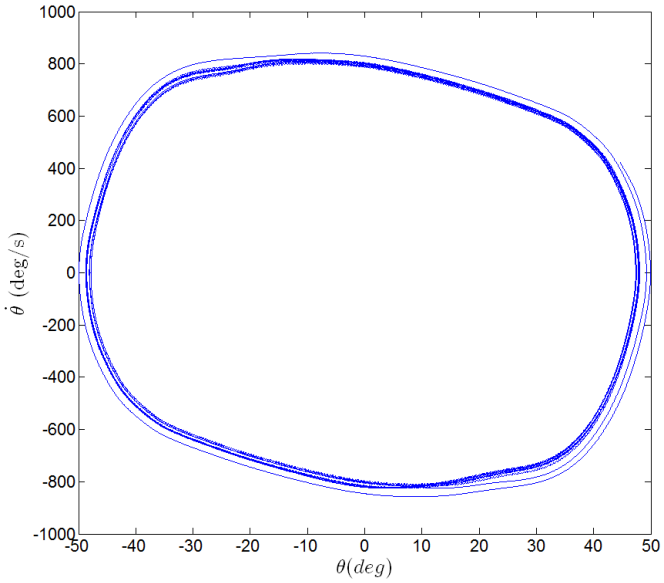

Figure 5.36: Phase plane plot of simulation at $U = 8.00$ m/s, Re = 80500

The LAOs are similarly symmetrical in both the experiments and simulations. However the simulation phase plane plot shows a much larger derivative, and consequently larger amplitude, when compared to the experiment. Both the experiment and the simulation reach their maximum angular velocity around 0 degrees AOA, but the calculation maintains a high angular velocity for much longer, leading to the non-elliptical shape of the phase plot diagram. Again, this is likely caused by the inaccurate prediction of flow separation in 2D computations. An over-prediction of the lift at the higher angles of attack leads to a higher amplitude, and in turn is related to the higher frequency of the simulated oscillations.

5.2.3 Dynamic Coefficient Curves

Examining Figures 5.38 and 5.39, it can be seen that at around 30 degrees AOA, the airfoil stalls leading to a negative pitching moment. The C_l plummets at about the same AOA. The C_m curve also shows where the work happens during the course of the cycle. A clockwise loop indicates work being done on the airfoil and a counter-clockwise loop indicates work being done by the airfoil. The clockwise loops at high AOAs indicate that most of the work being done on the airfoil occurs around the peaks of the cycles, rather than when the airfoil is pitching through 0 degrees AOA. In order to get a stable LAO, the pitch must initially be high enough to allow for sufficient work to be done on the airfoil for the oscillations to be self-sustained. In contrast to the SAO results, the six-cycle phase-averaged LAO dynamic curves paint a clear picture of what occurs over the course of a limit cycle without having to be re-sampled or filtered. While a band of high frequency peaks at around 100 Hz which likely correspond to von Karman vortex shedding can be seen in Figures 5.40 and 5.41, the shedding peaks are several orders of magnitude lower than the oscillation frequencies and its odd harmonics. Thus, the dynamics are dominated by the low frequency components in contrast to the SAOs.

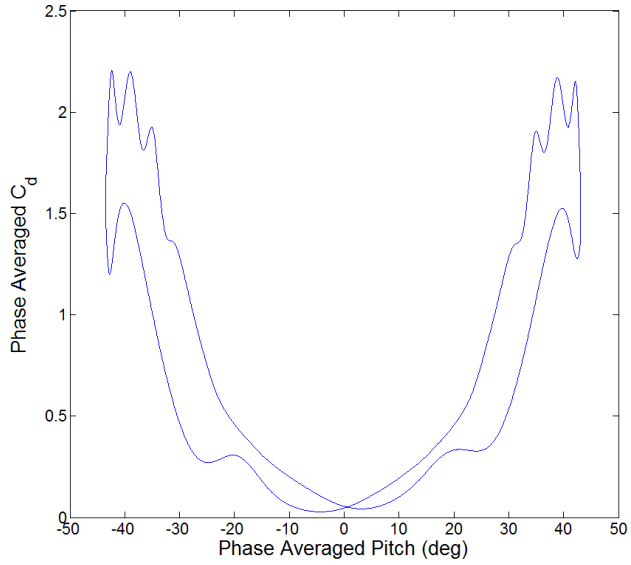

Figure 5.37: Phase averaged C_d curve of simulation at $U = 8.00$ m/s, Re = 80500

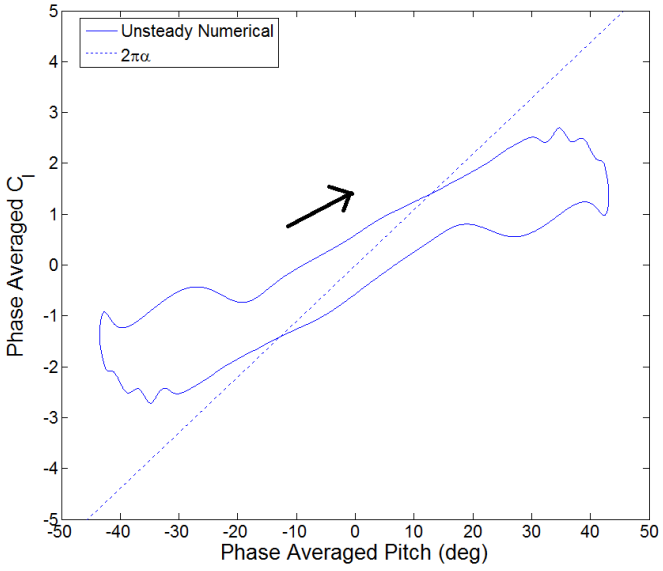

Figure 5.38: Phase averaged C_l curve of simulation at $U = 8.00$ m/s, Re = 80500

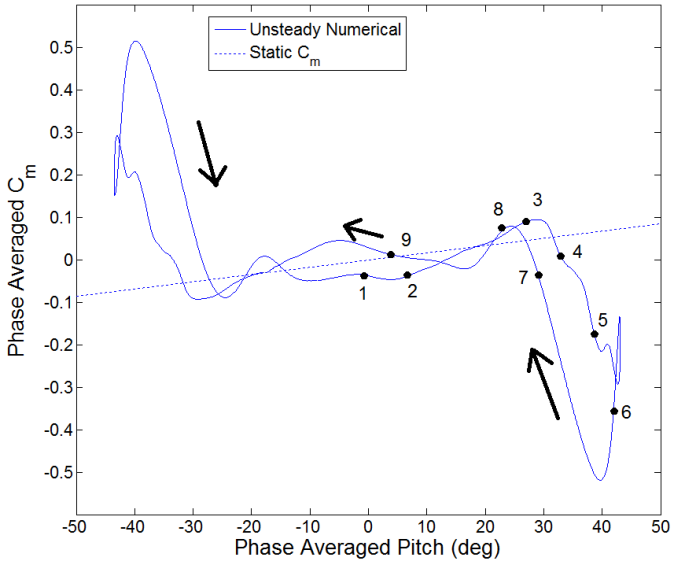

Figure 5.39: Phase averaged $C_{m_{EA}}$ curve of simulation at U = 8.00 m/s, Re = 80500

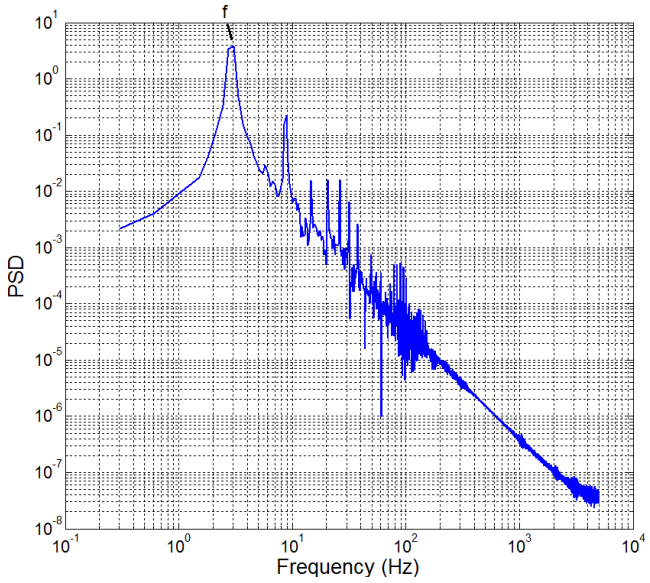

Figure 5.40: PSD of C_l curve of simulation at U = 8.00 m/s, Re = 80500, f = 3.05 Hz, Δf_{DFT} = 0.28 Hz

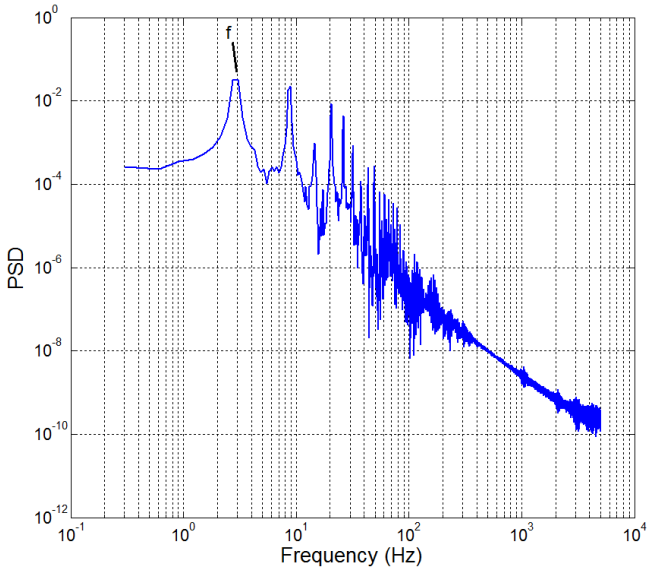

Figure 5.41: PSD of $C_{m_{EA}}$ curve of simulation at $U = 8.00$ m/s, Re = 80500, $f = 3.05$ Hz, $\Delta f_{DFT} = 0.28$ Hz

In order to generate Figure 5.42 the original time trace data was put through a very narrow stop-band filter in order to remove the 2nd harmonics. This allows the C_m plot to be mostly symmetrical. The experimental C_m curve contains significant differences when compared to the simulations. Although both the experimental and simulation results indicate that the work done on the airfoil takes place about high angles of attack, the scale of the C_m differs by an order of magnitude. It was hypothesized that this difference was caused by high frequencies in the simulation that were not retained in the experimental data after filtering. In order to determine if this was the case, the simulation C_m data was re-sampled and filtered, thus removing any harmonics above $3f$. The filtered C_m curve can be seen in Figure 5.43. Although some of the smaller fluctuations are filtered out, the magnitude of the maximum C_m is consistent with the unfiltered data. This would seem to indicate that the difference in the magnitude of the C_m curves is related to the difference in the LCO amplitudes. In order to further explore this, a filter with a cutoff frequency of 25 Hz was used on the experimental data. This C_m curve can be seen in Figure 5.44.

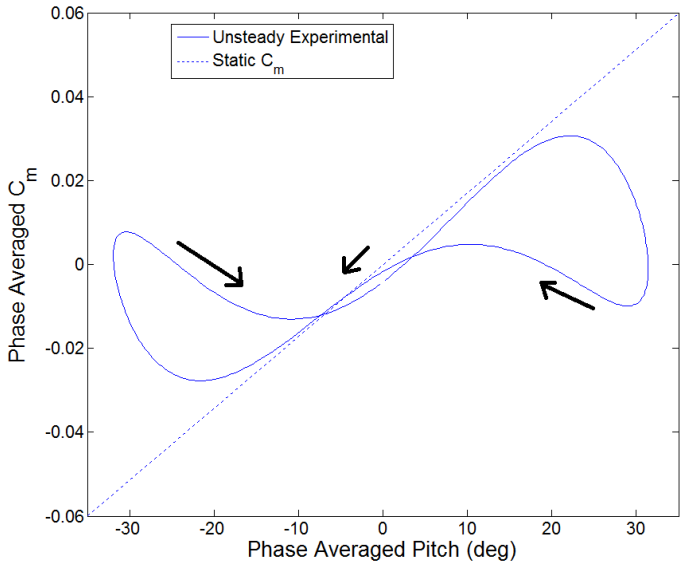

Figure 5.42: Filtered (f_c = 12 Hz) eight cycle phase averaged C_m curve of experiment at U = 7.87 m/s, Re = 79000

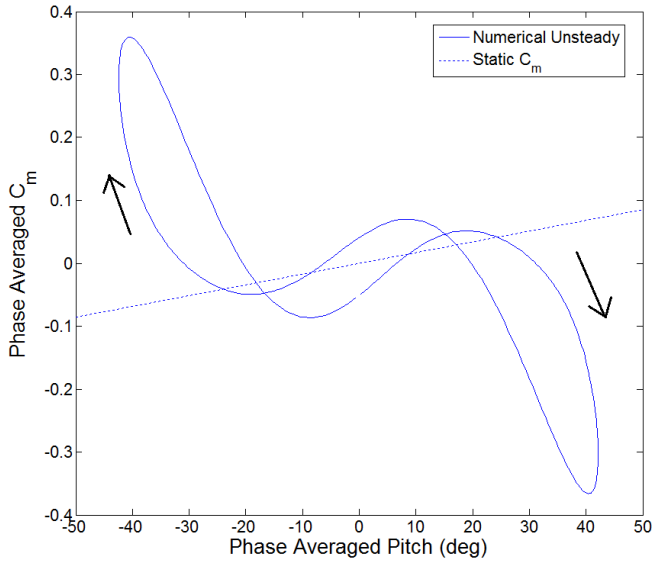

Figure 5.43: Filtered phase averaged $C_{m_{EA}}$ curve of simulation at U = 8.00 m/s, Re = 80500

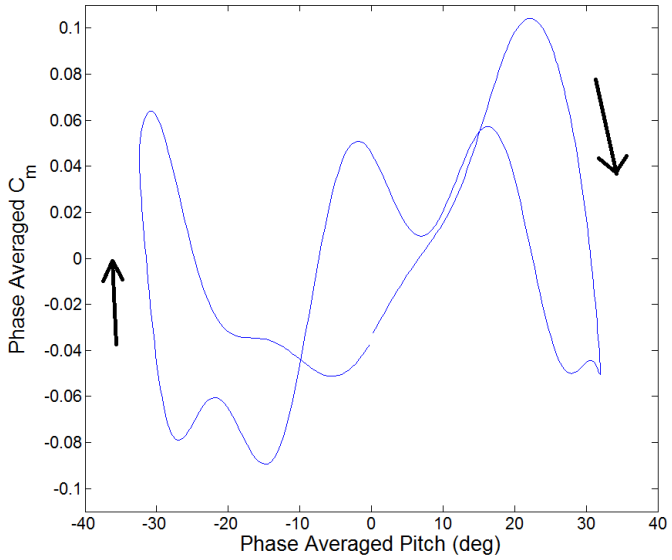

Figure 5.44: Filtered (f_c = 25 Hz) eight cycle phase averaged C_m curve of experiment at U = 7.87 m/s, Re = 79000

With a higher cutoff frequency, the C_m curve maintains a similar shape, and it can be seen that the work is done on the airfoil at high angles of attack, although some higher frequency fluctuations are clearly visible. The magnitude of the peak C_m is higher with a higher cutoff frequency because of the differentiation of the high frequency components.

5.2.4 CFD Flow Field Analysis

Roughly one half of a large amplitude oscillation cycle will be examined in this section. In order to better visualize what point of the C_m cycle is being displayed, each set of graphs corresponds to a labelled point in Figure 5.39.

Firstly, as can be seen in Figures 5.45 and 5.46, at a roughly zero angle of attack there is some vorticity on the lower surface coming off the leading edge that is caused by the upward pitching motion of the wing.

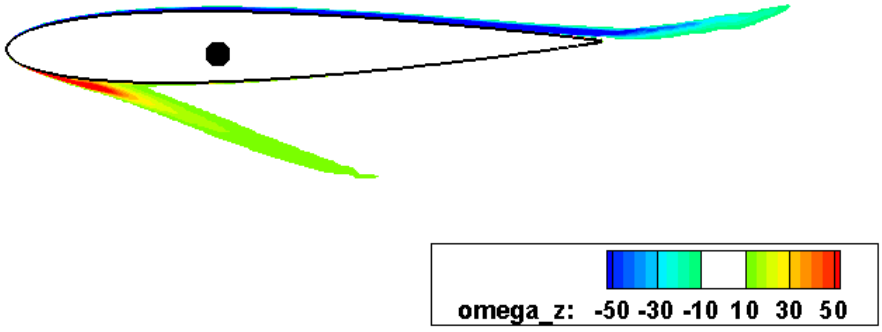

Figure 5.45: Vorticity contours, AOA = −0.8 degrees, pitching up, Point (1)

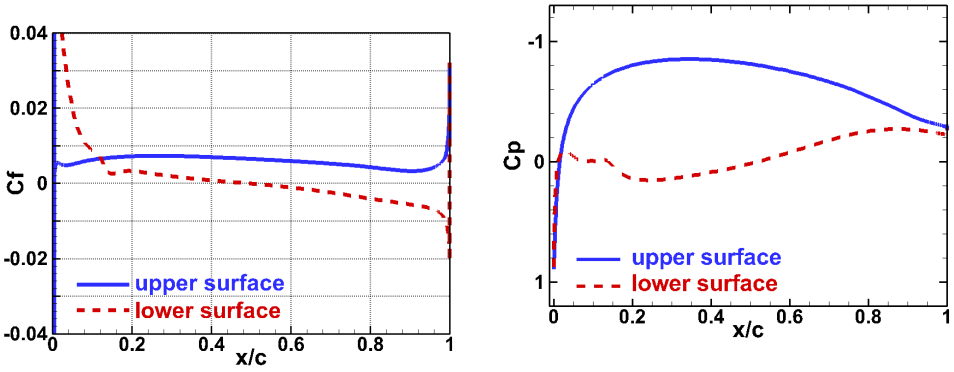

(a) C_f profile

(b) C_p profile

Figure 5.46: Profiles of the C_f and C_p at AOA = −0.8 degrees, pitching up, Point (1)

Figures 5.47 and 5.48 show development of the flow as the airfoil continues to pitch up. In particular, 5.48b shows a larger amount of pressure on the top side of the airfoil compared to Figure 5.46b.

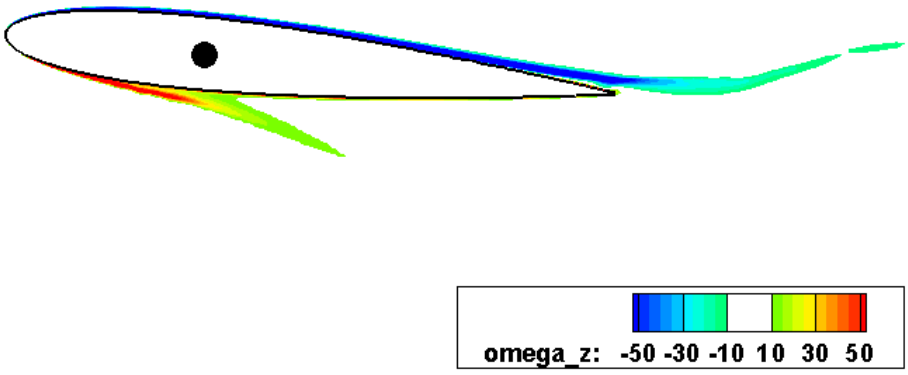

Figure 5.47: Vorticity contours, AOA = 5.6 degrees, pitching up, Point (2)

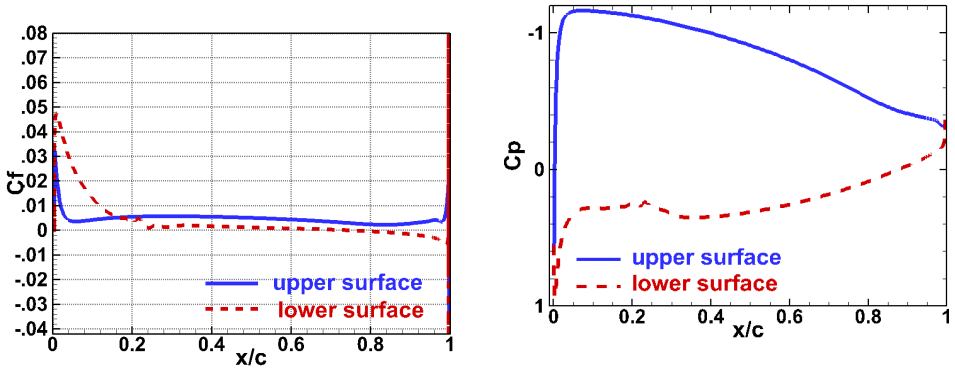

(a) C_f profile

(b) C_p profile

Figure 5.48: Profiles of the C_f and C_p at AOA = 5.6 degrees, pitching up, Point (2)

In Figures 5.49 5.49 and 5.51 it is seen that as the pitch increases, leading edge separation is developing. In addition, trailing edge separation can be seen in Figure 5.50. Where the C_f profile crosses the 0 axis is defined as a separation point. The flow over much of the suction side of the wing may be turbulent as can be seen in the fluctuations in the C_f profile.

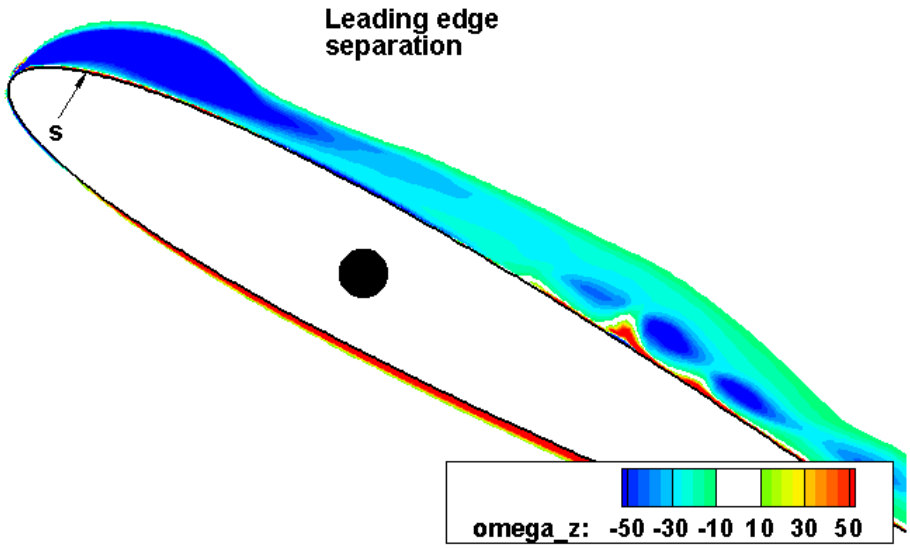

Figure 5.49: Vorticity contours, AOA = 28.3 degrees, pitching up, Point (3)

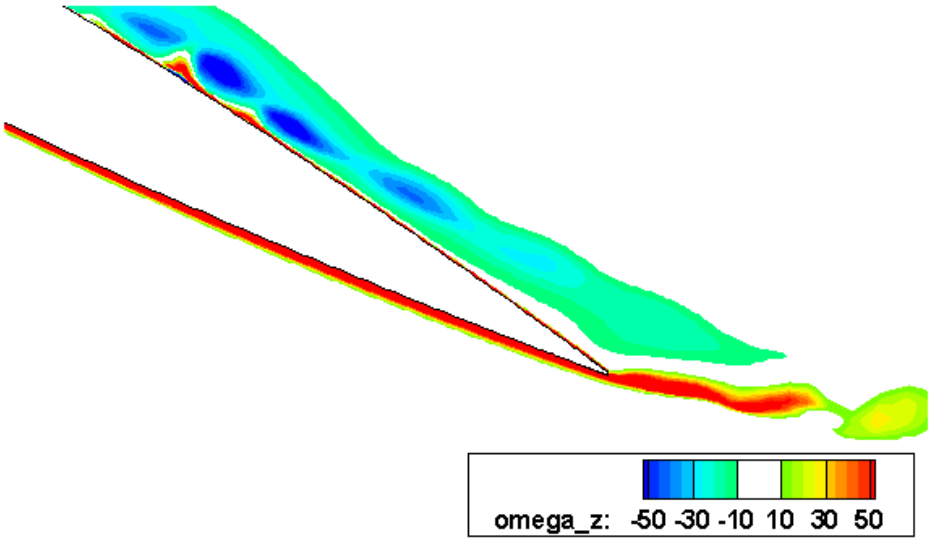

Figure 5.50: Vorticity contours, AOA = 28.3 degrees, pitching up, Point (3)

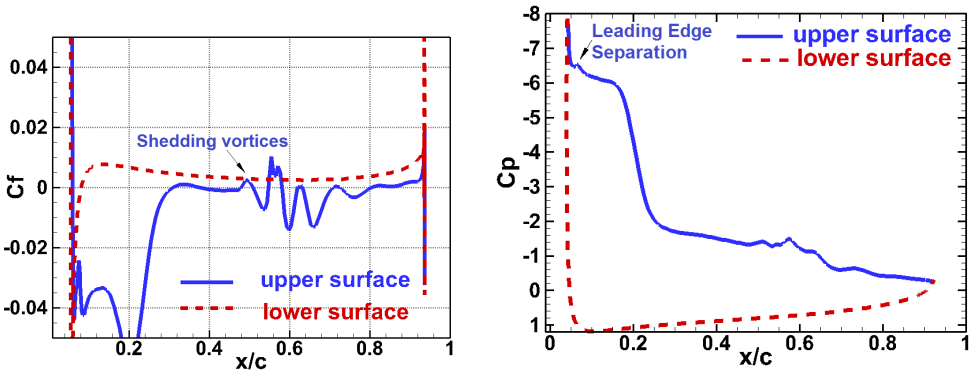

(a) C_f profile

(b) C_p profile

Figure 5.51: Profiles of the C_f and C_p at AOA = 28.3 degrees, pitching up, Point (3)

Figures 5.52 and 5.53 show that as the airfoil continues to pitch up, the trailing edge separation moves up the airfoil towards the leading edge.

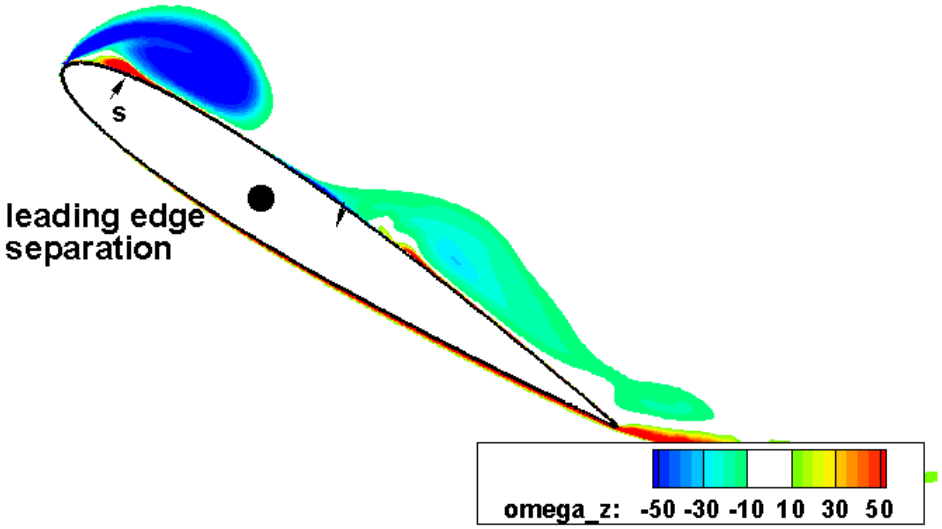

Figure 5.52: Vorticity contours, AOA = 32.9 degrees, pitching up, Point (4)

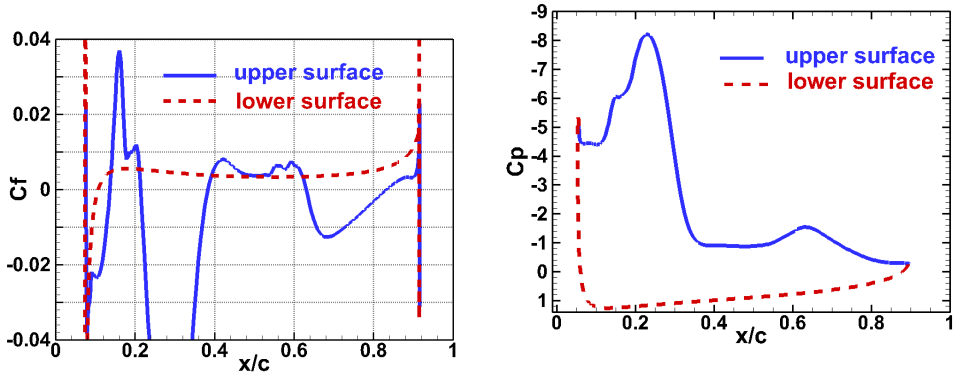

(a) C_f profile

(b) C_p profile

Figure 5.53: Profiles of the C_f and C_p at AOA = 32.9 degrees, pitching up, Point (4)

Figures 5.54 and 5.55 show that as the airfoil approaches maximum pitch, the trailing edge separation and the leading edge separation meet near the leading edge of the airfoil leading to counter-rotating vortices in the vortices labelled 1 and 2. The wing has already begun to stall at this point according to Figure 5.38. Figure 5.55a indicates massively detached flow, as there are a number of areas where the C_f crosses the zero axis, indicating separation on the surface of the wing.

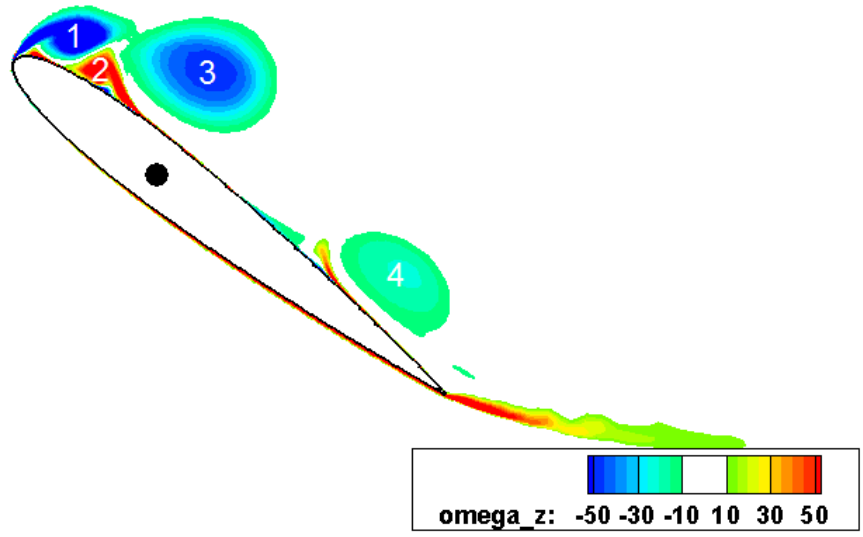

Figure 5.54: Vorticity contours, AOA = 37.8 degrees, pitching up, approaching maximum pitch, Point (5)

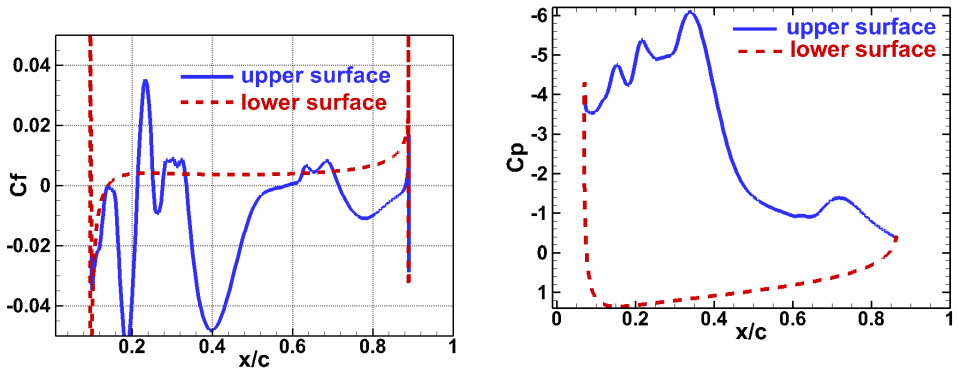

(a) C_f profile

(b) C_p profile

Figure 5.55: Profiles of the C_f and C_p at AOA = 37.8 degrees, pitching up, approaching maximum pitch, Point (5)

Figures 5.56 and 5.57 show that around the airfoil's maximum pitch, there is a large vortex over the trailing edge. This corresponds to a large pressure peak that can be seen in Figure 5.57b. As most of the pressure is behind the elastic axis of the airfoil, this corresponds to the pitch down moment.

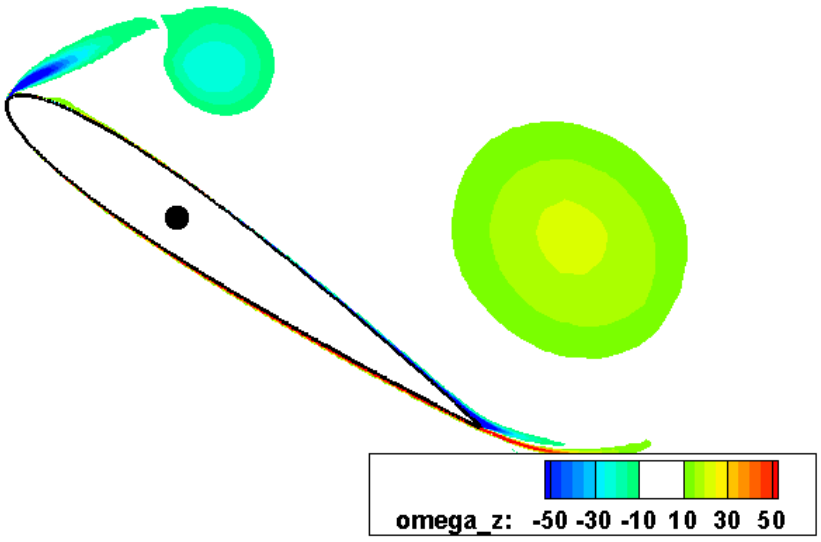

Figure 5.56: Vorticity contours, AOA = 43.6 degrees, pitching down, roughly maximum pitch, Point (6)

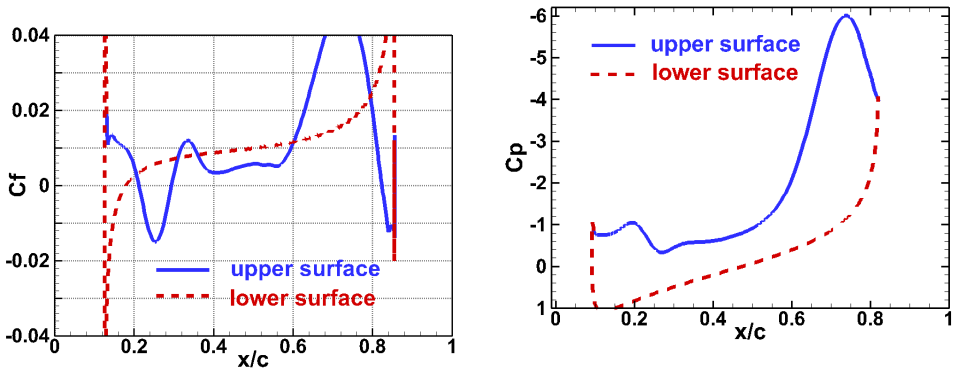

(a) C_f profile

(b) C_p profile

Figure 5.57: Profiles of the C_f and C_p at AOA = 43.6 degrees, pitching down, roughly maximum pitch, Point (6)

Figures 5.58 and 5.59 show that the vortex on the leading edge of the airfoil persists in the wake caused by the pitching down motion of the wing. Figure 5.59a shows an area of reversed flow between $0.3c$ and $0.62c$ on the top side of the airfoil. The vortex labelled 5 is the result of flow from the bottom

of the trailing edge reversing along the top side of the airfoil and separating from the structure.

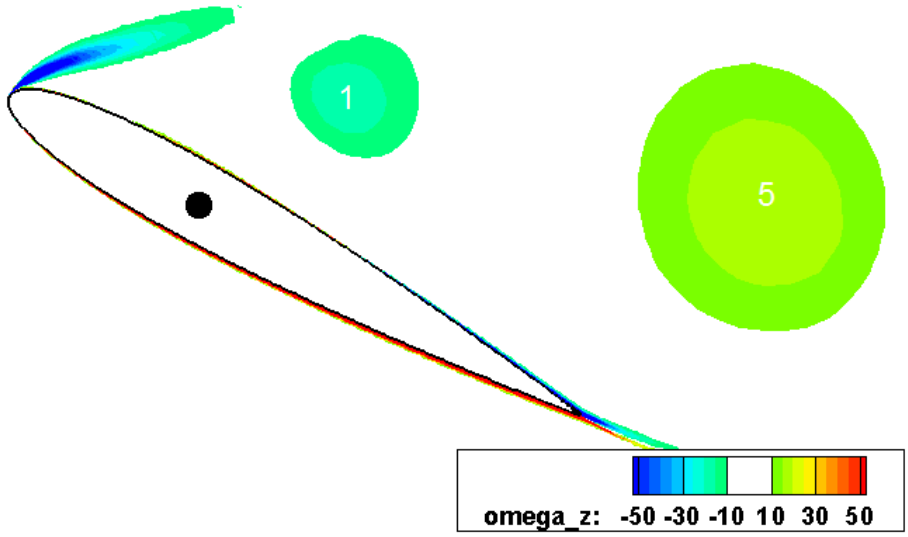

Figure 5.58: Vorticity contours, AOA = 29.2 degrees, pitching down, Point (7)

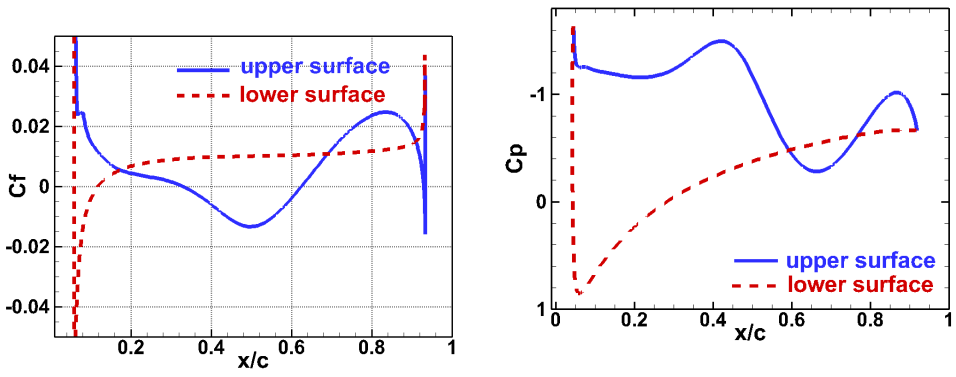

(a) C_f profile

(b) C_p profile

Figure 5.59: Profiles of the C_f and C_p at AOA = 29.2 degrees, pitching down, Point (7)

Figures 5.60 and 5.61 show that the large vortex around the airfoil's trailing edge no longer affects the pressure distribution on the top side of the airfoil.

The airfoil has recovered from its stall somewhat, which agrees with Figure 5.38 which shows a positive C_m at this point in the cycle.

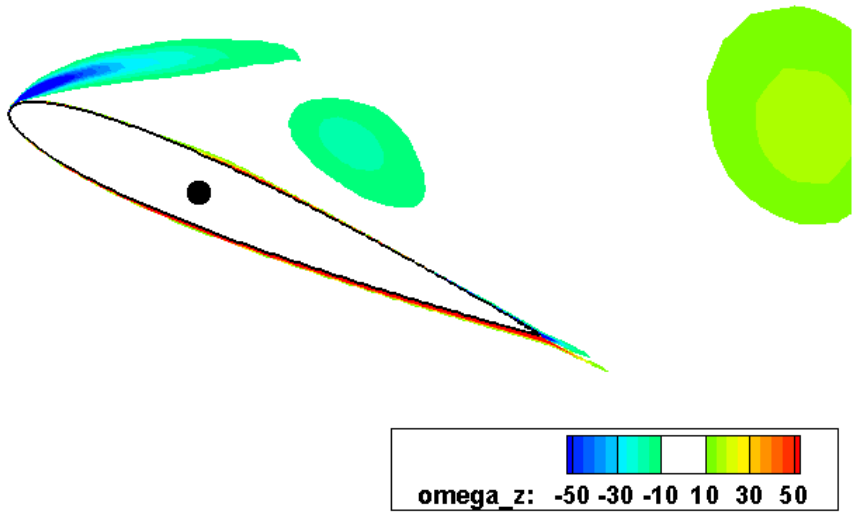

Figure 5.60: Vorticity contours, AOA = 23.0 degrees, pitching down, roughly maximum pitch, Point (8)

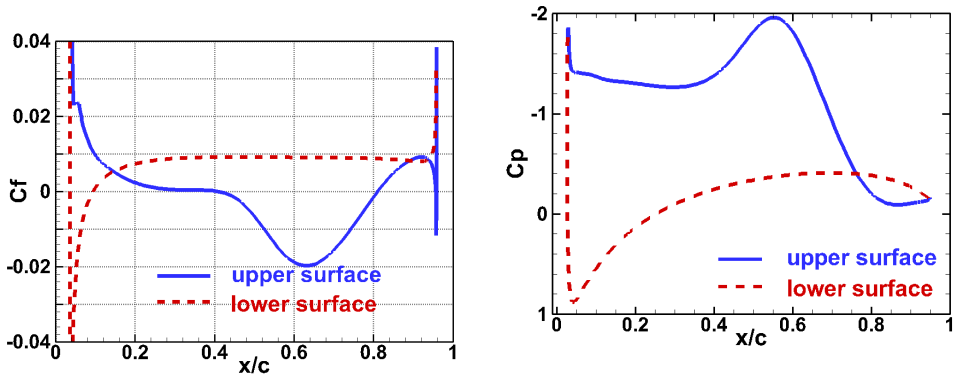

(a) C_f profile

(b) C_p profile

Figure 5.61: Profiles of the C_f and C_p at AOA = 23.0 degrees, pitching down, roughly maximum pitch, Point (8)

Figures 5.62 and 5.63 and based on the pressure distribution seen in Figure

5.63b, it can be seen that despite the positive angle of attack, the bottom side of the airfoil is now the suction side. This corresponds well with the phase lag between the C_l and the angle of attack that can be seen in Figure 5.38, where the lift crosses the x-axis roughly 10 degrees before a 0 degree AOA. This loss of lift on the top side is related to the open separation that is evident from Figure 5.63a where the C_f is at 0 around $0.4c$ and does not recover.

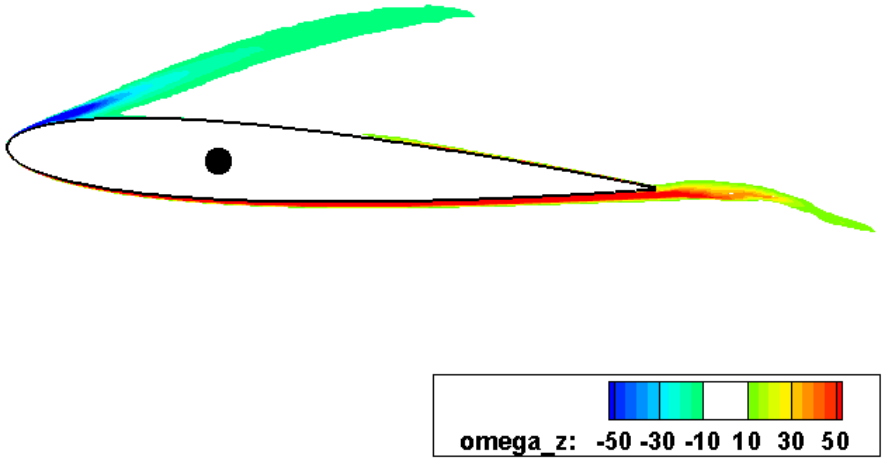

Figure 5.62: Vorticity contours, AOA = 3.6 degrees, pitching down, Point (9)

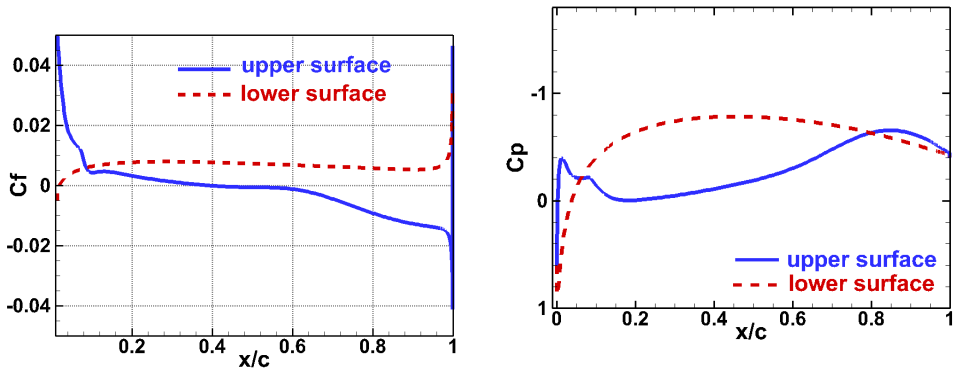

(a) C_f profile

(b) C_p profile

Figure 5.63: Profiles of the C_f and C_p at AOA = 3.6 degrees, pitching down, Point (9)

5.2.5 Boundary Layer Tripping

As per Yuan *et al.* [8], if the turbulent intensity of the airflow is high enough (>0.7% experimentally), the LCOs are not sustained. This is due to early turbulent transition and subsequent lack of a laminar separation bubble. This indicates that separation and transition is an important mechanism in the SAOs. In order to investigate the effect of early transition, the boundary layer of the experimental airfoil was tripped by placing sandpaper over the leading edge and first 15% of the wing. SAOs were not observed with this boundary layer tripping. However, LAOs were seen over the same range of airspeeds as with the smooth airfoil. The time trace, PSD, histogram, phase plane plot and C_m curve of a typical tripped boundary layer test can be seen in Figures 5.64 through 5.68. Figures 5.66 and 5.67 display a very similar symmetry when compared to the experiments without a tripped boundary layer. Figure 5.68 is also similar to 5.42, differing only in the magnitude of the peak C_m. However, Figure 5.64 shows an amplitude with an oscillation that is larger than the one in Figure 5.29 by about 8 degrees. In addition, Figure 5.65 shows a greater number of odd harmonic peaks in the PSD compared to Figure 5.31. The tripped boundary layer tests, therefore, more closely resemble the simulation results in terms of amplitude and the frequency response. The increased amplitude and odd harmonics may be caused by the turbulent transition in the boundary layer leading to reattached flow at comparably higher angles of attack, thus delaying stall.

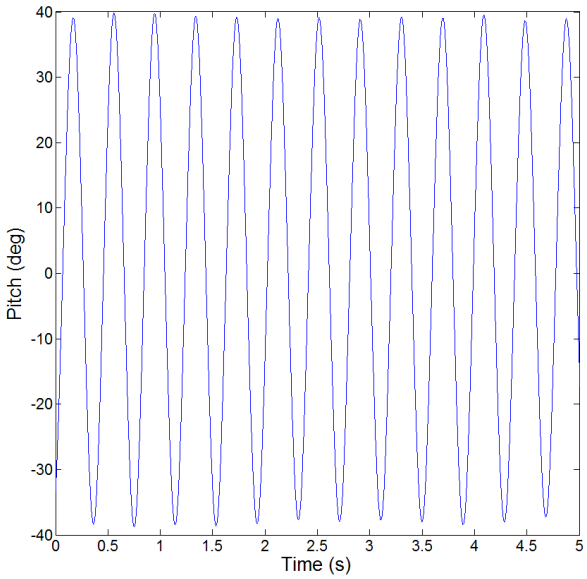

Figure 5.64: Time trace of experiment with a tripped boundary layer at $U = 8.28$ m/s, Re = 81000

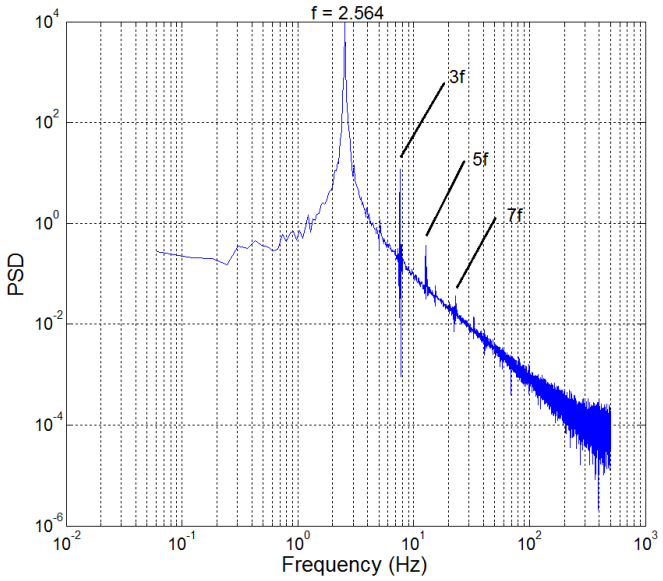

Figure 5.65: Pitch PSD of experiment with a tripped boundary layer at $U = 8.28$ m/s, Re = 81000, $f = 2.56$ Hz, $\Delta f_{DFT} = 0.05$

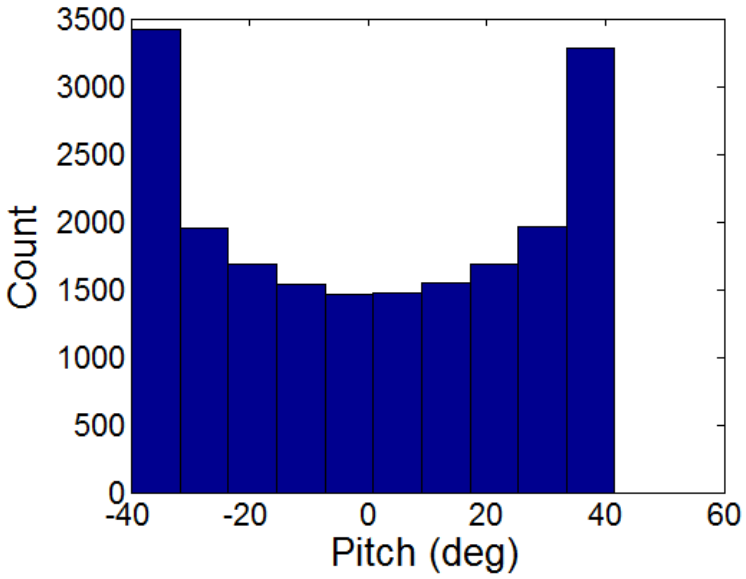

Figure 5.66: Histogram of experiment with a tripped boundary layer at $U = 8.28$ m/s, Re = 81000

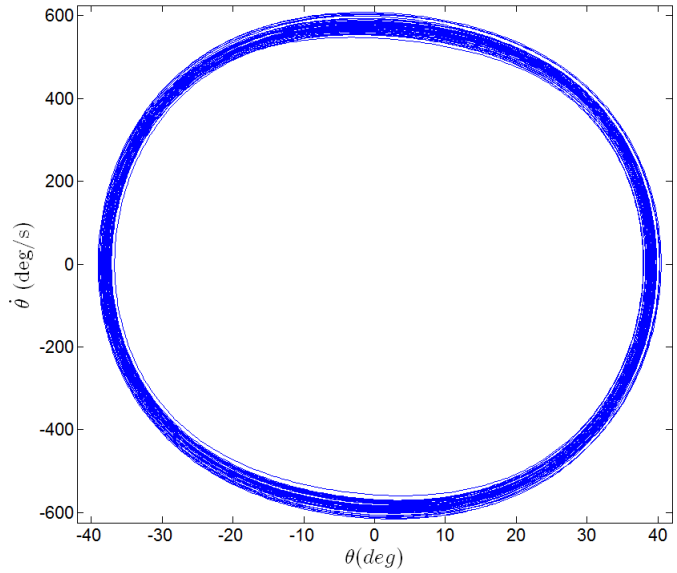

Figure 5.67: Phase plane plot of experiment with a tripped boundary layer at $U = 8.28$ m/s, Re = 81000

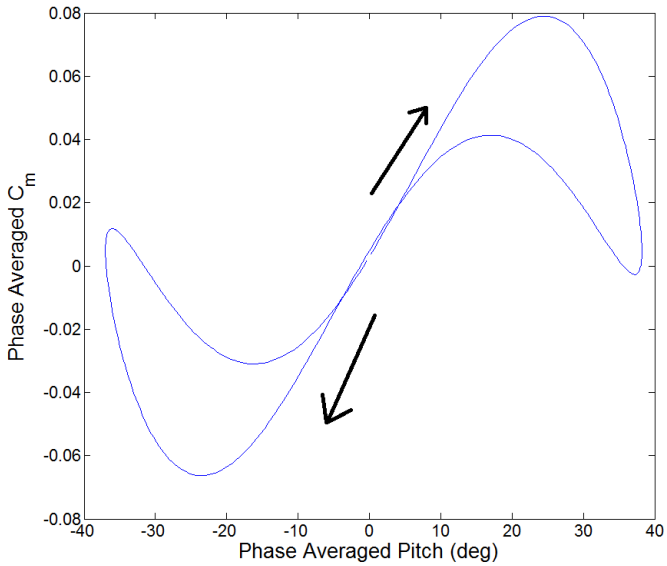

Figure 5.68: Filtered (f_c = 12 Hz) eight cycle phase averaged C_m curve of experiment with a tripped boundary layer at U = 8.28 m/s, Re = 81000

From these experiments it can be seen that, in contrast to the SAOs, the turbulent transition does not appear to have a detrimental effect on the LAOs and even seems to increase their amplitude. This confirms that the mechanism that causes LAOs is fundamentally different from the one that causes the SAOs and that they are separate phenomena that can occur in the same system.

5.3 Parallels to Other Work

The SAOs contain two distinct frequency regimes, one related to vortex shedding and one related to the LCO behaviour. The high frequency does not interact with the LCO because their frequencies differ by orders of magnitude. However, it has been shown that the turbulent transition is an important part of the mechanism behind SAOs, and the subsequent vortex shedding is evidence of that transition. Transition is not related to the LAOs, except as a factor that slightly affects the quantitative properties of the behaviour i.e. amplitude and frequency. This is further evidenced by the lack of a Strouhal frequency in the dynamic curves seen in Section 5.2.3. The loss of a high frequency component associated with a hysteresis effect in C_l was also observed by Schewe [33].

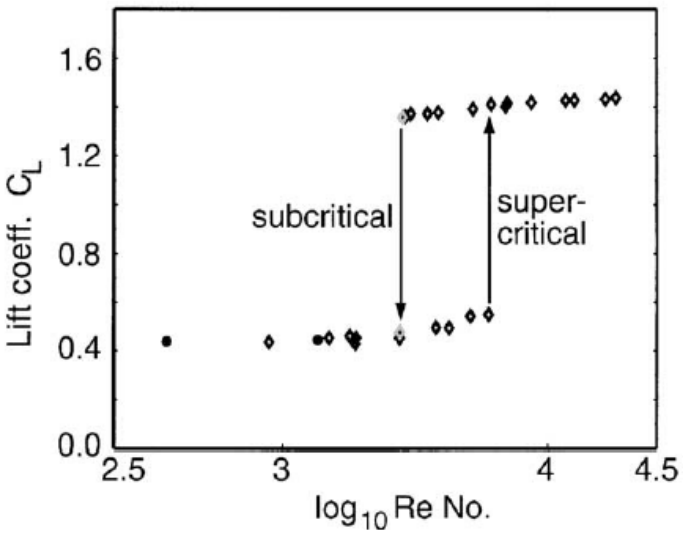

Figure 5.69: Subcritical and supercritical C_l values from Schewe for an airfoil held at 12 degrees AOA [33].

In examining Reynolds number effects around bluff bodies, Schewe examined the flow around a wind-power plant airfoil held at both 0 degrees AOA and 12 degrees AOA at various Reynolds numbers [33]. From this, Schewe determined Reynolds number dependant flow regimes that he called the subcritical and supercritical. The subcritical regime was associated with low C_l values and a well defined Strouhal shedding peak in the PSD of the flow spectra. The supercritical regime was associated with higher C_l values and no defined Strouhal shedding visible from the PSD of the flow spectra. This can be seen in Figures 5.69 and 5.70 respectively. At 12 degrees, the supercritical C_l value corresponds to the linear C_l of $2\pi\alpha$. Therefore, the subcritical C_l corresponds with stall and associated non-linearities.

As can be seen in Figure 5.69, either flow regime can occur over a range of Reynolds numbers displaying what Schewe refers to as a hysteresis effect. This is similar to the behaviour of the steady state LCO amplitude, where both the LAO and SAO regimes can be present over a range of Reynolds numbers.

The similarities in the PSDs of the flow in Figure 5.70 and the PSDs of the CFD dynamical coefficients in Figures 5.41 and 5.18 should also be noted. This transition between flow regimes may be a associated with the stability boundary between LAOs and SAOs. At a high enough angle of

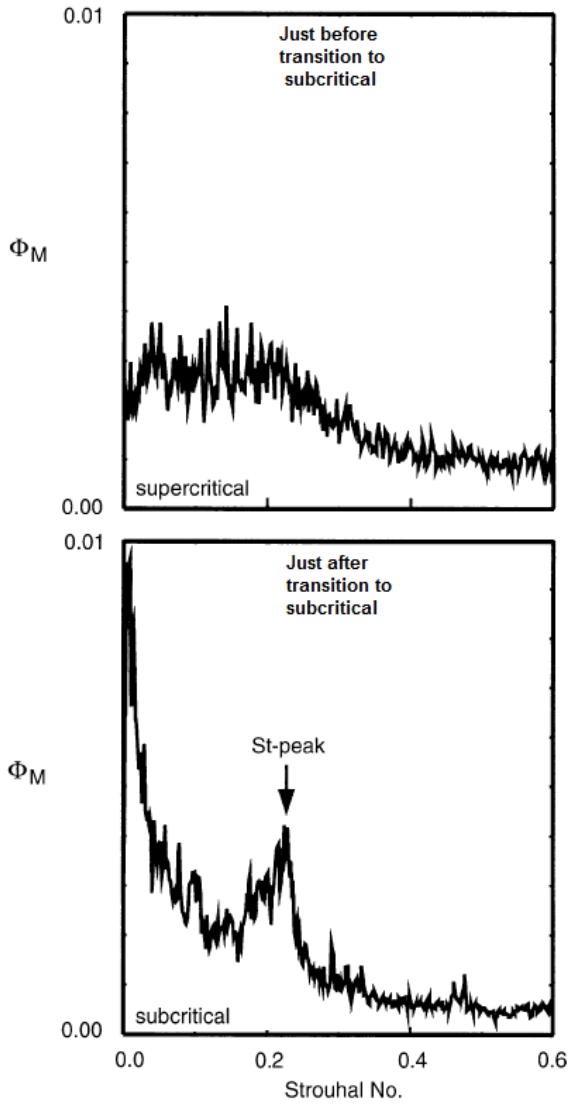

Figure 5.70: Subcritical and supercritical flow spectra from Schewe for an airfoil held at 12 degrees AOA [33].

attack, the transition of the flow from subcritical to supercritical results in an increase in C_l before stall occurs. In the transient process, the pitch amplitude increases until an LCO is reached when the structural and aerodynamic forces balance each other. Schewe also notes that 3-D flow structures are present regardless of flow regime, so it is likely that these are responsible for some of the discrepancy between the calculations and experiments in this work as the 3D flow structures cannot be accounted for in the 2D CFD calculations.

Fernandes and Armandei were able to achieve similar large amplitude oscillations using a flat plate attached to a torsional spring system [34]. They described these oscillations as torsional galloping and found that this would only occur within a certain range of fluid speeds, outside of which either no oscillation or a static instability (i.e. divergence) would occur. They found that they could use the van der Pol-Duffing equation as a phenomenological model that could provide decent agreement with their experimental results. This equation can be seen below in equation (5.5).

$$\ddot{\theta} + \mu\left(\frac{4}{\theta_0^2}\theta^2 - 1\right)\dot{\theta} + \theta + \delta\theta^3 = 0 \tag{5.5}$$

This equation consists of both a non-linear stiffness and non-linear damping term, both of which may be incorporated into a model that could be used to describe the airfoil behaviour in this work. A simpler van der Pol model of the following form could be used:

$$I_{EA}\ddot{\theta} + (C_s + C_a + C_n\theta^2)\dot{\theta} + (k_s + k_a)\theta = 0 \tag{5.6}$$

In equation (5.6), the C_s and k_s are structural damping and stiffness respectively, the C_a and k_a terms are aerodynamic damping and stiffness, and the C_n term is a non-linear damping that would be responsible for the amplitude of the LCO. If this model were to take into account the possibility of both the LAOs and SAOs, further non-linear terms would have to be added in the damping, such that there could be a destabilizing attractor between zero degrees and the SAO amplitude, and also between the SAO and LAO amplitudes. In fact, in order to fully capture the bifurcation behaviour described in Figure 5.2, the model would have to be at least of 5^{th} order. Note that a model with only non-linear damping terms will not capture the "S" shape of the C_m curve, as a non-linear stiffness term will have to be added. Poirel and Yuan [31] and Khalil *et al.* [6] used a generalized Duffing van der Pol equation to model the SAOs. Khalil used a 5th order polynomial in the damping and stiffness to generate a model that was accurate at predicting both the LCO frequency and amplitude in addition to the transient behaviour of the SAOs.

Harris also noted a LAO regime in his work [2], although this occurred with a 2-spring or 0-spring system (cutting the structural stiffness in half, or eliminating it altogether), and with an EA that was at $0.269c$ behind the airfoil's leading edge rather than $0.35c$.

6 Recommendations and Conclusion

6.1 Recommendations for Future Work

6.1.1 Experimental Work

With the current structural parameters, a study should be done on the precise nature of the Reynolds dependence of the LAOs. If laminar separation is not a necessary process in the development of the LAOs, it should be examined if LAOs can be found over a wider range of Reynolds numbers by adjusting structural parameters such as stiffness and damping. In addition, detailed work on the limits of the unstable attractor that is present between the LAO and SAO regimes should be done.

Further experimental work can be performed simply by adjusting the geometry and structural properties. The LAOs were not a phenomenon that occurred until the EA of the wing was moved aft of the quarter chord point. Further tests should be done to study the effects of the EA on the LAOs and general system stability. In a similar vein, the structural stiffness or moment of inertia of the system could be varied in order to study the effects.

One main application of the LAOs would be for use in energy harvesting. Studying the effects of the structural properties would make it possible to find the ideal configuration that could be used to extract the greatest amount of energy from the flow. These experiments would also be useful to provide a basis with which to compare CFD results and to confirm that they are valid (or invalid) over a range of structural physical parameters.

Harris made a number of suggestions to improve the experimental rig which remain valid [2]. In particular, the rig would benefit from a way to easily reset the wing to 0 degrees AOA and adjust the zero flow pitch angle relative to the wind tunnel. Currently, the zero angle must be determined via determination of the angle at which the airfoil is subjected to the minimum aerodynamic

force and noting that pitch angle using the potentiometer. The potentiometer is prone to drift over time due to physical changes in the environment, and therefore the zero pitch angle must be remeasured prior to every test. The angle of the airfoil can only be changed adjusting the pretension in the springs by hand which can be time consuming and difficult to do accurately. In addition, the placement of a scale close to the point at which the angle is adjusted would be useful even as a rough guide in finding aerodynamic zero AOA.

6.1.2 Computational Work

Further computational results could be obtained by prescribing an oscillatory motion to the wing, rather than coupling it to the flow field calculations. This would allow for a better comparison of the C_m results to the experimental work.

3D LES should be performed in order to resolve the flow structures of the massively detached flow of the LAO regime. This should reduce the discrepancies between the CFD and experimental LCO amplitudes and frequencies. An overlapping scheme should also be considered to limit the grid motion to the near region around the airfoil. Studying the effects of the turbulent intensity on the LAOs could also be considered, given that it has already been found that an increase in turbulent intensity will result in SAOs not being sustained. These results should also be compared to experimental work for validation.

6.2 Conclusions

This work has sought to examine aeroelastic oscillations in pitch of a spring-supported NACA0012 airfoil at transitional Reynolds numbers. The response of the airfoil was studied experimentally in addition to computationally, with experimental results being compared to the numerical results. The numerical results were also used to gain insight into the flow field around the wing at various points of interest. The airfoil's EA position was set at $0.35c$ behind the leading edge throughout.

6.2.1 Experimental Work

From the experiments performed in the wind tunnel, it was found that over the range of airspeeds between 5.2 and 10.3 m/s, two distinct LCO regimes existed. One regime was characterized by oscillation amplitudes of >25 degrees. This was called the large amplitude oscillation (LAO) regime. The second

is characterized by oscillation amplitudes of <3 degrees. This was called the small amplitude oscillation (SAO) regime. These results are summarized in Figure 3.6. The LAO regime exhibits a gradual increase in frequency with airspeed, whereas the SAO regime's frequencies start out higher at airspeeds below 7 m/s, make a sudden dip, and then increase with airspeed after 7.75 m/s. These results are summarized in Figure 3.9. This behaviour can be classified as a bifurcation, as the LCO frequency and amplitude change qualitatively with airspeed. The presence of two different steady states which are dependant on the initial conditions or perturbation given to the system is an indicator of highly non-linear dynamics.

6.2.2 Computational Work

2D URANS simulations utilizing the $\gamma - Re_\theta$ model were performed using 2D LES simulations as a point from which to start the calculations. The 2D LES simulations were prone to non-periodic and pseudo-chaotic behaviour due to inaccurate laminar separation prediction, whereas the URANS simulations produced stable LCOs in both the LAO and SAO regimes. The SAO calculations display similar amplitudes to the experiments, while having a lower frequency, whereas the LAO calculations display higher amplitudes and frequencies when compared to the experiments. These results are summarized in Figures 4.7 and 4.8. The discrepancy between the calculations and the experiments is likely due to the failure of the URANS model to accurately model the massive flow separation that occurs at high angles of attack.

Small Amplitude Oscillations

The PSD spectra of the SAO C_m and C_l data taken from the simulations show peaks at the fundamental frequency of the LCOs, odd order harmonic peaks thereof, and also a peak at the Strouhal shedding frequency. The PSD of the simulation time traces show only odd order harmonics, in contrast to the experimental results which show both even and odd order harmonics. The even order harmonics are caused by asymmetry in the experimental system. Analysis of the flow field throughout an SAO cycle shows trailing edge separation and laminar separation which moves towards the leading edge of the wing as the AOA increases. Turbulent transition also occurs near the trailing edge. This leads to a lag in the lift and moment as the wing pitches through a small amplitude oscillation cycle. It is this lag that feeds the SAOs. The experimental rig is not able to pick up the high frequency components due to

electrical noise, however, Figure 5.16 shows similar dynamics to Figure 5.15 in that work is done on the airfoil as it pitches through 0 degrees AOA.

Large Amplitude Oscillations

The PSD spectra of the LAO C_m and C_l data show the fundamental oscillation frequency and several harmonics, with what may be a von Karman peaks at around 100 Hz. The simulation C_m curve and the experimental C_m curve both indicated that the airfoil has work done on it about high angles of attack, but the value of the C_m differs by about an order of magnitude. This is related to the discrepancy in LCO amplitude, as the delayed onset of stall in the simulation leads a large downward pitching moment when it does occur. Analysis of the flowfield throughout an LAO cycle shows that trailing edge separation starts at relatively low AOAs ($\sim$ 10 degrees) and quickly moves up towards the leading edge as the AOA increases. This separation eventually reaches the leading edge separation leading to counter-rotating vortices near the leading edge of the airfoil around the maximum AOA. As the airfoil pitches down, the leading edge separation remains as it is caused by the fast downwards pitching motion of the airfoil. At around 10 degrees AOA, the side of the airfoil towards which the airfoil is pitching becomes the suction side. This can be seen in the phase lag between the AOA and C_l curve in Figure 5.38. The effect of tripping the boundary layer was examined experimentally by placing sandpaper over the leading edge of the airfoil. It was found that the boundary layer tripping increased the amplitude of the LAOs, in contrast to previous work done with SAOs where an increase in turbulence led to the LCOs failing to occur. This indicates that the LAOs and SAOs are not related phenomena.

Bibliography

[1] P. B. S. Lissaman, "Low-reynolds-number airfoils," *Annual Review of Fluid Mechanics*, vol. 15, no. 1, pp. 223–239, 1983.

[2] Y. Harris, "The aeroelastic dynamics of a NACA 0012 airfoil oscillating in pitch at transitional Reynolds numbers," Master's thesis, Royal Military College of Canada, Kingston, Ontario, Canada, 2007.

[3] D. Poirel, V. Metivier, and G. Dumas, "Computational aeroelastic simulations of self-sustained pitch oscillations of a NACA0012 at transitional Reynolds numbers," *Journal of Fluids and Structures*, vol. 27, no. 8, pp. 1262–1277, 2011.

[4] D. Rudmin, A. Benaissa, and D. Poirel, "Detection of laminar flow separation and transition on a NACA-0012 airfoil using surface hot-films," *Journal of Fluids Engineering*, vol. 135, no. 10, p. 101104, 2013.

[5] D. Poirel and F. Mendes, "Experimental small-amplitude self-sustained pitch–heave oscillations at transitional Reynolds numbers," *AIAA Journal*, vol. 52, no. 8, pp. 1581–1590, 2014.

[6] M. Khalil, D. Poirel, and A. Sarkar, "Probabilistic parameter estimation of a fluttering aeroelastic system in the transitional Reynolds number regime," *Journal of Sound and Vibration*, vol. 332, no. 15, pp. 3670–3691, 2013.

[7] R. Sandhu, M. Khalil, A. Sarkar, and D. Poirel, "Bayesian model selection for nonlinear aeroelastic systems using wind-tunnel data," *Computer Methods in Applied Mechanics and Engineering*, 2014.

[8] W. Yuan, D. Poirel, B. Wang, and A. Benaissa, "Effect of freestream turbulence on airfoil limit-cycle oscillations at transitional Reynolds numbers," *Journal of Aircraft*, 2014.

[9] S. Lapointe and G. Dumas, "Improved numerical simulations of self-sustained oscillations of a NACA0012 with transition modeling," in *41st AIAA Fluid Dynamics Conference and Exhibit*, AIAA, 2011.

[10] S. Burgmann and W. Schröder, "Investigation of the vortex induced unsteadiness of a separation bubble via time-resolved and scanning piv measurements," *Experiments in fluids*, vol. 45, no. 4, pp. 675–691, 2008.

[11] D. Poirel, Y. Harris, and A. Benaissa, "Self-sustained aeroelastic oscillations of a NACA0012 airfoil at low-to-moderate reynolds numbers," *Journal of Fluids and Structures*, vol. 24, no. 5, pp. 700–719, 2008.

[12] R. Huang, W. W. Shy, S. Lin, and F. Hsiao, "Influence of surface flow on aerodynamic loads of a cantilever wing," *AIAA journal*, vol. 34, no. 3, pp. 527–532, 1996.

[13] H. Lee and R. Huang, "Frequency selection of wake flow behind a NACA 0012 wing," *Journal of Marine science and technology*, vol. 6, no. 1, pp. 29–37, 1998.

[14] R. Huang and H. Lee, "Turbulence effect on frequency characteristics of unsteady motions in wake of wing," *AIAA journal*, vol. 38, no. 1, pp. 87–94, 2000.

[15] G. Dimitriadis and J. Li, "Bifurcation behavior of airfoil undergoing stall flutter oscillations in low-speed wind tunnel," *AIAA journal*, vol. 47, no. 11, pp. 2577–2596, 2009.

[16] N. A. Razak, T. Andrianne, and G. Dimitriadis, "Flutter and stall flutter of a rectangular wing in a wind tunnel," *AIAA journal*, vol. 49, no. 10, pp. 2258–2271, 2011.

[17] J. H. Watmuff, "Evolution of a wave packet into vortex loops in a laminar separation bubble," *Journal of Fluid Mechanics*, vol. 397, no. 119-169, p. 31, 1999.

[18] Z. Yang and P. R. Voke, "Large-eddy simulation of boundary-layer separation and transition at a change of surface curvature," *Journal of Fluid Mechanics*, vol. 439, pp. 305–333, 2001.

[19] M. Lang, U. Rist, and S. Wagner, "Investigations on controlled transition development in a laminar separation bubble by means of lda and piv," *Experiments in Fluids*, vol. 36, no. 1, pp. 43–52, 2004.

[20] S. Yarusevych, P. E. Sullivan, and J. G. Kawall, "On vortex shedding from an airfoil in low-Reynolds-number flows," *Journal of Fluid Mechanics*, vol. 632, pp. 245–271, 2009.

[21] B. R. McAuliffe and M. I. Yaras, "Transition mechanisms in separation bubbles under low and elevated freestream turbulence," *Journal of Turbomachinery*, vol. 132, no. 1, p. 011004, 2010.

[22] W. Yuan, D. Poirel, B. Wang, and M. Khalid, "Simulations of airfoil limit-cycle oscillations at transitional Reynolds numbers," in *Proceedings of the 50th AIAA Aerospace Sciences Conference, AIAA Paper*, no. 2012-0041, 2012.

[23] B. Wang, D. Poirel, and W. Yuan, "Turbulence effects on airfoil limit-cycle oscillations at transitional Reynolds numbers," in *CASI 60th Aeronautics Conference and AGM*, (Toronto, Ontario, Canada), 2013.

[24] W. Yuan, D. Poirel, and B. Wang, "Simulations of pitch–heave limit-cycle oscillations at a transitional Reynolds number," *AIAA journal*, vol. 51, no. 7, pp. 1716–1732, 2013.

[25] S. Yabili, M. Smith, and G. Dimitriadis, "Unsteady Navier–Stokes simulation of low-Reynolds stall flutter," in *50th AIAA Aerospace Sciences Meeting including the New Horizons Forum and Aerospace Exposition*, AIAA, 2012.

[26] D. Poirel, Y. Harris, and A. Benaissa, "Aeroelastic dynamics of a NACA 0012 airfoil in the transitional Reynolds number regime," in *Proceedings of PVP 2006/ICPVT-11*, 2006.

[27] J. B. Barlow, W. H. Rae, and A. Pope, *Low-speed wind tunnel testing*. John Wiley & Sons, Canada, 1999.

[28] H. K. Versteeg and W. Malalasekera, *An introduction to computational fluid dynamics: the finite volume method*. Pearson Education, 2007.

[29] R. B. Langtry and F. R. Menter, "Correlation-based transition modeling for unstructured parallelized computational fluid dynamics codes," *AIAA Journal*, vol. 47, no. 12, pp. 2894–2906, 2009.

[30] W. Yuan and M. Khalid, "Computation of unsteady flows past aircraft wings at low Reynolds numbers," *Canadian Aeronautics and Space Journal*, vol. 50, no. 4, pp. 261–271, 2004.

[31] D. Poirel and W. Yuan, "Aerodynamics of laminar separation flutter at a transitional Reynolds number," *Journal of Fluids and Structures*, vol. 26, no. 7, pp. 1174–1194, 2010.

[32] W. Yuan, M. Khalid, J. Windte, U. Scholz, and R. Radespiel, "Computational and experimental investigations of low-Reynolds-number flows past an airfoil," *The Aeronautical Journal*, vol. 111, no. 1115, pp. 17–29, 2007.

[33] G. Schewe, "Reynolds-number effects in flow around more-or-less bluff bodies," *Journal of Wind Engineering and Industrial Aerodynamics*, vol. 89, no. 14, pp. 1267–1289, 2001.

[34] A. C. Fernandes and M. Armandei, "Phenomenological model for torsional galloping of an elastic flat plate due to hydrodynamic loads," *Journal of Hydrodynamics, Ser. B*, vol. 26, no. 1, pp. 57–65, 2014.

Appendices

A Experimental Data

A.1 SAO

A.1.1 U=5.26 m/s

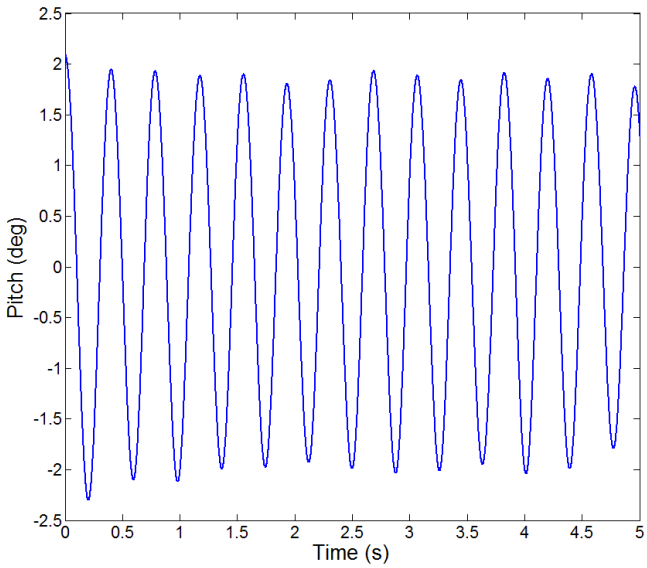

Figure A.1: Filtered time trace of experiment at $U = 5.26$ m/s, Re = 53000

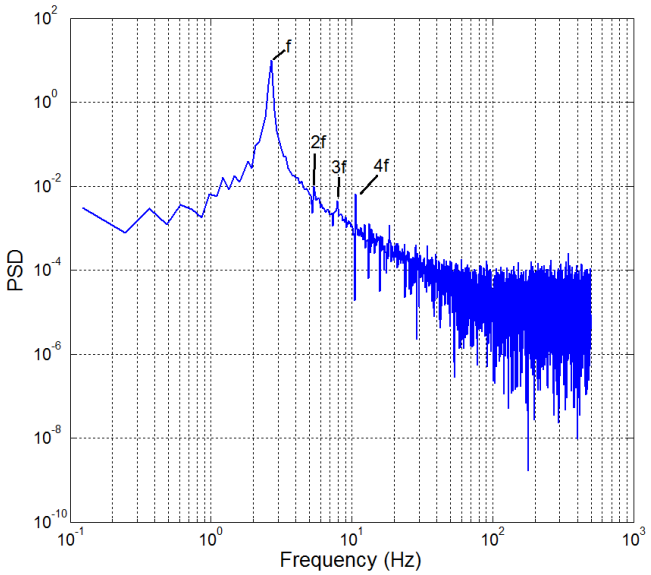

Figure A.2: PSD of experiment at $U = 5.26$ m/s, Re = 53000, $f = 2.686$ Hz

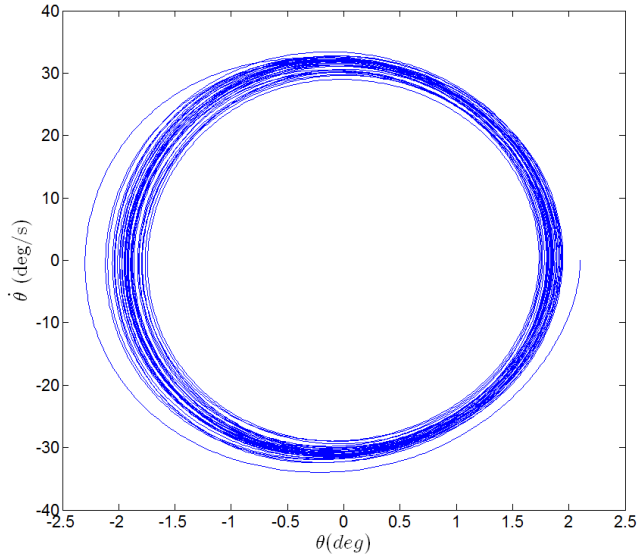

Figure A.3: Filtered phase plane plot of experiment at $U = 5.26$ m/s, Re = 53000

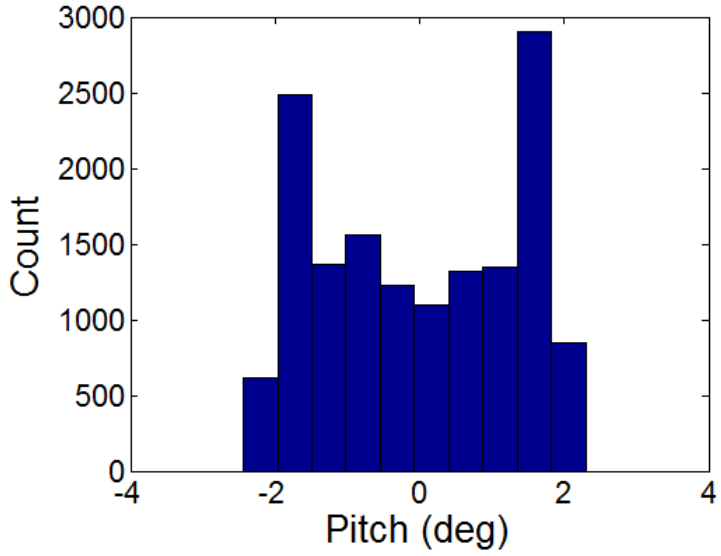

Figure A.4: Histogram of experiment at $U = 5.26$ m/s, Re = 53000

A.1.2 U=5.85 m/s

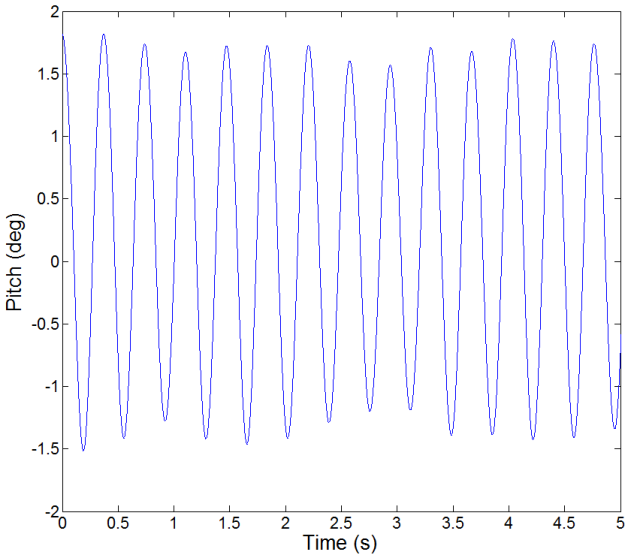

Figure A.5: Filtered time trace of experiment at $U = 5.85$ m/s, Re = 59000

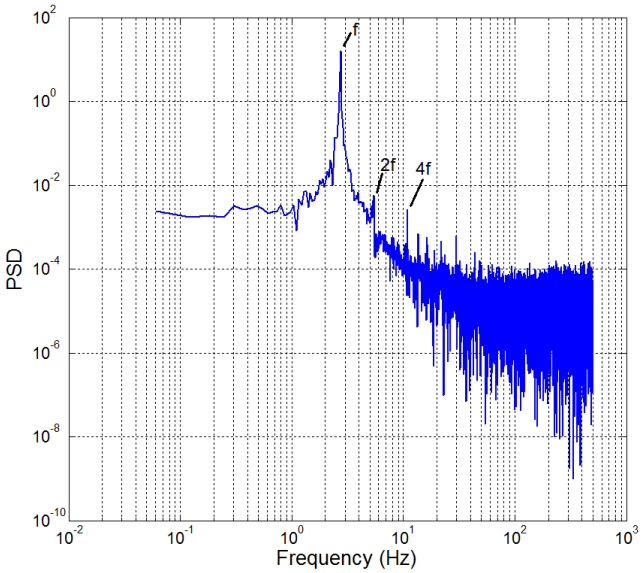

Figure A.6: PSD of experiment at $U = 5.85$ m/s, Re = 59000, $f = 2.747$ Hz

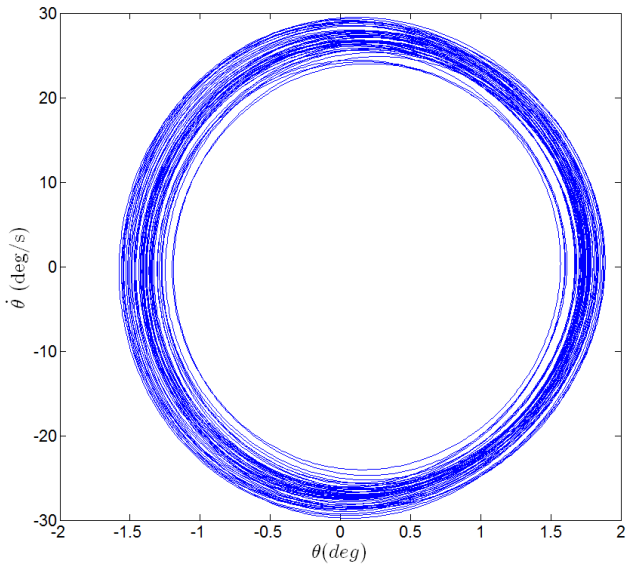

Figure A.7: Filtered phase plane plot of experiment at $U = 5.85$ m/s, Re = 59000

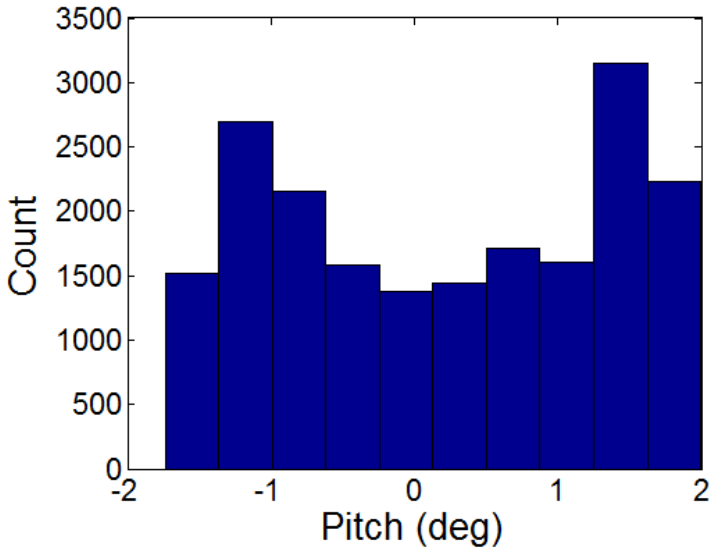

Figure A.8: Histogram of experiment at $U = 5.85$ m/s, Re = 65500

A.1.3 U=6.51 m/s

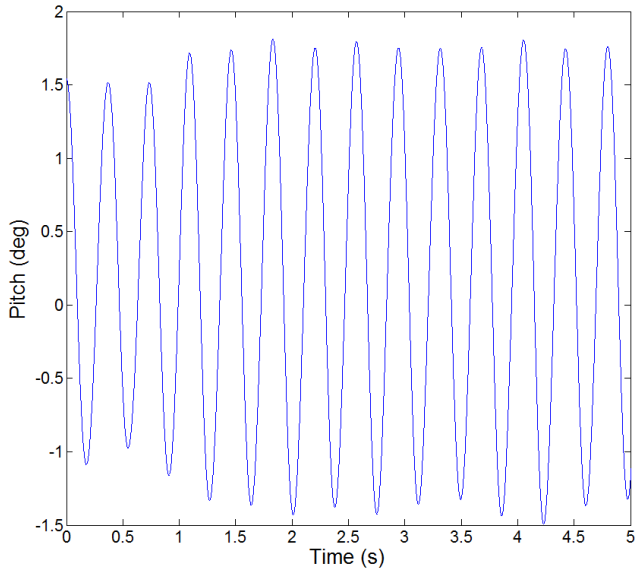

Figure A.9: Filtered time trace of experiment at $U = 6.51$ m/s, Re = 65500

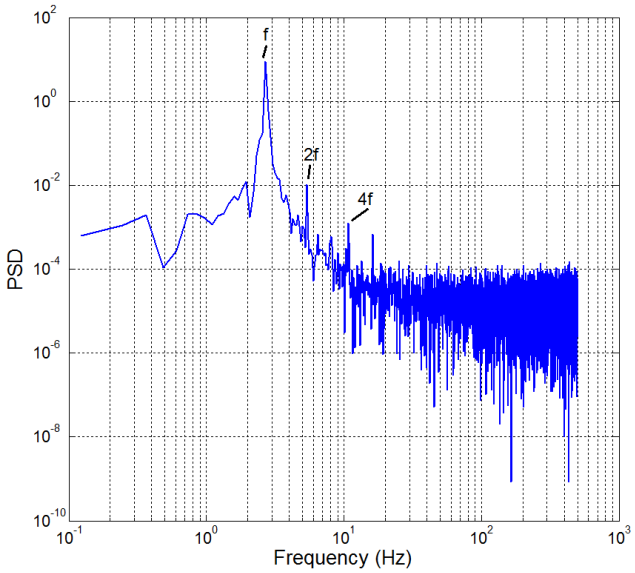

Figure A.10: PSD of experiment at $U = 6.51$ m/s, Re $= 65500$, $f = 2.747$ Hz

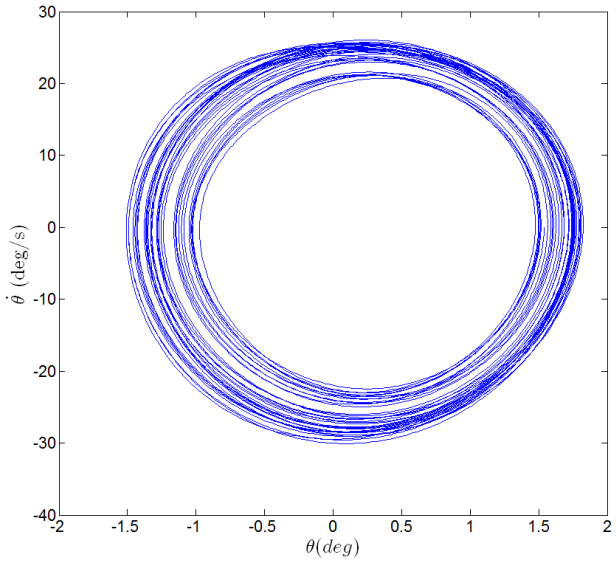

Figure A.11: Filtered phase plane plot of experiment at $U = 6.51$ m/s, Re $=$ 65500

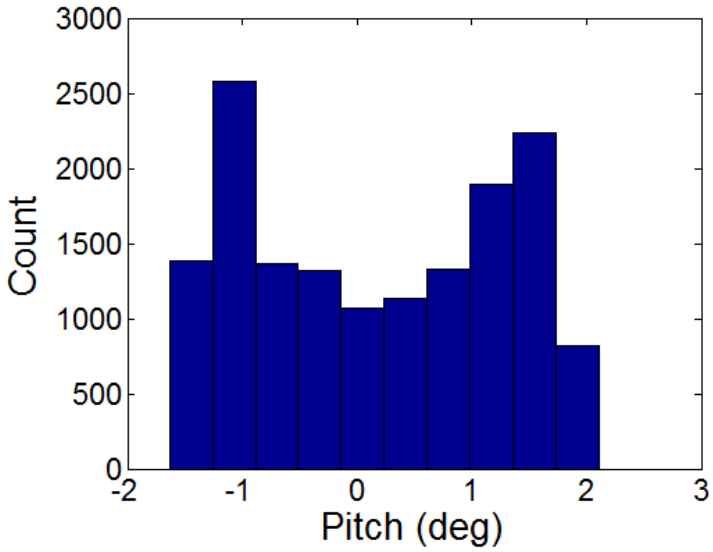

Figure A.12: Histogram of experiment at $U = 6.51$ m/s, Re = 65500

A.1.4 U=6.88 m/s

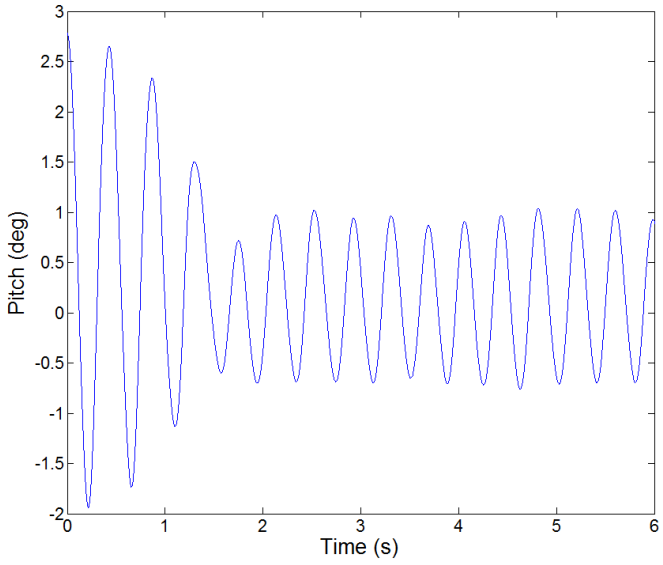

Figure A.13: Filtered time trace of experiment at $U = 6.88$ m/s, Re = 69000

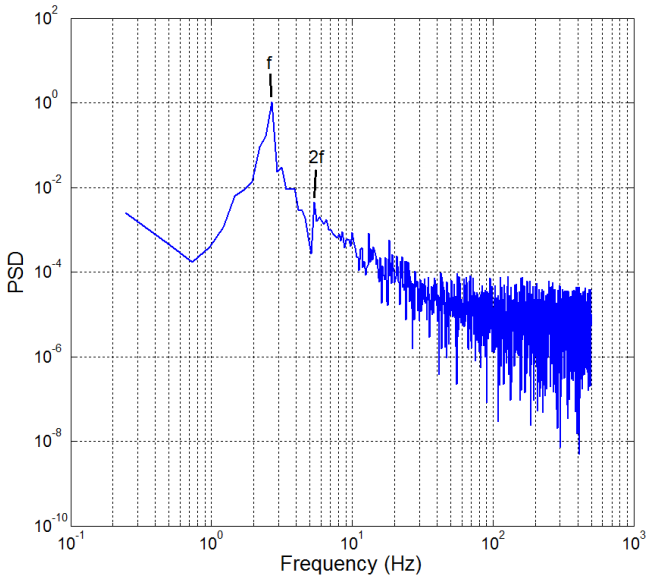

Figure A.14: PSD of experiment at $U = 6.88$ m/s, Re = 69000, f= 2.564 Hz

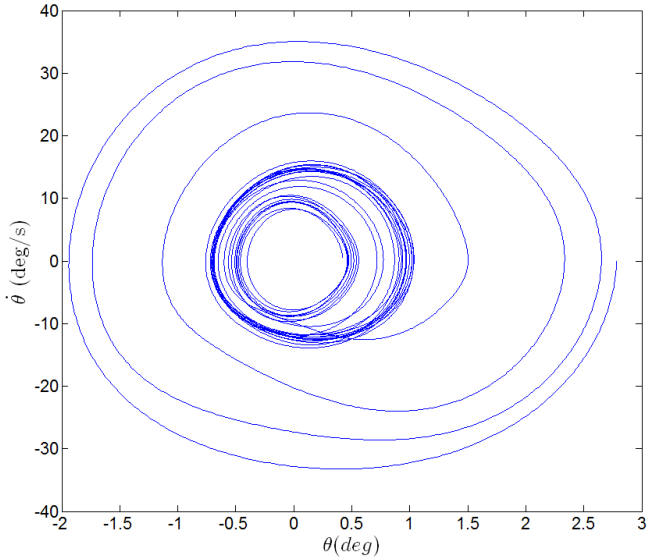

Figure A.15: Filtered phase plane plot of experiment at $U = 6.88$ m/s, Re = 69000

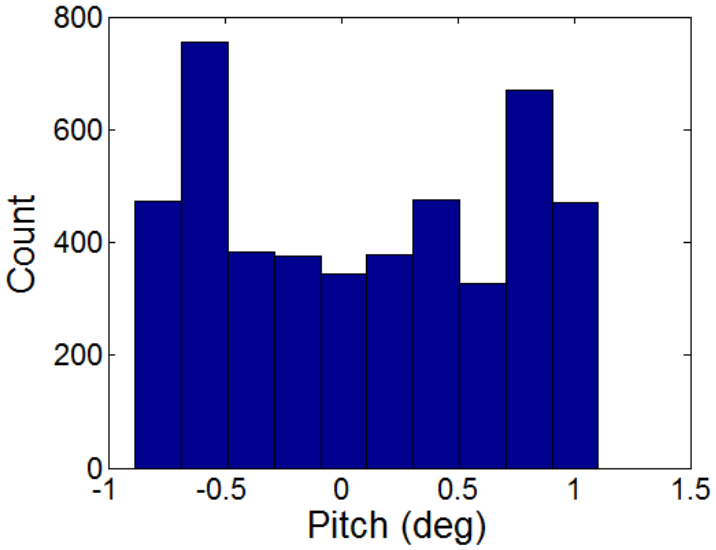

Figure A.16: Histogram of experiment at $U = 6.88$ m/s, Re = 69000

A.1.5 U=7.67 m/s

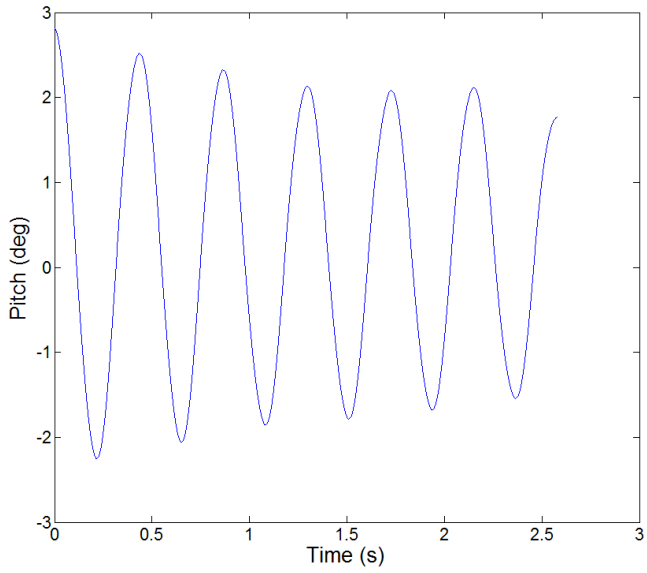

Figure A.17: Filtered time trace of transient experiment at $U = 7.67$ m/s, Re = 77000

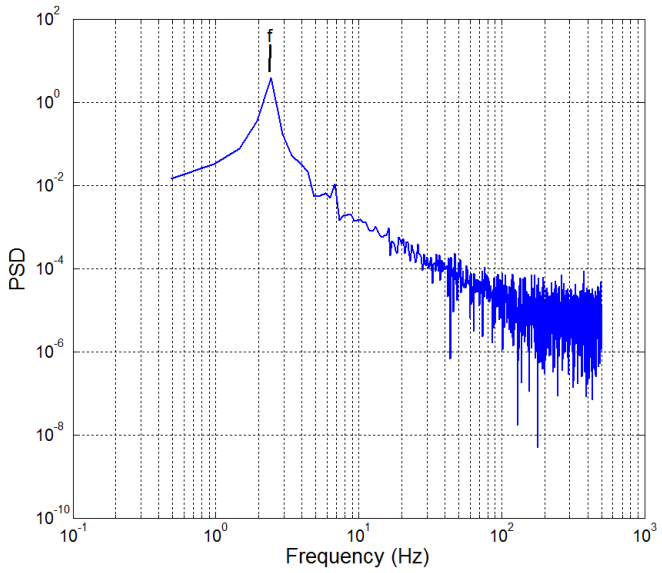

Figure A.18: PSD of transient experiment at $U = 7.67$ m/s, Re = 77000, f= 2.443 Hz

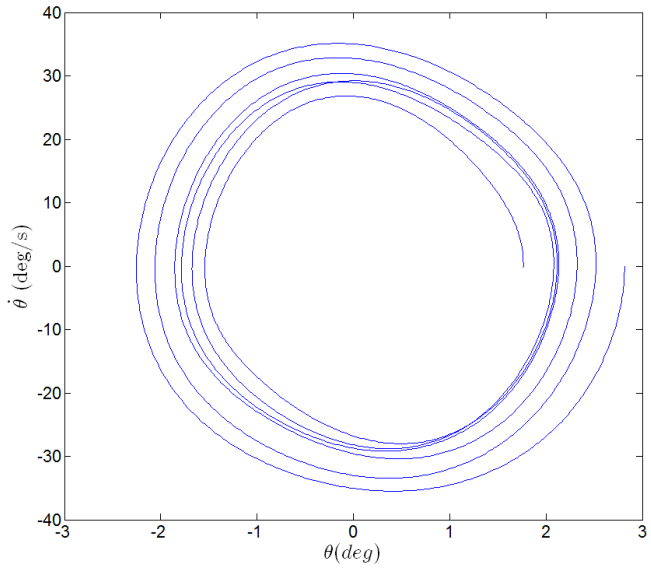

Figure A.19: Filtered phase plane plot of transient experiment at $U = 7.76$ m/s, Re = 77000

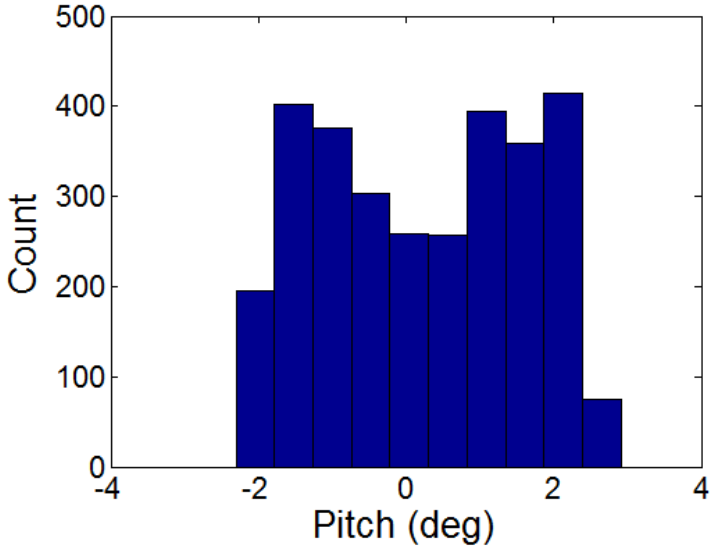

Figure A.20: Histogram of transient experiment at $U = 7.67$ m/s, Re = 77000

A.1.6 U=7.98 m/s

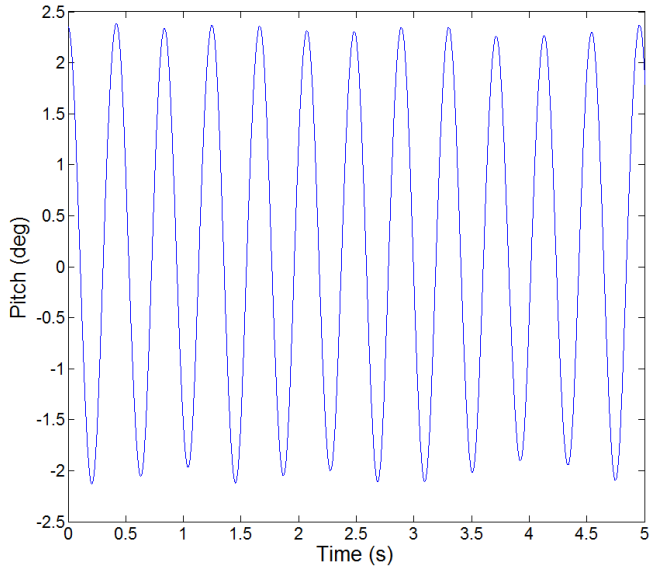

Figure A.21: Filtered time trace of experiment at $U = 7.98$ m/s, Re = 80000

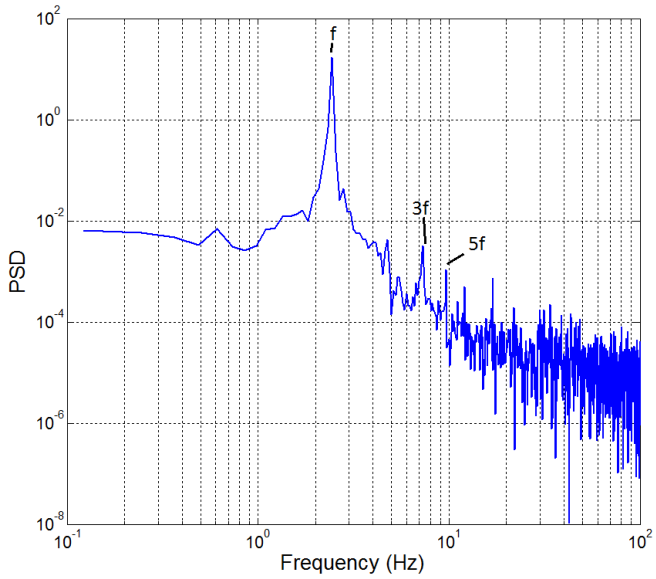

Figure A.22: PSD of experiment at $U = 7.98$ m/s, Re = 80000, f= 2.442 Hz

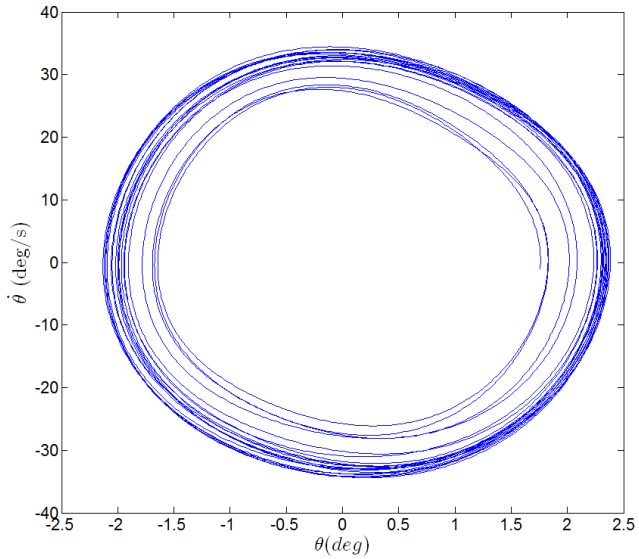

Figure A.23: Filtered phase plane plot of experiment at $U = 7.98$ m/s, Re = 80000

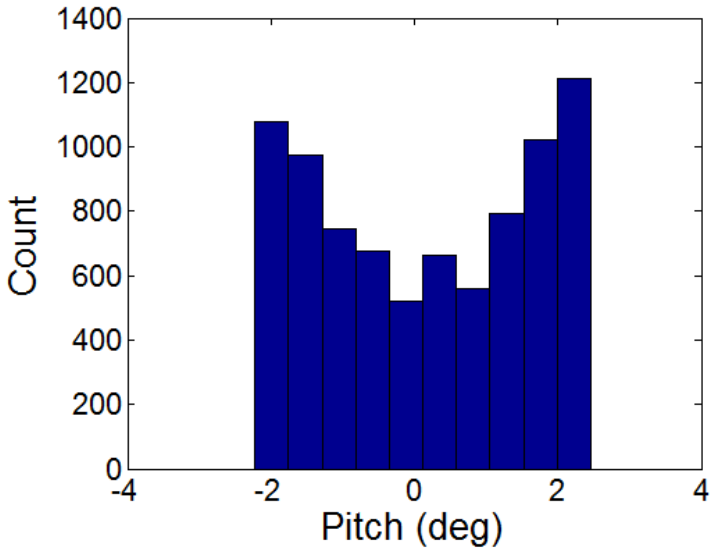

Figure A.24: Histogram of experiment at $U = 7.98$ m/s, Re = 80000

A.1.7 U=8.18 m/s

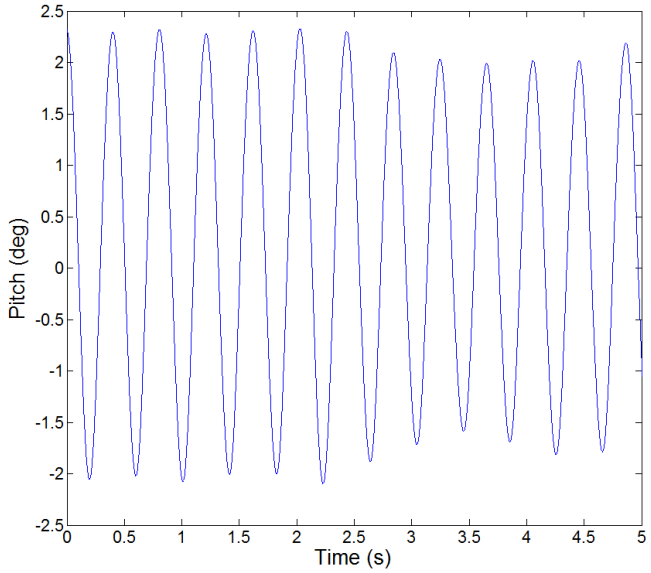

Figure A.25: Filtered time trace of experiment at $U = 8.18$ m/s, Re = 82000

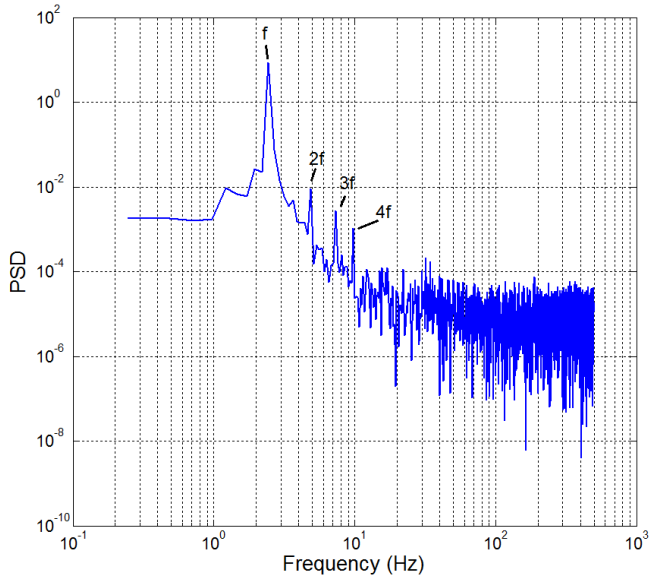

Figure A.26: PSD of experiment at $U = 8.18$ m/s, Re = 82000, f= 2.442 Hz

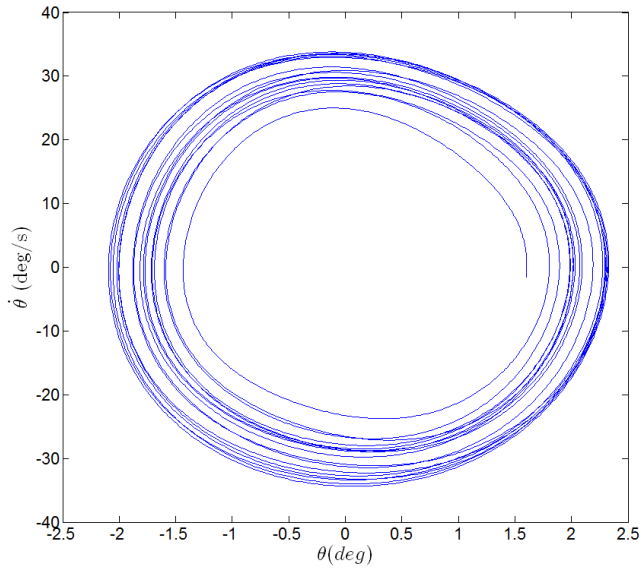

Figure A.27: Filtered phase plane plot of experiment at $U = 8.18$ m/s, Re = 82000

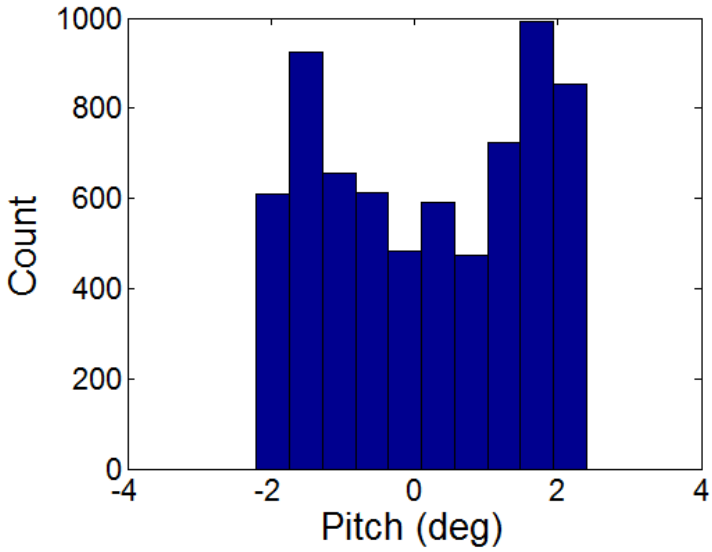

Figure A.28: Histogram of experiment at $U = 8.18$ m/s, Re = 82000

A.1.8 U=8.94 m/s

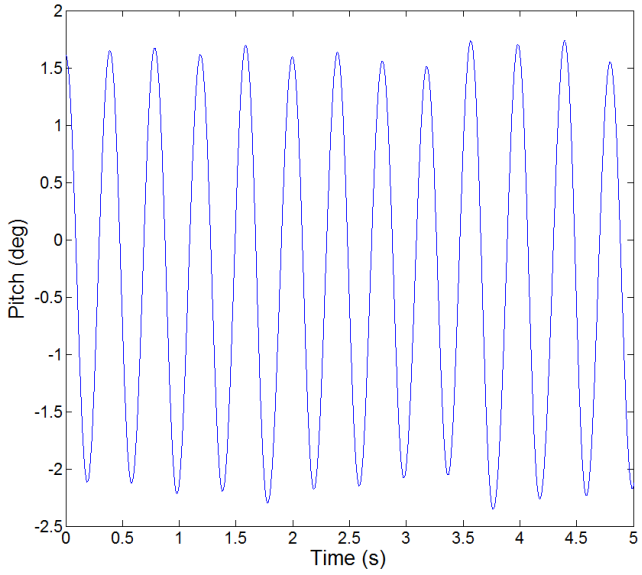

Figure A.29: Filtered time trace of experiment at $U = 8.94$ m/s, Re = 90000

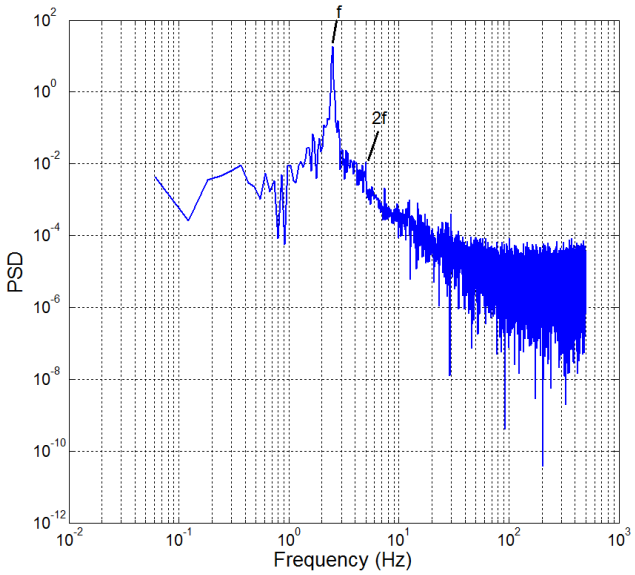

Figure A.30: PSD of experiment at $U = 8.94$ m/s, Re = 90000, f= 2.503 Hz

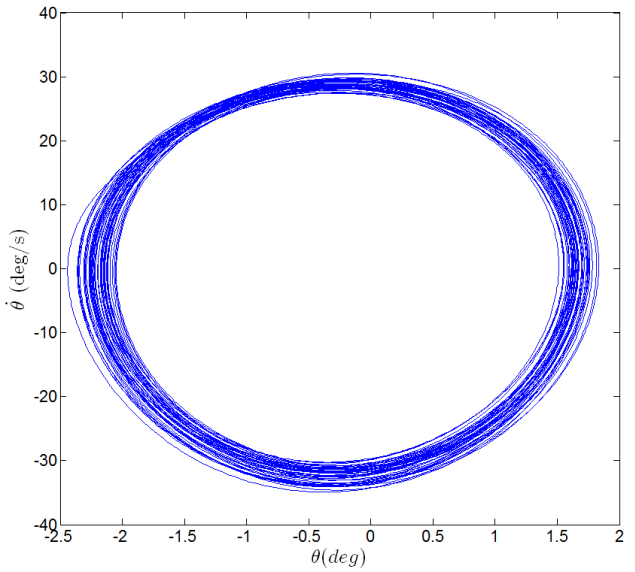

Figure A.31: Filtered phase plane plot of experiment at $U = 8.94$ m/s, Re = 90000

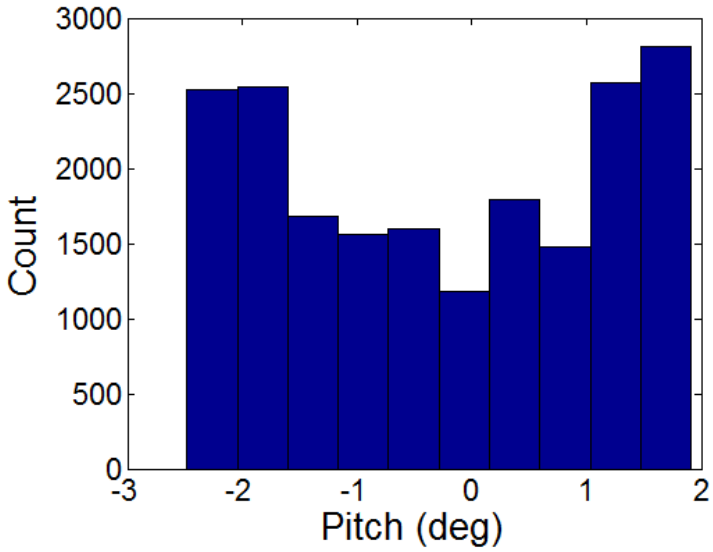

Figure A.32: Histogram of experiment at $U = 8.94$ m/s, Re = 90000

A.1.9 U=9.30 m/s

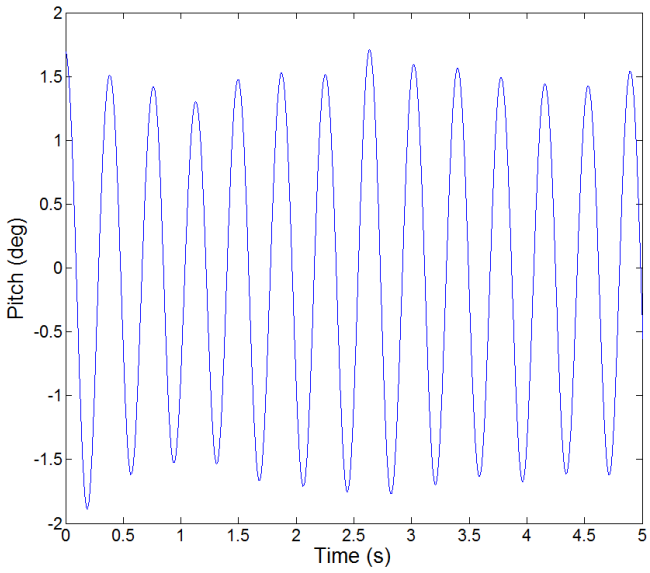

Figure A.33: Filtered time trace of experiment at $U = 9.30$ m/s, Re = 93500

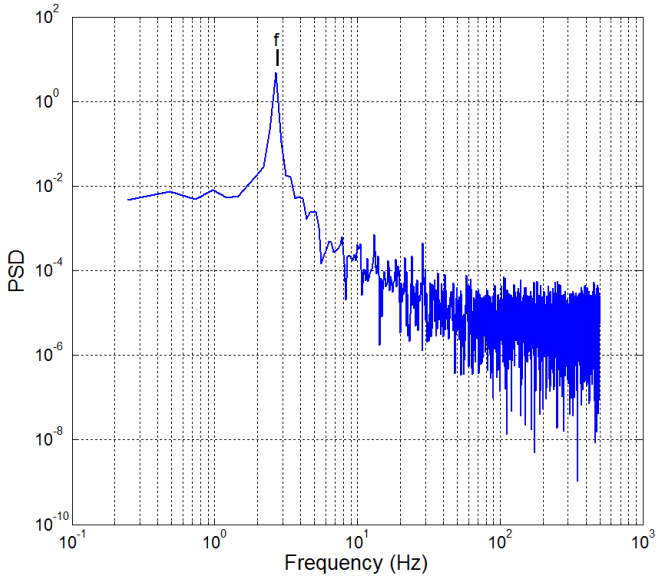

Figure A.34: PSD of experiment at $U = 9.30$ m/s, Re = 93500, f= 2.686 Hz

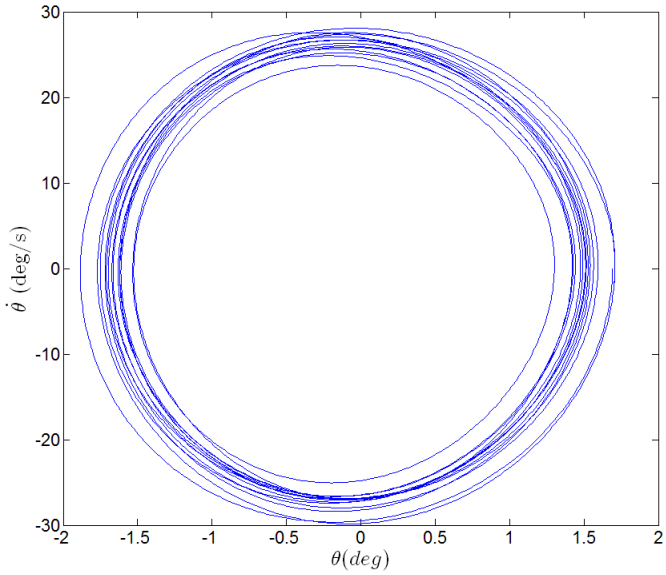

Figure A.35: Filtered phase plane plot of experiment at $U = 9.30$ m/s, Re = 93500

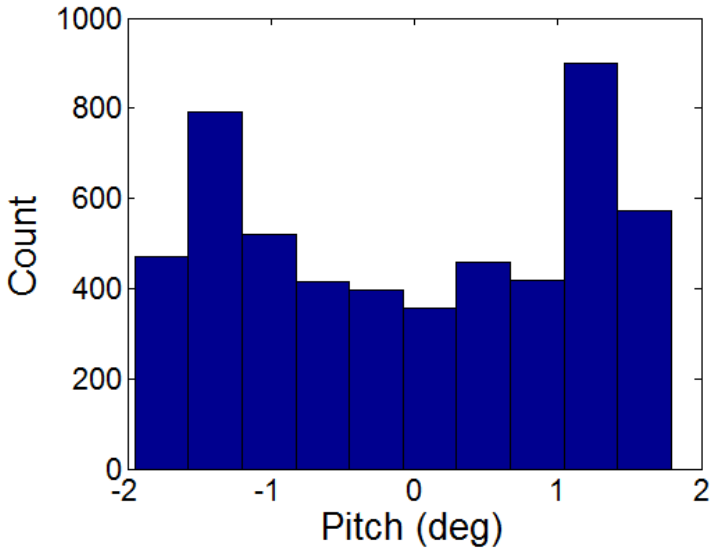

Figure A.36: Histogram of experiment at $U = 9.30$ m/s, Re = 93500

A.1.10 U=9.56 m/s

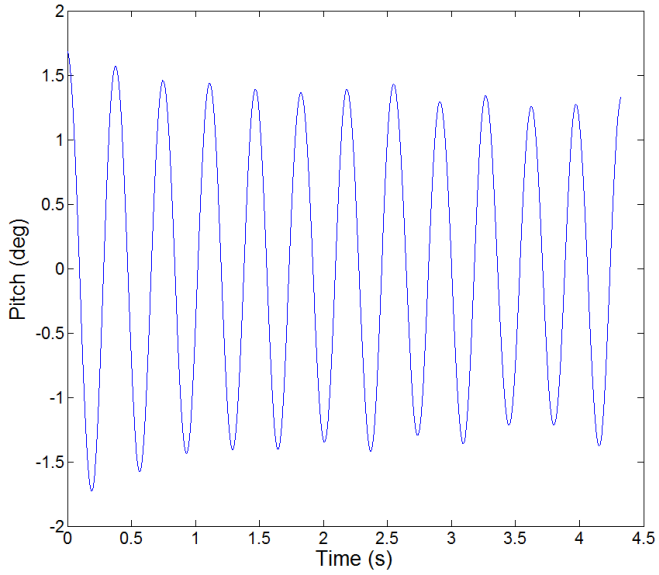

Figure A.37: Filtered time trace of experiment at $U = 9.56$ m/s, Re = 96000

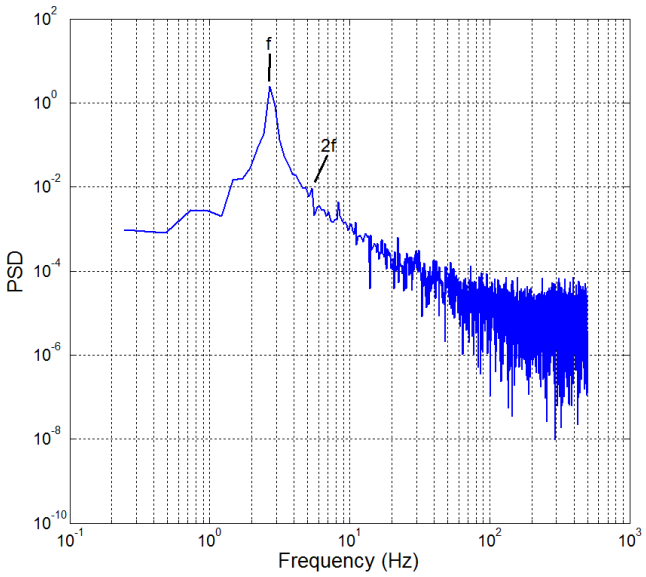

Figure A.38: PSD of experiment at $U = 9.56$ m/s, Re = 96000, f= 2.686 Hz

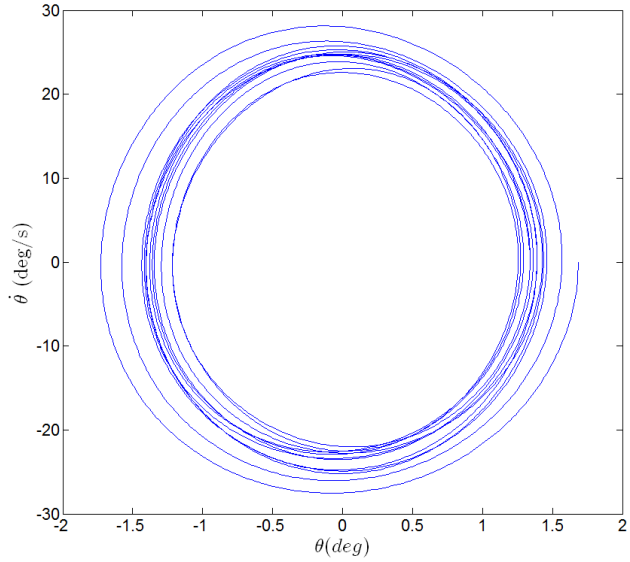

Figure A.39: Filtered phase plane plot of experiment at $U = 9.56$ m/s, Re = 96000

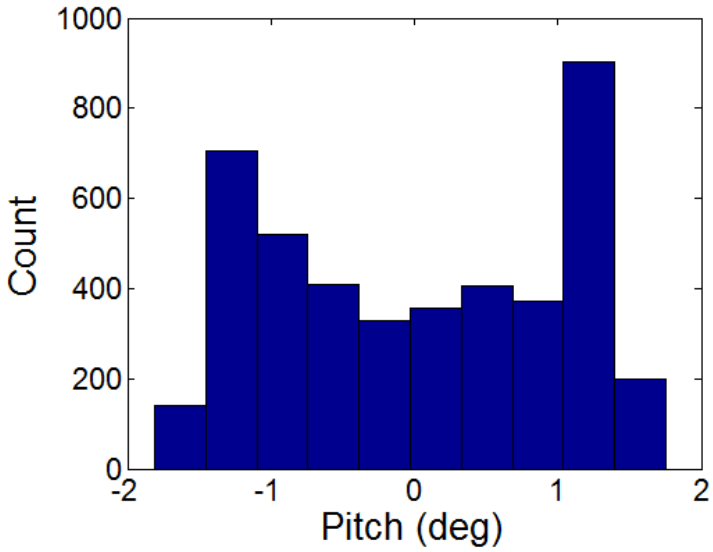

Figure A.40: Histogram of experiment at $U = 9.56$ m/s, Re = 96000

A.2 LAO

A.2.1 U=6.51 m/s

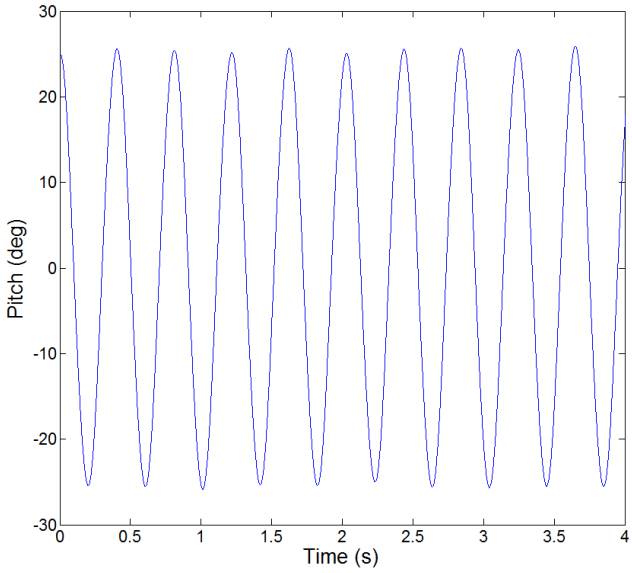

Figure A.41: Filtered time trace of experiment at $U = 6.51$ m/s, Re = 65500

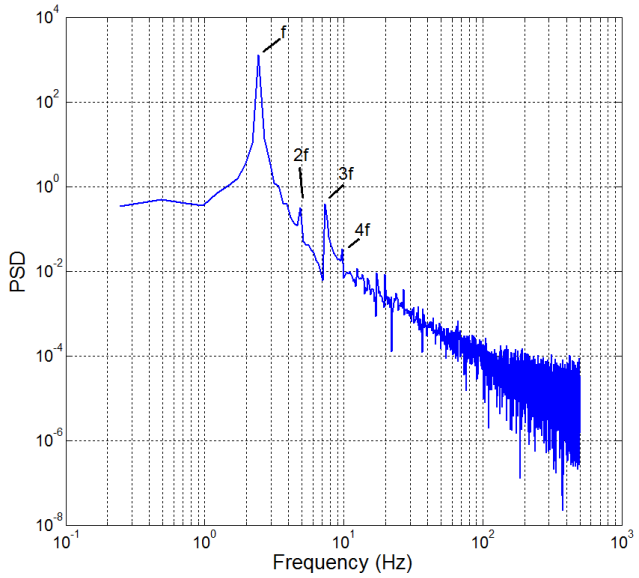

Figure A.42: PSD of experiment at $U = 6.51$ m/s, Re = 65500, f= 2.442 Hz

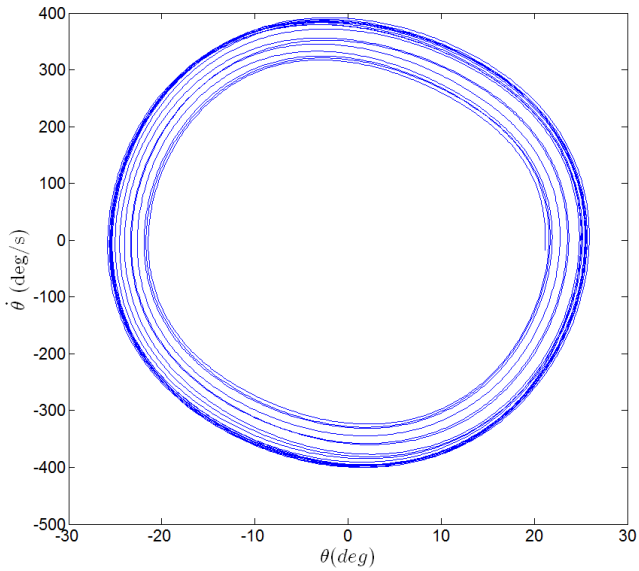

Figure A.43: Filtered phase plane plot of experiment at $U = 6.51$ m/s, Re = 65500

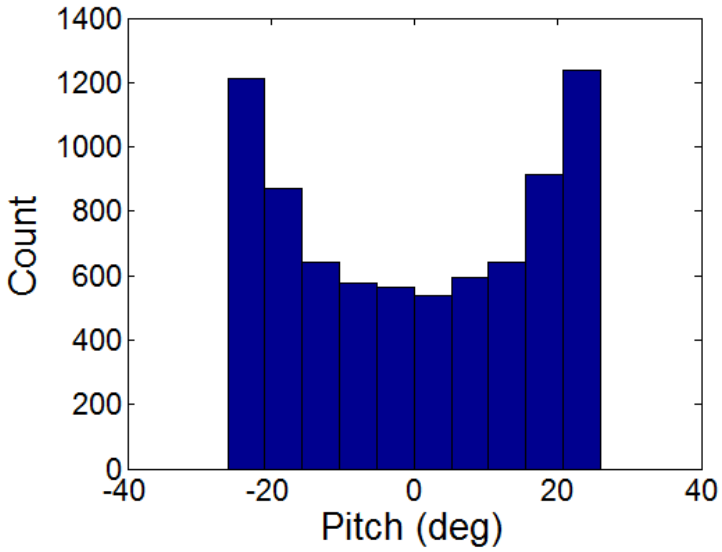

Figure A.44: Histogram of experiment at $U = 6.51$ m/s, Re = 65500

A.2.2 U=6.64 m/s

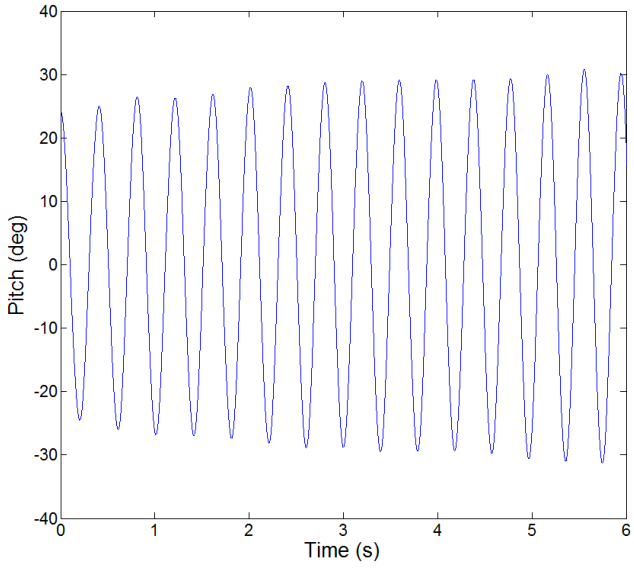

Figure A.45: Filtered time trace of experiment at $U = 6.64$ m/s, Re = 67000

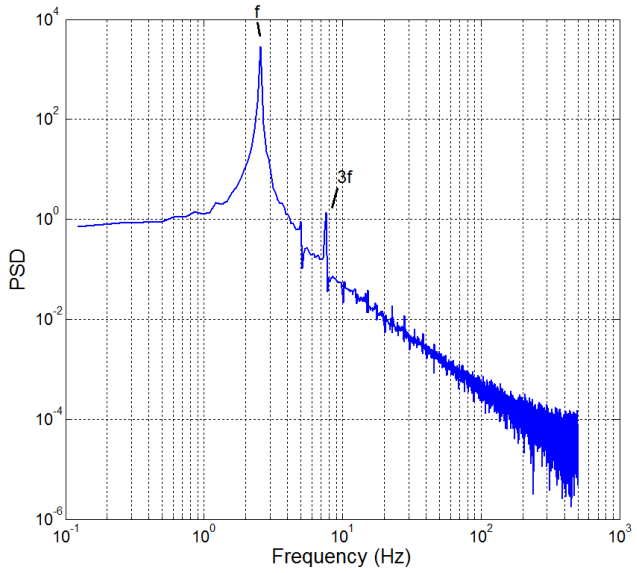

Figure A.46: PSD of experiment at $U = 6.64$ m/s, Re = 67000, f= 2.564 Hz

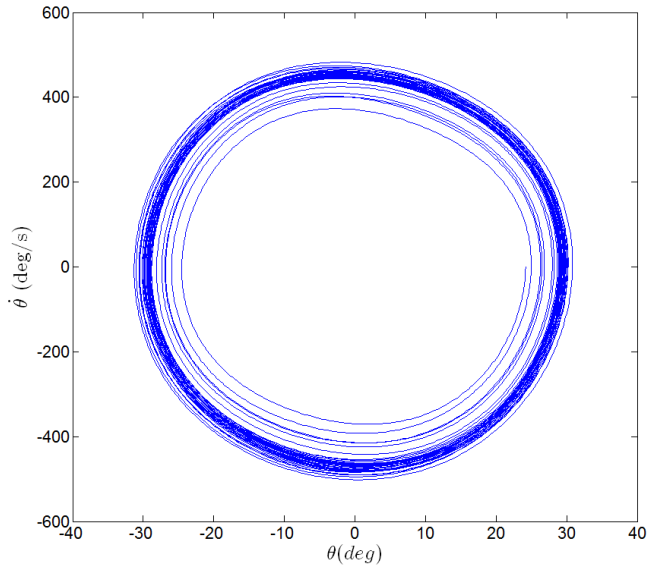

Figure A.47: Filtered phase plane plot of experiment at $U = 6.64$ m/s, Re = 67000

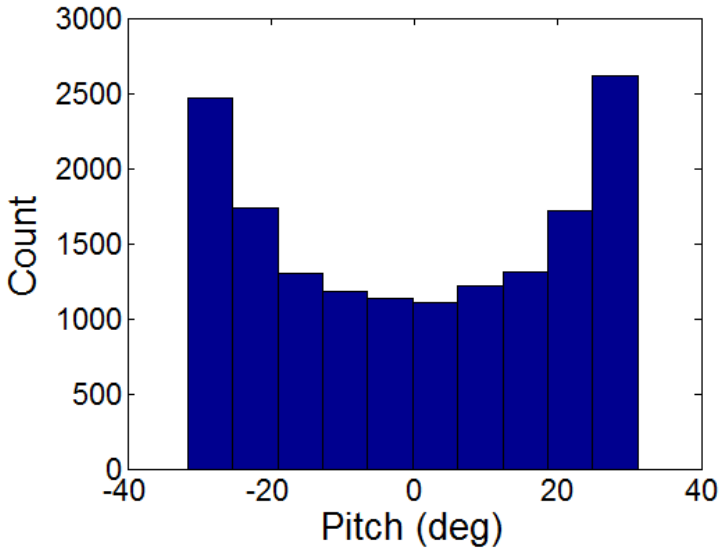

Figure A.48: Histogram of experiment at $U = 6.64$ m/s, Re = 67000

A.2.3 U=6.76 m/s

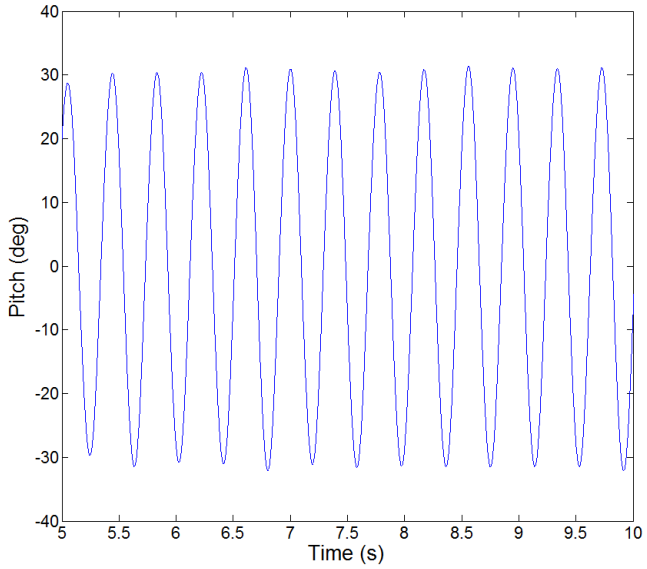

Figure A.49: Filtered time trace of experiment at $U = 6.76$ m/s, Re = 68000

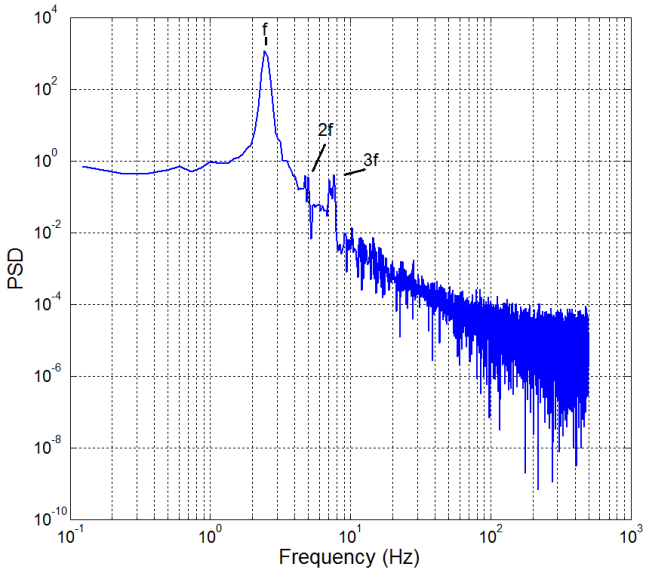

Figure A.50: PSD of experiment at $U = 6.76$ m/s, Re = 68000, f= 2.564 Hz

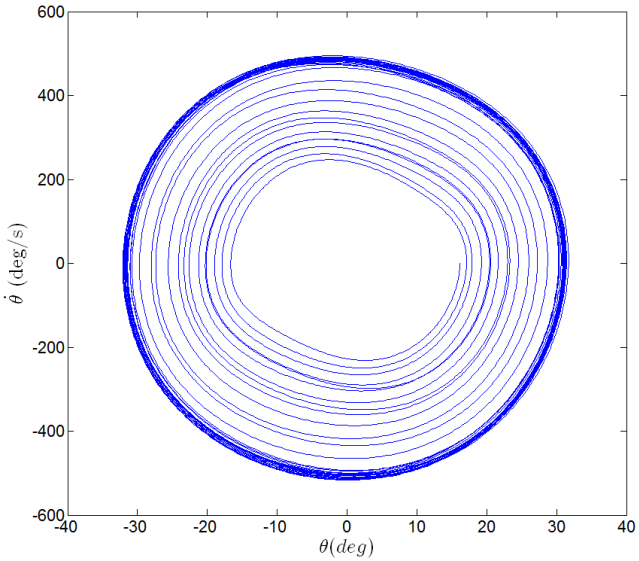

Figure A.51: Filtered phase plane plot of experiment at $U = 6.76$ m/s, Re = 68000

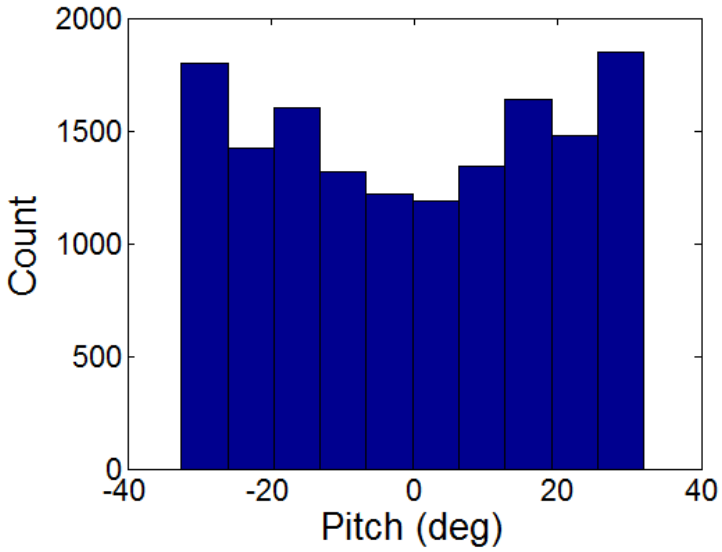

Figure A.52: Histogram of experiment at $U = 6.76$ m/s, Re = 68000

A.2.4 U=6.88 m/s

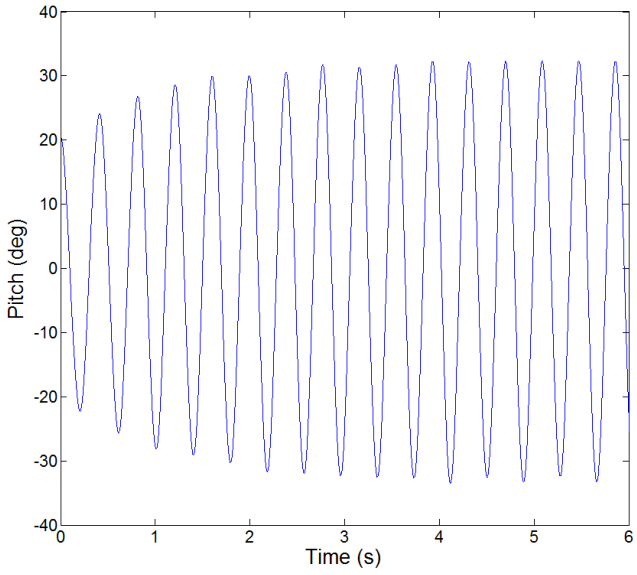

Figure A.53: Filtered time trace of experiment at $U = 6.88$ m/s, Re = 69000

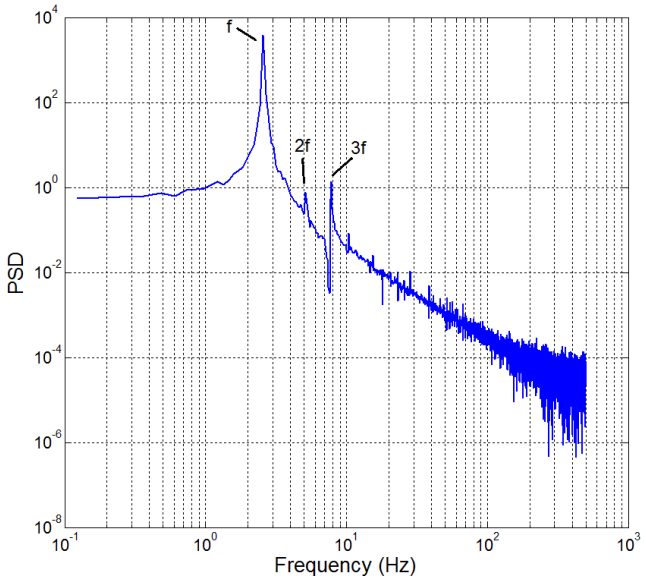

Figure A.54: PSD of experiment at $U = 6.88$ m/s, Re = 69000, f= 2.564 Hz

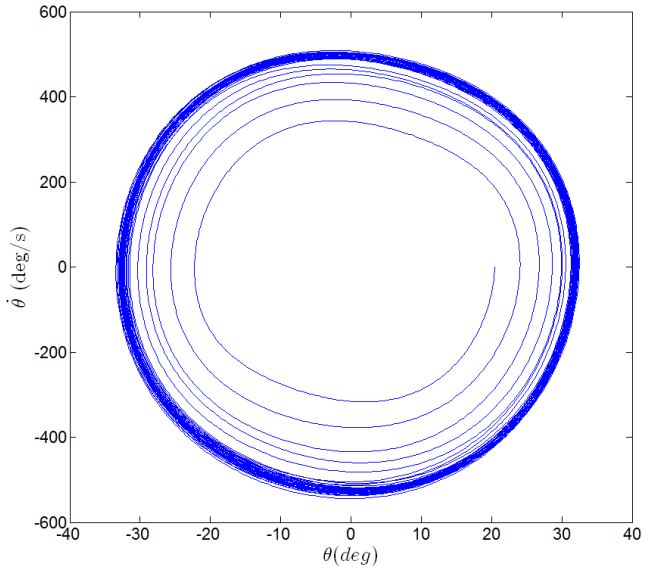

Figure A.55: Filtered phase plane plot of experiment at $U = 6.88$ m/s, Re = 69000

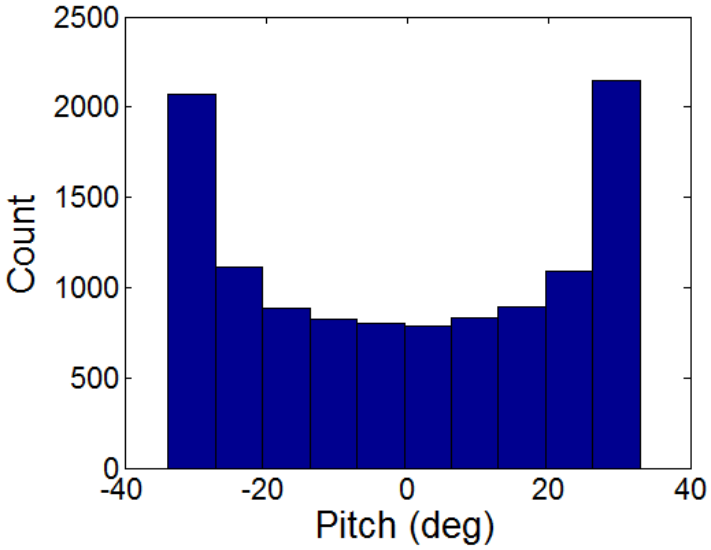

Figure A.56: Histogram of experiment at $U = 6.88$ m/s, Re = 69000

A.2.5 U=7.34 m/s

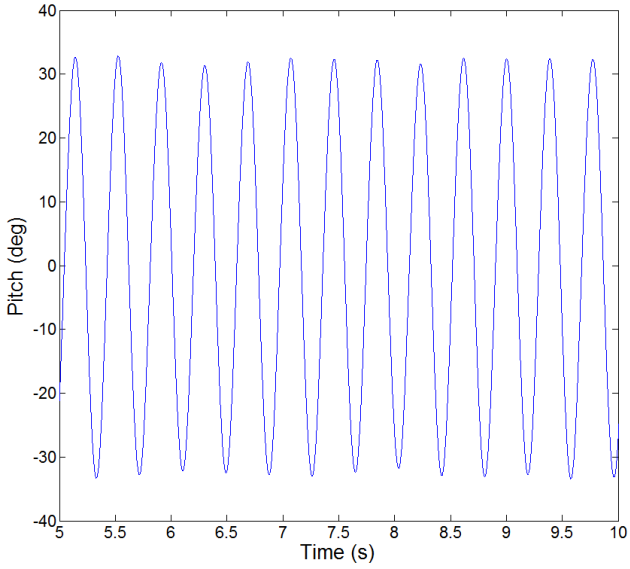

Figure A.57: Filtered time trace of experiment at $U = 7.34$ m/s, Re = 74000

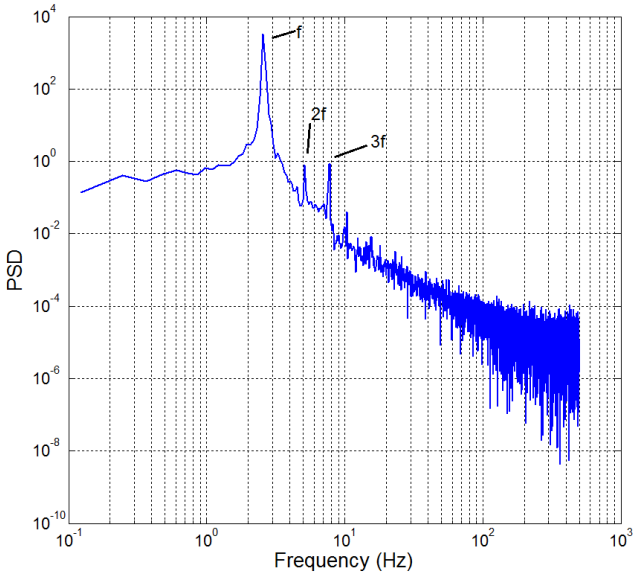

Figure A.58: PSD of experiment at $U = 7.34$ m/s, Re = 74000, f= 2.564 Hz

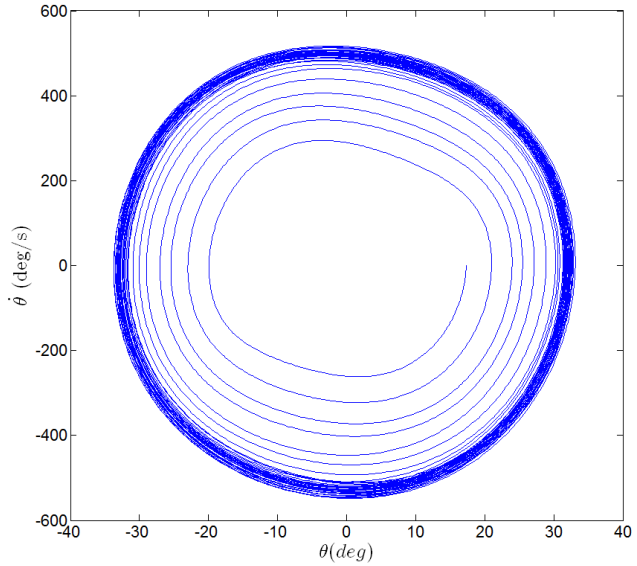

Figure A.59: Filtered phase plane plot of experiment at $U = 7.34$ m/s, Re = 74000

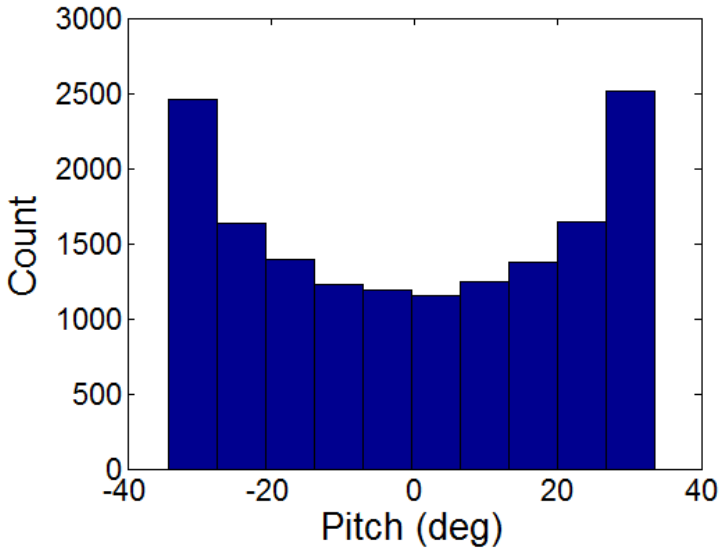

Figure A.60: Histogram of experiment at $U = 7.34$ m/s, Re = 74000

A.2.6 U=7.67 m/s

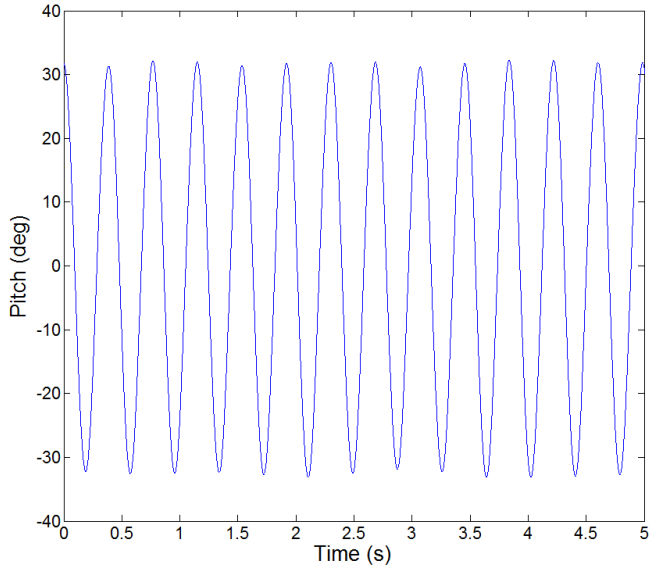

Figure A.61: Filtered time trace of experiment at $U = 7.67$ m/s, Re = 77000

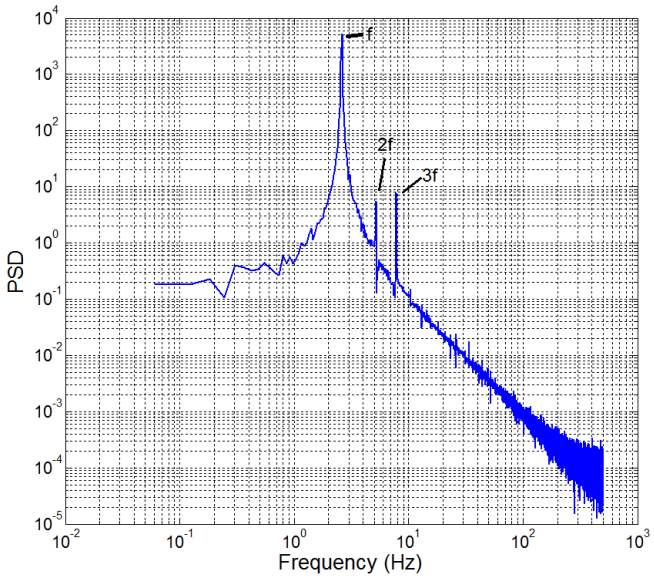

Figure A.62: PSD of experiment at $U = 7.67$ m/s, Re = 77000, f= 2.625 Hz

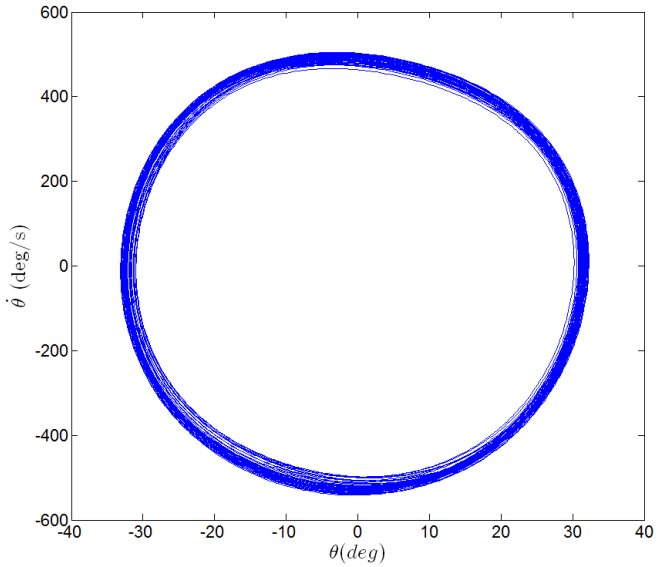

Figure A.63: Filtered phase plane plot of experiment at $U = 7.67$ m/s, Re = 77000

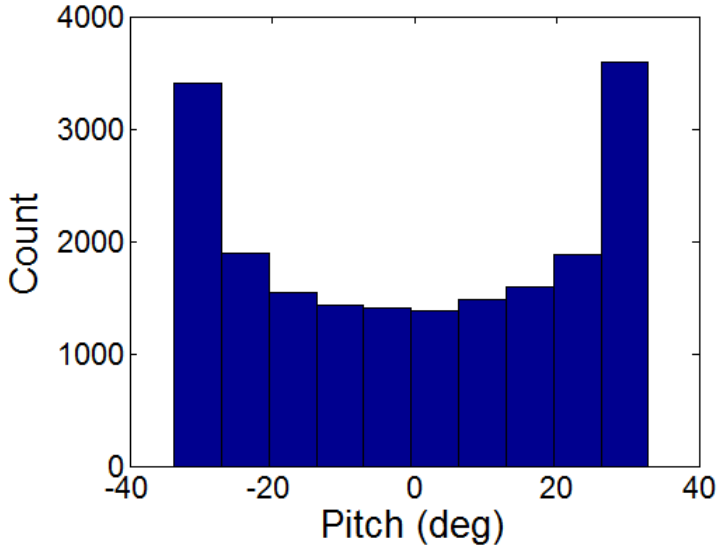

Figure A.64: Histogram of experiment at $U = 7.67$ m/s, Re = 77000

A.2.7 U=7.87 m/s

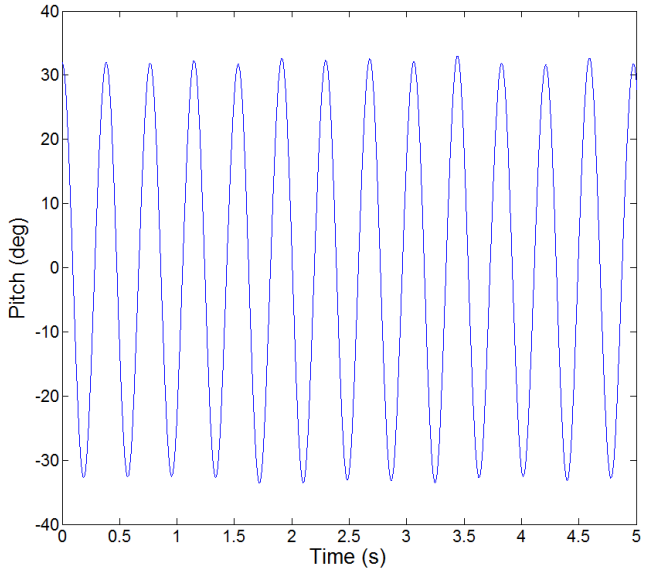

Figure A.65: Filtered time trace of experiment at $U = 7.87$ m/s, Re = 79000

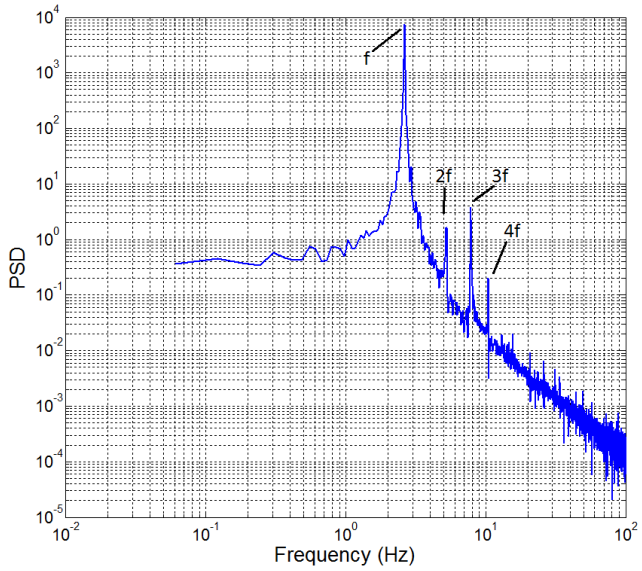

Figure A.66: PSD of experiment at $U = 7.87$ m/s, Re = 79000, f= 2.625 Hz

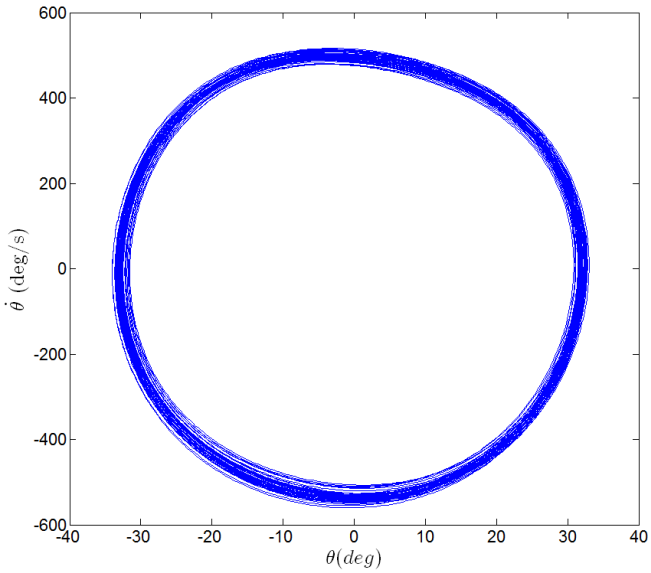

Figure A.67: Filtered phase plane plot of experiment at $U = 7.87$ m/s, Re = 79000

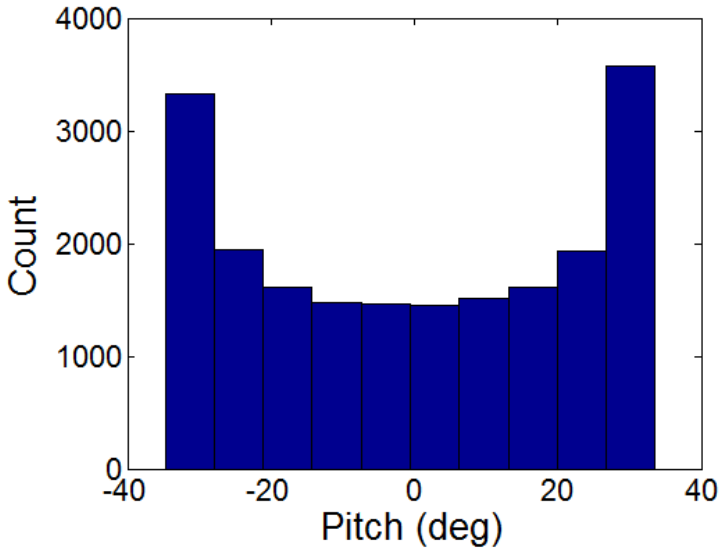

Figure A.68: Histogram of experiment at $U = 7.87$ m/s, Re = 79000

A.2.8 U=8.18 m/s

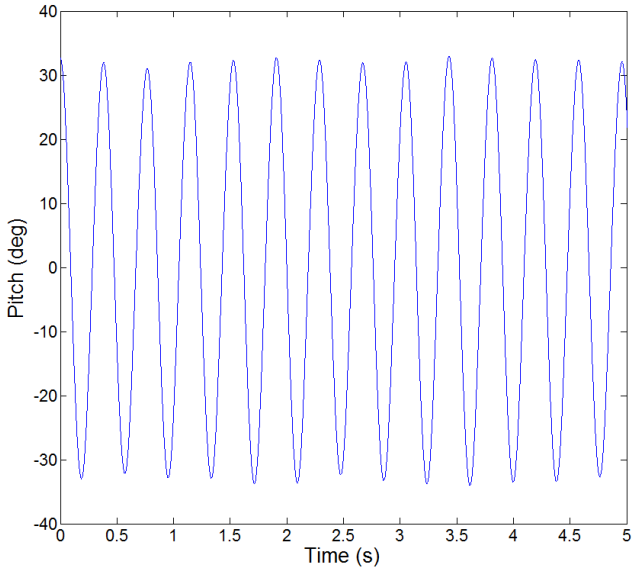

Figure A.69: Filtered time trace of experiment at $U = 8.18$ m/s, Re = 82000

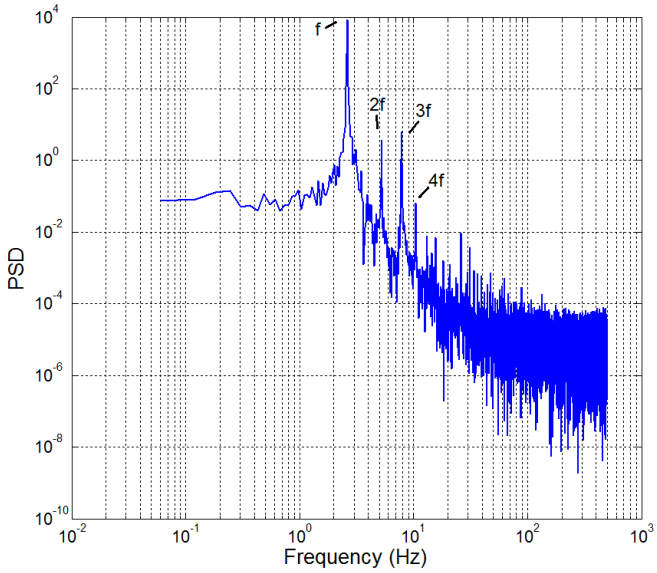

Figure A.70: PSD of experiment at $U = 8.18$ m/s, Re = 82000, f= 2.625 Hz

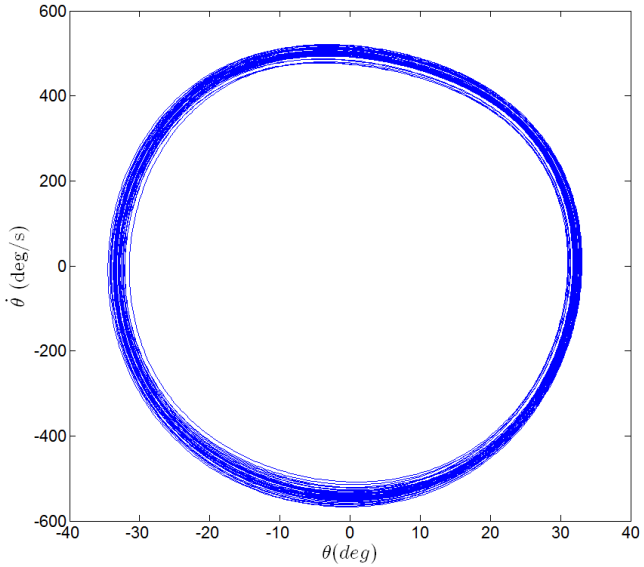

Figure A.71: Filtered phase plane plot of experiment at $U = 8.18$ m/s, Re = 82000

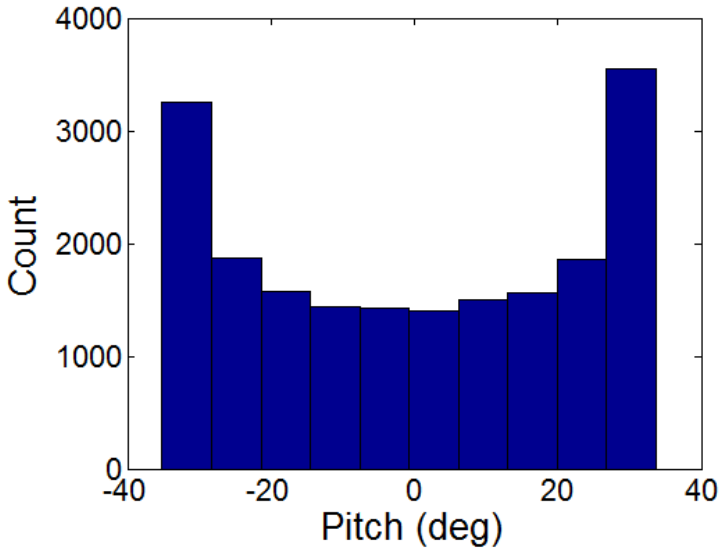

Figure A.72: Histogram of experiment at $U = 8.18$ m/s, Re = 82000

A.2.9 U=8.57 m/s

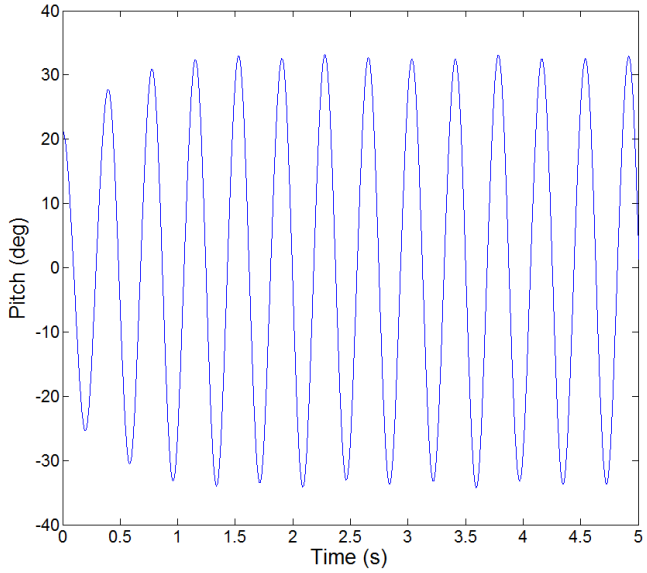

Figure A.73: Filtered time trace of experiment at $U = 8.57$ m/s, Re = 86000

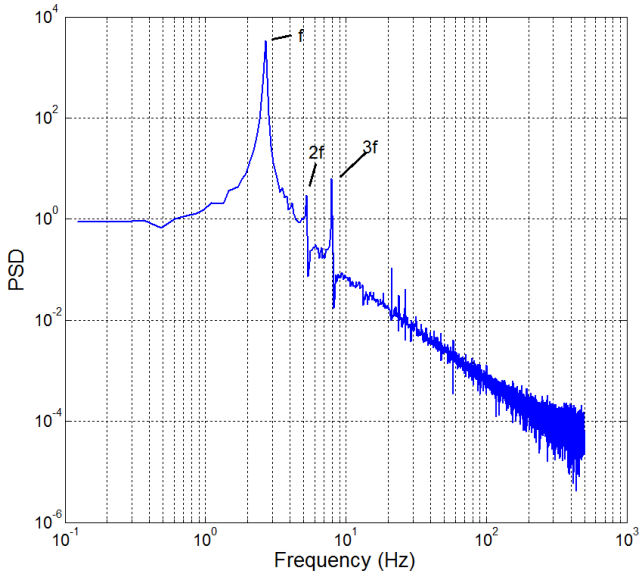

Figure A.74: PSD of experiment at $U = 8.57$ m/s, Re = 86000, f= 2.686 Hz

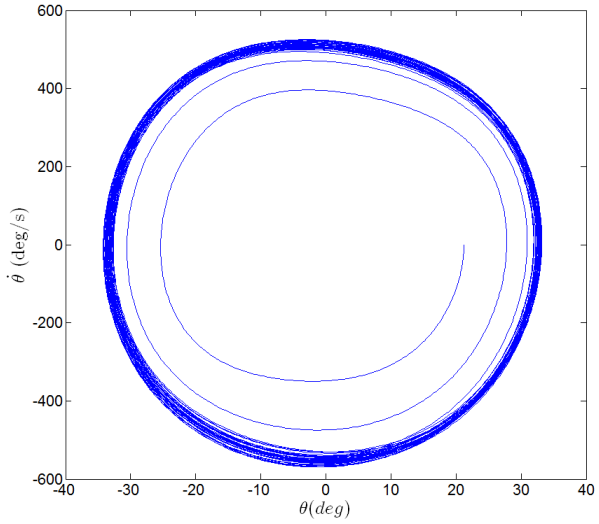

Figure A.75: Filtered phase plane plot of experiment at $U = 8.57$ m/s, Re = 86000

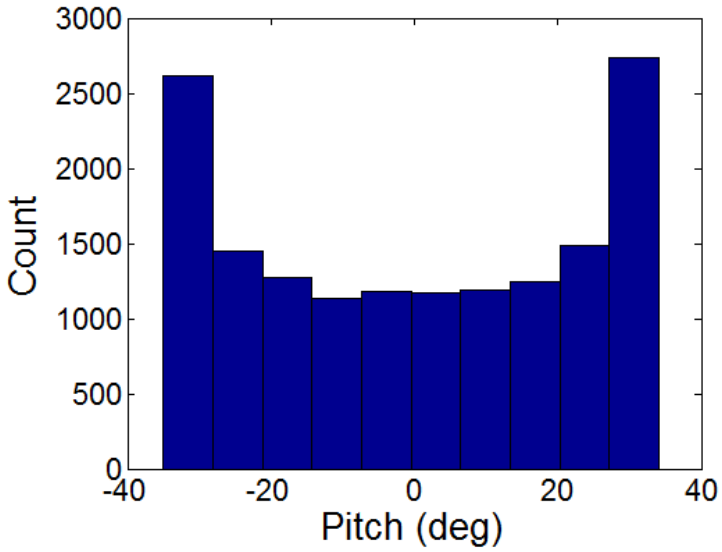

Figure A.76: Histogram of experiment at $U = 8.57$ m/s, Re = 90000

A.2.10 U=8.94 m/s

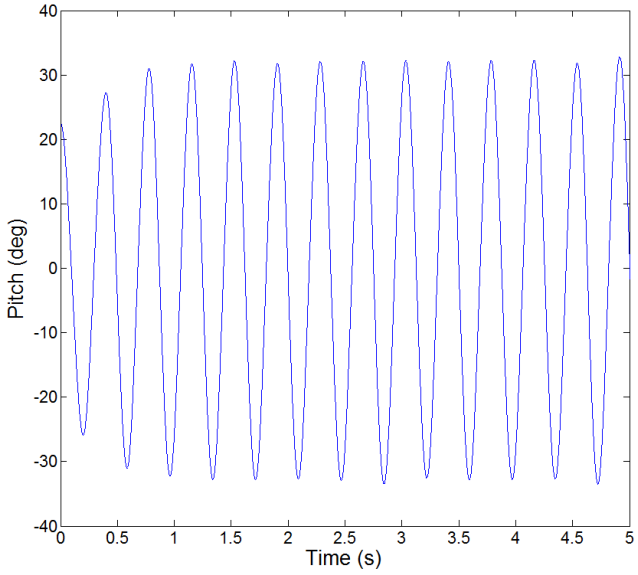

Figure A.77: Filtered time trace of experiment at $U = 8.94$ m/s, Re = 90000

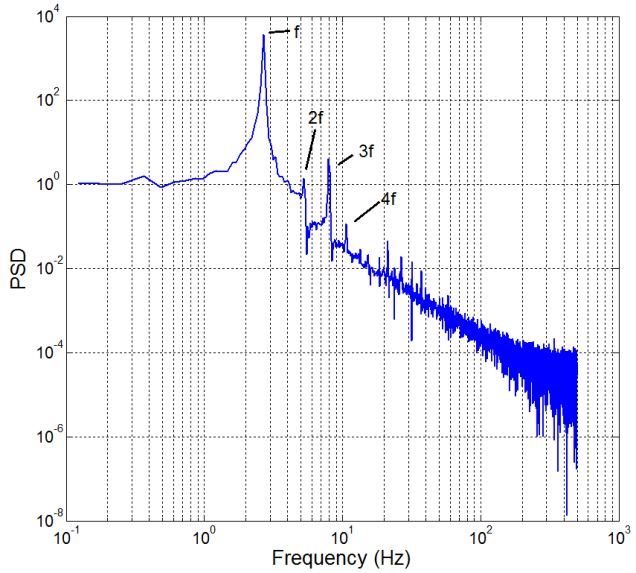

Figure A.78: PSD of experiment at $U = 8.94$ m/s, Re = 90000, f= 2.686 Hz

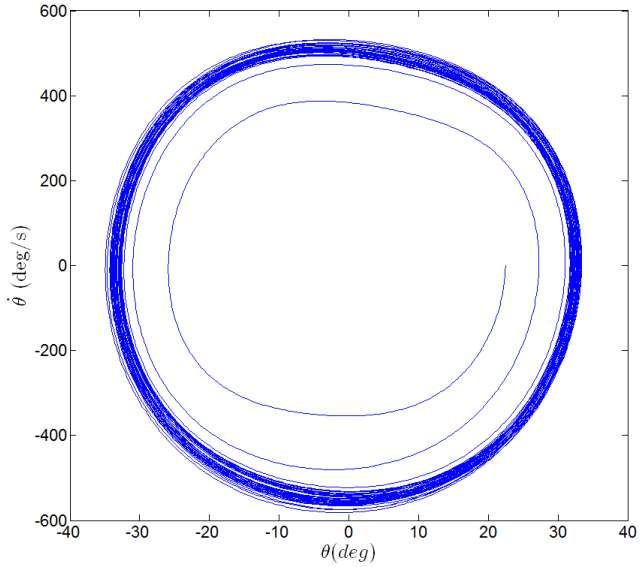

Figure A.79: Filtered phase plane plot of experiment at $U = 8.94$ m/s, Re = 90000

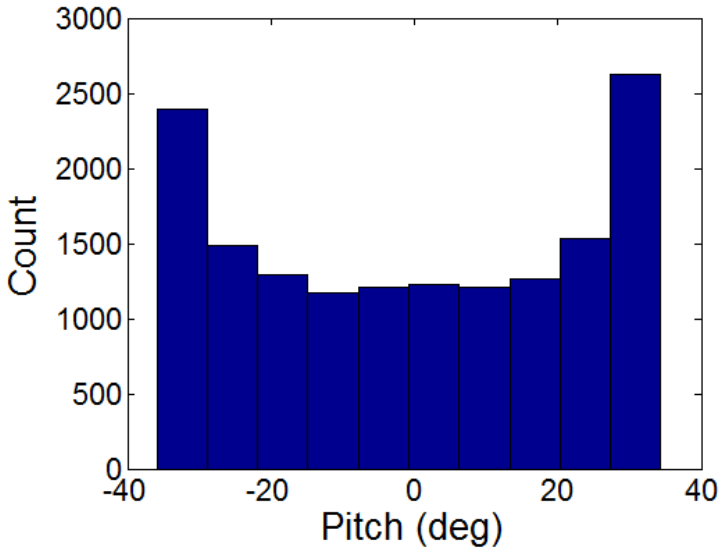

Figure A.80: Histogram of experiment at $U = 8.94$ m/s, Re = 90000

A.2.11 U=9.30 m/s

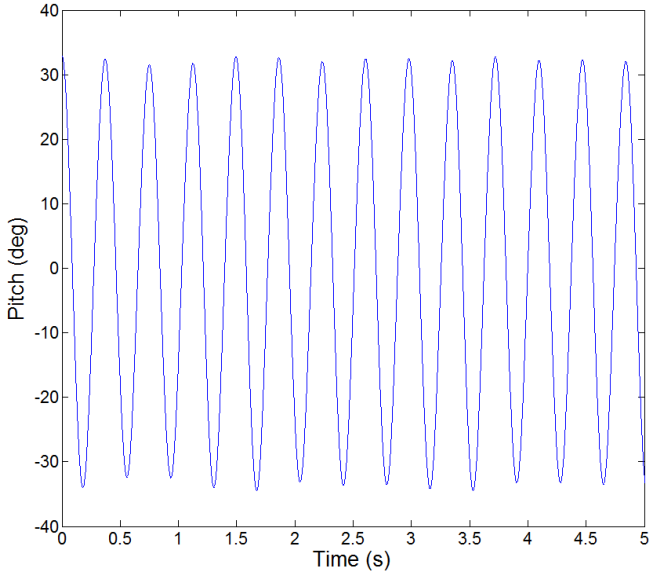

Figure A.81: Filtered time trace of experiment at $U = 9.30$ m/s, Re = 93500

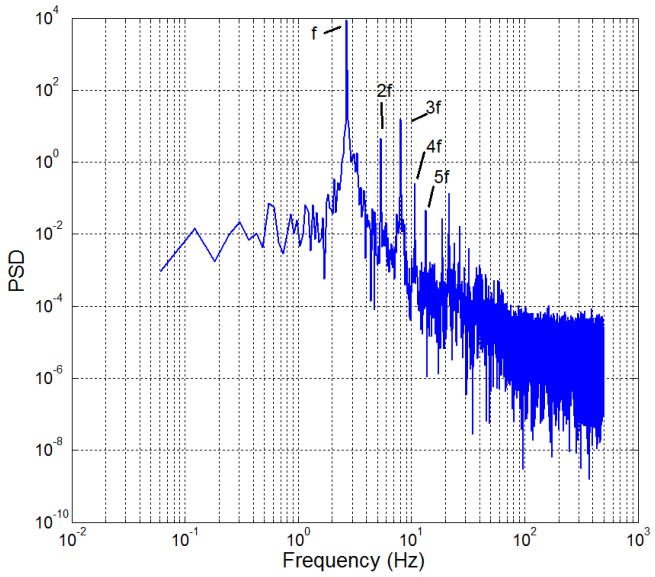

Figure A.82: PSD of experiment at $U = 9.30$ m/s, Re = 93500, f= 2.686 Hz

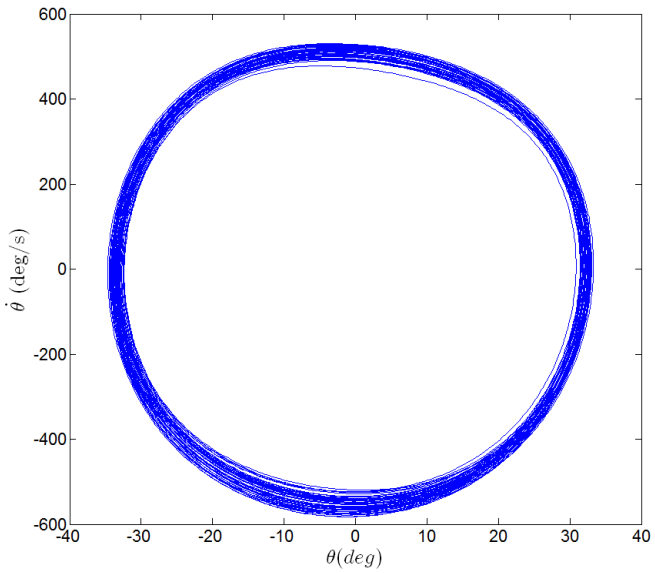

Figure A.83: Filtered phase plane plot of experiment at $U = 9.30$ m/s, Re = 93500

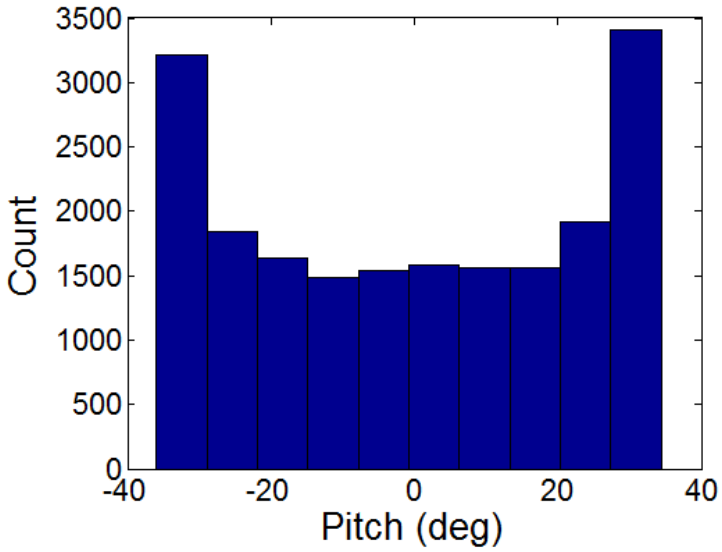

Figure A.84: Histogram of experiment at $U = 9.30$ m/s, Re = 93500

A.2.12 U=9.89 m/s

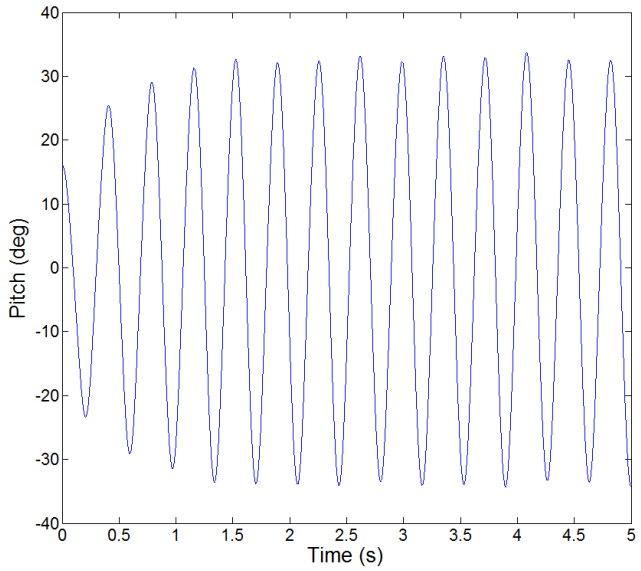

Figure A.85: Filtered time trace of experiment at $U = 9.89$ m/s, Re = 99500

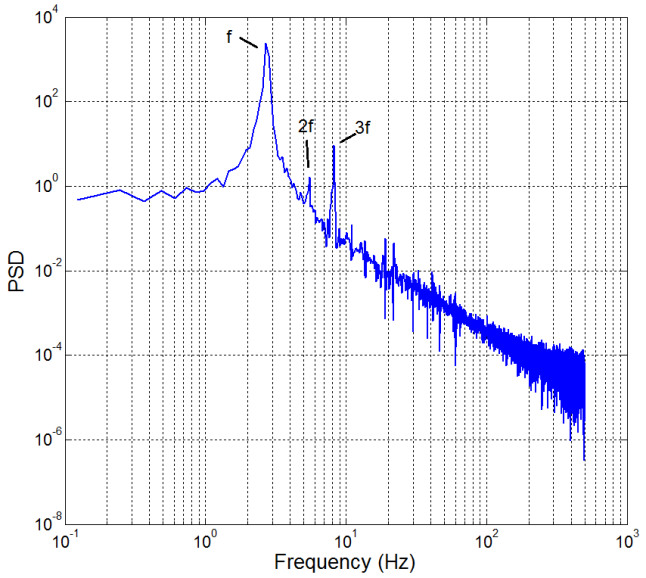

Figure A.86: PSD of experiment at $U = 9.89$ m/s, Re = 99500, f= 2.686 Hz

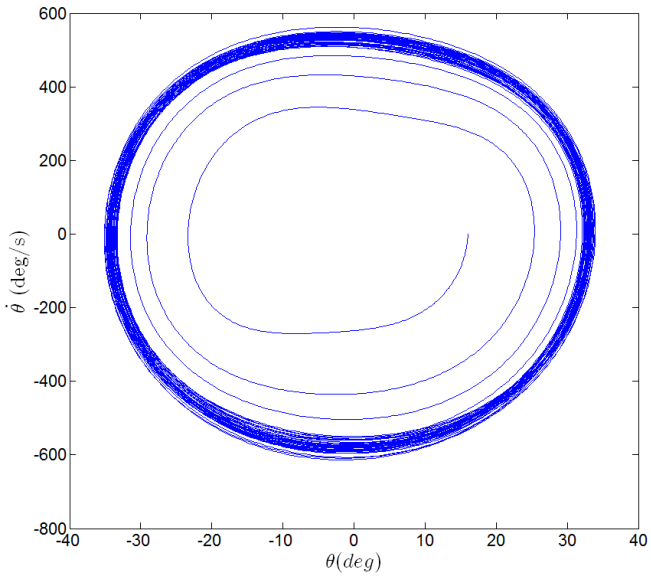

Figure A.87: Filtered phase plane plot of experiment at $U = 9.89$ m/s, Re = 99500

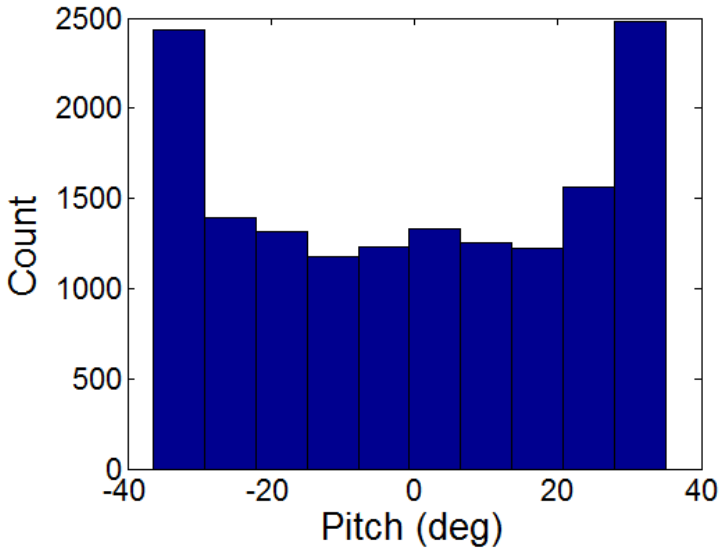

Figure A.88: Histogram of experiment at $U = 9.89$ m/s, Re = 99500

A.2.13 U=10.38 m/s

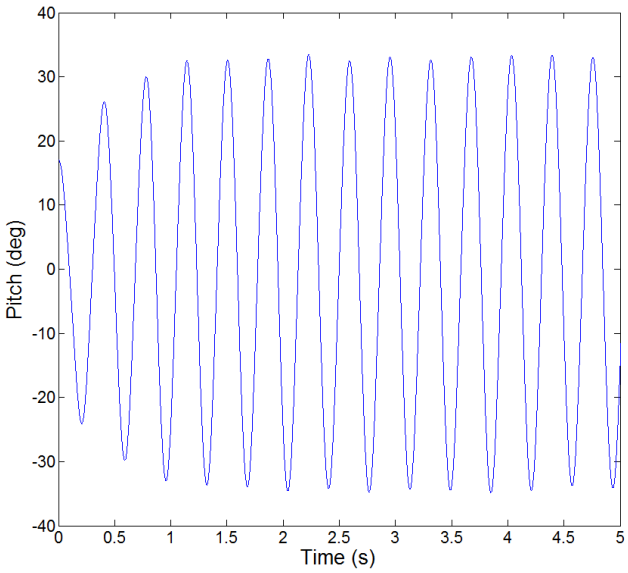

Figure A.89: Filtered time trace of experiment at $U = 10.38$ m/s, Re = 104500

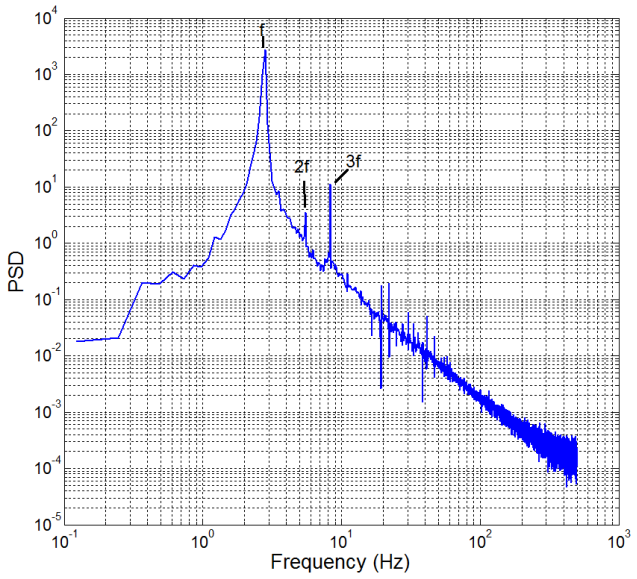

Figure A.90: PSD of experiment at U = 10.38 m/s, Re = 104500, f= 2.808 Hz

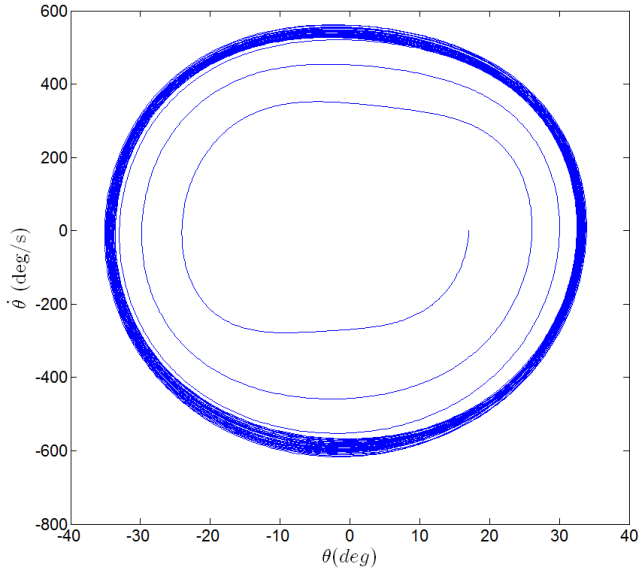

Figure A.91: Filtered phase plane plot of experiment at U = 10.38 m/s, Re = 104500

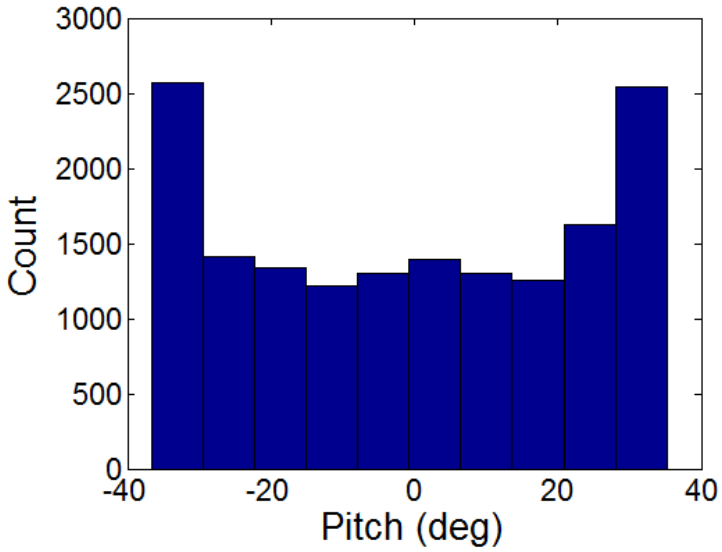

Figure A.92: Histogram of experiment at $U = 10.38$ m/s, Re = 104500

B Numerical Data

Note: all data generated with $\gamma - Re_\theta$ model. Phase averaged data has been averaged over six cycles.

B.1 SAO

B.1.1 U=6.13 m/s

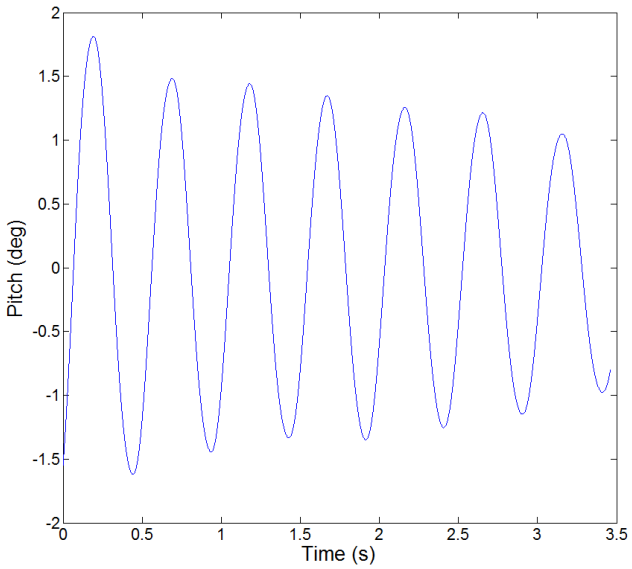

Figure B.1: Time trace of simulation at $U = 6.13$ m/s, Re = 61500

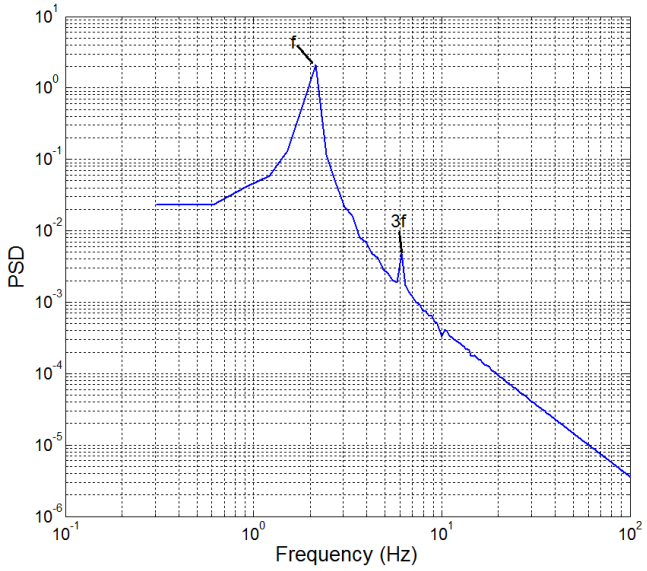

Figure B.2: PSD of simulation at $U = 6.13$ m/s, Re = 61500, f= 2.133 Hz

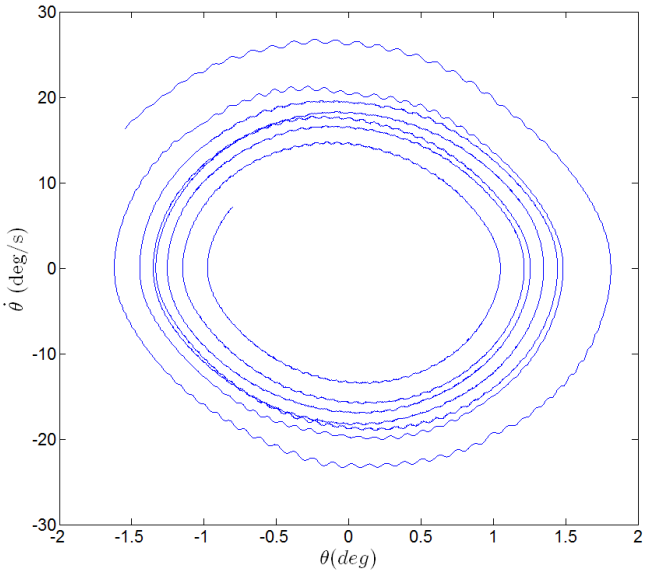

Figure B.3: Phase plane plot of simulation at $U = 6.13$ m/s, Re = 61500

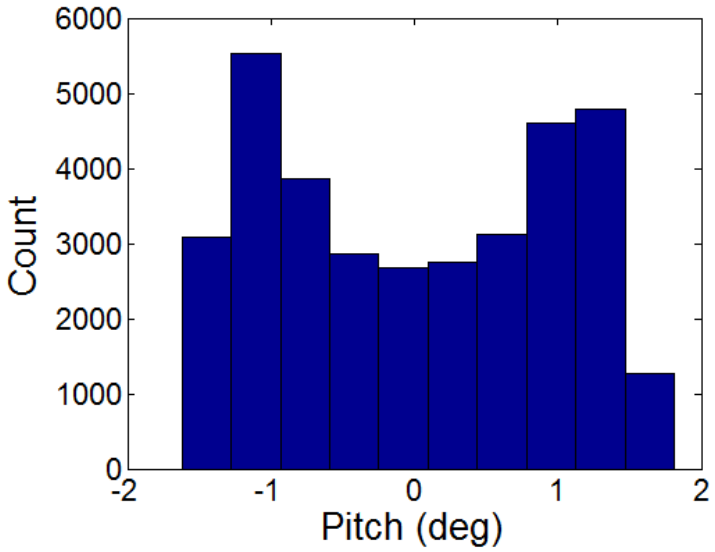

Figure B.4: Histogram of simulation at $U = 6.13$ m/s, Re = 61500

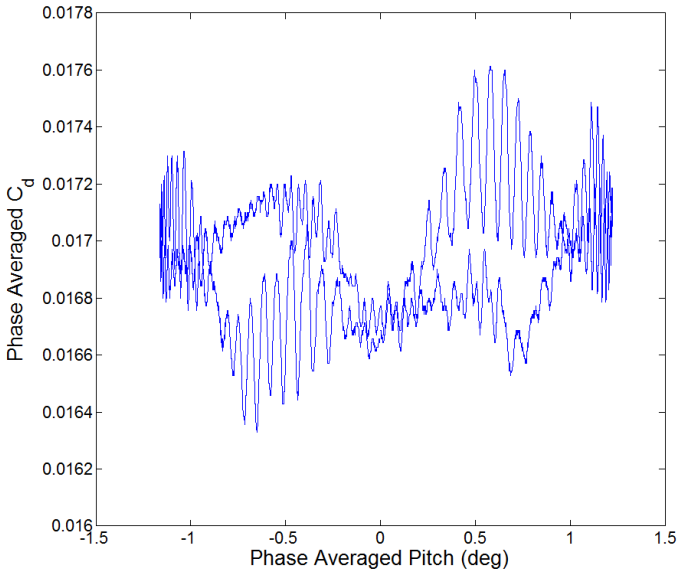

Figure B.5: Phase averaged C_d curve of simulation at $U = 6.13$ m/s, Re = 61500

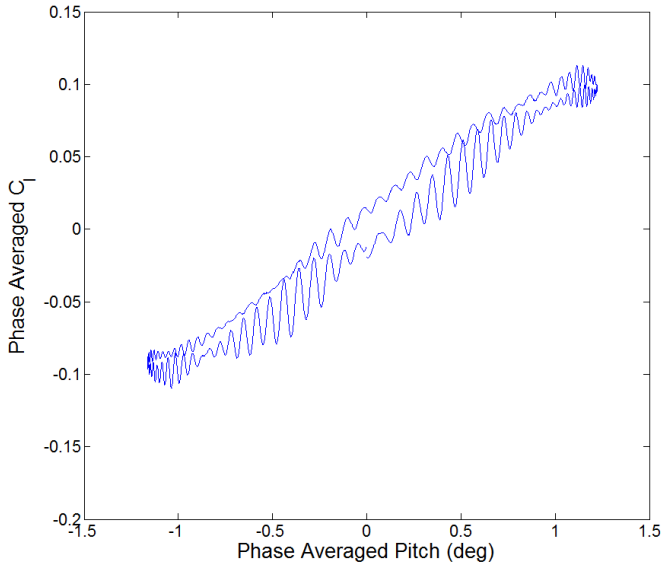

Figure B.6: Phase averaged C_l curve of simulation at $U = 6.13$ m/s, Re = 61500

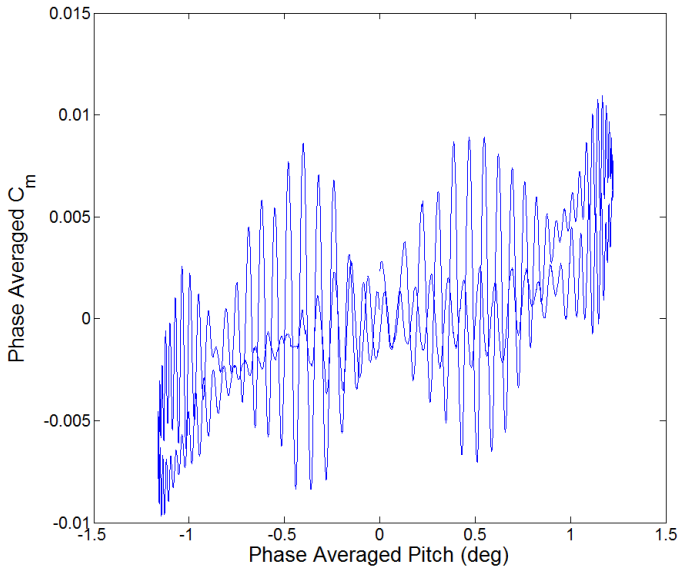

Figure B.7: Phase averaged C_m curve of simulation at $U = 6.13$ m/s, Re = 61500

B.1.2 U=7.00 m/s

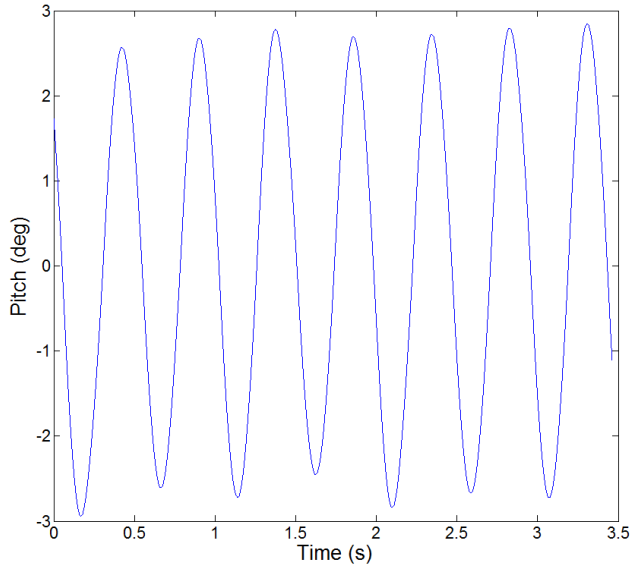

Figure B.8: Time trace of simulation at U = 7.00 m/s, Re = 70500

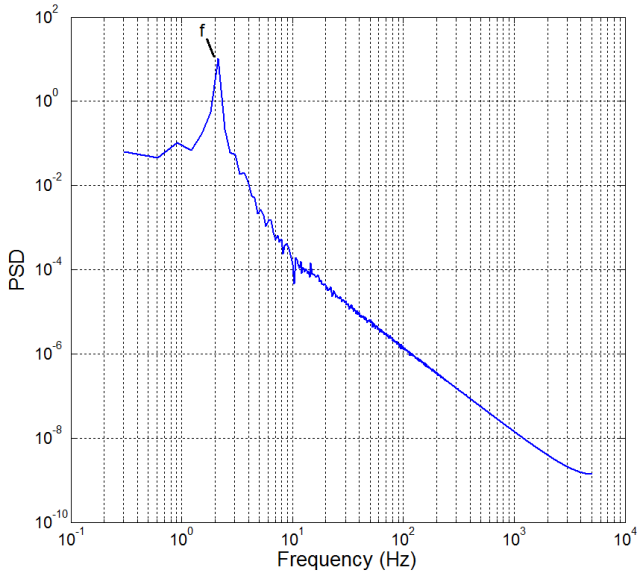

Figure B.9: PSD of simulation at U = 7.00 m/s, Re = 70500, f= 2.133 Hz

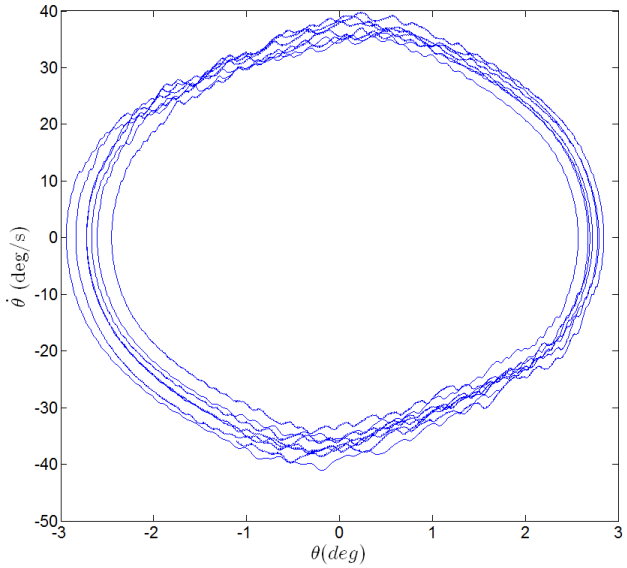

Figure B.10: Phase plane plot of simulation at $U = 7.00$ m/s, Re = 70500

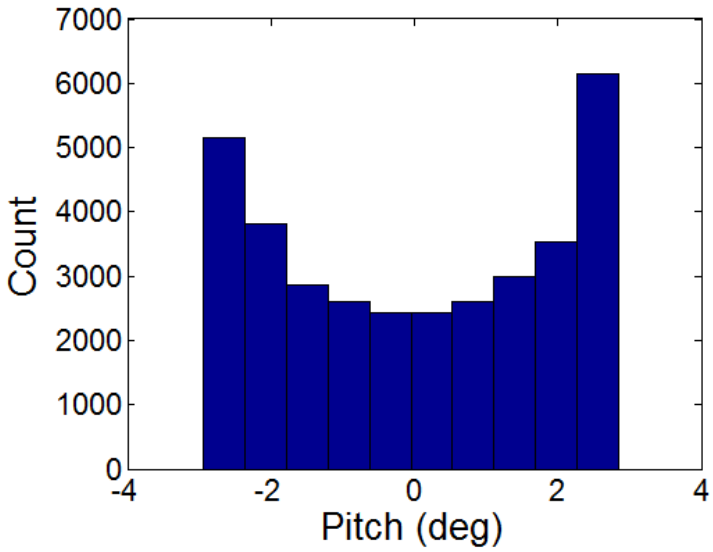

Figure B.11: Histogram of simulation at $U = 7.00$ m/s, Re = 70500

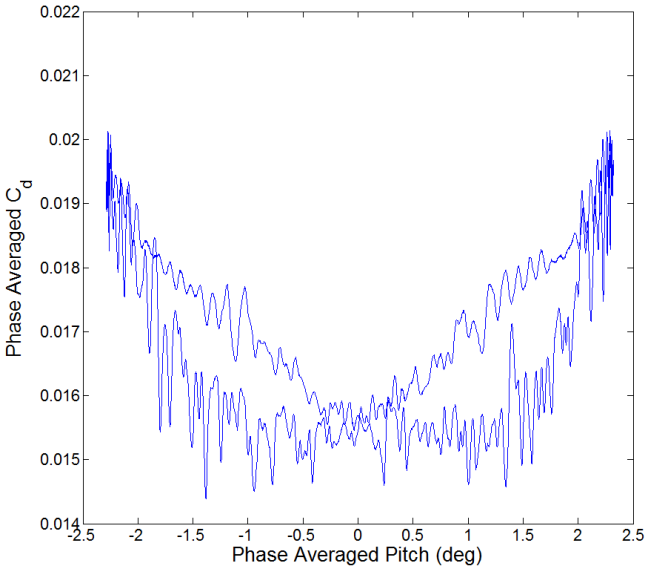

Figure B.12: Phase averaged C_d curve of simulation at $U = 7.00$ m/s, Re = 70500

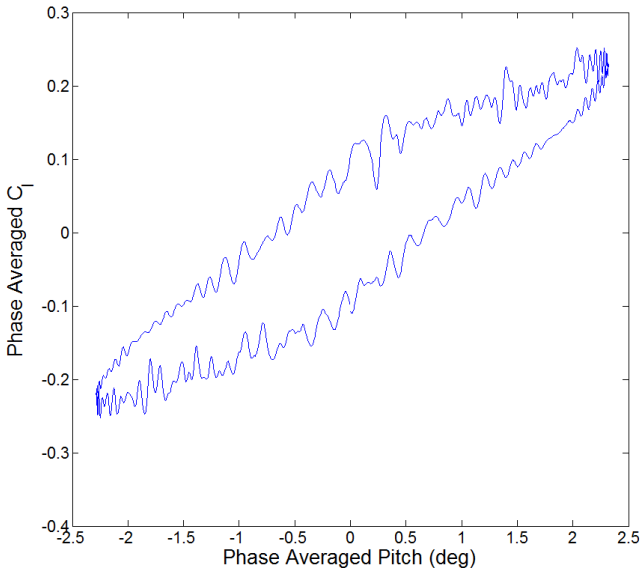

Figure B.13: Phase averaged C_l curve of simulation at $U = 7.00$ m/s, Re = 70500

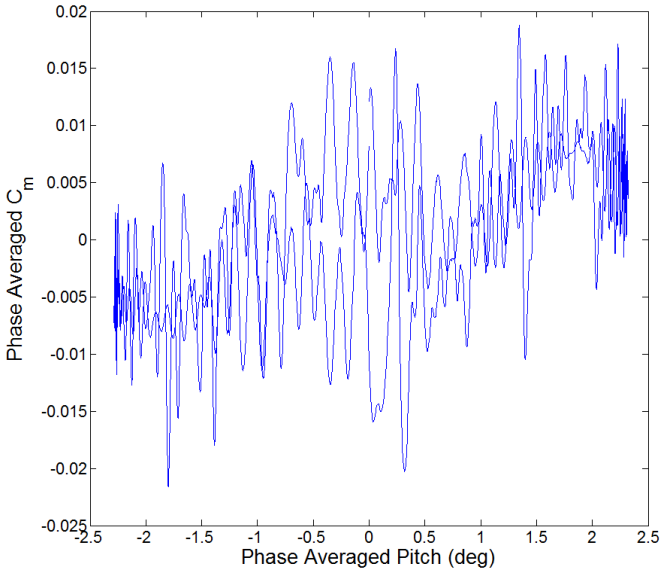

Figure B.14: Phase averaged C_m curve of simulation at $U = 7.00$ m/s, Re = 70500

B.1.3 U=7.50 m/s

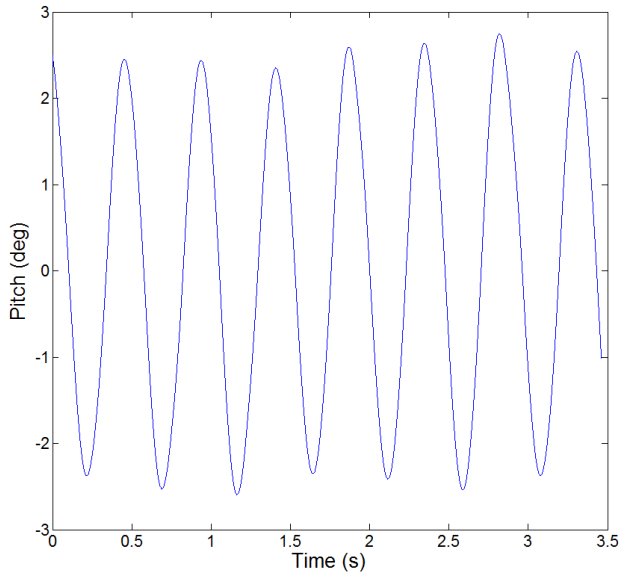

Figure B.15: Time trace of simulation at $U = 7.50$ m/s, Re = 75500

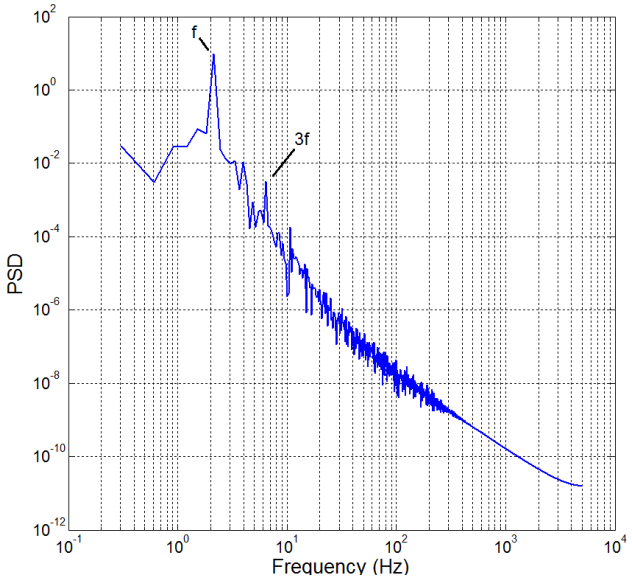

Figure B.16: PSD of simulation at $U = 7.50$ m/s, Re = 75500, f= 2.133 Hz

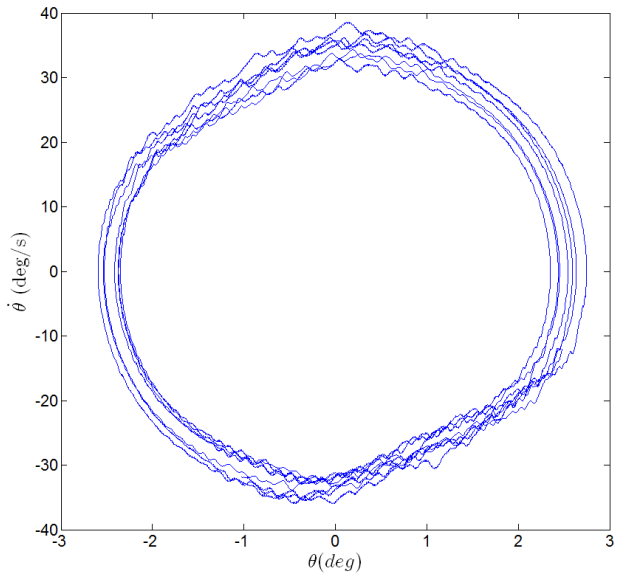

Figure B.17: Phase plane plot of simulation at $U = 7.50$ m/s, Re = 75500

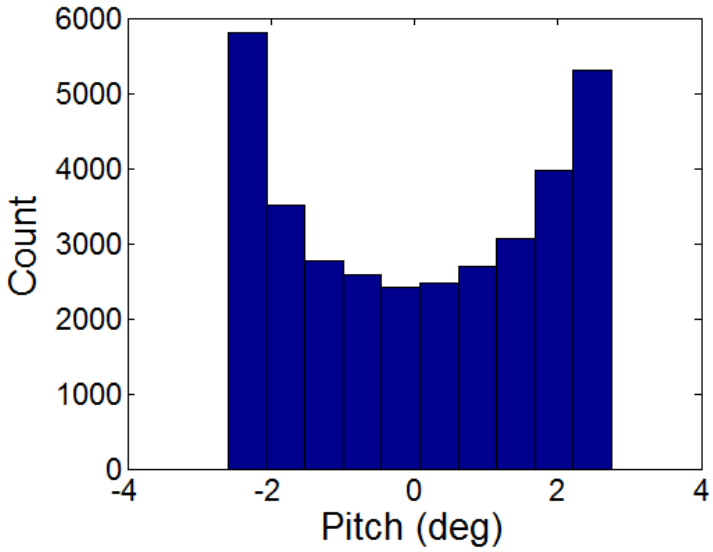

Figure B.18: Histogram of simulation at $U = 7.50$ m/s, Re = 75500

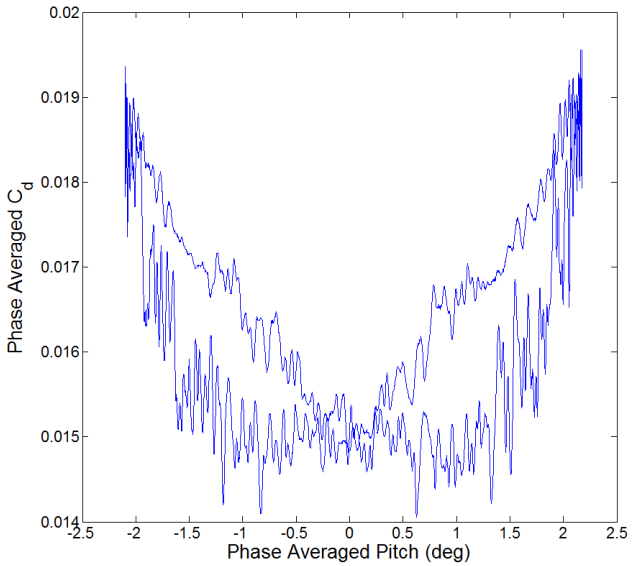

Figure B.19: Phase averaged C_d curve of simulation at $U = 7.50$ m/s, Re = 75500

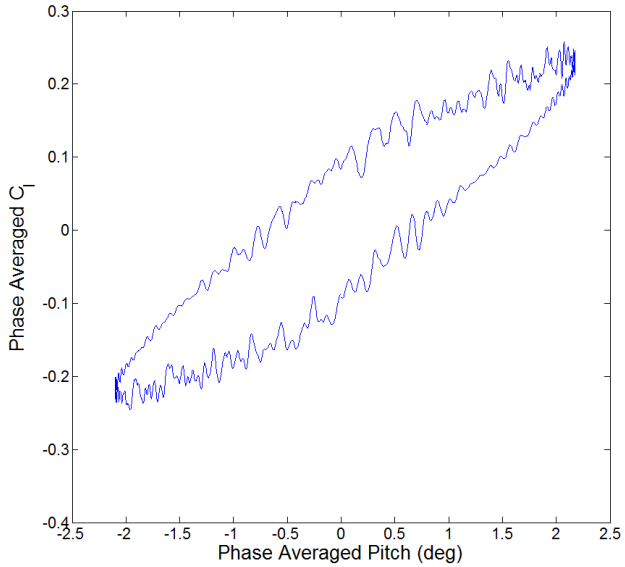

Figure B.20: Phase averaged C_l curve of simulation at $U = 7.50$ m/s, Re = 75500

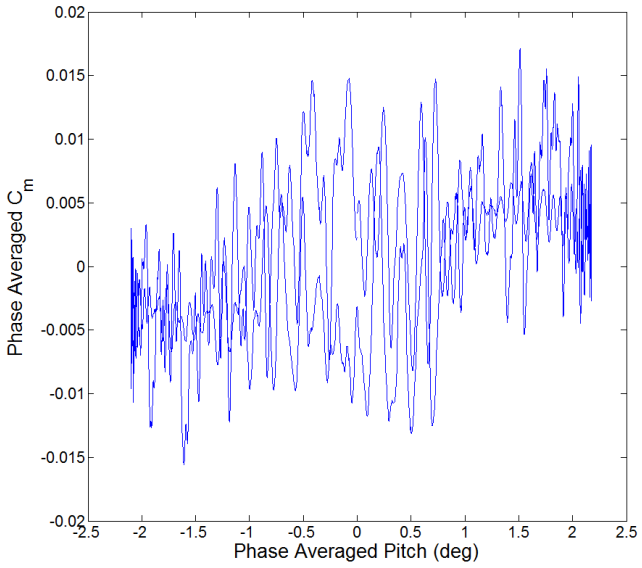

Figure B.21: Phase averaged C_m curve of simulation at $U = 7.50$ m/s, Re = 75500

B.1.4 U=7.75 m/s

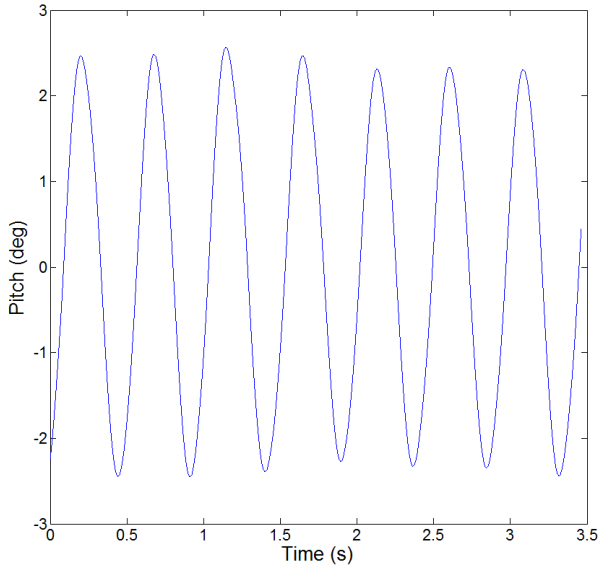

Figure B.22: Time trace of simulation at v = 7.75 m/s, Re = 78000

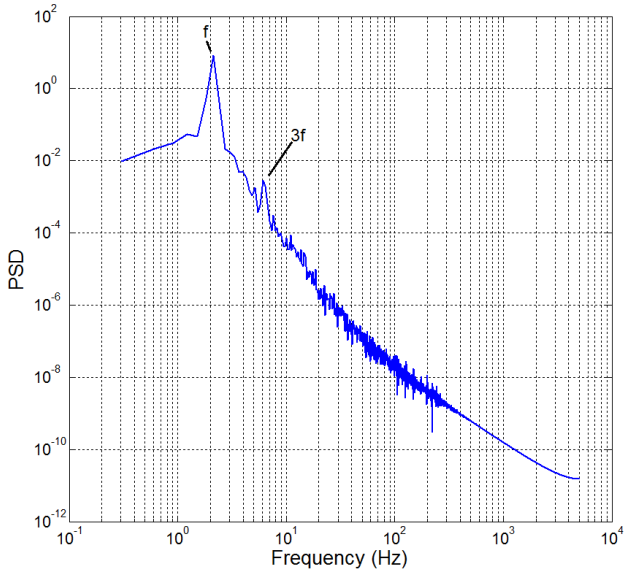

Figure B.23: PSD of simulation at U = 7.75 m/s, Re = 78000, f= 2.133 Hz

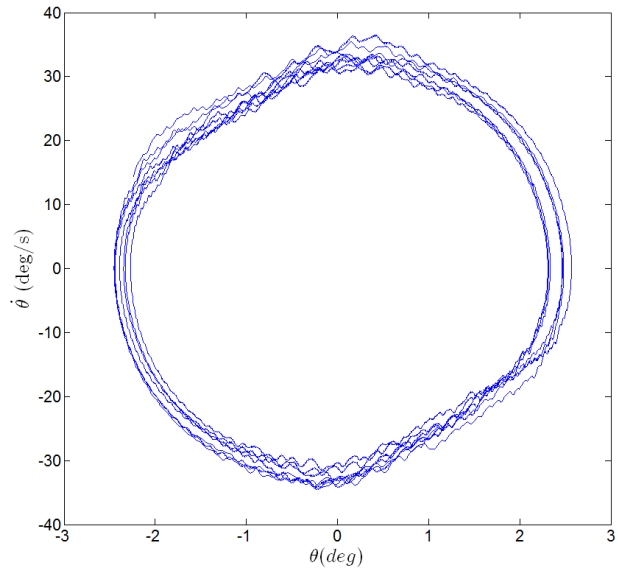

Figure B.24: Phase plane plot of simulation at U= 7.75 m/s, Re = 78000

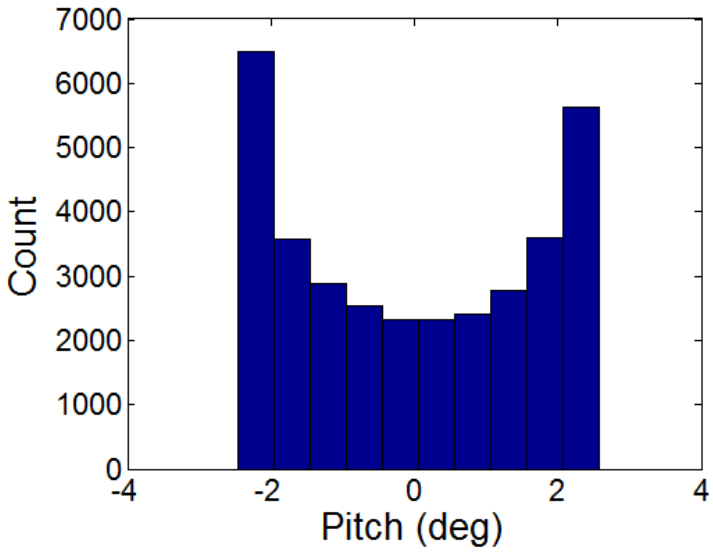

Figure B.25: Histogram of simulation at U = 7.75 m/s, Re = 78000

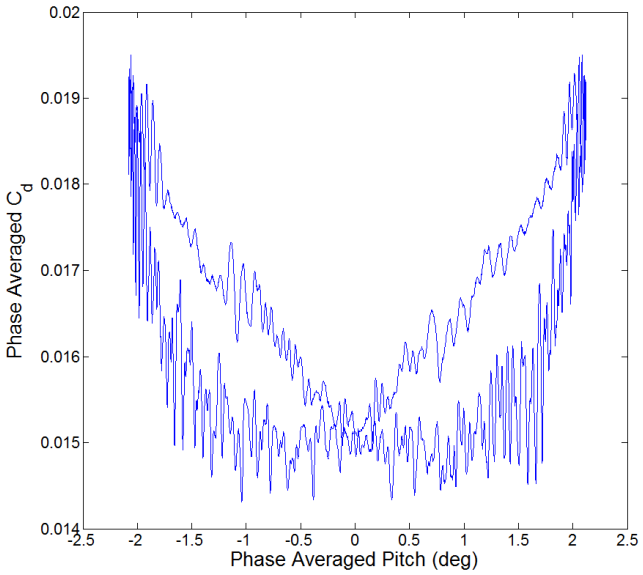

Figure B.26: Phase averaged C_d curve of simulation at $U = 7.75$ m/s, Re = 78000

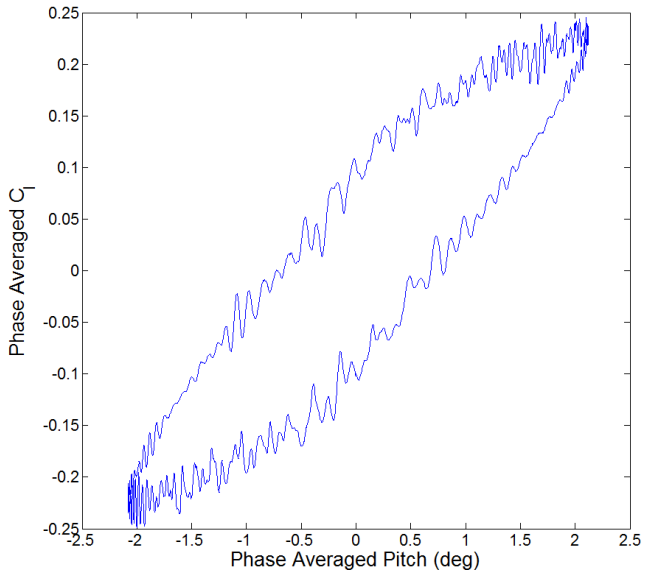

Figure B.27: Phase averaged C_l curve of simulation at $U = 7.75$ m/s, Re = 78000

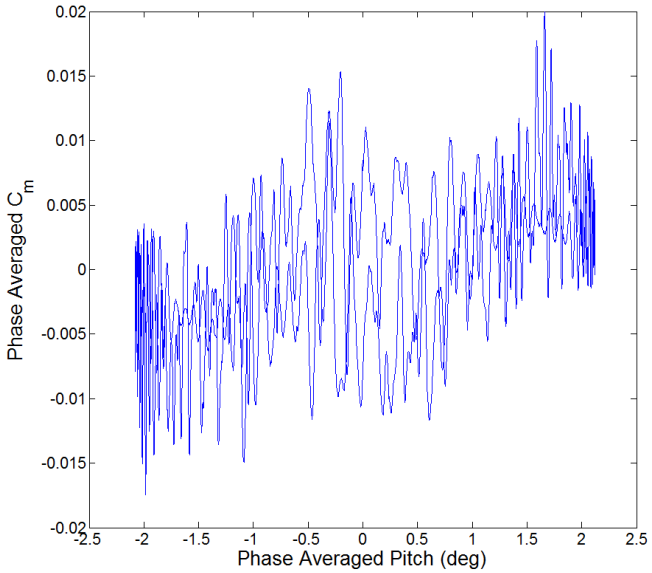

Figure B.28: Phase averaged C_m curve of simulation at $U = 7.75$ m/s, Re = 78000

B.1.5 U=8.00 m/s

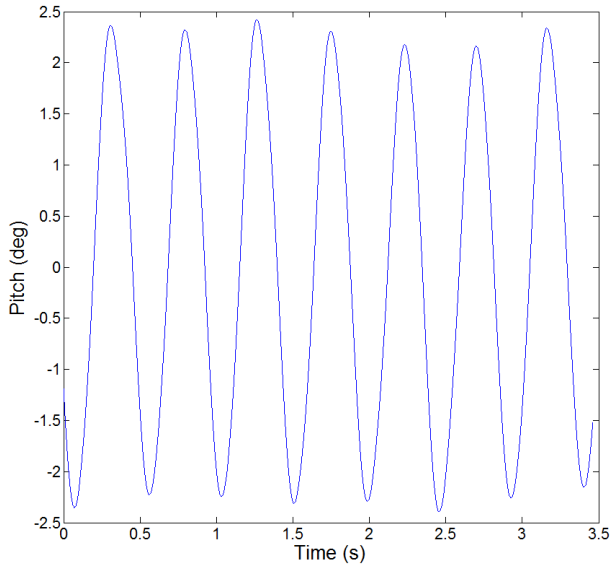

Figure B.29: Time trace of simulation at $U = 8.00$ m/s, Re = 80500

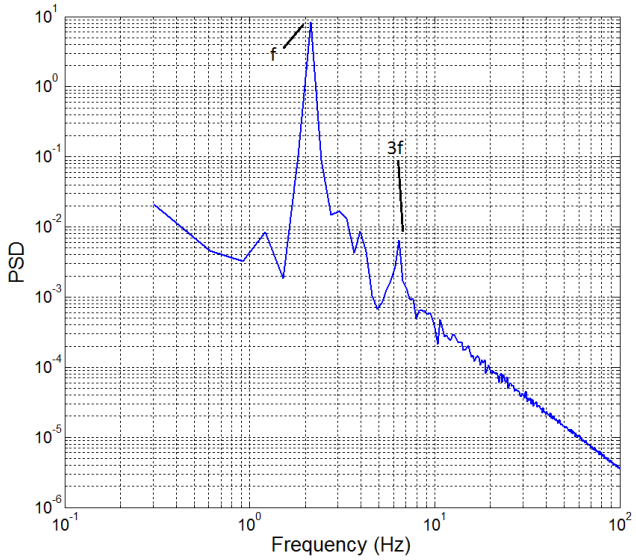

Figure B.30: PSD of simulation at $U = 8.00$ m/s, Re = 80500, f= 2.133 Hz

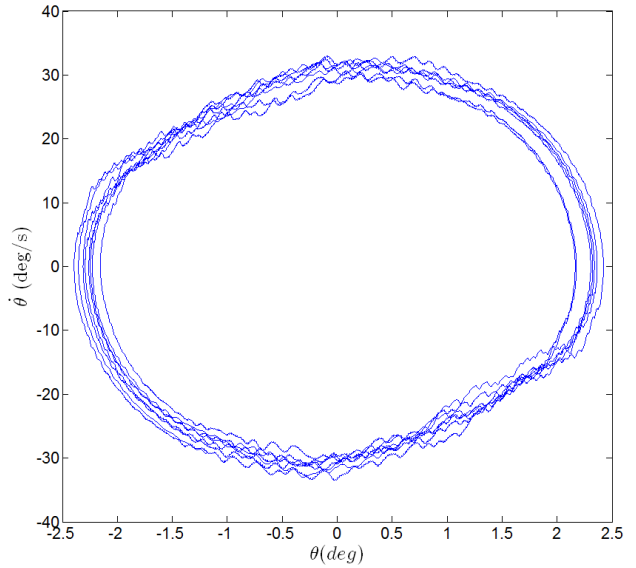

Figure B.31: Phase plane plot of simulation at $U = 8.00$ m/s, Re = 80500

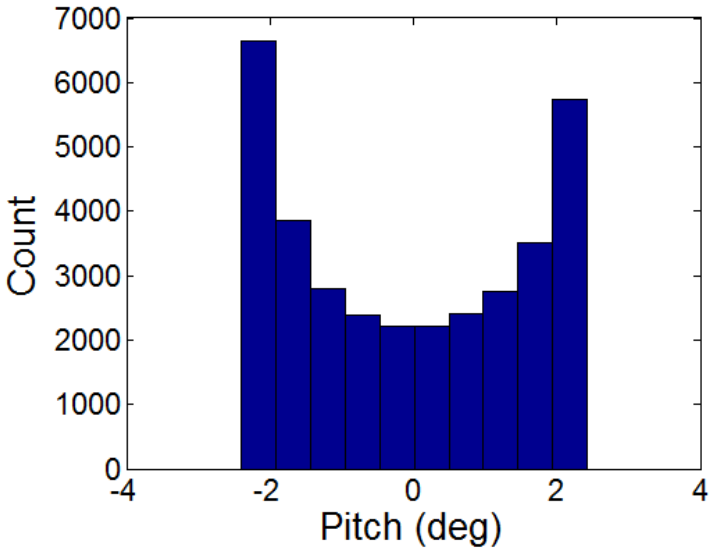

Figure B.32: Histogram of simulation at $U = 8.00$ m/s, Re = 80500

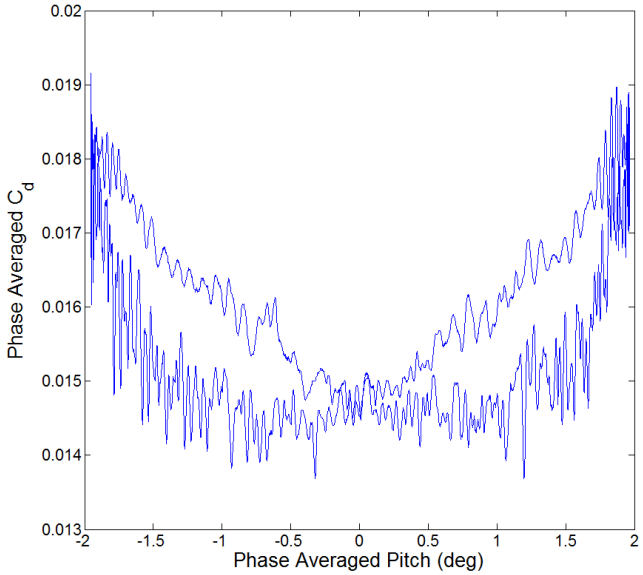

Figure B.33: Phase averaged C_d curve of simulation at $U = 8.00$ m/s, Re = 80500

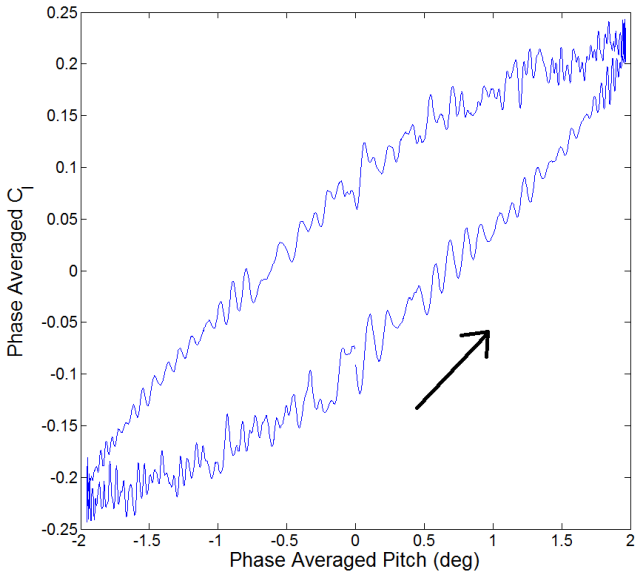

Figure B.34: Phase averaged C_l curve of simulation at $U = 8.00$ m/s, Re = 80500

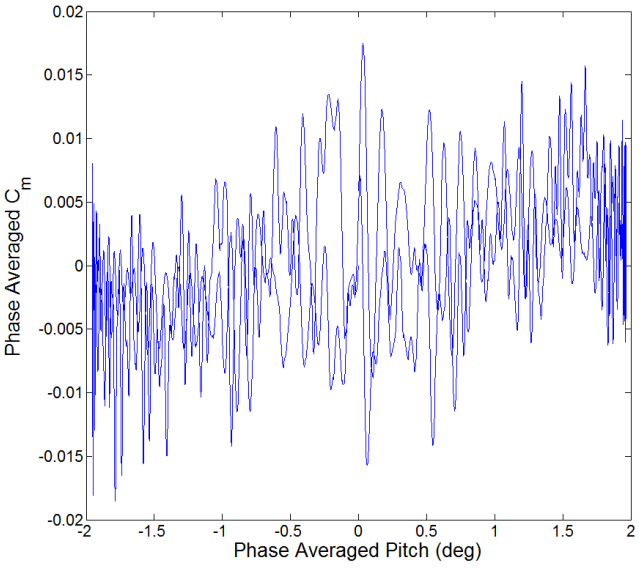

Figure B.35: Phase averaged C_m curve of simulation at $U = 8.00$ m/s, Re = 80500

B.1.6 U=8.50 m/s

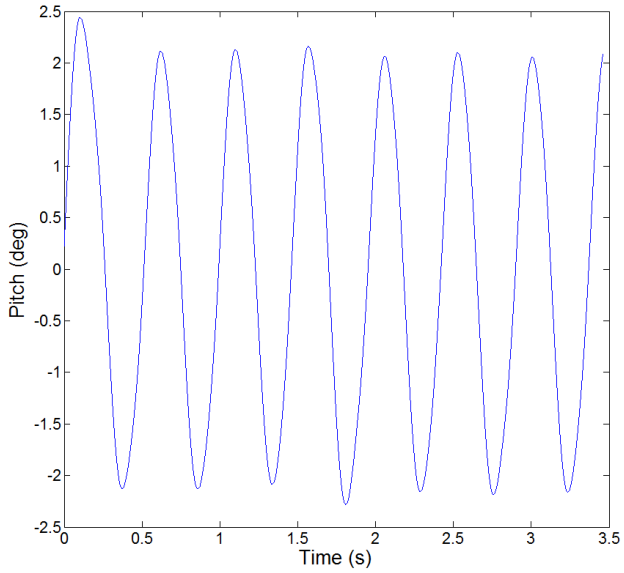

Figure B.36: Time trace of simulation at U = 8.50 m/s, Re = 85500

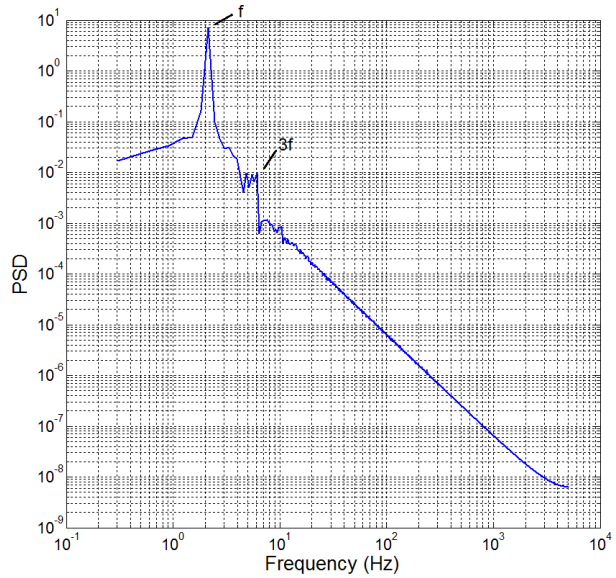

Figure B.37: PSD of simulation at U = 8.50 m/s, Re = 85500, f= 2.133 Hz

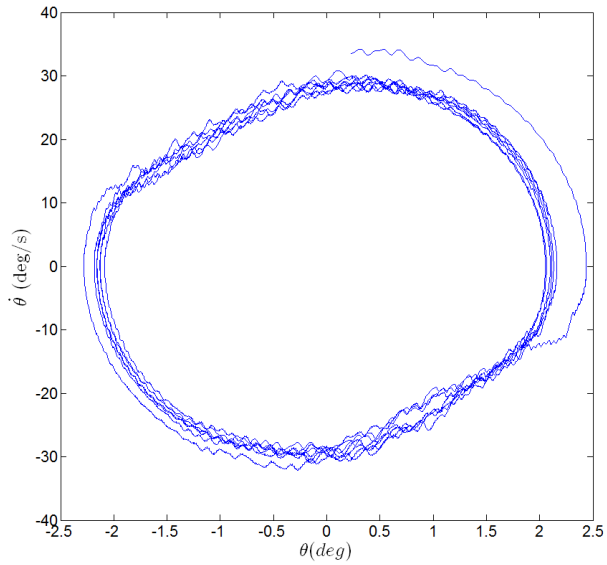

Figure B.38: Phase plane plot of simulation at $U = 8.50$ m/s, Re = 85500

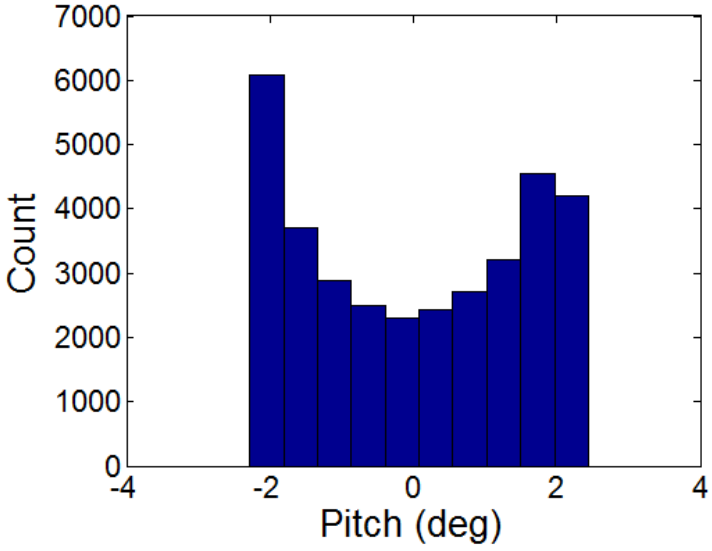

Figure B.39: Histogram of simulation at $U = 8.50$ m/s, Re = 85500

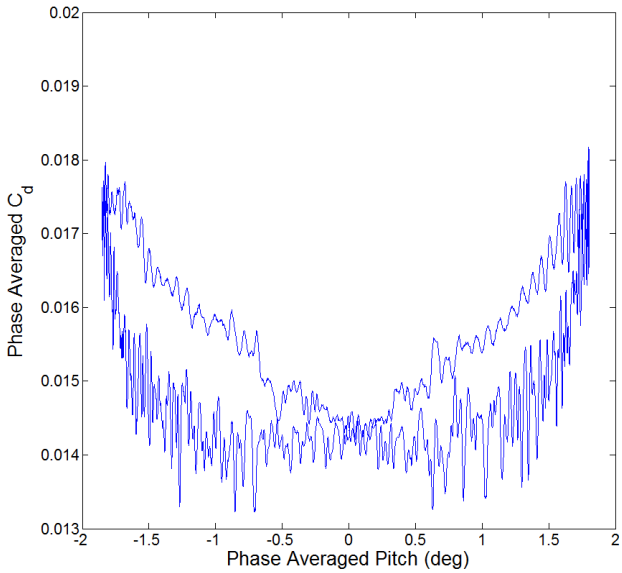

Figure B.40: Phase averaged C_d curve of simulation at $U = 8.50$ m/s, Re = 85500

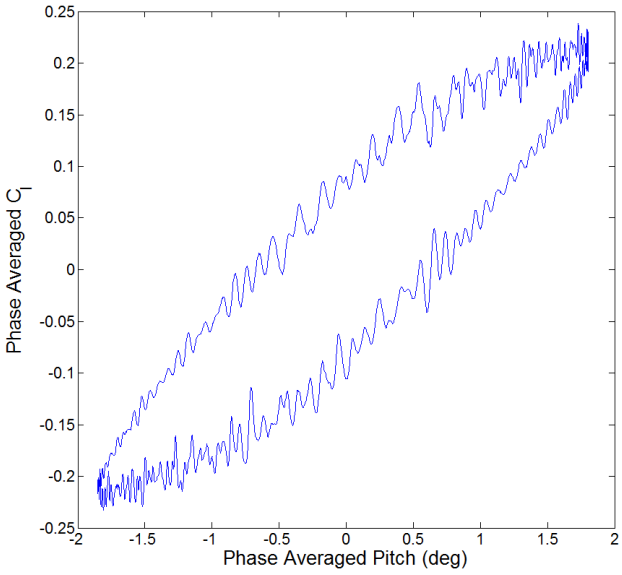

Figure B.41: Phase averaged C_l curve of simulation at $U = 8.50$ m/s, Re = 85500

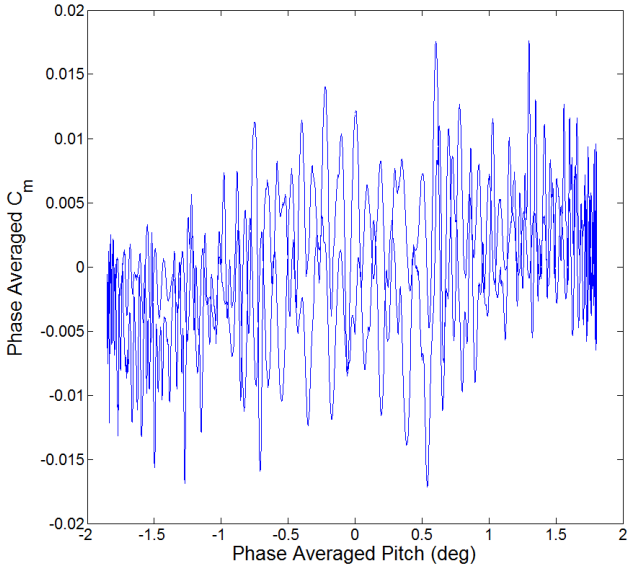

Figure B.42: Phase averaged C_m curve of simulation at $U = 8.50$ m/s, Re = 85500

B.2 LAO

B.2.1 U=6.13 m/s

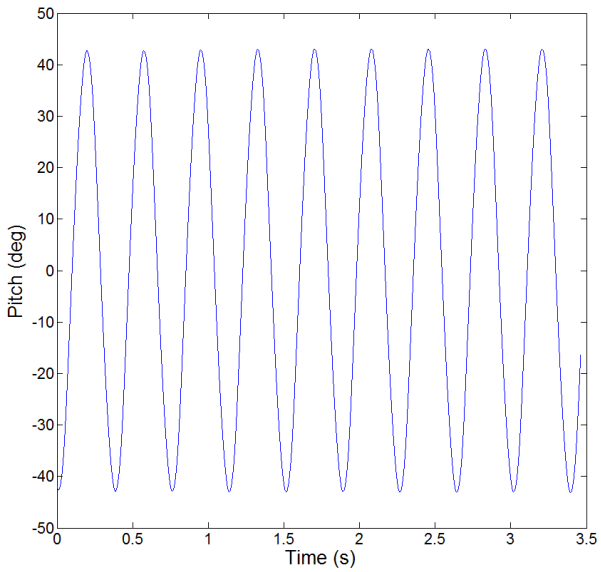

Figure B.43: Time trace of simulation at $U = 6.13$ m/s, Re = 61500

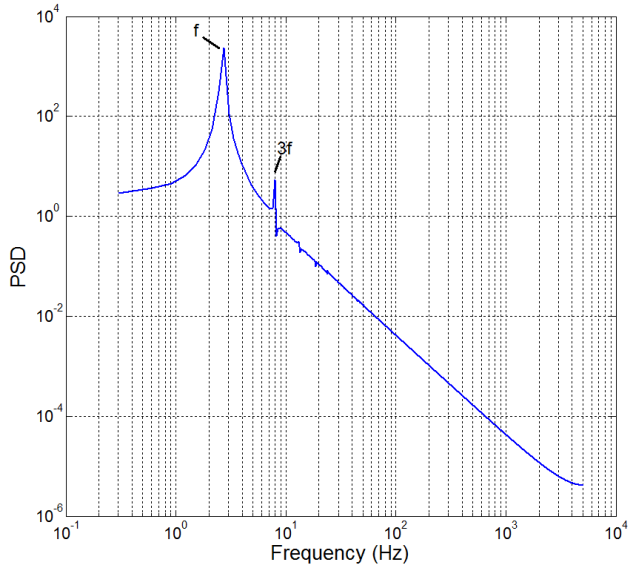

Figure B.44: PSD of simulation at $U = 6.13$ m/s, Re = 61500, f= 2.742 Hz

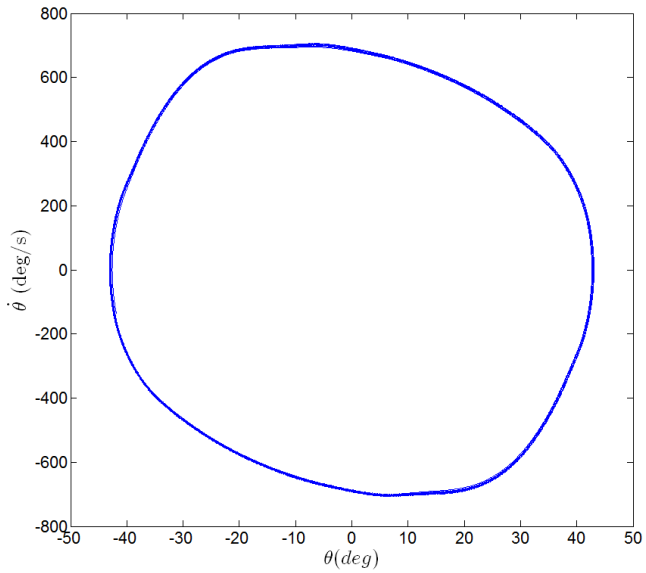

Figure B.45: Phase plane plot of simulation at $U = 6.13$ m/s, Re = 61500

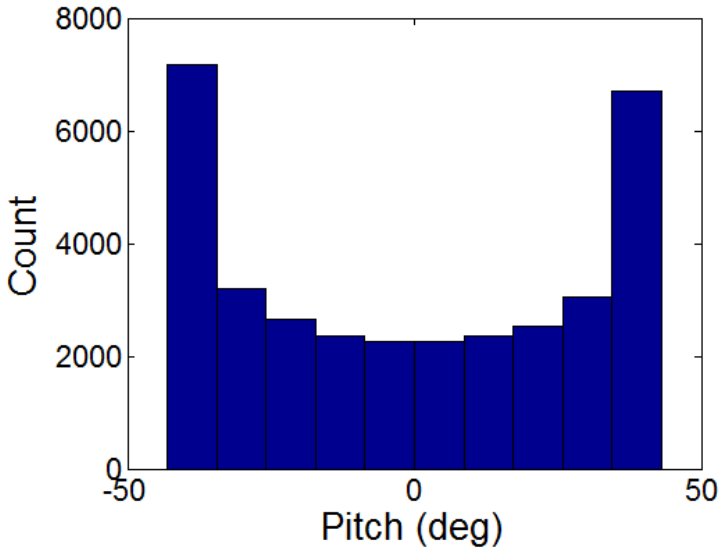

Figure B.46: Histogram of simulation at $U = 6.13$ m/s, Re = 61500

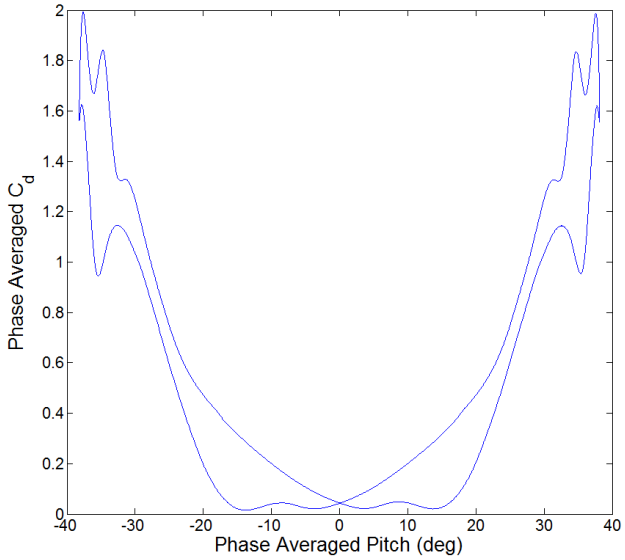

Figure B.47: Phase averaged C_d curve of simulation at $U = 6.13$ m/s, Re = 61500

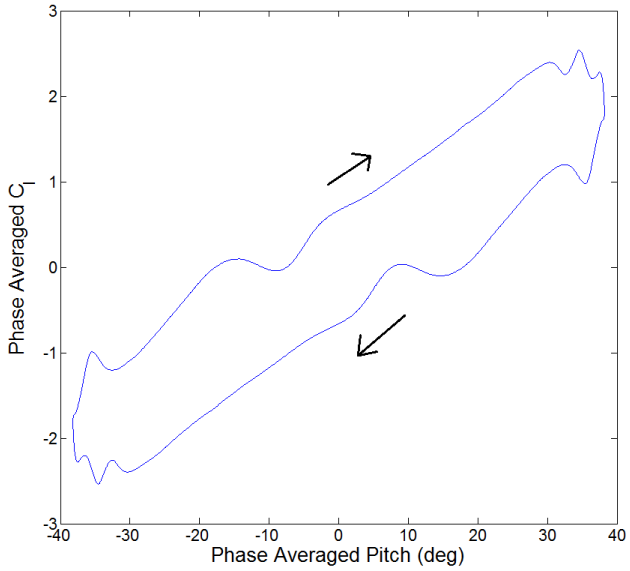

Figure B.48: Phase averaged C_l curve of simulation at $U = 6.13$ m/s, Re = 61500

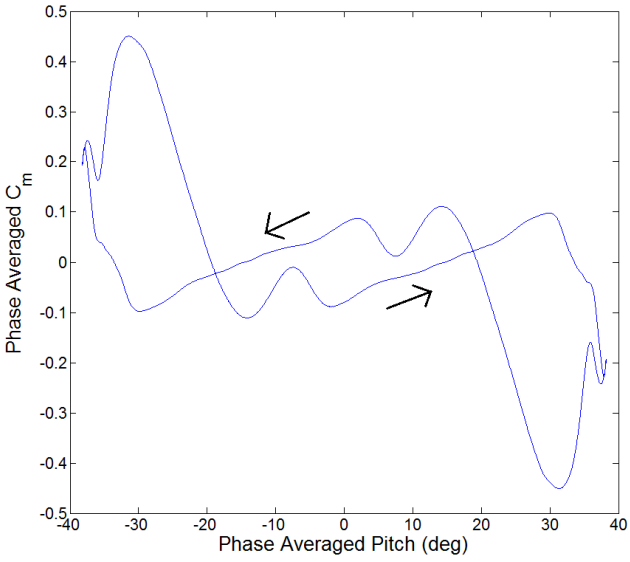

Figure B.49: Phase averaged C_m curve of simulation at $U = 6.13$ m/s, Re = 61500

B.2.2 U=7.00 m/s

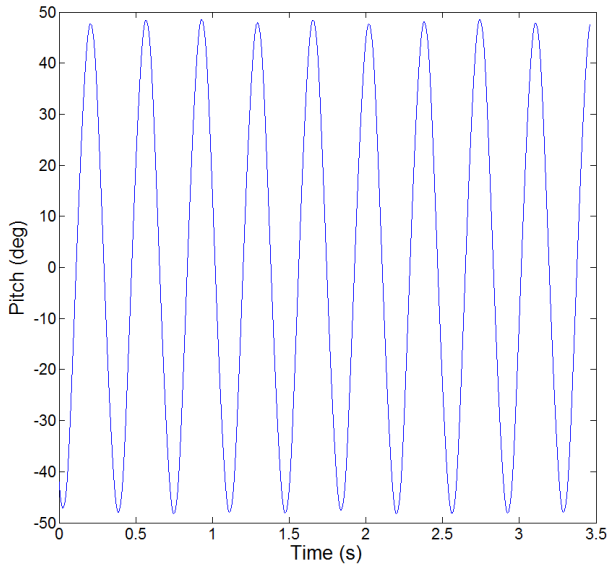

Figure B.50: Time trace of simulation at U = 7.00 m/s, Re = 70500

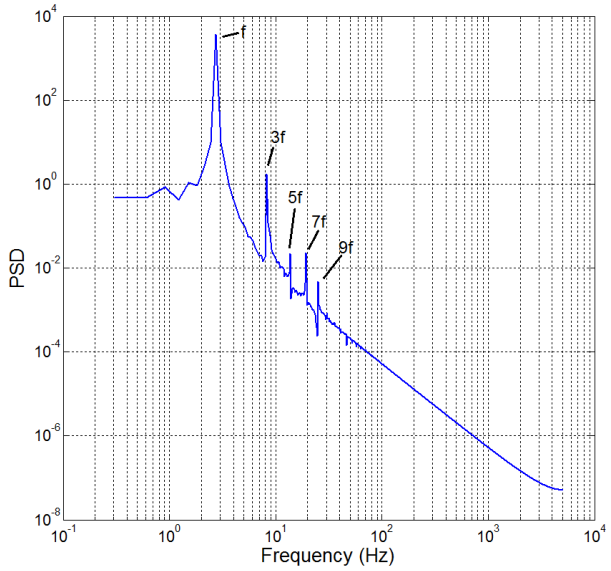

Figure B.51: PSD of simulation at U = 7.00 m/s, Re = 70500, f= 2.742 Hz

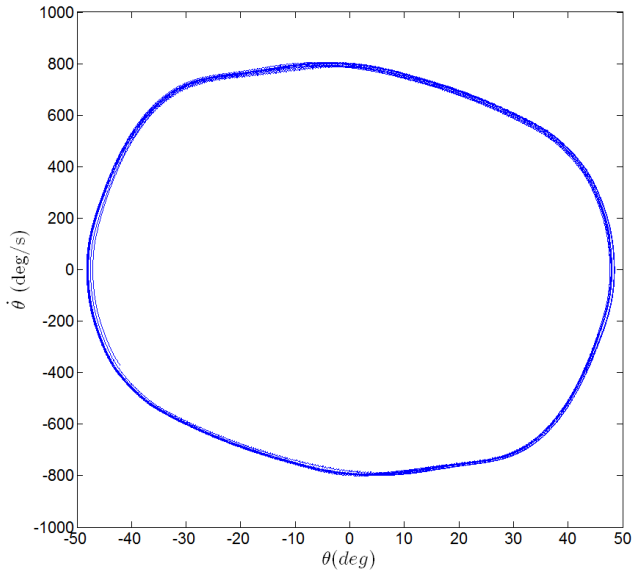

Figure B.52: Phase plane plot of simulation at $U = 7.00$ m/s, Re = 70500

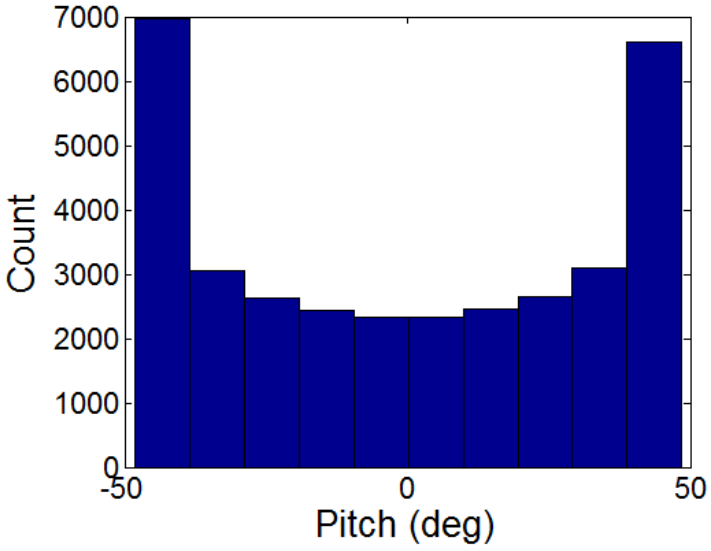

Figure B.53: Histogram of simulation at $U = 7.00$ m/s, Re = 70500

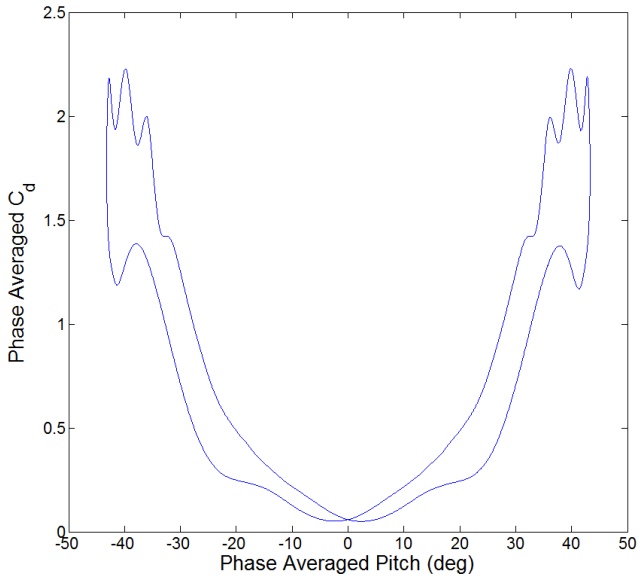

Figure B.54: Phase averaged C_d curve of simulation at $U = 7.00$ m/s, Re = 70500

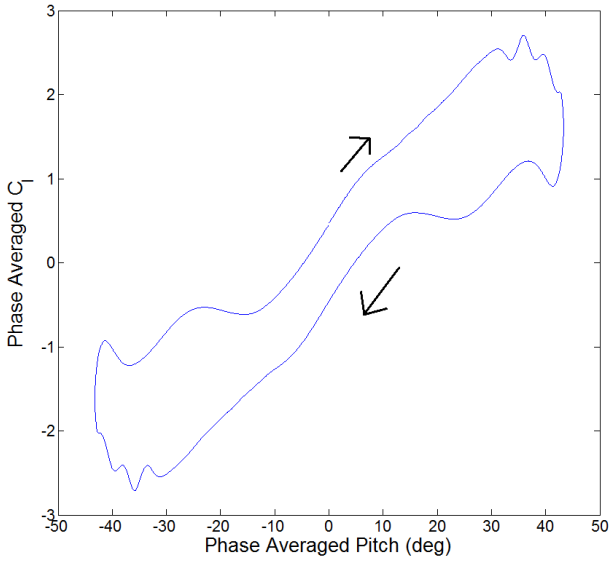

Figure B.55: Phase averaged C_l curve of simulation at $U = 7.00$ m/s, Re = 70500

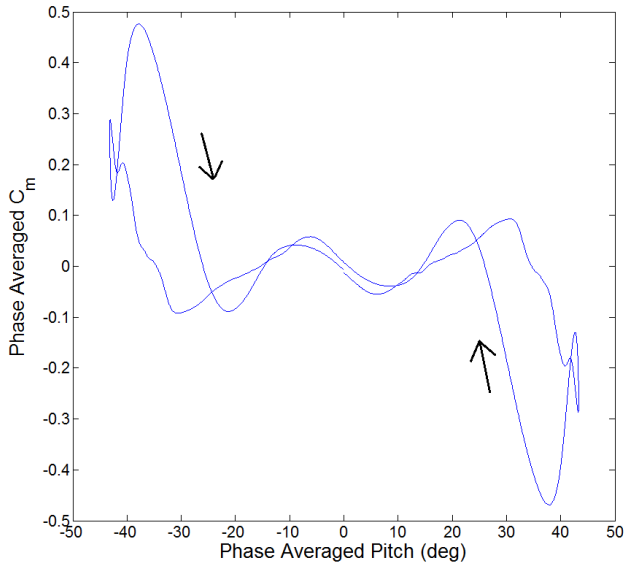

Figure B.56: Phase averaged C_m curve of simulation at $U = 7.00$ m/s, Re = 70500

B.2.3 U=7.50 m/s

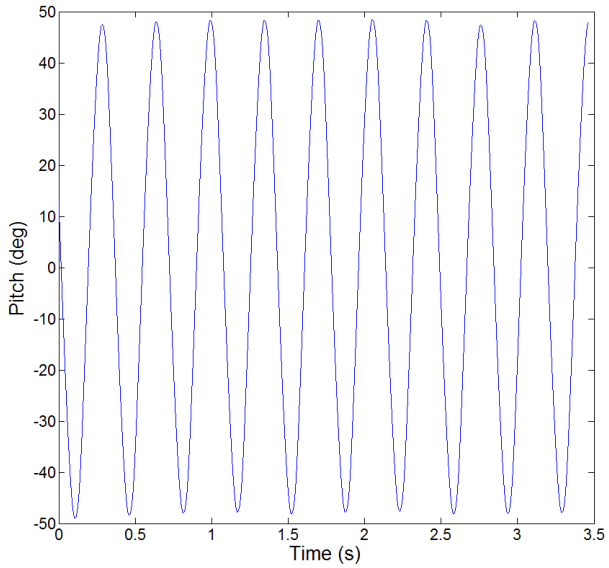

Figure B.57: Time trace of simulation at $U = 7.50$ m/s, Re = 75500

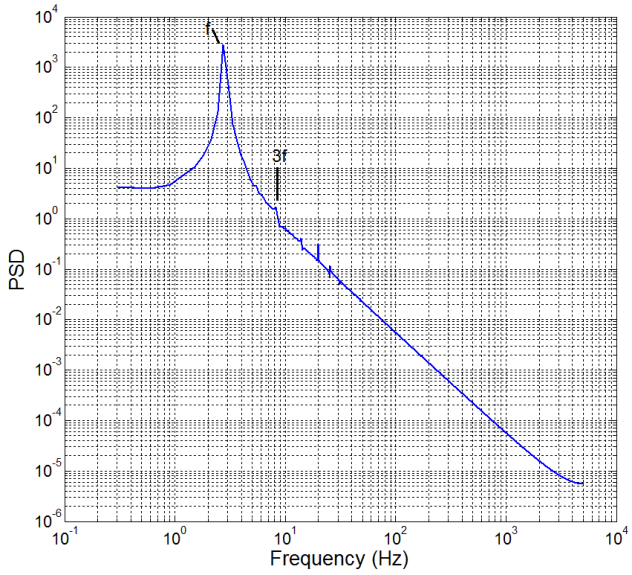

Figure B.58: PSD of simulation at $U = 7.50$ m/s, Re = 75500, f= 2.742 Hz

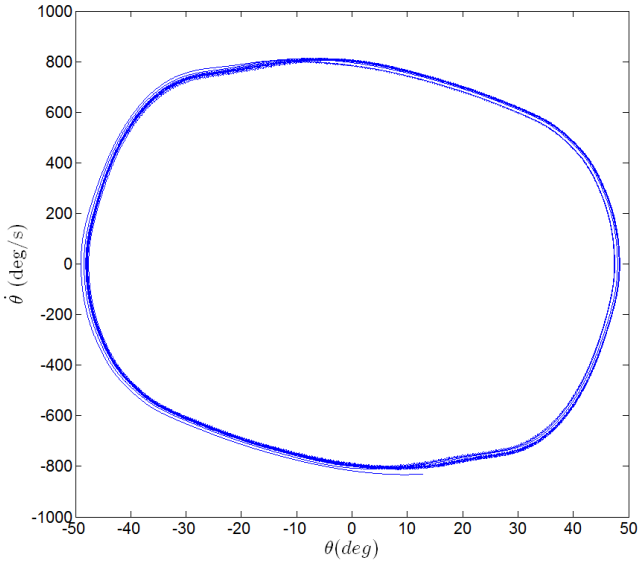

Figure B.59: Phase plane plot of simulation at $U = 7.50$ m/s, Re = 75500

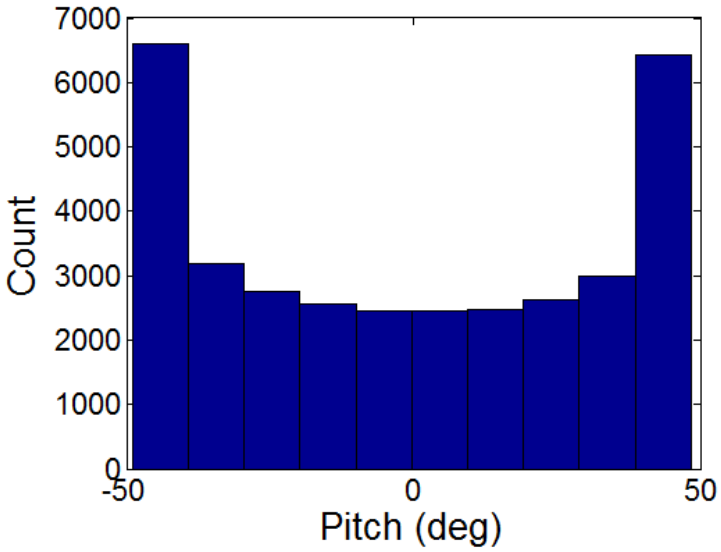

Figure B.60: Histogram of simulation at $U = 7.50$ m/s, Re = 75500

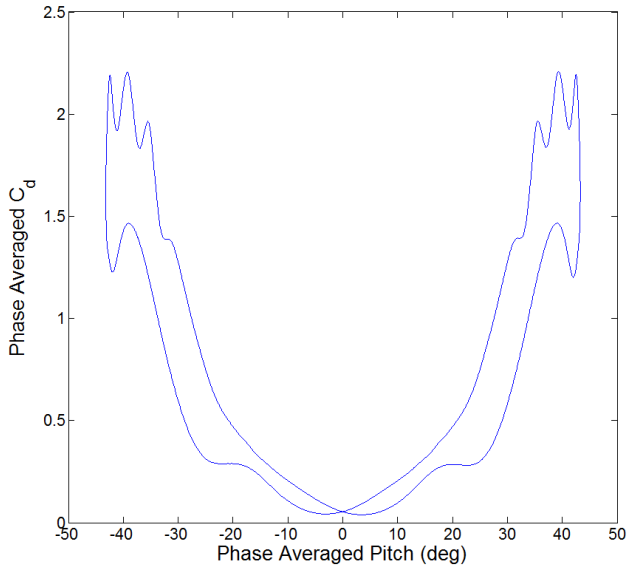

Figure B.61: Phase averaged C_d curve of simulation at $U = 7.50$ m/s, Re = 75500

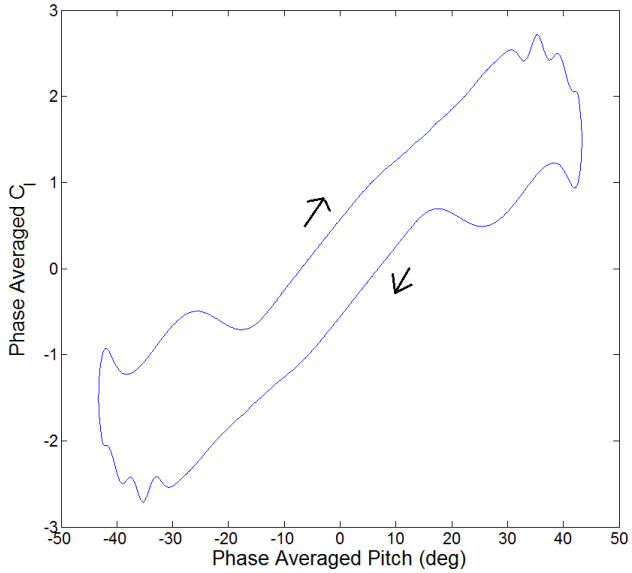

Figure B.62: Phase averaged C_l curve of simulation at $U = 7.50$ m/s, Re = 75500

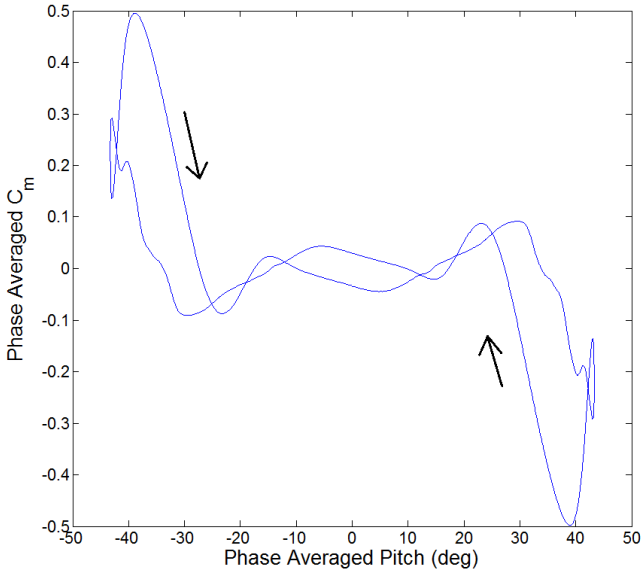

Figure B.63: Phase averaged C_m curve of simulation at $U = 7.50$ m/s, Re = 75500

B.2.4 U=7.75 m/s

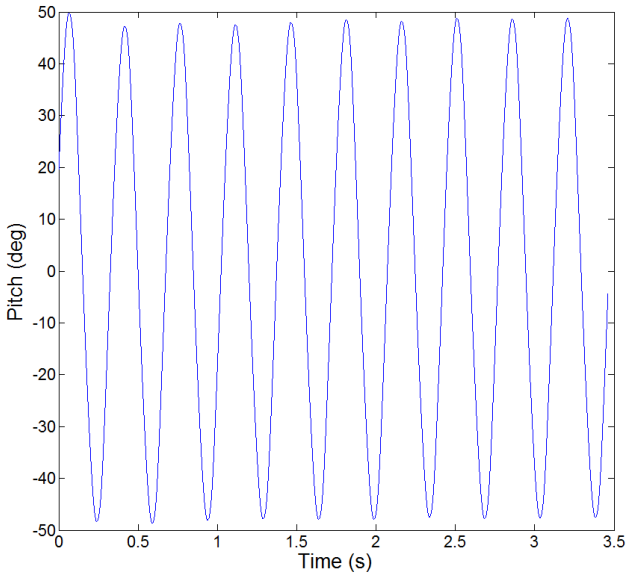

Figure B.64: Time trace of simulation at U = 7.75 m/s, Re = 78000

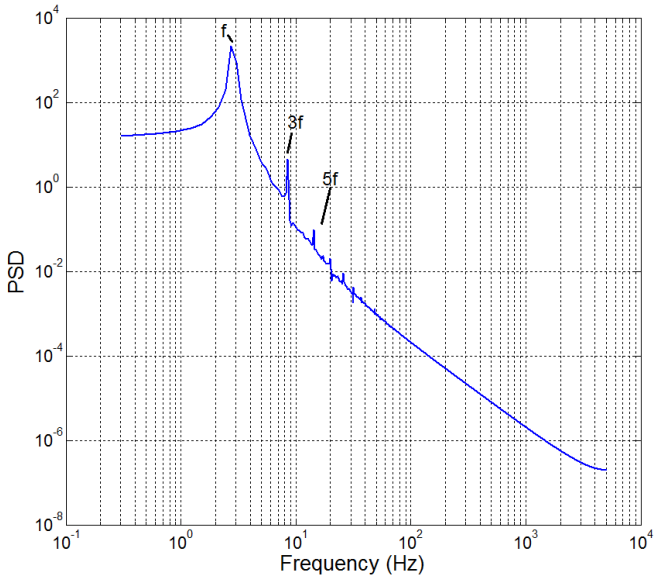

Figure B.65: PSD of simulation at U = 7.75 m/s, Re = 78000, f= 3.047 Hz

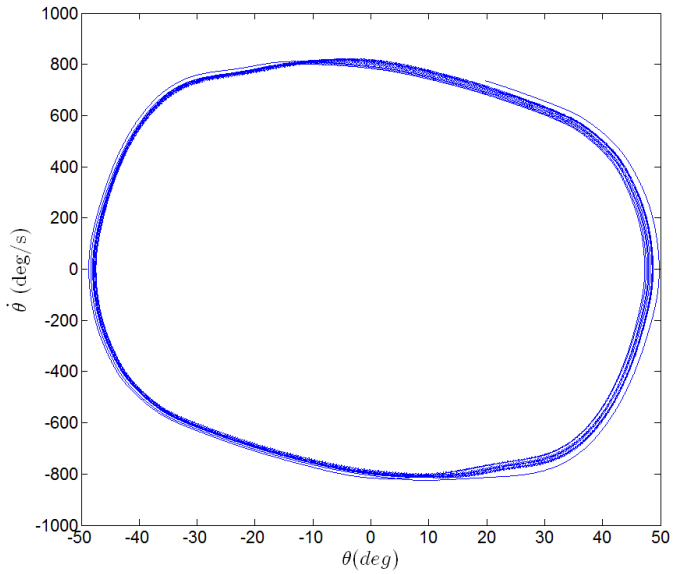

Figure B.66: Phase plane plot of simulation at $U = 7.75$ m/s, Re = 78000

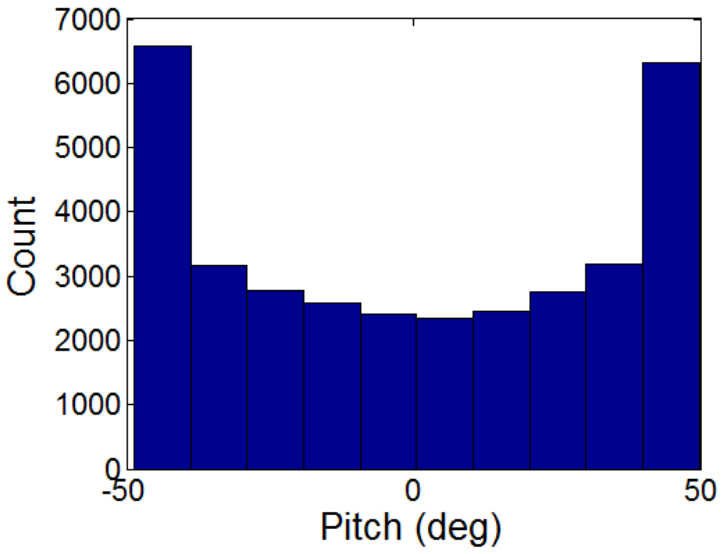

Figure B.67: Histogram of simulation at $U = 7.75$ m/s, Re = 78000

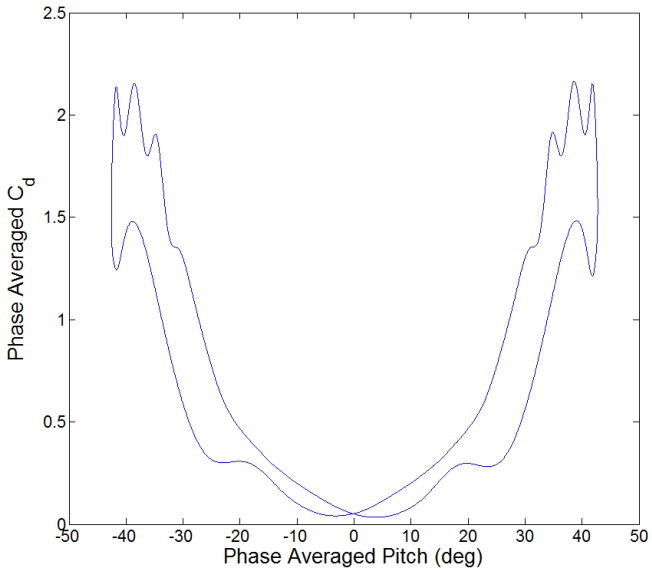

Figure B.68: Phase averaged C_d curve of simulation at $U = 7.75$ m/s, Re = 78000

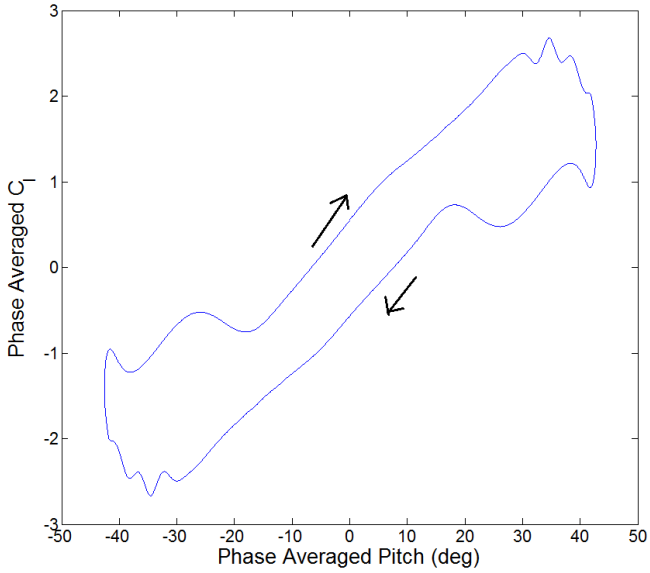

Figure B.69: Phase averaged C_l curve of simulation at $U = 7.75$ m/s, Re = 78000

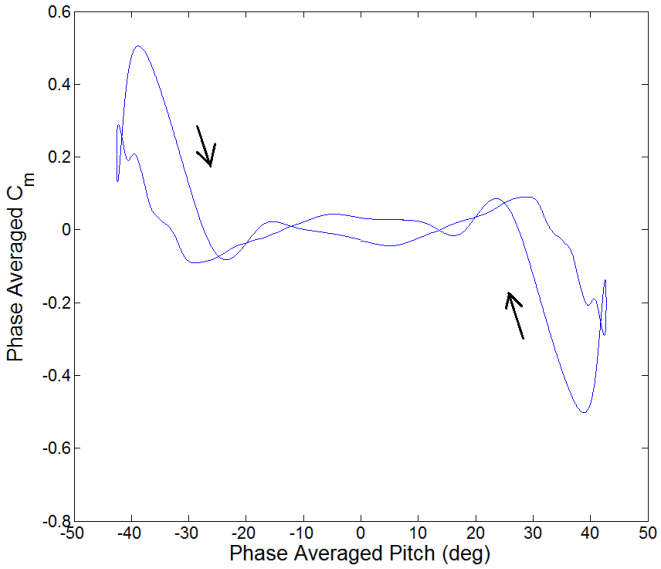

Figure B.70: Phase averaged C_m curve of simulation at $U = 7.75$ m/s, Re = 78000

B.2.5 U=8.00 m/s

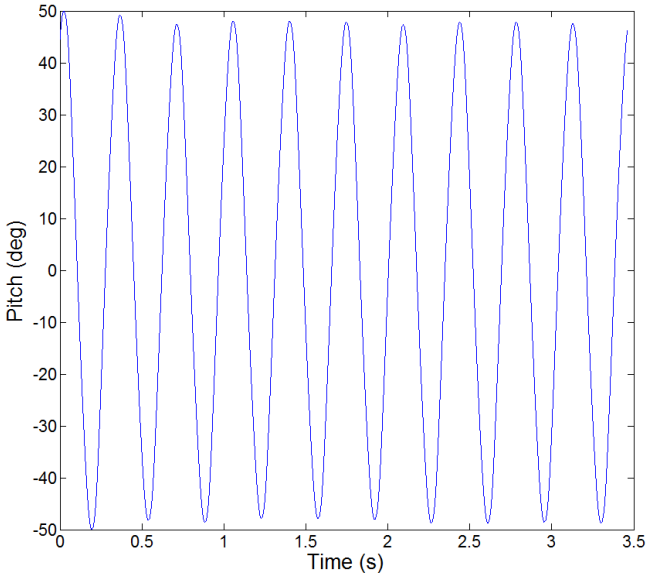

Figure B.71: Time trace of simulation at $U = 8.00$ m/s, Re = 80500

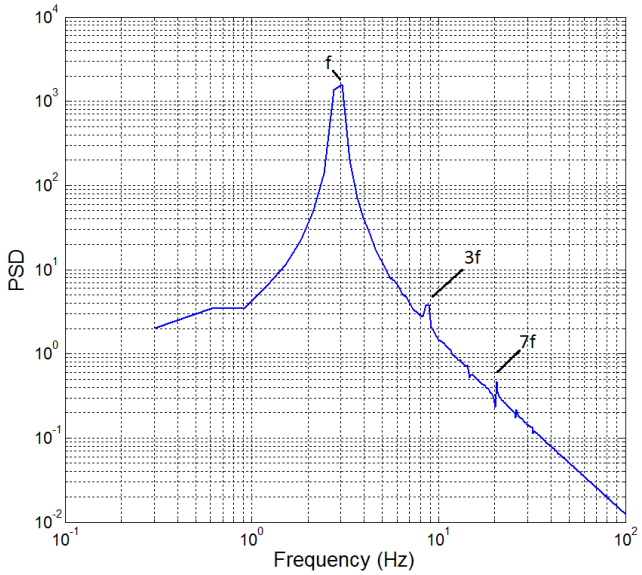

Figure B.72: PSD of simulation at $U = 8.00$ m/s, Re = 80500, f= 3.047 Hz

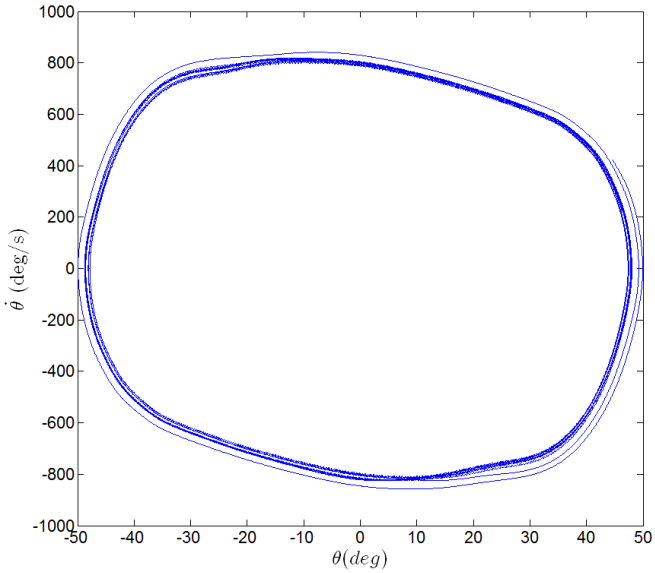

Figure B.73: Phase plane plot of simulation at $U = 8.00$ m/s, Re = 80500

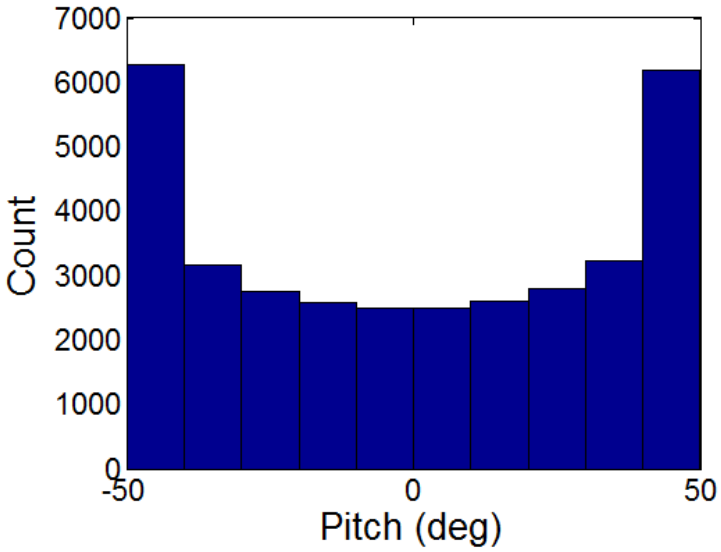

Figure B.74: Histogram of simulation at $U = 8.00$ m/s, Re = 80500

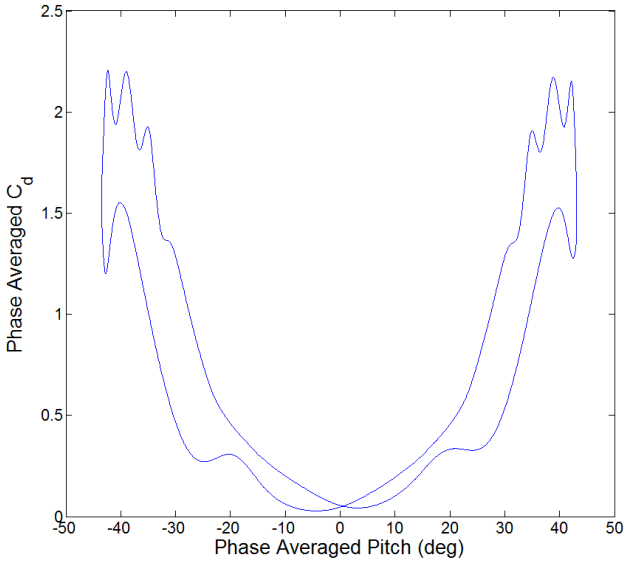

Figure B.75: Phase averaged C_d curve of simulation at $U = 8.00$ m/s, Re = 80500

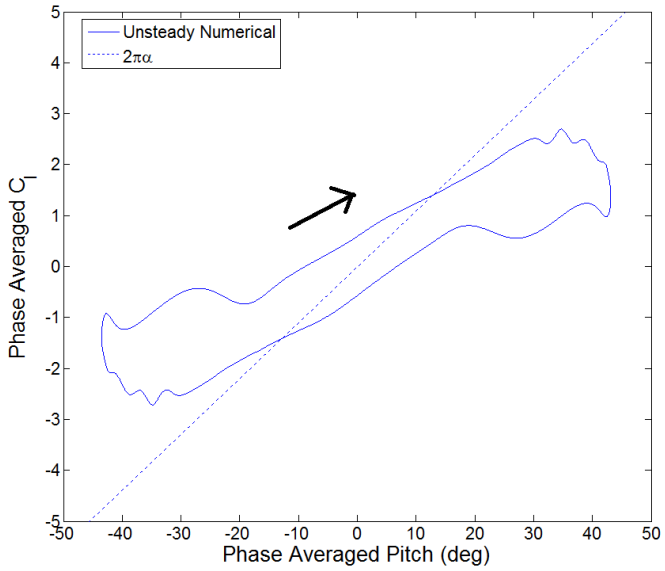

Figure B.76: Phase averaged C_l curve of simulation at $U = 8.00$ m/s, Re = 80500

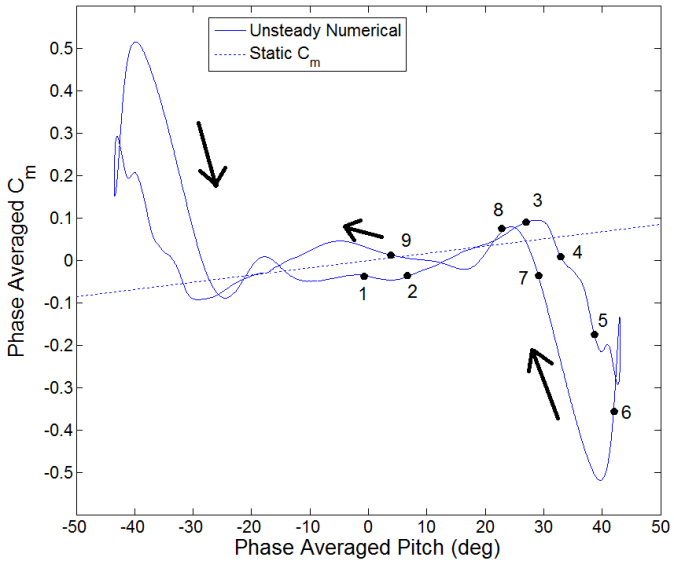

Figure B.77: Phase averaged C_m curve of simulation at $U = 8.00$ m/s, Re = 80500

B.2.6 U=8.50 m/s

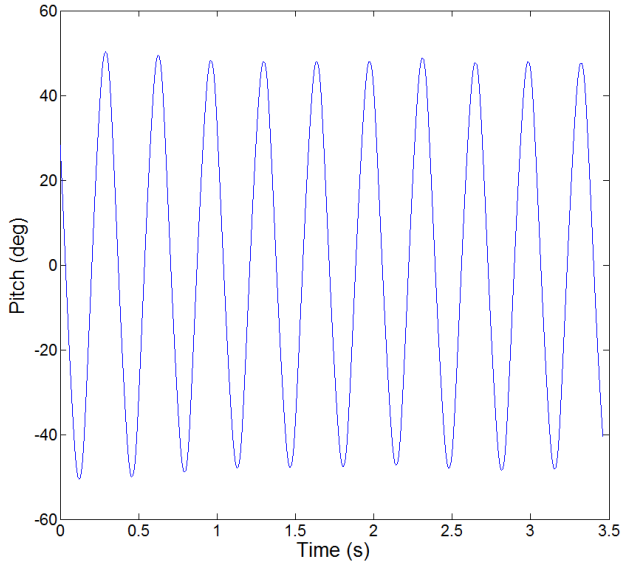

Figure B.78: Time trace of simulation at U = 8.50 m/s, Re = 85500

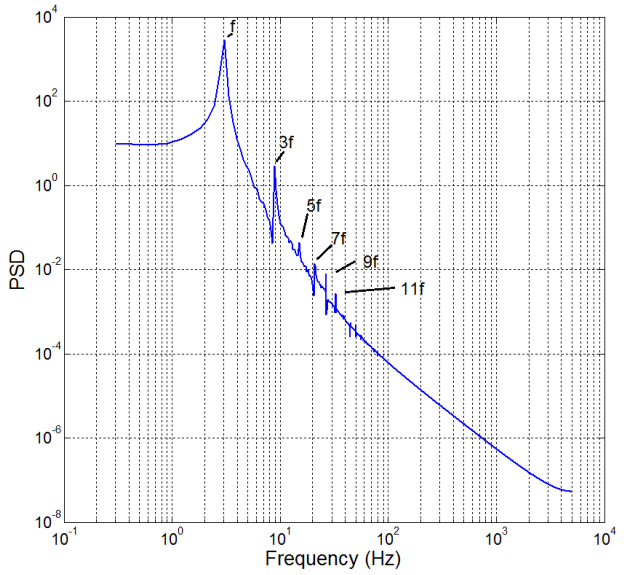

Figure B.79: PSD of simulation at U = 8.50 m/s, Re = 85500, f= 3.047 Hz

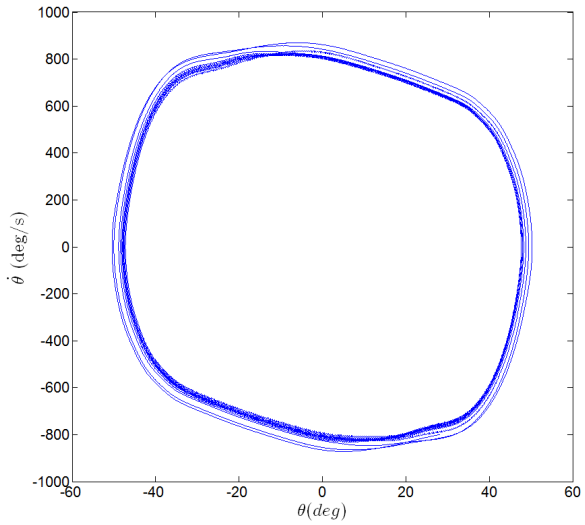

Figure B.80: Phase plane plot of simulation at $U = 8.50$ m/s, Re = 85500

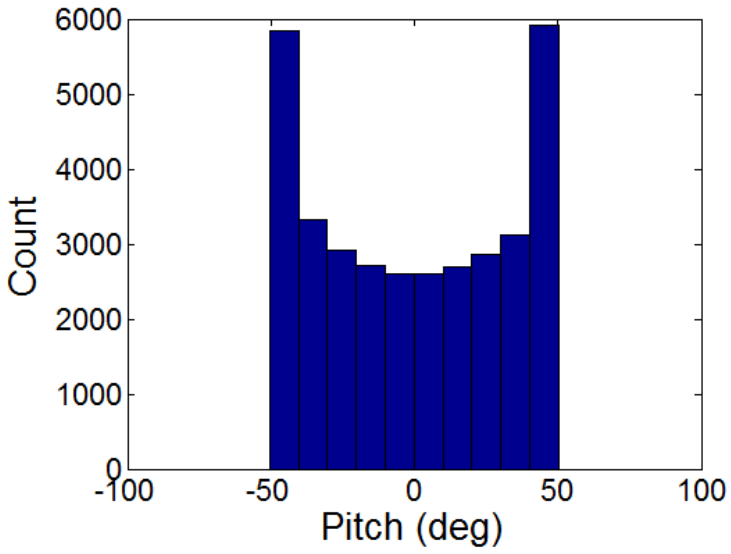

Figure B.81: Histogram of simulation at $U = 8.50$ m/s, Re = 85500

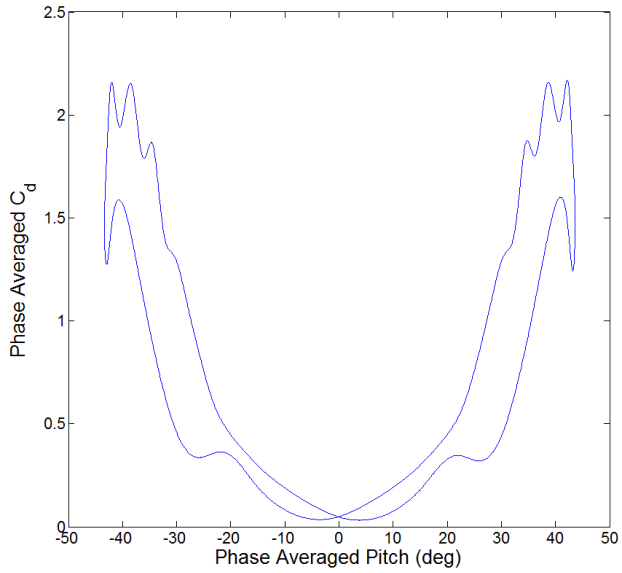

Figure B.82: Phase averaged C_d curve of simulation at $U = 8.50$ m/s, Re = 85500

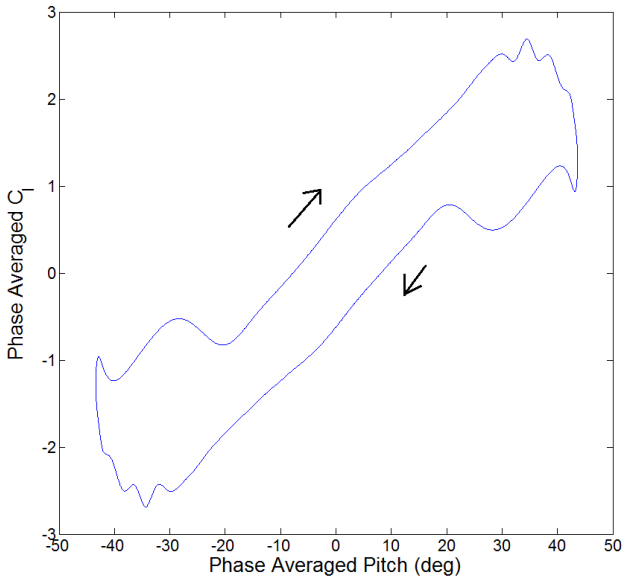

Figure B.83: Phase averaged C_l curve of simulation at $U = 8.50$ m/s, Re = 85500

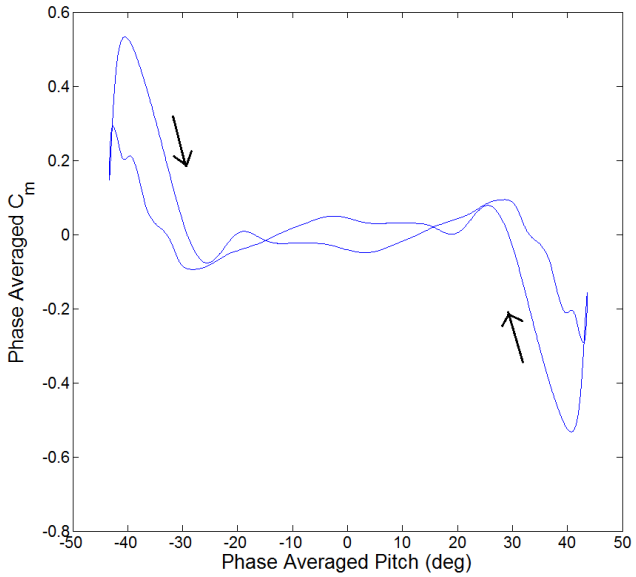

Figure B.84: Phase averaged C_m curve of simulation at $U = 8.50$ m/s, Re = 85500

B.2.7 U=10.00 m/s

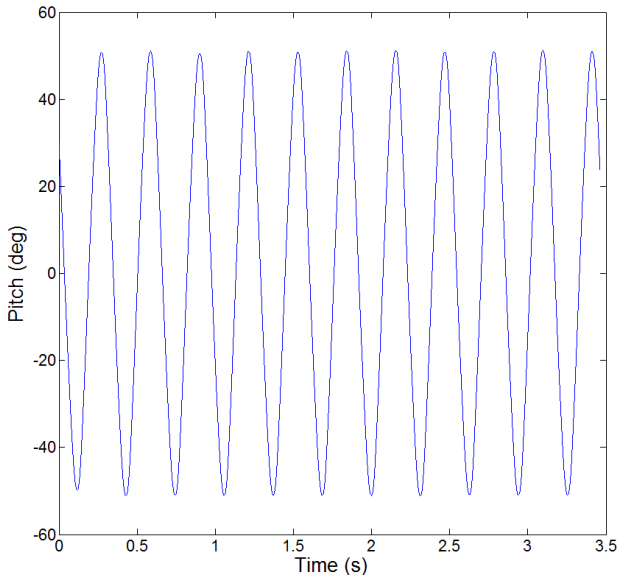

Figure B.85: Time trace of simulation at $U = 10.0$ m/s, Re = 100500

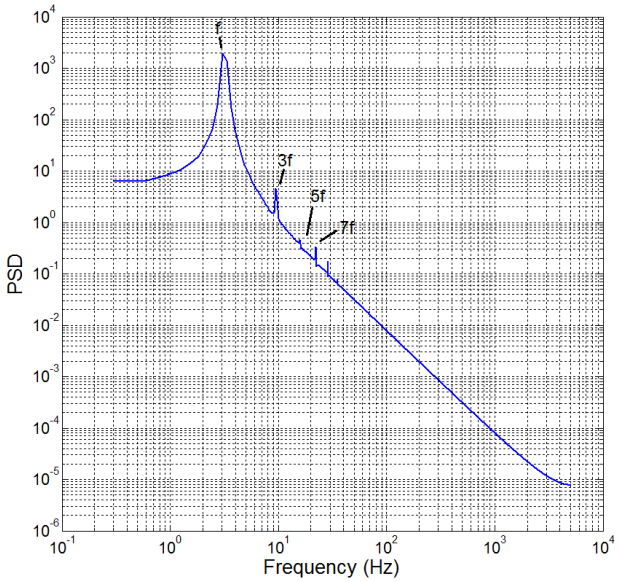

Figure B.86: PSD of simulation at $U = 10.00$ m/s, Re $= 100500$, $f=$ 3.047 Hz

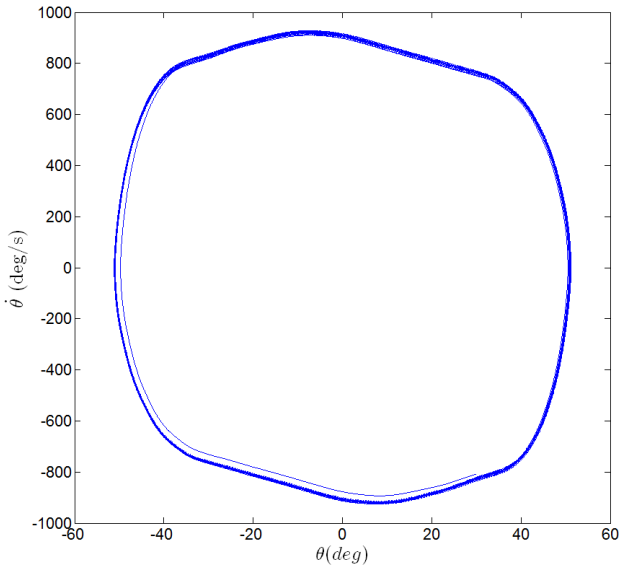

Figure B.87: Phase plane plot of simulation at $U = 10.00$ m/s, Re $= 100500$

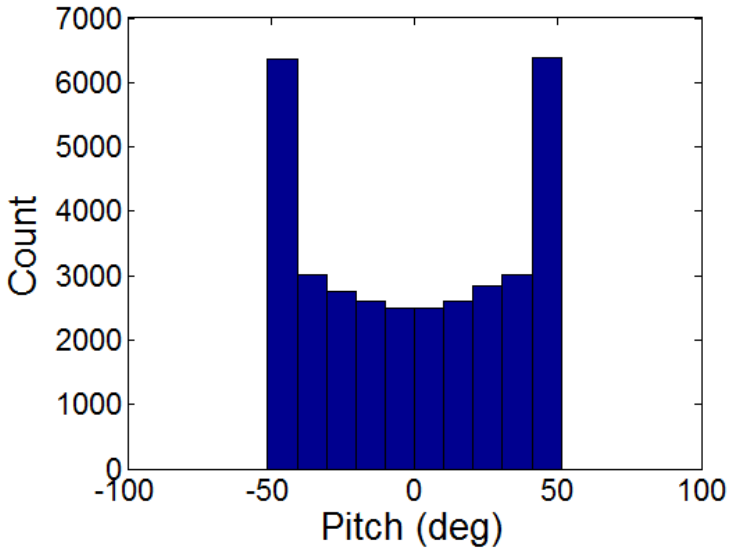

Figure B.88: Histogram of simulation at $U = 10.00$ m/s, Re = 100500

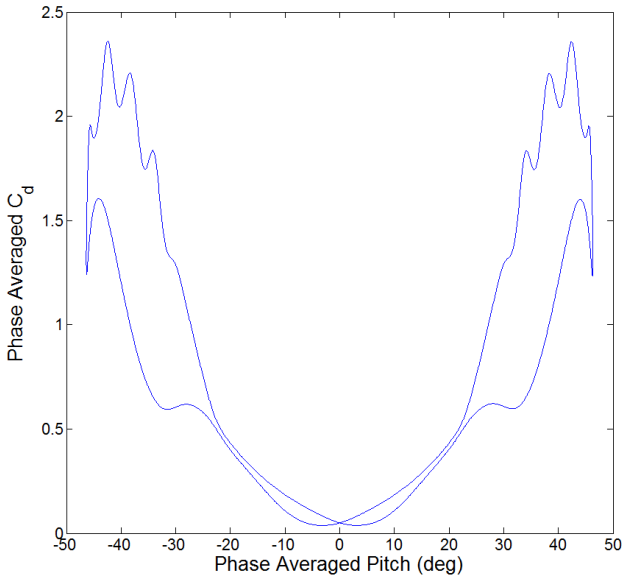

Figure B.89: Phase averaged C_d curve of simulation at $U = 10.00$ m/s, Re = 100500

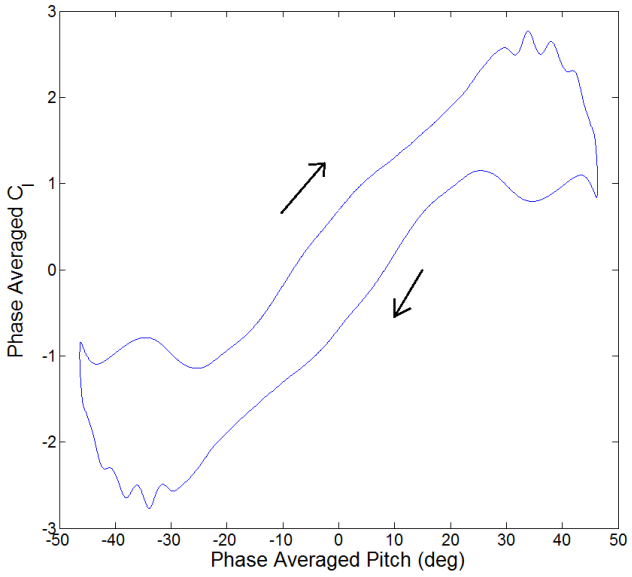

Figure B.90: Phase averaged C_l curve of simulation at $U = 10.0$ m/s, Re = 100500

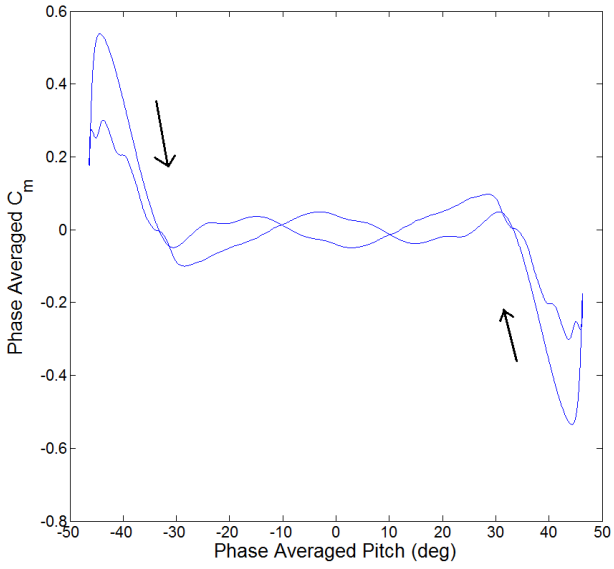

Figure B.91: Phase averaged C_m curve of simulation at $U = 10.0$ m/s, Re = 100500